

HIGH FREQUENCY MULTI-BEAM AERIAL ARRAY

A thesis submitted for the  
degree of Doctor of Philosophy  
in the Faculty of Engineering,  
University of London

by

JIN TEONG ONG

April 1971

Department of Electrical Engineering,  
Imperial College of Science and  
Technology,  
London, S.W.7.

ACKNOWLEDGEMENTS

The author would like to thank Professor John Brown for his valuable advice and encouragement throughout this programme of research, and members of the Electromagnetic Wave Group, in particular Mr. H. Page and Dr. A. dos Santos for their contributions in many discussions.

The author also wishes to thank the University of London for the Scholarship awarded for the period October 1966 to September 1969 and Signals Research and Development Establishment for their financial support (from October 1969 to March 1971) and for their sponsorship of this research project.

Thanks also go to Miss Joan Cobb for typing the thesis.

ABSTRACT

The multi-beam aerial array is studied with emphasis on the processing network required for multi-beam operation.

The general properties of the rotationally symmetric network (RSN) are investigated. A well known example of the RSN is the Luneburg Lens used in conjunction with a proposed feeding arrangement. The outputs from the lens are fed to radiators in an array of the same lens size (in wavelength) to obtain the far-field array pattern. Three types of radiators are used for the array - omni-directional, cardioid ( $1 + \cos \theta$ ), and beverage aerial radiators. The use of a lumped equivalent circuit lens in place of the continuously varied dielectric lens is considered. The effects on the array performance of varying numbers of radial lines and numbers of elements per radial line used in the equivalent lens are considered. Also considered is the effect of finite Q values for the inductors used in the circuit.

A synthesis technique to obtain the equivalent network for an 'optimum' Luneburg type lens is proposed. This network is built by interconnecting 2 port transmission line networks between the N feeds of the lens.

CONTENTS

	<u>Page</u>
ACKNOWLEDGEMENTS	II
ABSTRACT	III
CONTENTS	IV
<u>1. INTRODUCTION</u>	1
1.1 Survey of Some Existing H.F. Multibeam	2
1.1.1 Rhombic Aerials	2
1.1.2(a) Medusa System	2
1.1.2(b) Pusher System	3
1.1.2(c) Array of Beverage Aerials	4
1.1.3 The Luneburg Lens	5
1.1.3(a) The H.F. Wire Grid Luneburg Lens	7
1.2	
1.2.1 The Butler Matrix (for Linear Array)	8
1.2.2 The Rotationally Symmetric Network	9
1.3	
1.3.1 The Scaled Lens (with Frequency Translation)	10
1.3.2 The Equivalent Circuit Lens	11
<u>2. NETWORKS FOR MULTIPLE BEAM ARRAYS</u>	
2.1 Introduction	13
2.2 For Linear Array (Butler Matrix)	14
2.3 Rotationally Symmetric Network for Circular Array	16
2.3.1	17
2.3.2 Eigenvalue Solution	18

	<u>Page</u>
2.3.3 The Relationship between Butler Matrix and the Rotationally Symmetric Network	22
2.4 Rotational Symmetric Coupler - Butler Matrix Transform	23
2.5 Summary	27
Appendix A2.1 The Rotationally Symmetric Operator, [R]	28
<u>3. THE MULTIBEAM LUNEBURG LENS FED CIRCULAR ARRAY</u>	
3.1 Introduction	31
3.2 Arrangement for Multibeam Lens Fed Circular Array	32
3.2.1 Multiple Beam Lens Fed Circular Array (One Lens)	32
3.2.2 Multiple Beam Lens Fed Array (Two Lenses)	34
3.3 Behaviour of the Multibeam Lens Circular Array	39
3.3.1(a) Electromagnetic Solution of the Luneburg Lens ( $\mu_r = \epsilon_r$ )	39
3.3.1(b) Electromagnetic Solution of the Ordinary Luneburg Lens $\epsilon(r) = n^2(r) = (2-r^2)$	44
3.3.1(c) The Series $U_m(Za)$ and ${}_1F_1(\alpha, \gamma, Za)$	45
3.3.2 The Output Distribution of the Lens at the Feeds	47
3.3.2(a) Effects of Spacing Between Feeds	48
3.3.2(b) Effects of Mode Reflection Coefficients on Output Distribution	49
3.3.3 Far-Field Radiation Pattern	56
3.3.3(a) Behaviour of Lens System for Small Lens Diameters	57
3.3.3(b) Effect of Feed Spacing and Lens Diameter	60
3.3.3(c) Use of Omni-directional and Beverage Aerial Radiators	72
Summary	80
<u>Appendix 3</u>	
A3.1 Scattering Matrix of a 2N-Port Formed from Two N-Port Luneburg Lens Type Structures	82

	<u>Page</u>
A3.2.1 Solution of Equation 3.11	85
A3.2.2 Series Solution for $U_m(Z)$	88
A3.3 Description of Program Subroutines	90
<u>4. THE EQUIVALENT CIRCUIT LUNEBURG LENS</u>	102
4.2 Equivalent Circuit for the TE Mode Luneburg Lens	102
4.2.1 Decomposition of Circular Network into a Ladder Network for Each Mode	106
4.2.2 Behaviour of the Equivalent Ladder Network for Different Modes	109
4.3 Minimum Number of Elements Required for the Equivalent Circuit Lens	111
4.3.1 Component Values for Equivalent Circuit Lens	113
4.3.2 Equivalent Circuit Lens Behaviour	115
4.3.2(a) Effect of Variation of NELR on the Behaviour of Mode Reflection Coefficient	115
4.3.2(b) Effect of Variation of N on the Behaviour of Mode Reflection Coefficient	116
4.3.3 Far-field Pattern from the Equivalent Circuit Lens (Using Cardioid (1+cosine) Radiators)	124
4.3.4 The Effect of Losses in the Equivalent Circuit due to Losses in the Inductors	135
4.4	139
4.4.1 Reduction of Modes	141
4.4.2 Other Methods of Reducing Feed Numbers	142
4.5 Use of the Equivalent Circuit Lens with Beverage Aerial Radiators	145
4.6 Summary	152
Appendix 4.1 Description of Program Subroutines	154
Appendix 4.2 Mode Reduction by a Factor, k	160

	<u>Page</u>
<u>5. THE OPTIMUM LENS AND ITS DESIGN</u>	
5.1 Introduction	165
5.2 Equivalence Between Linear and Circular Arrays	166
5.2.1 Relationship Between Near and Far-field Excitations	169
5.3 The Optimum Lens	173
5.3.1 Behaviour of Mode Reflection Coefficient	173
5.3.2 Feed Output Distribution	176
5.3.3 Far-field Patterns	176
5.4 Synthesis of the Optimum Lens Network	180
5.5 Possible realisation of 2-Port Network from the $Y_{12}$ Parameter Obtained	187
5.5.1 A Single Section Transmission Line Network	188
5.5.2 The Three Section Transmission Line Network	189
5.5.3 The Two Section Transmission Line Network with Shunt Loading	191
(a) Capacitive Loading	191
(b) Inductive Loading	192
(c) Parallel Resonant Loading	193
5.6 Summary	195
Appendix A5.1 Far-field Excitation due to Exponential Mode Excitation for (1+cosine) Radiators	197
Appendix A5.2 Description of Computer Program Subroutines	200
<u>6. CONCLUSIONS AND SUGGESTION FOR FURTHER WORK</u>	204
REFERENCES	207

## CHAPTER 1

### 1. INTRODUCTION

This thesis deals with the study and design of a compact wide band high frequency (3-30 Mhz) multibeam aerial array. The emphasis in this investigation is on the processing network required for multibeam operation.

This chapter briefly surveys some multiple beam array systems. It also serves as an introduction to the following chapters. Section 1.1 surveys some existing H.F. multibeam aerial systems. In section 1.2 some processing networks for multiple beam operation are reviewed. Some ideas for a multiple beam system are considered briefly in section 1.3.

Chapter 2 will deal with the general properties of the combining networks used for multibeam operation - the Butler Matrix for linear arrays and the Rotationally Symmetric Network for circular arrays. In chapter 3 the use of a Luneburg Lens in conjunction with N surrounding feeds and circulators or directional couplers to obtain a 2N port rotationally symmetric network is proposed. Chapter 4 investigates the behaviour of the equivalent circuit Luneburg Lens. Chapter 5 deals with the synthesis of a Luneburg-type combining network for multibeam operation.



## 1.1 Survey of Some Existing H.F. Multibeam Aerial System

### 1.1.1 Rhombic Aerials<sup>1</sup>

A widely used aerial is a form of two or three nested or interleaved Rhombic aerials, each covering a 2:1 frequency range. Each nest of Rhombic aerials is directional and can receive from only two opposite directions. For multiple beam reception several nests of Rhombics are positioned so that all directions in azimuth are covered. The Rhombics have to be spaced sufficiently apart to minimise coupling. Because of this a large ground area is required (approximately 240 acres for a system covering the frequency range 3 MHz to 30 MHz). This is one of the disadvantages of this system. The other drawback of this system is the relatively high side-lobe of between -7db to -10db.

### 1.1.2

Systems described under this sub-section have each output in the array divided, generally, into as many outputs as the number of beams required at any one time. Each sub-divided output from all or some of the aerials are phase so that for any particular direction of reception, the signal adds up in phase.

#### 1.1.2(a) Medusa System<sup>2,3</sup>

In this system the aerials are omni-directional inverted cones, positioned randomly in an array of several wavelength dimensions. The outputs are phased for any combination of frequency

and direction using a high speed computer. This system provides a number of independent outlets each of which can be steered by the direction control equipment. This system though flexible in design and operation is expensive due mainly to the high cost of the high speed computer which makes up the direction-control-equipment. The area occupied by such a system (5-25MHz) would occupy about 64 acres.

#### 1.1.2(b) Pusher System<sup>4</sup>

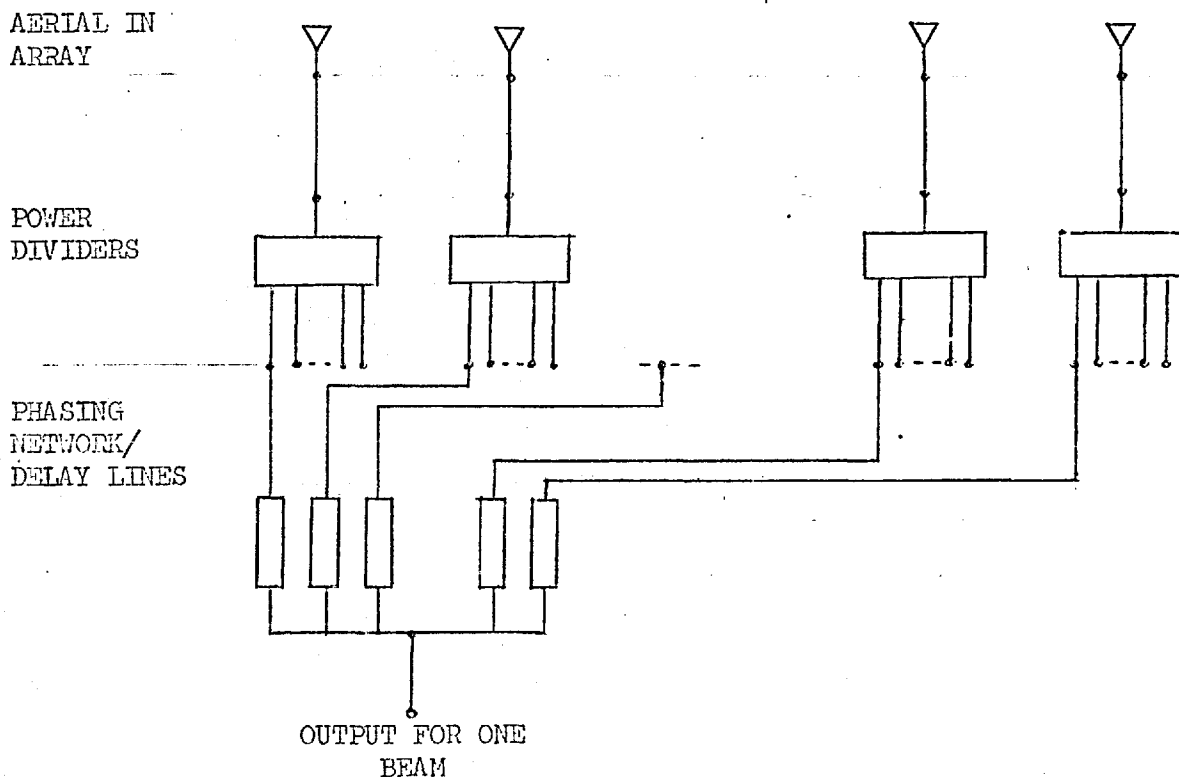


Fig. 1.1 TYPICAL ARRANGEMENT FOR THE PUSHER SYSTEM

The aerials (monopoles) are arranged in a circular array in

the Pusher system. Typically each output from the aerials is divided into eight parts. There are eight phasing networks so that the array can receive simultaneously from any eight (of the total of 24 directions - there are 24 radiators equally spaced around the array).

Although the actual area occupied by the array itself is small (about 5 acres for a 150m diameter array for the 1.5 to 10MHz band) the performance of the system is poor. The side lobe ratio is high - about -4.2db at 2MHz and -6.6db at 8MHz. The gain is also poor.

#### 1.1.2(c) Array of Beverage Aerials<sup>5</sup>

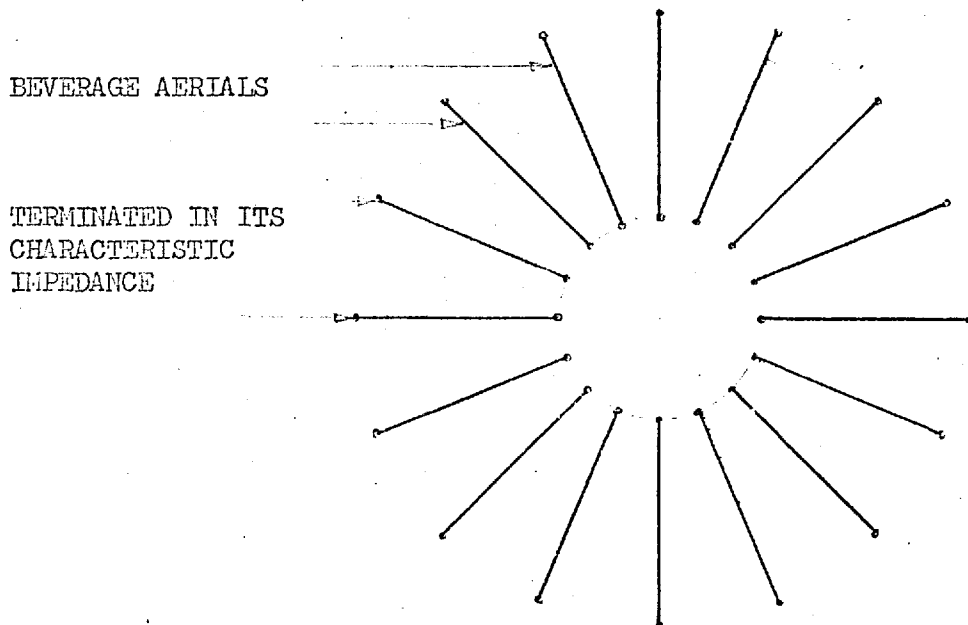


Fig. 1.2 CIRCULAR ARRAY OF BEVERAGE AERIALS

A system under study in conjunction with the work reported here uses Beverage aerials arranged radially to form an array. The outputs are combined as in the Pusher system. The advantage of this system is the simplicity and the wide bandwidth of the individual Beverage aerials.

Because of the need for power division at the output of each of the aerials, amplification may be required to give an acceptable signal to noise ratio.

### 1.1.3 The Luneburg Lens<sup>6</sup>

The Luneburg Lens was first proposed as an optical lens. It has been used at microwave frequencies and lately at the H.F. band. The Luneburg Lens is a cylindrical or spherical structure, with refractive index which varies with distance from the centre of the lens.

Owing to the variation of refractive index a plane wave arriving in any direction is focussed onto a point on the other side of the lens. As long as there are feeds at the focal point, the lens can receive from any direction (due to rotational symmetry).

Such lenses are used at microwave frequencies. At such frequencies dielectric materials are used. In optics the dimensions of the lens are assumed to be large compared with the wavelength. In chapter 2 the electromagnetic solution to the Luneburg Lens is given for the case where  $\mu_r = \epsilon_r = \sqrt{2-r^2}$ ,  $r$  = normalised radius. This and other solutions ( $\epsilon_r = (2-r^2)$ ,  $\mu_r = 1$ ) suggest that a minimum

diameter of about 1.5 wavelength is required for the lens to behave properly.

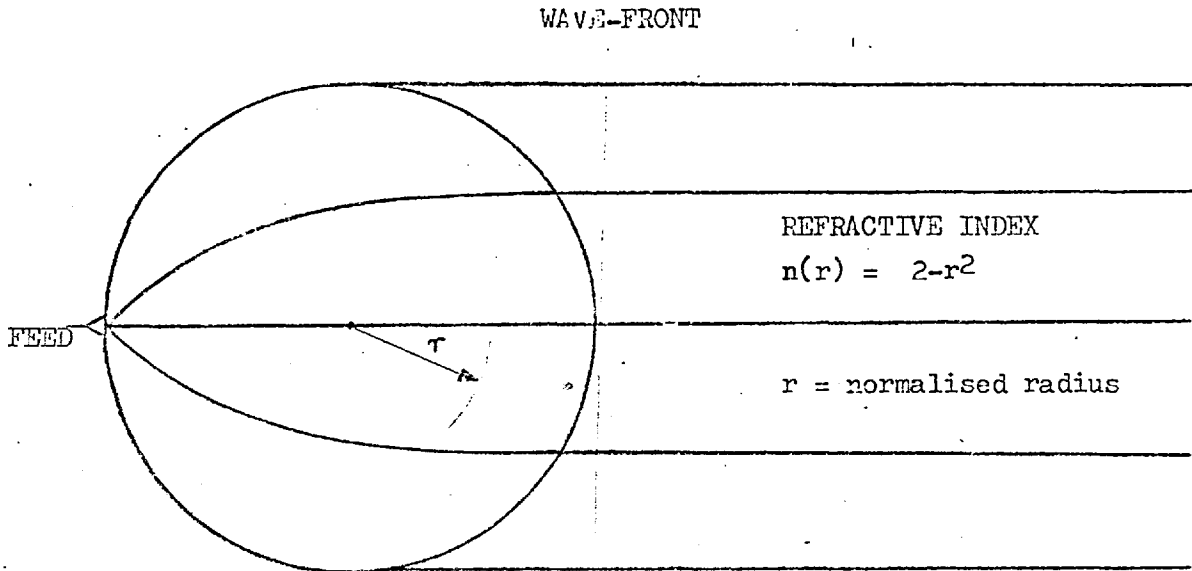


Fig. 1.3 THE LUNEBURG LENS

The Luneburg Lens has so far been used as part of the radiating structure in an aerial system. But the "Lens" can be thought of as a processing network - used in conjunction with feeds connecting the lens to radiators as fully described in Chapter 3. The H.F. Wire Grid lens (described in the following paragraph) could be looked upon as a processing network, directly connected via feeds to the radiators (extended horns). It is probably more economical at H.F. to use a network to simulate this lens type behaviour (e.g. the equivalent circuit lens proposed in section 1.3.3).

### 1.1.3(a) The H.F. Wire Grid Luneburg Lens<sup>7,8</sup>

The variation of dielectric constant can be achieved by using two wire meshes, one above the other. By varying the spacing between the grids (as a function of radius) the equivalent refractive index can be varied as required in a Luneburg Lens. Such a lens with horns extending from the edges has produced quite satisfactory results (9).

One of the major drawbacks of the H.F. Wire-Grid antenna is its high cost - most probably due to the close tolerances involved in the construction of the lens. For a 600 ft. diameter lens the spacing between the mesh at the centre of the lens is 7"; at the edge of the lens the spacing is 12". The other disadvantage of this aerial is the low efficiency of the system due to blocking by the feeds around the lens.

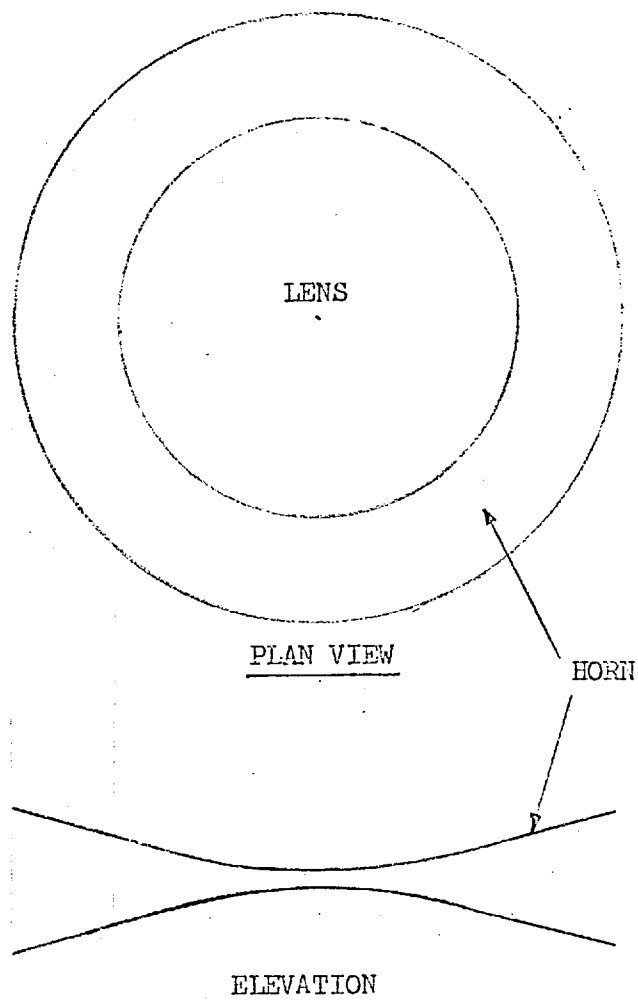


Fig. 1.4 H.F. WIRE GRID LUNEBURG  
LENS ANTENNA

## 1.2

This section looks at processing networks for multibeam operation, which do not involve power division. The Butler Matrix (for linear arrays) and a rotationally symmetric network (for circular arrays) will be examined briefly. This subject will be studied in detail in Chapter 2.

### 1.2.1 The Butler Matrix<sup>10</sup> (for Linear Array)

The Butler Matrix is a network obtained by interconnecting 3db directional couplers and phase shifters in a matrix to obtain N output and N input ports. The ports are uncoupled. For the transmission mode, the N outputs are connected by equal length transmission lines to equally spaced aerials in a linear array. N independent beams can be obtained by

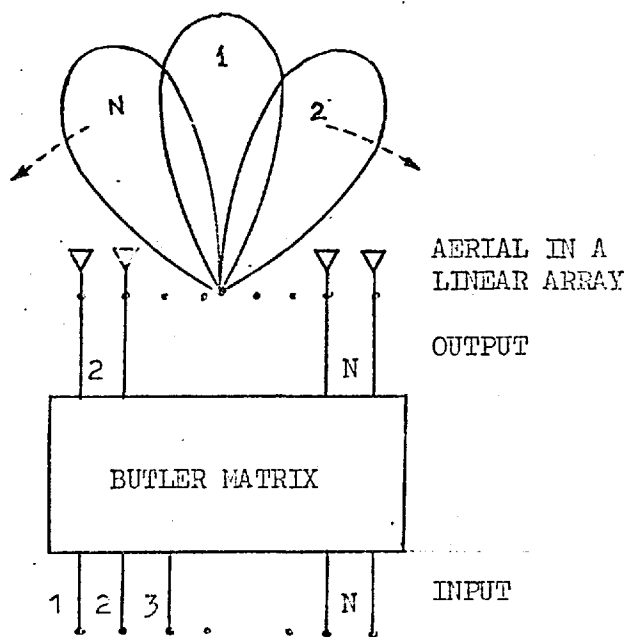


Fig. 1.5 THE BUTLER ARRAY

exciting the corresponding input ports. Because the array is linear, the effective aperture of the array decreases cosinusoidally with the angle of the beam from broadside. A circular array will avoid this drawback. The limitations of the Linear Butler Array in terms of output amplitude distribution has been obtained by Shelton (11)

for a lossless matched feed network.

### 1.2.2 Rotationally Symmetric Network

The main property of such a network is its rotational symmetry. Also the outputs from the network must be such that when connected to radiators in a circular array, a directive beam is obtained in the far-field. The network has  $N$  input and  $N$  output ports. By changing the excitation from one input port to the next the signals at the  $N$ -output ports would be unchanged except for a rotation of the signals by one port.

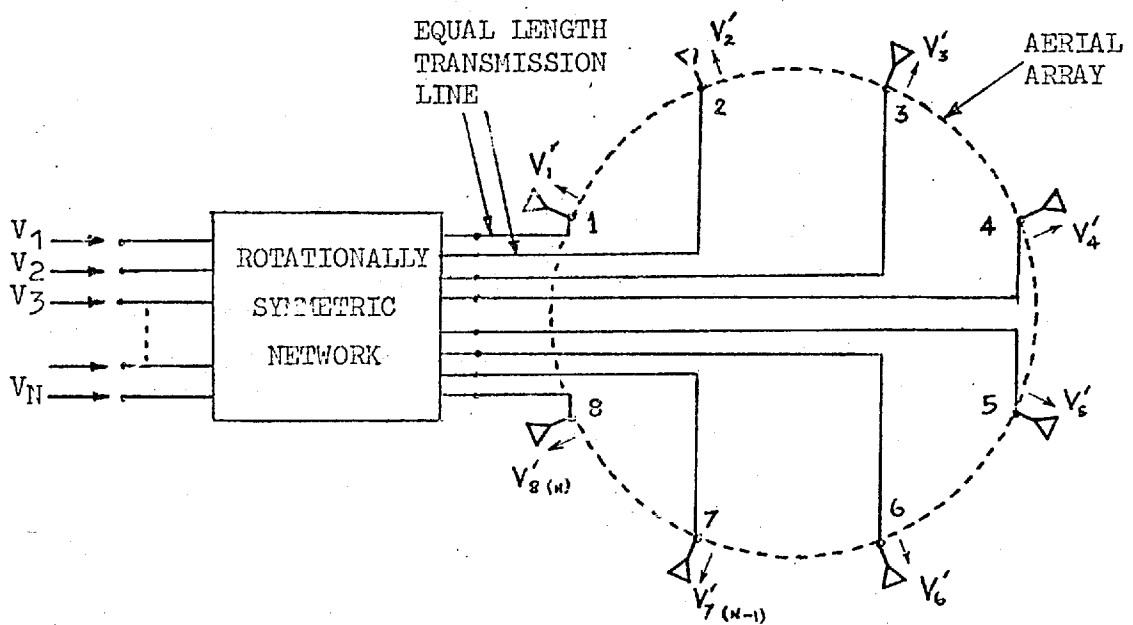


Fig. 1.6 ROTATIONALLY SYMMETRIC ARRAY

For  $V_1 = 1$  only

$$V'_1 = a ; V'_2 = b ; V'_3 = c ; \dots\dots V'_{N-1} = c ; V'_N = b$$



For  $V_2 = 1$  only

$$V'_1 = b \ ; \ V'_2 = a \ ; \ V'_3 = b \ ; \ \dots\dots V'_{N-1} = d \ ; \ V'_N = c,$$

etc.

One way of achieving this characteristic is by the use of two linear Butler type matrices. The limitations involved are considered in Chapter 2. A Luneburg type lens or its equivalent used in conjunction with N surrounding feeds satisfies the necessary properties required for a multibeam circular array.

### 1.3

Some ideas derived from the concept discussed in the preceding paragraph will be considered briefly in this section, and in detail in Chapter 3 and following chapters.

#### 1.3.1 Scaled Lens (with Frequency Translation)

At the High Frequency band a full scale dielectric Luneburg Lens is not practicable because of the large diameters (some hundred metres) involved. However, a much smaller lens could be used if signals arriving at the periphery of the "lens" are picked up at a discrete number of feed points and translated to U.H.F. band (amplification is obtained in this up-conversion process). The signals are then processed using the much scaled down lens and the frequency is down-converted to produce the original H.F. signal.

The Luneburg Lens is basically a wideband device but with the introduction of frequency translation the system becomes frequency

dependent. Calculations for a H.F. system (3-30MHz) suggest that for a 200 metre array a scaled-down lens has a bandwidth of only 1.5 MHz. Therefore over the whole H.F. range 18 scaled-down lenses will be needed, together with extensive use of filters and other components. The cost of this system became excessive due to the large numbers of filters needed plus mixers, circulators and local oscillators. Therefore, over such a wide frequency band this system is not practicable.

### 1.3.2 Equivalent Circuit Lens

The close tolerances required in the construction of the H.F. Wire Grid lens was one of the reasons for the high cost of the system. It was thought that there could be a trade-off between mechanical and electrical tolerances if an equivalent circuit Luneburg Lens were used. The equivalent network is made up of an inter-connection of inductors and capacitors - their values depending on the "distance" of the equivalent element away from the centre of the lens.

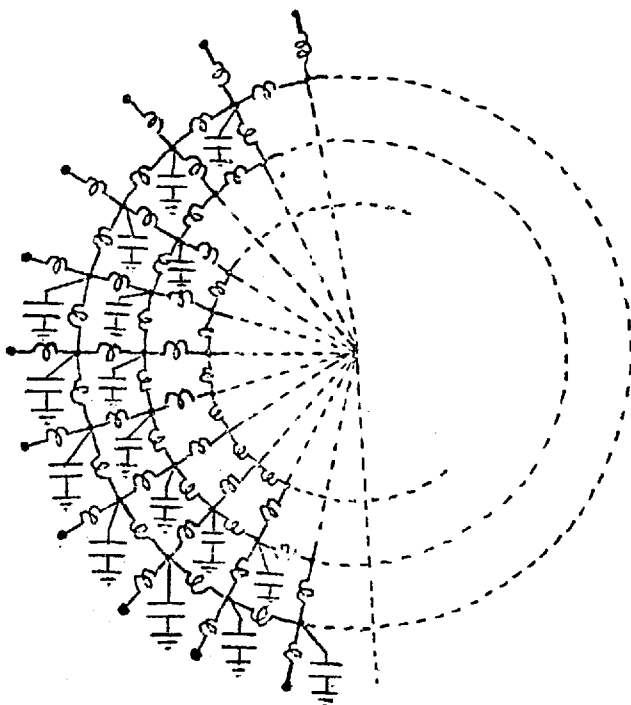


Fig. 1.7 EQUIVALENT CIRCUIT LENS

The equivalent circuit will be used in conjunction with

circulators and radiating structures (typically, doublets, beverage  
aerials and monopole) using the arrangement described in Chapter 3.  
The equivalent circuit is studied in Chapter 4. Among the problems  
studied are: the minimum number of elements required to simulate a  
dielectric lens, coupling between feeds, types of radiators used  
and the effect of finite  $Q$  of the inductors used in the circuit.

## CHAPTER 2

### 2. NETWORKS FOR MULTIPLE BEAM ARRAYS

#### 2.1 Introduction

This chapter studies the general properties of the network used for feeding an array to facilitate multiple beam operation.

In a linear array the Butler Matrix<sup>10</sup> is already well known. For a circular array a rotationally symmetric network will be studied as a  $2N$  port network with  $N$  outputs feeding the  $N$  radiators and  $N$  inputs, for each of the  $N$  beams (for the transmitting case).

A special type of the rotationally symmetric network, designated the "Rotationally Symmetric Coupler" (RSC) can be transformed into a Butler Matrix Network by connecting two sets of  $N$  appropriate phase shifters to the  $N$ -input and  $N$ -output ports. The transformation is reversible.

## 2.2 For Linear Array (Butler Matrix)<sup>10</sup>

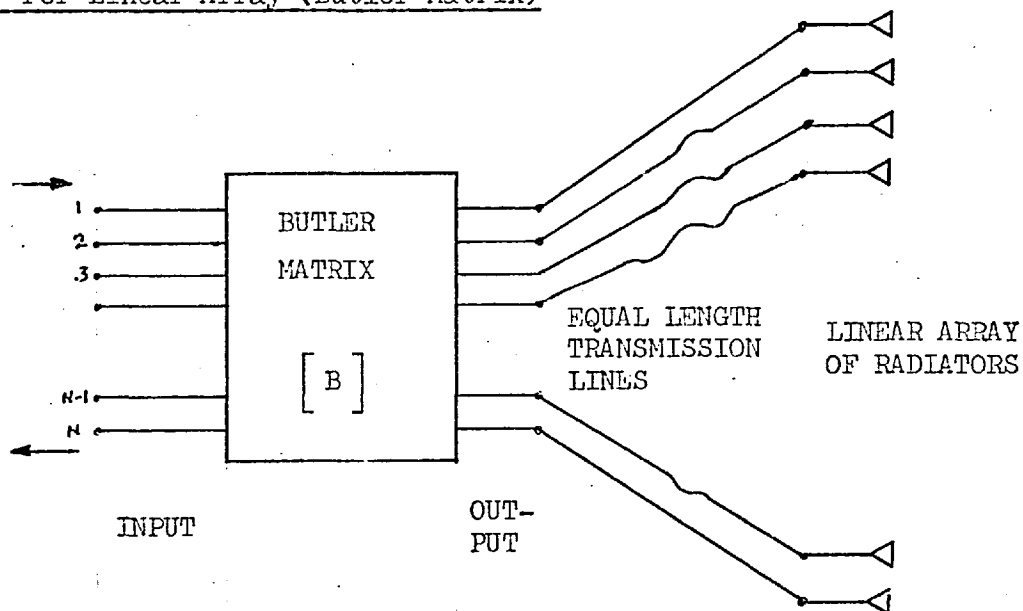


Fig. 2.1 BUTLER ARRAY

The Butler Matrix can be described as a  $2N \times 2N$  matrix, i.e. a network with  $N$  input ports and  $N$  output ports. The  $N$  output ports are connected to a linear array of radiators via equal length transmission lines. The scattering matrix can be written as:-

$$B = \begin{bmatrix} P_{11} & P_{12} \\ P_{21} & P_{22} \end{bmatrix} \quad (1)$$

The input and output ports are decoupled so that  $[P_{11}] = [P_{22}] = [0]$ . Owing to reciprocity  $P_{21} = \tilde{P}_{12} = [\tilde{P}]$

i.e.

$$B = \begin{bmatrix} 0 & P \\ \tilde{P} & 0 \end{bmatrix} \quad (2)$$

where  $\tilde{P} = \left[ \{p_1\} , \{p_2\} \dots \dots \{p_N\} \right]$  (3)

$\{p_1\} = \{p\}$  represents the outputs from the matrix network when input 1 is excited, i.e. the current distribution of the array. For multibeam operation  $\{p_2\}$  will be similar to  $\{p_1\}$  and  $\{p_3\}$ ,  $\{p_2\}$ , etc., except for a progressive phase difference. Therefore for N equally spaced beams

$$\{p_2\} = D \{p_1\} = D \{p\}$$

and more generally (4)

$$\{p_r\} = D^r \{p\}$$

where  $D = \text{diag.} (1, e^{j\phi}, \dots \dots e^{j(N-1)\phi})$  (5)

and  $\phi = \frac{2\pi}{N}$

Rewriting P from eqn. (3)

$$[\tilde{P}] = \left[ \{p\} , D \{p\} \dots \dots D^{N-1} \{p\} \right] \quad (6)$$

Substituting for D in (6) on rearranging the R.H.S.

$$P = \begin{bmatrix} p_1 & & & \\ & p_2 & & \\ & & \cdot & \\ & & & \cdot \\ & & & & p_N \end{bmatrix} \begin{bmatrix} x^* \end{bmatrix} \quad (7)$$

$$= \text{diag.} \{p\} \begin{bmatrix} x^* \end{bmatrix}$$

$$\text{where } X = \frac{1}{\sqrt{N}} \begin{bmatrix} 1 & 1 & 1 & \dots & 1 \\ 1 & e^{-j\phi} & e^{-j2\phi} & \dots & e^{-j(N-1)\phi} \\ 1 & e^{-j2\phi} & e^{-j4\phi} & \dots & e^{-j(N-1)2\phi} \\ \dots & \dots & \dots & \dots & \dots \\ 1 & e^{-j(N-1)\phi} & e^{-j(N-1)2\phi} & \dots & e^{-j(N-1)^2\phi} \end{bmatrix} \quad (8)$$

The  $r$ th column of  $[X]$  is the eigenvector corresponding to the eigenvalue,  $e^{j(r-1)\phi}$ , of the symmetrical operator,  $[R]$  (Appendix A2.1).

For a lossless network  $P \tilde{P}^* = I$

$$\text{i.e. } p_r p_r^* = 1 \quad \text{for all } r^+ \quad (9)$$

Rewriting (1) for a lossless network,

$$[B] = \begin{bmatrix} 0 & X^* \\ \tilde{X}^* & 0 \end{bmatrix} \quad (10)$$

### 2.3 Rotationally Symmetric Network for Circular Array

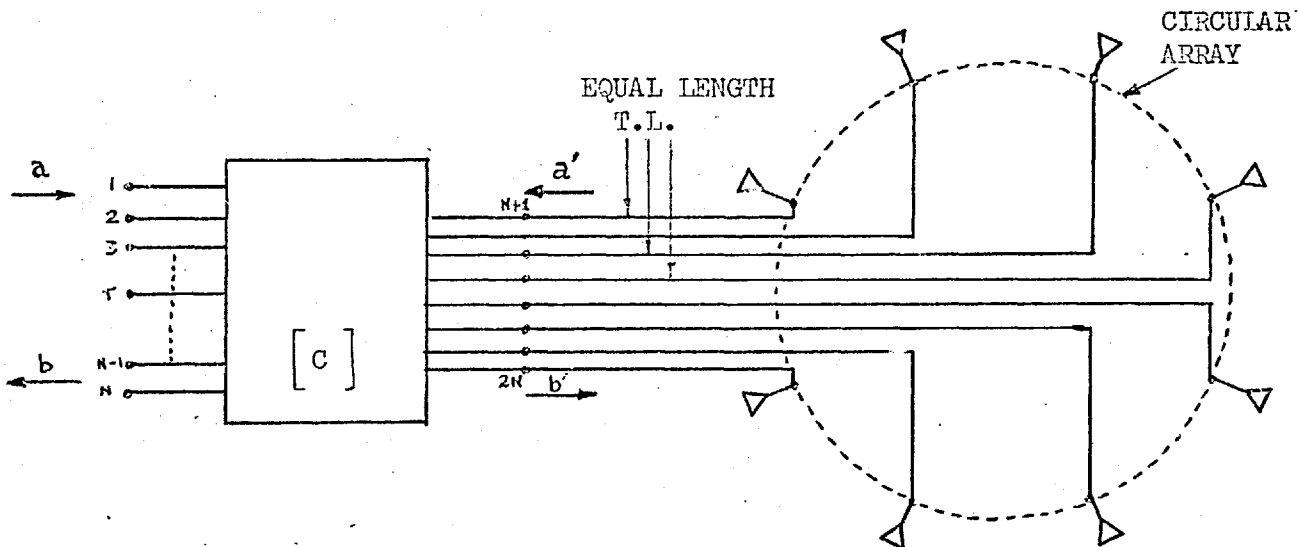


Fig. 2.2 ROTATIONALLY SYMMETRIC ARRAY

<sup>+</sup> implying orthogonal beams, Shelton, Allen, etc. (11, 29, 30)

### 2.3.1

As in the case for linear array we can write  $C$  as

$$[C] = \left[ \begin{array}{c|c} 0 & T \\ \hline \tilde{T} & 0 \end{array} \right] \quad (11)$$

with  $T \tilde{T}^* = [I]$ , (12)

for a lossless network . Using scattering matrix formulations

$$\begin{Bmatrix} b \\ b' \end{Bmatrix} = \begin{bmatrix} 0 & T \\ \tilde{T} & 0 \end{bmatrix} \begin{Bmatrix} a \\ a' \end{Bmatrix} \quad (13)$$

Let  $\tilde{T} = [ \{t_1\} , \{t_2\} , \dots , \{t_N\} ]$  , (14)

where  $\{t_1\}$  ,  $\{t_2\}$  ,  $\dots$  and  $\{t_N\}$  represent the current distributions on the array when the respective input ports 1, 2,  $\dots$  , N, are excited.  $\{t_1\}$  and  $\{t_2\}$  ,  $\{t_2\}$  and  $\{t_3\}$  ,  $\{t_r\}$  , and  $\{t_{r+1}\}$  differ from one another only in a rotation of the ports positions, i.e.

$$\tilde{T} = [ \{t\} , R \{t\} \dots R^{N-1} \{t\} ] \quad (15)$$

where  $[R] = \begin{bmatrix} 0 & 0 & \dots & 1 \\ 1 & 0 & \dots & 0 \\ 0 & 1 & \dots & 0 \\ \dots & \dots & \dots & \dots \\ 0 & 0 & \dots & 1 \end{bmatrix} = X D X^*$  (Appendix A2.1) (16)

i.e.  $\tilde{T} = X [ X^* \{t\} , D X^* \{t\} , \dots , D^{N-1} X^* \{t\} ]$

$$= X [ \{p'\} , D \{p'\} , \dots , D^{N-1} \{p'\} ]$$

i.e.  $\tilde{T} = X [ p' ]_d X^*$ , (17)



$$\text{where } \{p'\} = X^* \{t\} \quad (18)$$

$$\text{and } [p']_d = \text{diag} (\{p'\})$$

For lossless network

$$T \tilde{T}^* = I$$

$$\text{i.e. } [p']_d [p']_d^* = [I]$$

$$|p'_r|^2 = 1, \text{ for } r = 1 \text{ to } N \quad (19)$$

from (18)

$$p'_r = \sum_{i=1}^N t_i e^{j(r-1)(i-1)\theta} \quad (20)$$

$$\text{i.e. } |p'_r| = 1, \text{ from (19)}$$

$$\text{i.e. } p'_r = e^{j\theta r}, \quad (21)$$

$$r = 1 \text{ to } N$$

(20) gives  $N$  equations, with  $2N$  unknowns ( $t_i$  is complex). If either the phases or the amplitudes of  $t_i$  is specified the other unknowns can be obtained.

We will see in the next section that  $p'_r$  is in fact the eigenvalue corresponding to the  $r$ th mode.

### 2.3.2 Eigenvalue Solution

For a rotationally symmetric system of  $N$  ports, using the following matrix notation:-

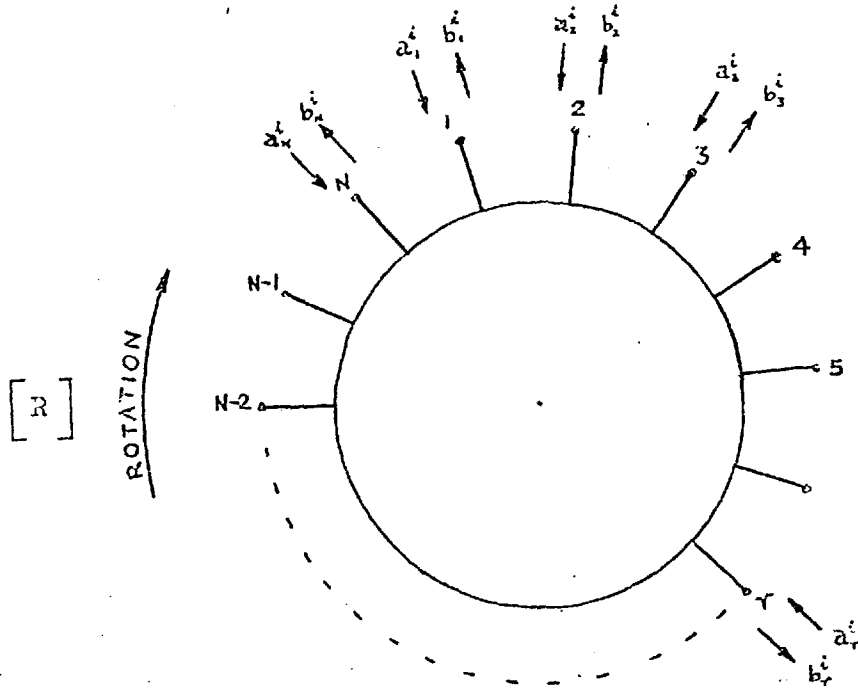


Fig. 2.3 ROTATIONAL SYMMETRY

$$\{a^i\} = \begin{Bmatrix} a_1^i \\ a_2^i \\ \cdot \\ \cdot \\ \cdot \\ a_N^i \end{Bmatrix}, \text{ the incident field} \tag{22}$$

$\{b\}$  = the reflected fields

$[S]$  = scattering matrix of the Rotationally Symmetric network

$$R = \begin{bmatrix} 0 & 0 & \dots & 0 & 1 \\ 1 & 0 & \dots & 0 & 0 \\ 0 & 1 & & \cdot & \cdot \\ \cdot & & & \cdot & \cdot \\ \cdot & & & 0 & \cdot \\ 0 & \cdot & \dots & 1 & 0 \end{bmatrix}, \text{ the rotational operator,}$$

$$\{b\} = [S] \{a^i\} \quad (23)$$

Owing to rotational symmetry [R] operating on the input signals will give an output

$$\{b\}' = [S][R] \{a^i\} \quad (24)$$

this output should be the same as that obtained by [R] operating on {b} in equation (23)

$$\text{i.e. } R \{b\} = \{b\}' \quad (25)$$

Substituting for {b} from eqn.(23) and for {b}' from equation 24,

$$[R][S] \{a^i\} = [S][R] \{a^i\}$$

$$\text{i.e. } [R][S] = [S][R]$$

[R] and [S] commutes, therefore they share the same eigen solutions (obtained in Appendix A2.1)

$$\text{i.e. } \{a^m\} = \left\{ \begin{array}{c} 1 \\ e^{jm\phi} \\ \cdot \\ \cdot \\ e^{jm(N-1)\phi} \end{array} \right\} \quad \begin{array}{l} \text{is the } m\text{th eigenvector for} \\ [R] \text{ and } S \\ \phi = \frac{2\pi}{N} \end{array}$$

or {a<sup>m</sup>} is the solution for the mth mode

Since {a<sup>m</sup>} is the mth eigenvector for the system, a signal {a<sup>m</sup>} applied to the N ports of the structure will give rise to a reflected signal {b} which is similar in form to {a<sup>m</sup>} except for the constant λ<sub>m</sub> which is the reflection coefficient of the mth mode.

$$\text{i.e. } \{b\} = \lambda_m \{a^m\} \quad (26)$$

$$\text{but } \{b\} = [S] \{a^m\} \quad (23)$$

Equating (23) and (26)

$$[S] \{a^m\} = \lambda_m \{a^m\}, \quad (27)$$

so that  $\lambda_m$  is the  $m$ th eigenvalue corresponding to the  $m$ th eigenvector or mode.

Extending equ.(27) to take into account all the eigenvector  $\{a^m\}$ ,  $m = 1$  to  $N$

$$[S][X] = [X][\lambda]_d \quad (28)$$

where  $[X] = [\{a^1\}, \{a^2\}, \dots, \{a^N\}]$  (Appendix A2.1)

and  $[\lambda]_d = \text{diag}(\lambda_1, \dots, \lambda_N)$

and  $\lambda_r =$  reflection coefficient of  $r$ th mode

hence  $S = [X][\lambda]_d X^{-1}$

$$S = X[\lambda]_d X^* \quad (29)$$

$$\text{or } S_{rs} = \sum_{m=1}^N \lambda_m e^{j(m-1)(r-s)\phi} \quad (30)$$

For a symmetrical current distribution

$$S_{rs} = S_{sr}, \text{ giving from eqn.(30) -}$$

$$\lambda_k = \lambda_{N-k} \quad (k = 1 \text{ to } N-1) \quad (31)$$

$$\text{i.e. } S_{rs} = \sum_{m=1}^{\frac{N'}{2}} (\lambda_0 + \lambda_n \cos(m-1)(r-s)\phi) \quad (32)$$

$$\left( + \lambda_{\frac{N}{2}(-1)^{N/2}}, \text{ if } N \text{ is even} \right)$$

where  $\frac{N'}{2} = \frac{N}{2} - 1$ , for  $N$ , even

$$= \frac{N-1}{2}, \text{ for } N, \text{ odd}$$

### 2.3.3 Relationship between Butler Matrix and Rotationally Symmetric Network.

for Butler Matrix

$$B = \begin{bmatrix} 0 & X \\ \tilde{X} & 0 \end{bmatrix} \quad (10)$$

for Rotationally Symmetric Network

$$C = \begin{bmatrix} 0 & X[\lambda]_d X^* \\ X^*[\lambda]_d X & 0 \end{bmatrix} \quad (\text{from (11) and (17)}) \quad (33)$$

The form of equation (33) suggests that a rotationally symmetric network can be constructed by cascading two Butler type matrix via suitable phase shifters corresponding to the phase of the eigenvalues. One of the two Butler type matrix corresponding to [B]

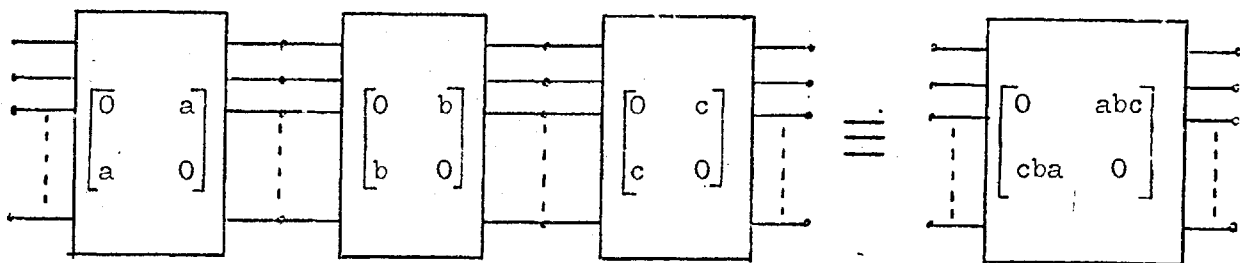


Fig. 2.4 CASCADE OF THREE 2-N NETWORKS

is obtained by interchanging the input port 1 and N, 2 and N-1, etc., of the matrix network [B]\*. Similar results have been obtained by Davis (12).

It is significant that the phase delays required corresponds to

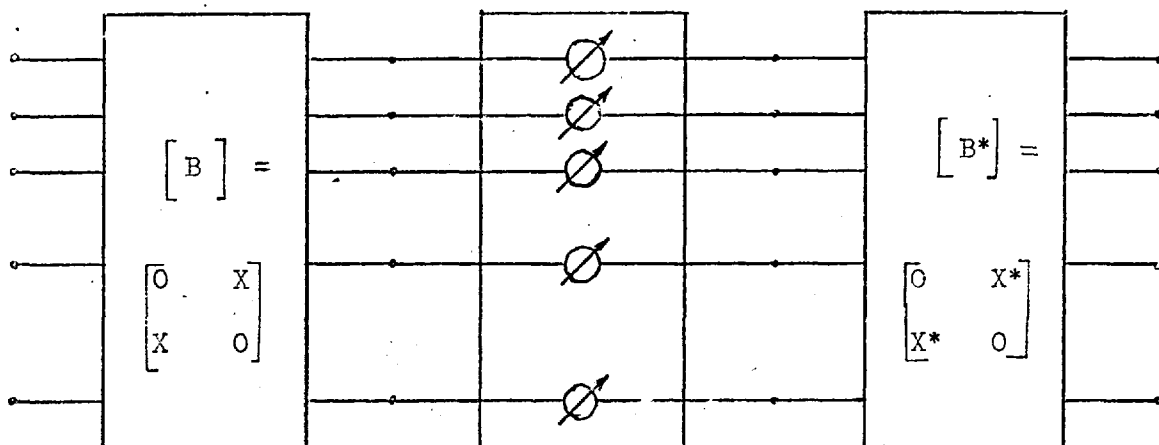


Fig. 2.5 ROTATIONALLY SYMMETRIC MATRIX FROM TWO BUTLER MATRICES

the exponents of reflection coefficients of the network. Therefore by varying the reflection coefficients for the various modes the outputs from a RSN can be controlled. A network, with the required mode reflection coefficient values can then be synthesised.

#### 2.4 Rotationally Symmetric Coupler - Butler Matrix Transform

In the preceding section a rotationally symmetric network for circular array was obtained from two Butler type matrices and a series of phase shifters. In a special case it will be shown that the Butler matrix can be transformed into a special rotationally symmetric network to be called Rotationally Symmetric Coupler (RSC) which has equal amplitude outputs. It is thought that the reverse transform is more significant.

For the R.S.N.

$$[C'] = \begin{bmatrix} 0 & T' \\ \tilde{T}' & 0 \end{bmatrix} \quad (11)$$

where

$$[T'] = \begin{bmatrix} t_1 & t_2 & \dots & t_N \\ t_2 & t_1 & & t_{N-1} \\ t_3 & t_2 & & \cdot \\ \vdots & & & \vdots \\ t_N & \cdot & \dots & t_1 \end{bmatrix}, \quad \text{implying circulant properties and symmetry of outputs.}$$

for Butler Matrix

$$[B] = \begin{bmatrix} 0 & X^* \\ \tilde{X}^* & 0 \end{bmatrix} \quad (10)$$

where

$$X_{rs}^* = \frac{1}{\sqrt{N}} \exp [j(r-1)(s-1)\theta] \quad (34)$$

We shall first assume that

$$[T'] = D X^* D \quad (\text{since } [T'] \text{ , symmetrical}) \quad (35)$$

i.e.

$$[X^*] = D^{-1} T' D^{-1} \quad (36)$$

where

$$D = \text{diag} (1, e^{-j\alpha_2}, e^{-j\alpha_3}, \dots, e^{-j\alpha_N}) \quad (37)$$

$$D^{-1} = \text{diag} (1, e^{j\alpha_2}, e^{j\alpha_3}, \dots, e^{j\alpha_N}) \quad (38)$$

Owing to its circulant properties and symmetry

$$T'_{rs} = \frac{1}{\sqrt{N}} \exp [j\Psi_{s-r+1}] \quad (39)$$

(for equal amplitude outputs and for  $s \geq r$ )

from (36), (38), and (39)

$$X_{rs}^* = \frac{1}{\sqrt{N}} \exp [j\alpha_r + j\Psi_{s-r+1} + j\alpha_s]$$

$$\text{but } x_{rs}^* = \frac{1}{\sqrt{N}} \exp [j(r-1)(s-1)\phi] \quad (34)$$

$$\text{i.e. } (r-1)(s-1)\phi = \alpha_r + \alpha_s + \Psi_{s-r+1} + k.2\pi \quad (40)$$

for  $r = 1, \dots, N$

$$s \geq r$$

Let  $s = r$

$$\text{i.e. } (r-1)^2\phi = 2\alpha_r + \Psi_1 + 2\pi k$$

put  $\Psi_1 = 0$

$$\text{i.e. } \alpha_r = \frac{(r-1)^2\phi}{2} - 2\pi k \quad (41)$$

Substituting (41) in (40)

$$(r-1)(s-1)\phi = \frac{(r-1)^2}{2}\phi + \frac{(s-1)^2}{2}\phi + \Psi_{s-r+1} + \text{Ars}.2\pi$$

where Ars is an integer const.

$$\text{i.e. } \Psi_{s-r+1} = -\frac{1}{2} [(r-1) - (s-1)]^2 \phi + \text{Ars}.2\pi$$

$$\Psi_{s-r+1} = -\frac{1}{2} (r-s)^2 \phi + \text{Ars}.2\pi \quad (42)$$

The multiples of  $2\pi$  in equations (41) and (42) may be conveniently dropped since  $\alpha_r$  and  $\Psi_{r-s+1}$  are phase values; hence equation (41) and (42) becomes:-

$$\alpha_r = \frac{(r-1)^2}{2} \phi \quad (41a)$$

$$\Psi_{s-r+1} = -\frac{1}{2} (r-s)^2 \phi \quad (42a)$$

Hence equation (35) is proved

$$[T'] = D X^* D \quad (35)$$



where  $[D] = \text{diag} (1, e^{-j\phi}, \dots, e^{-j\frac{(r-1)^2}{2}\phi}, \dots, e^{j\frac{(N-1)^2}{2}\phi})$

Therefore the rotationally symmetric network defined by  $[C']$  can be constructed from a Butler Matrix with two sets of  $N$  delay lines connected to its input and output ports. The phase delays are given by:-

$$\theta_r = \frac{(r-1)^2}{2} \phi \quad \text{for the } r\text{th and } (N+r)\text{th ports.}$$

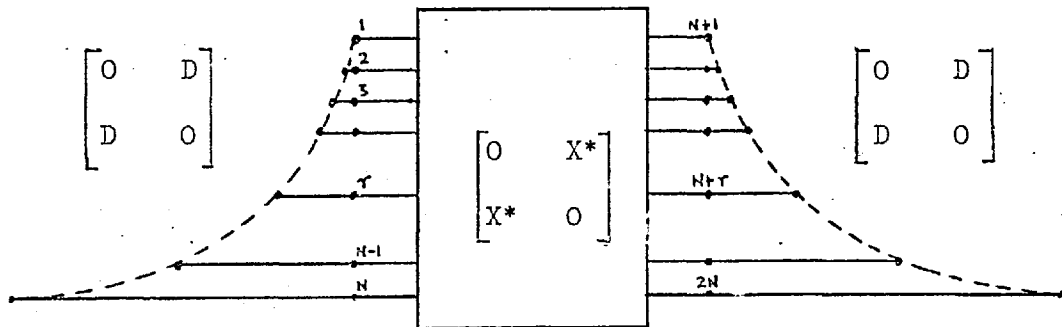


Fig. 2.6 ROTATIONALLY SYMMETRIC COUPLER FROM BUTLER MATRIX

Conversely a rotationally symmetric coupler (RSC) can be converted into a Butler matrix with a different set of delay lines as can be seen from equation (36).

If the outputs from a RSC are fed into omni-directional radiators in a circular array of appropriate dimensions, a radiation pattern with a sidelobe level of about  $-10\text{db}$  is obtained. With the use of  $(1+\text{Cosine})$  radiator or beverage aerials, no useful patterns were obtained. This suggests that the RSC should be used to produce Butler matrices rather

than the converse.

## 2.5 Summary

In section 1.3.1 it has been shown that once either the  $N$  amplitudes of the outputs or the  $N$  phase of the outputs of a lossless rotationally symmetric network are specified, the other unspecified parameters are fixed.

In section 1.3.1 and 1.3.2 we see that a rotationally symmetric network can be realised by cascading two Butler type matrices via  $N$  phase-shifters. The values of these phase shifters correspond to the exponents of the eigenvalues of the scattering matrix which describes the outputs from the network. The eigenvalues are in fact the reflection coefficients of the corresponding mode. Therefore the output from a rotationally symmetric network can be altered by controlling the values of the eigenvalues or phase shifter. As an alternative to the use of Butler matrices a network with the required mode reflection coefficient may be synthesized. One obvious example of this type of network is a Luneburg Lens or its equivalent structure with  $N$  feeds around the circumference (Ch. 3).

If the outputs of a  $kSN$  are equal a rotationally symmetric coupler (RSC) is obtained. This network can be transformed from a Butler matrix network by connecting two sets of  $N$  phase-shifters to the  $N$ -input and  $N$ -output ports. Conversely the RSC could be transformed into a Butler matrix using a complementary set of phase-shifters. It is thought that this transformation is more significant.

APPENDIX A2.1

ROTATIONAL SYMMETRY OPERATOR, [R]

If the fields in each of the N-ports of a rotationally symmetric structure were rotated in say, the clockwise direction, the behaviour of the structure will be unchanged owing to rotational symmetry. [R] is the rotationally symmetric operator which will effect this covering operation.

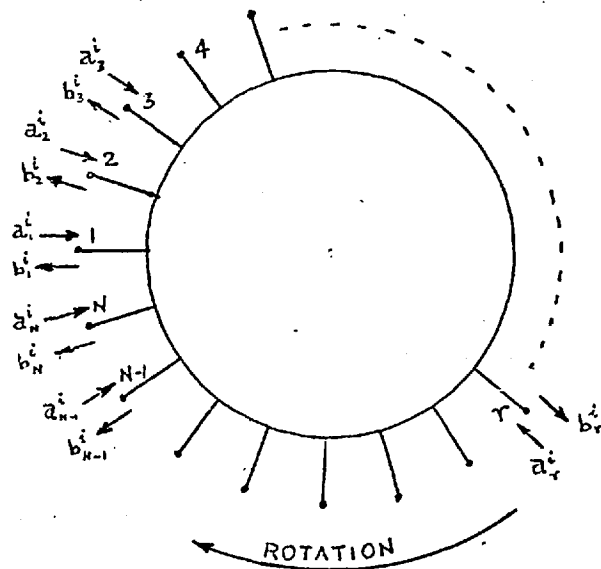


Fig. A2.1 ROTATION SYMMETRY

$$[R] = \begin{bmatrix} 0 & 0 & \cdot & \cdot & \cdot & \cdot & \cdot & \cdot & 1 \\ 1 & 0 & \cdot & \cdot & \cdot & \cdot & \cdot & \cdot & \cdot \\ \cdot & 1 & 0 & \cdot & \cdot & \cdot & \cdot & \cdot & \cdot \\ \cdot & \cdot & \cdot & \cdot & \cdot & \cdot & \cdot & \cdot & \cdot \\ \cdot & \cdot & \cdot & \cdot & \cdot & \cdot & \cdot & \cdot & \cdot \\ 0 & \cdot & \cdot & \cdot & \cdot & \cdot & \cdot & 1 & 0 \end{bmatrix} \quad (A2.1)$$

Fields at port 1 replace fields at port 2, port 2, at port 3, etc.

Eigenvalue Solution

$$[R] \{a^i\} = g^i \{a^i\} \quad (A2.2)$$

where  $\{a^i\}$  is the  $i$ th eigenvector or solution which satisfies the boundary condition,

and  $g^i$  is the corresponding eigenvalue of  $[R]$ .

i.e.  $([R] - g^i[I])\{a^i\} = [0]$ , yielding  $N$  simultaneous equations which determines  $\{a^i\}$  in terms of the coefficient of the matrix  $([R] - g^i[I])$ . The eigenvectors have non-vanishing solutions only if the determinant is zero,

$$\text{i.e.} \quad F(g) = |[R] - g^i[I]| = 0 \quad (\text{A2.3})$$

(The Characteristic Equation)

When expanded the characteristic equations result in a polynomial of degree  $N$ , whose roots,  $g^1, g^2, \dots, g^N$  are the  $N$  eigenvalues of  $R$ . Owing to symmetry  $[R]^N = [I]$ . It can be shown that the eigenvalue of  $[R]$  are the roots of 1 ((13) - Altman, pp.82).

$$\text{i.e.} \quad g^1, g^2, \dots, g^r, \dots, g^N = \exp \left[ j \frac{2\pi(r-1)}{N} \right] \quad (\text{A2.4})$$

( $r = 1$  to  $N$ )

The eigenvector,  $\{a^i\}$ , corresponding to  $g^i$  is determined within a constant by

$$\frac{a_1^i}{A_{p_1}} = \frac{a_2^i}{A_{p_2}} = \dots = \frac{a_N^i}{A_{p_N}} \quad (\text{A2.5})$$

(Cramer's Rule)

where  $A_{pn}$  is the co-factor of the  $(p,q)$  element of  $|[R] - g^i[I]|$

and  $p$  may be any row.

$$|[R] - g^i[I]| = \begin{vmatrix} -g^i & 0 & \dots & 0 & 1 \\ \vdots & -g^i & \dots & \dots & 0 \\ 0 & 1 & -g^i & \dots & \dots \\ \dots & \dots & \dots & \dots & \dots \\ 0 & \dots & \dots & 1 & -g^i \end{vmatrix} \quad (\text{A2.6})$$

It can be shown that:-

$$\frac{a_1^i}{\pm(g^i)^{N-1}} = \frac{a_2^i}{\pm(g^i)^{N-2}} = \dots = \frac{a_r^i}{\pm(g^i)^{N-r}} = \frac{a_N^i}{\pm 1} \quad (\text{A2.7})$$

$$\text{i.e. } a_i^r = (g^i)^{1-r} \quad (\text{A2.8})$$

$$\text{i.e. } \left[ \{a^1\}, \{a^2\}, \dots, \{a^N\} \right]$$

$$= \left[ \begin{array}{c} \left\{ \begin{array}{c} 1 \\ 1 \\ \cdot \\ \cdot \\ \cdot \\ 1 \end{array} \right\}, \left\{ \begin{array}{c} 1 \\ e^{-j\phi} \\ e^{-j2\phi} \\ \cdot \\ \cdot \\ e^{-j(N-1)\phi} \end{array} \right\}, \dots, \left\{ \begin{array}{c} 1 \\ e^{-j(N-1)\phi} \\ e^{-j2(N-1)\phi} \\ \cdot \\ \cdot \\ e^{-j(N-1)2\phi} \end{array} \right\} \end{array} \right] \quad (\text{A2.9})$$

$$\text{where } \phi = \frac{2\pi}{N}$$

Normalising A2.9

$$X = \frac{1}{\sqrt{N}} \left[ \{a^1\}, \{a^2\}, \dots, \{a^N\} \right] \quad (\text{A2.10})$$

$$\text{so that } X_{rs} = \frac{1}{\sqrt{N}} e^{-j(r-1)(s-1)\phi} \quad (\text{A2.11})$$

From (A2.2)

$$[R] \{a^i\} = g^i \{a^i\} \quad (\text{A2.2})$$

$$\text{or } [R][X] = [X][G_d] \quad (\text{A2.12})$$

$$\text{where } [G_d] = \text{diag}(g^1, g^2, \dots, g^N) \quad (\text{A2.13})$$

$$\text{i.e. } [R] = X [G_d] X^{-1}$$

$$\text{but } X^{-1} = \tilde{X}^* = X^* \quad (\text{X symmetrical})$$

$$\text{i.e. } [R] = X [G_d] X^* \quad (\text{A2.14})$$

## CHAPTER 3

### 3. THE MULTIBEAM LUNEBURG LENS FED CIRCULAR ARRAY

#### 3.1 INTRODUCTION

The general properties of a  $2N$ -port network for multibeam operation were studied in Chapter 2. The use of a Luneburg Lens in conjunction with  $N$  surrounding fields as a  $2N$ -port network will be studied in detail in this chapter.

Two schemes are proposed to facilitate multiple beam operation using either one or two lenses. In one arrangement one lens is used together with  $N$  three port circulators. In the other two identical lenses are used together with  $N$  3-db (quadrature) directional couplers.

To verify the feasibility of the proposal, the electromagnetic solution of the Luneburg Lens (with  $\mu = \epsilon$ ) is obtained. The reflection coefficient is calculated for each mode and the values used to obtain the scattering matrix (i.e. the output distribution at the outputs of the Luneburg Lens).

The outputs from the lens are fed to  $(1 + \cos \theta)$  pattern radiators in an array of the same size (in wavelength) as that of the lens, to obtain the far-field radiation pattern of the array.

The use of omni-directional radiators and beverage aerials in the array is also considered.

### 3.2 ARRANGEMENT FOR MULTIBEAM LENS FED CIRCULAR ARRAY

Two feeding arrangements are proposed for obtaining multiple directional beams using Luneburg Lens type combining networks. The first arrangement uses one lens with its feeds connected to radiators and to the transmitters or receivers via three port circulators. In the other arrangement two identical lenses are used. Two outputs from the two lenses - one each from the two feeds in the same position for the two lenses, are connected to the radiators and the transmitters or receivers via 3db quadrature directional couplers. Theoretically the two arrangements can be used for simultaneous transmission and reception. Both systems can be used for scanning if each beam output is fed into a scanning network.

#### 3.2.1 Multiple Beam Lens Fed Circular Array (One Lens)

The main feature of this arrangement is the Luneburg Lens type combining network, L. This could be a full-scale dielectric lens, a scaled Luneburg Lens (if frequency translation is used), a lumped circuit equivalent circuit lens or any rotationally symmetric structure with focussing properties. The circumference of the lens is totally surrounded by N feeds so that ideally no loss of power occurs in the lens and feed arrangement. Horns could be used as feeds in microwave

lenses. The feeds are connected by equal length transmission lines to the radiators and the transmitters or receivers via three port

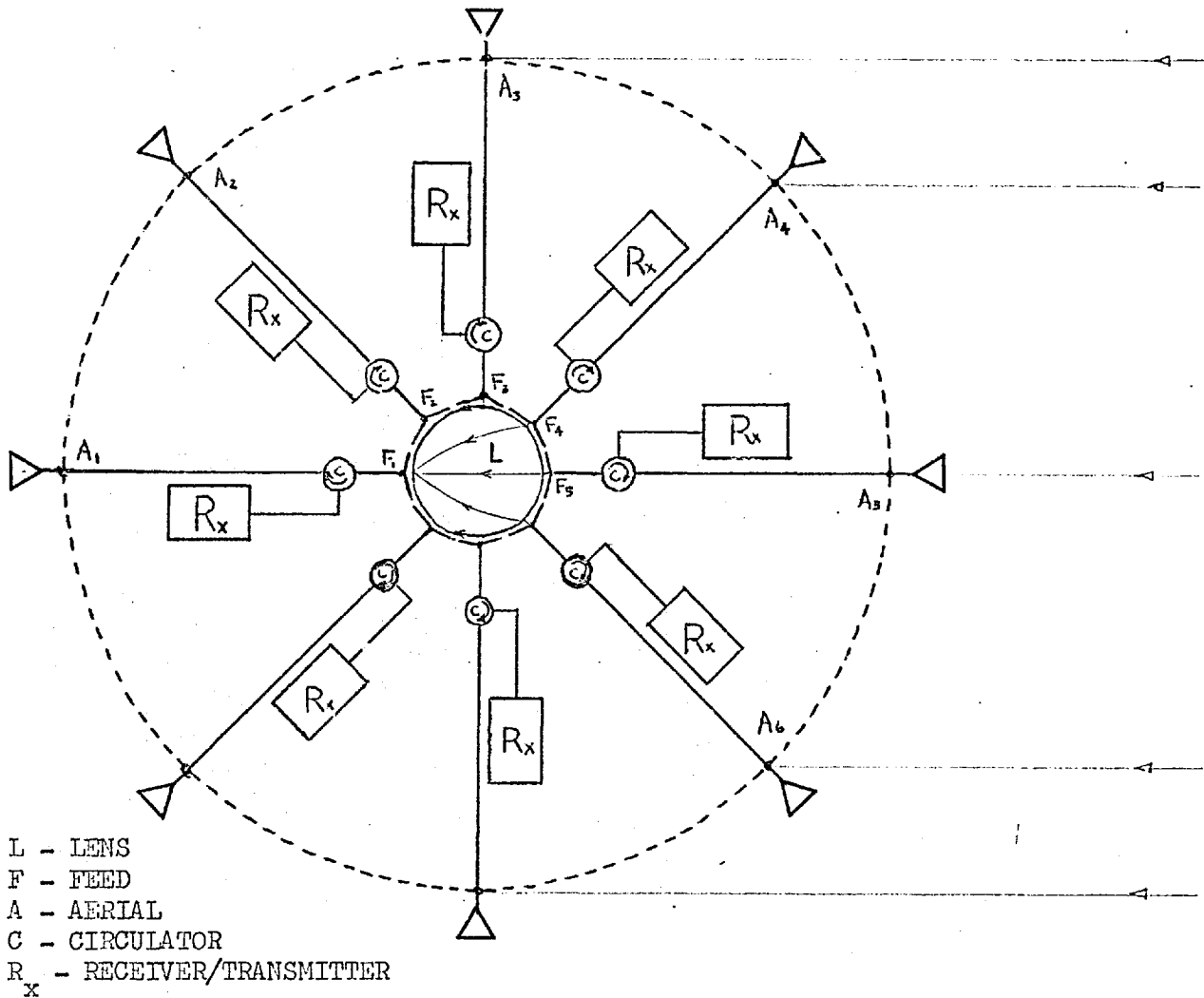


Fig. 3.1 MULTIPLE BEAM LENS-FED ARRAY (ONE LENS - FOR RECEIVE MODE)

circulators. A  $2N$  port network with rotationally symmetric properties is thus obtained. The radiators are arranged in a circular array of



the same dimensions (electrically) as that of the combining <sup>in</sup> lens.

The arrangement may be used either for transmission or reception. To illustrate the mode of operation, the receiving mode will be considered. The radiators in the array pick up signals from a plane wave arriving from the direction shown in fig. 3.1. The signals travel down the transmission lines to the circulators, C, where they are directed into the lens, L, through the feeds, F. In the lens the signals are focussed on to a point at the circumference, on the other side of the lens. This focussed signal is picked up at feed,  $F_1$ , travels to the circulator and is directed into the receiver,  $R_x$ . Signals arriving from any of the N directions are similarly combined.

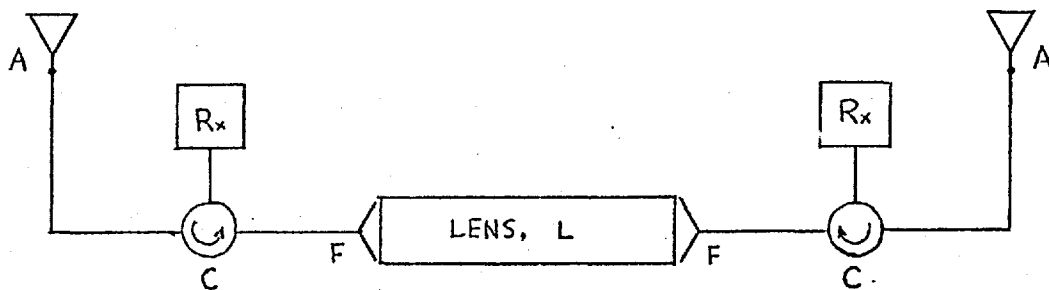


Fig. 3.2(a) RECEIVE MODE

For transmission the positions of the radiators and the feed ports are reversed. However, if common TR mode is required two of the lens-fed system already described will be needed - one for transmission and the other for reception. The output ports from two feeds in identical positions from each of the two structures are

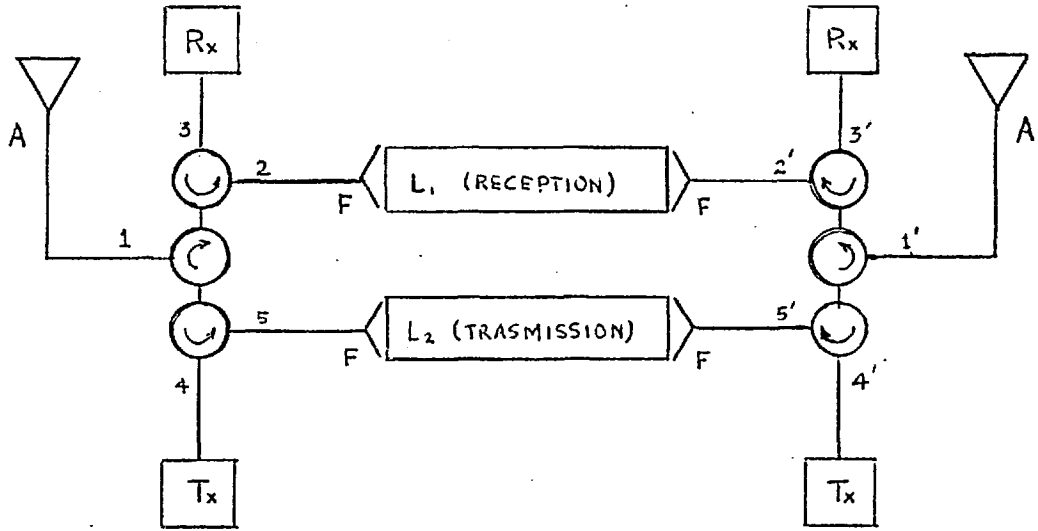


Fig. 3.2(b) COMMON TR MODE (With Three 3-Port Circulators  
or a 5-Port Circulator)

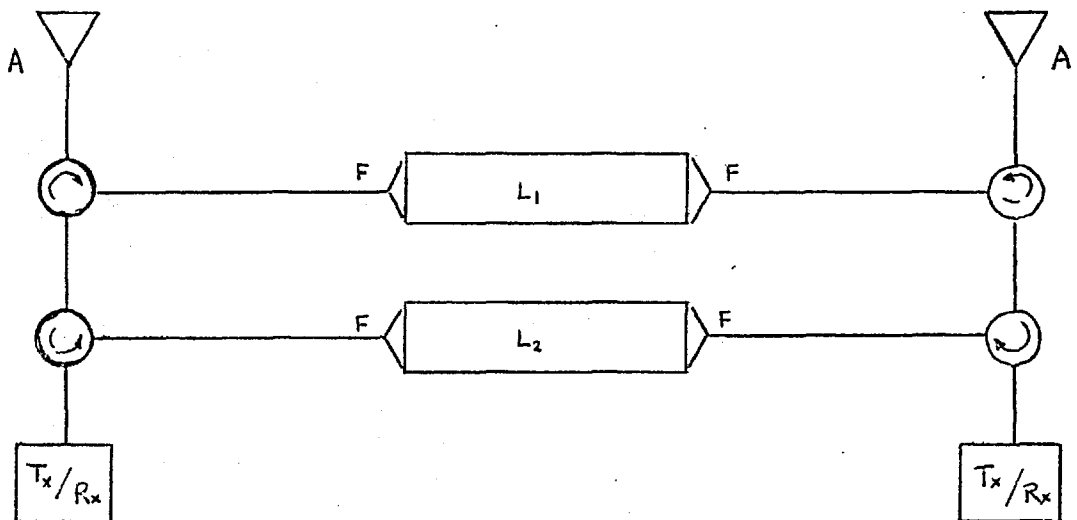


Fig. 3.3 TRANSMIT/RECEIVE MODE (Using 4-Port Circulators)  
(Marston (19))

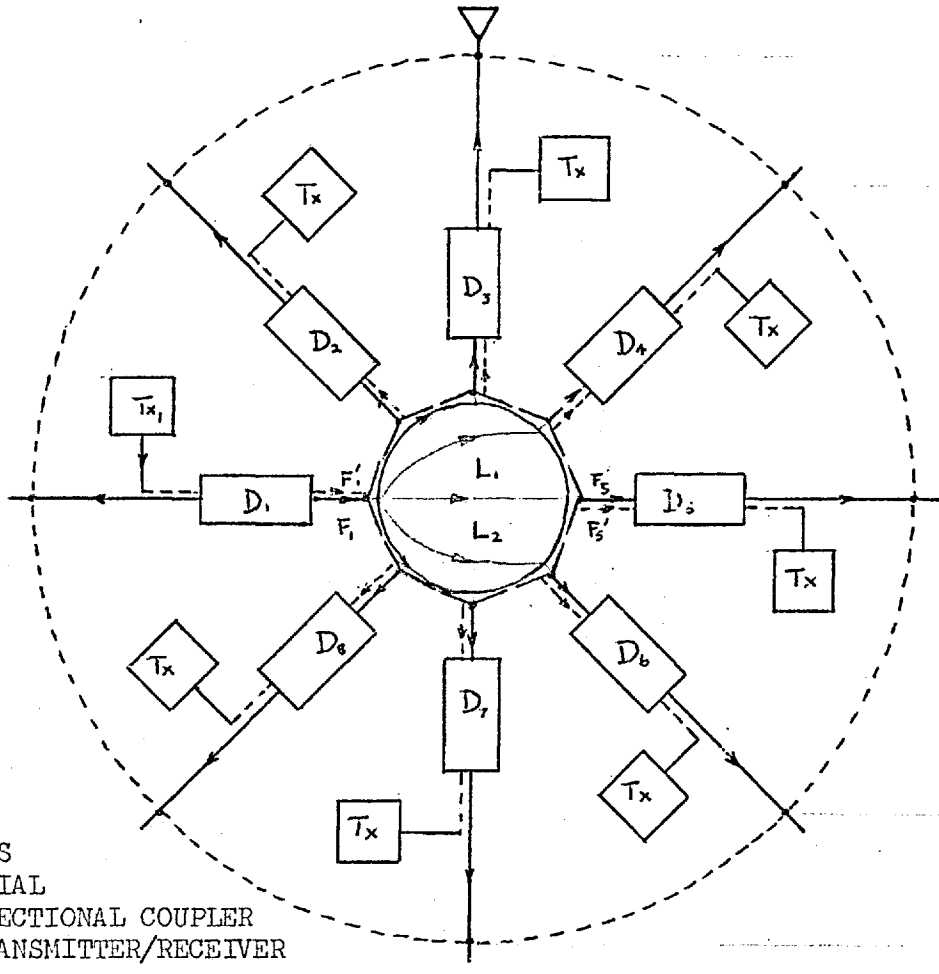
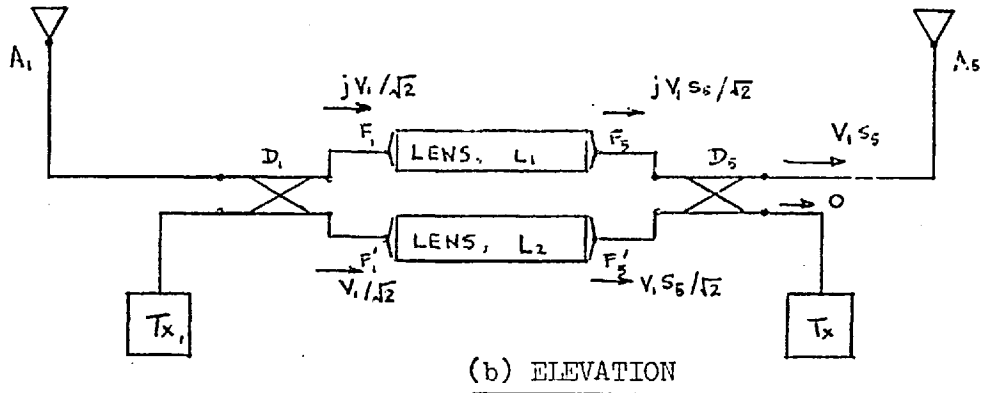
connected to the radiators in the array via 3-port circulator as illustrated in fig. 3.2(b). The ports numbered 1 to 5 then constitutes a 5 port circulator.

A similar arrangement proposed by Marston (19) is illustrated in fig. 3.3.

### 3.2.2 Multiple Beam Lens Fed Array (Two Lenses)

An arrangement which permits simultaneous reception and transmission is illustrated in fig. 3.4. Two identical lenses,  $L_1$  and  $L_2$  together with feeds are employed. The outputs from two feeds in identical positions from each of the two lenses are fed into two ports of a 3db-directional coupler. The other two ports of the coupler are connected to the radiator and the receiver or transmitter as indicated in fig. 3.4(a).

For transmission in the direction B1, a signal  $V_1$  is applied to the lower input branch of the directional couplers by the transmitter  $Tx_1$ , giving outputs  $\frac{jV_1}{2}$  and  $\frac{V_1}{2}$  at the upper and lower ports respectively, i.e. at feeds  $F_1$  and  $F_1'$  respectively. Because of the lens action, the signals are distributed to the other ports and picked up by the feeds. The outputs at the upper and lower lenses are in phase quadrature. Hence at any two identical feed points, the signal travelling into the direction coupler ( ,  $D_5$ ; say) are in phase quadrature. Therefore no output is obtained at the receiver/transmitter port, but a signal  $jV_1 S_5$  appears at the radiator,



- L - LENS
- A - AERIAL
- D - DIRECTIONAL COUPLER
- T<sub>x</sub> - TRANSMITTER/RECEIVER

Fig. 3.4 MULTIPLE BEAM LENS FED ARRAY (TWO LENSES)

$A_5$  ( $S_n$  is a constant depending on the position of the port with respect to the transmitting port). Since the distributed signals are nearly cophasal due to the property of the lens a directional beam is obtained in the direction,  $B_1$ .

The array behaves similarly for reception. In such a case, the signals are received at the radiators, transmitted via the directional couplers to the lens where the signals are focussed on to a feed point on the other side of the two lenses. Since the two signals are equal but in phase quadrature the signals are transmitted only to the receiver port.

These arrangements can therefore be used for simultaneous transmission to or reception from as many directions as there are aerial radiators. For the common TR mode operation each output from the array is connected to a transmitter and a receiver via a 3-port circulator.

In both arrangements (sec. 3.2.1 and 3.2.2) a  $2N$ -port network is obtained from an  $N$ -port structure (the lens with its  $N$  feeds). Whereas there is no coupling between output ports in a Butler Array there is some coupling between output feeds of the Luneburg type network. It can be shown (Appendix 3.1) that the scattering matrix of the  $2N$ -port network work resulting from the use of two sets of lenses with direction couplers is

$$C = j \begin{bmatrix} 0 & S \\ S & 0 \end{bmatrix} \quad (3.1)$$

where  $[S]$  = scattering matrix of the N-port Lens Structure.

### 3.3 BEHAVIOUR OF THE MULTIBEAM LENS CIRCULAR ARRAY

Equation 2.3.2 suggests that the reflection coefficient of the various modes are required to obtain the distribution at the output feeds of the lens network. The electromagnetic solution for the Luneburg Lens is worked out in section 3.3.1. It is thought that a Luneburg Lens with  $\mu_r = \epsilon_r$  may prove more useful than the ordinary Luneburg Lens (with  $\mu_r = 1$ ) since there is one extra parameter,  $\mu_r$  (especially in relation to the equivalent circuit lens in Chapter 4). The electromagnetic solution of the ordinary two-dimensional Luneburg Lens has already been obtained by Jasik (14).

#### 3.3.1(a) Electromagnetic Solution of the Luneburg Lens ( $\mu_r = \epsilon_r$ )

For the Luneburg Lens, refractive index is given by

$$n(r) = \sqrt{2 - r^2/a^2} = \sqrt{\mu(r) \epsilon(r)} \quad (3.2)$$

where  $r$  = distance from centre of lens

$a$  = radius of lens

$\mu(r)$  = relative permeability

$\epsilon(r)$  = relative permittivity and the centre of the lens

corresponds to the origin of the cylindrical co-ordinate system.

For  $\mu(r) = \epsilon(r)$

$$\mu(r) = \epsilon(r) = \sqrt{2 - r^2/a^2} \quad (3.3)$$

For a lens of height less than half a wavelength only the Transverse Electric Mode exist.

Transverse Electric Mode  $E_z, H_\phi, H_r$  only

From Maxwell's equations,

$$\frac{1}{r} \frac{\partial E_z}{\partial \phi} = - \frac{\partial B_r}{\partial t} \quad (3.4)$$

$$\frac{\partial E_z}{\partial r} = \frac{\partial B_\phi}{\partial t} \quad (3.5)$$

$$\frac{1}{r} \frac{\partial}{\partial r}(rH_\phi) - \frac{1}{r} \frac{\partial H_r}{\partial \phi} = \frac{\partial D_z}{\partial t} \quad (3.6)$$

differentiating 3.4 w.r.t.  $\phi$  and 3.5 w.r.t.  $r$  and rearranging,

$$\frac{\partial H_r}{\partial \phi} = \frac{1}{j\omega\mu_0\mu(r)} \cdot \frac{1}{r} \cdot \frac{\partial^2 E_z}{\partial \phi^2} \quad (3.4(i))$$

$$\frac{\partial H_\phi}{\partial r} = \frac{1}{j\omega\mu_0\mu(r)} \cdot \frac{\partial^2 E_z}{\partial r^2} - \frac{\frac{\partial\mu(r)\mu_0}{\partial r} \cdot \frac{\partial E_z}{\partial r}}{j\omega[\mu_0\mu(r)]^2} \quad (3.5(i))$$

substituting for  $\frac{\partial H_\phi}{\partial r}$  and  $\frac{\partial H_r}{\partial \phi}$  in 3.6,

$$\frac{\partial H_\phi}{\partial r} + \frac{1}{r} H_\phi - \frac{1}{r} \frac{\partial H_r}{\partial \phi} = \frac{\partial D_z}{\partial t} \quad (3.6)$$

$$\begin{aligned} \text{i.e. } & \left\{ \frac{1}{j\omega\mu_0\mu(r)} \cdot \frac{\partial^2 E_z}{\partial r^2} - \frac{\partial[\mu_0\mu(r)]}{\partial r} \cdot \frac{1}{j\omega[\mu_0\mu(r)]^2} \cdot \frac{\partial E_z}{\partial r} \right\} + \frac{1}{j\omega r\mu_0\mu(r)} \cdot \frac{\partial E_z}{\partial r} \\ & + \frac{1}{r^2} \cdot \frac{1}{j\omega\mu_0\mu(r)} \cdot \frac{\partial^2 E_z}{\partial \phi^2} = j\omega \epsilon_0 \epsilon(r) E_z \end{aligned}$$

$$\begin{aligned} \text{i.e. } r^2 \frac{\partial^2 E_z}{\partial r^2} + \left\{ \frac{1}{r} - \frac{\partial \mu(r)}{\partial r} \cdot \frac{1}{\mu(r)} \right\} r^2 \frac{\partial E_z}{\partial r} + \omega^2 \mu_0 \epsilon_0 r^2 \epsilon(r) \mu(r) E_z \\ = - \frac{\partial^2 E_z}{\partial \phi^2} \end{aligned} \quad (3.6(i))$$

$$\text{Putting } E_z = R(r) \bar{\phi}(\phi), \quad (3.7)$$

$$\frac{\bar{\phi}''}{\bar{\phi}} = -m^2 \quad (3.8)$$

$$\begin{aligned} \text{and } r^2 \frac{R''}{R} + \left[ r - \frac{\partial \mu(r)}{\partial r} \cdot \frac{r^2}{\mu(r)} \right] \frac{R'}{R} + k^2 r^2 n^2(r) \\ = m^2 \end{aligned} \quad (3.9)$$

$$\text{where } k^2 = \omega^2 \mu_0 \epsilon_0$$

Solution of equation 3.8

$$\frac{\bar{\phi}''}{\bar{\phi}} = -m^2 \quad (3.8)$$

$$\bar{\phi} = A e^{jm\phi} \quad (3.10)$$

Solution of equation 3.9

$$\begin{aligned} r^2 R'' + \left[ r - \frac{\partial \mu(r)}{\partial r} \cdot \frac{r^2}{\mu(r)} \right] R' + k^2 r^2 n^2(r) R - m^2 R \\ = 0 \end{aligned} \quad (3.9)$$

$$\text{Substituting for } n^2(r) = 2 - \frac{r^2}{a^2}$$

$$\mu(r) = \epsilon(r) = \sqrt{2 - \frac{r^2}{a^2}}$$

$$\text{and } \frac{\partial \mu(r)}{\partial r} = - \frac{r}{\sqrt{2a^2 - r^2}} \text{ in eqn. 3.9}$$

$$r^2 R'' + \frac{2a^2 r^2}{2a^2 - r^2} R' - [m^2 - k^2 r^2 (2 - \frac{r^2}{a^2})] R$$



$$= 0 \quad (3.11)$$

Using the transformation obtained in Appendix A3.2.1

$$R = Z^{\frac{m}{2}} (2Za - Z)^{\frac{1}{4}} e^{-Z/2} U_m(Z) \quad (3.12)$$

where  $m = \text{mode number}$

$$Z = \frac{k r^2}{a} \quad (3.13)$$

$$Za = ka, \quad (3.14)$$

equation 3.11 becomes

$$U_m'' + \left[ \frac{\gamma}{Z} - 1 \right] U_m' - \left[ \frac{\alpha_1}{Z} + \frac{2\alpha_2}{(Z-2Za)} - \frac{2a_2\alpha_3}{(Z-2Za)} \right] U_m = 0 \quad (3.15)$$

where  $\gamma = m+1$

$$\alpha_1 = \frac{1}{2}(m+1 - Za + \frac{1}{4Za})$$

$$\alpha_2 = -\frac{1}{16Za} \quad (3.16)$$

$$\alpha_3 = -\frac{5}{64Za}$$

$$a_2 = 2Za$$

The function  $U_m$  which satisfies equation 3.15 is similar to the equation obtained by C.T. Tai (15) for the T.M. solution of the spherical Luneburg Lens. The constants  $\gamma$ ,  $\alpha$ ,  $\alpha_2$ ,  $\alpha_3$  differ slightly. The series solution to equation 3.15 (derived in appendix A3.2.2) is given by

$$U_m = \sum_{n=0}^{\infty} A_n Z^n \quad (3.17)$$

where 
$$\frac{A_1}{A_0} = \frac{\alpha_1}{\gamma} \quad (3.18(i))$$

$$\frac{A_2}{A_0} = \frac{1}{2} \frac{\alpha_1(\alpha_1+1)}{\gamma(\gamma+1)} - \frac{(\alpha_2+\alpha_3)}{a_2(\gamma+1)} \quad (3.18(ii))$$

$$\begin{aligned} \frac{A_3}{A_0} &= \frac{1}{3} \frac{\alpha_1(\alpha_1+1)(\alpha_1+2)}{\gamma(\gamma+1)(\gamma+2)} - \frac{1}{3} \frac{1}{(\gamma+2)} \frac{(\alpha_1+2)(\alpha_2+\alpha_3)}{(\gamma+1)a_2} \\ &+ \frac{2\alpha_1(\alpha_2+\alpha_3)}{\gamma(a_2)} + \frac{2(\alpha_2+2\alpha_3)}{a_2^2} \end{aligned} \quad (3.18(iii))$$

for  $n \geq 3$ , the coefficients are related by the following expression:-

$$\begin{aligned} &a_2^2(n+1)(n+\gamma) A_{n+1} - a_2 [a_2(n+\alpha_1)+2n(n+\gamma-1)] A_n \\ &+ [(n-1)(n+\gamma-2)+2a_2(\alpha_1+\alpha_2+\alpha_3+n-1)] \cdot A_{n-1} - [(n-2+\alpha_1+2\alpha_2)] A_{n-2} \\ &= 0 \end{aligned} \quad (3.18(iv))$$

The series is absolutely convergent for  $Z < 2Za$ .

Hence from equations 3.7, 3.8, and 3.12,

$$E_{Z_m} = A e^{jm\phi} Z^{m/2} (2Za-Z)^{\frac{1}{4}} e^{-Z/2} U_m(Z) \quad (3.19)$$

where A is a constant

From equation 3.5,

$$\begin{aligned} H_{\phi} &= \frac{1}{j\omega\mu_0\mu(r)} \cdot \frac{\partial E_Z}{\partial r} \\ \text{i.e. } H_{\phi_m} &= \frac{1}{j\omega\mu_0\mu(r)} \cdot \frac{\partial Z}{\partial r} \cdot \frac{\partial E_{Zm}}{\partial Z} \quad (3.20) \\ &= \frac{1}{j\omega\mu_0\mu(r)} \cdot \frac{2kr}{a} \cdot \left[ \frac{m}{2Za} - \frac{1}{4(2Za-Z)} - \frac{1}{2} + \frac{U'_m}{U_m} \right] E_{Z_m} \end{aligned} \quad (3.21)$$

At the edge of the lens,  $r = a$ ,  $Z = ka = Za$

$$\text{i.e.} \quad H_{\phi_m} = \frac{2k}{j\omega\mu_0} \cdot \frac{(2m-1)}{4ka} - \frac{1}{2} + \frac{U'_m}{U_m} E_{Z_m} \quad (3.22)$$

Looking into the lens, the characteristic impedance,

$$\begin{aligned} Z_m &= \frac{E_{Z_m}}{H_{\phi_m}} \\ &= \frac{j\mu_0}{2} \cdot \frac{\omega}{k} \left[ \frac{(2m-1)}{4Za} - 0.5 + \frac{U'_m}{U_m} \right] \\ Z_m &= \frac{j}{2} \eta_0 \left[ \frac{(2m-1)}{4Za} - 0.5 + \frac{U'_m}{U_m} \right] \end{aligned} \quad (3.23)$$

where  $\eta_0$  = free space characteristic impedance  $U_m$ ,  $U'_m$  and  $Z_m$  are computed using the subroutines described in appendix A3.3.2(b) and A3.3.3.

### 3.3.1(b) Electromagnetic Solution of the Ordinary Luneburg Lens

$$\text{with } \epsilon(r) = n^2(r) = (2-r^2)$$

The solution has been obtained by Jašik (14) for the cylindrical lens and Tai (15) for the spherical lens. The relevant transverse electric mode solution is given by

$$E_{Z_m} = A Z^{m/2} e^{-Z/2} {}_1F_1(\alpha, \gamma, Z) \quad (3.24)$$

$$\text{where} \quad \alpha = (m+1-ka)/2$$

$$\gamma = m+1 \quad (3.25)$$

$$Z = \frac{k r^2}{a}$$

and  ${}_1F_1(\alpha, \gamma, Z)$  is the confluent Hypergeometric function [16, 17, 18]

$${}_1F_1(\alpha, \gamma, Z) = 1 + \frac{\alpha}{\gamma} Z + \frac{\alpha(\alpha+1)Z^2}{(\gamma+1)2!} + \dots + \frac{\alpha(\alpha+1)\dots(\alpha+r-1)}{(\gamma+1)\dots(\gamma+r-1)} \cdot \frac{Z^r}{r!} \quad (3.26)$$

The series is absolutely convergent.

From equation 3.19,

$$H_{\phi_m} = \frac{1}{j\omega\mu_0\mu(r)} \cdot \frac{\partial Z}{\partial r} \cdot \frac{\partial E_{Z_m}}{\partial Z} \quad (3.20)$$

$$\text{i.e.} \quad H_{\phi_m} = \frac{2k}{j\omega\mu_0\mu(r)} \left[ \frac{m}{2Z} - \frac{1}{2} + \frac{{}_1F_1(\alpha, \gamma, Z)}{{}_1F_1'(\alpha, \gamma, Z)} \right] E_{Z_m} \quad (3.27)$$

and hence at the edge of the lens

$$Z_m = \frac{j}{2} \eta_0 \left[ \frac{m}{2Za} - 0.5 + \frac{{}_1F_1(\alpha, \gamma, Z)}{{}_1F_1'(\alpha, \gamma, Z)} \right] \quad (3.28)$$

The subroutine used to compute  ${}_1F_1(\alpha, \gamma, Z)$ ,  ${}_1F_1'$ , and  $Z_m$  are described in Appendix 3.3.2(a).

### 3.3.1(c) The Series $U_m(Z)$ and ${}_1F_1(\alpha, \gamma, Z)$

When the electromagnetic solution of the Luneburg Lens with  $\mu = \epsilon = \sqrt{2-r^2/a^2}$  was sought it was thought that there will be no difference between this and the solution for the ordinary Luneburg Lens ( $\mu = 1, \epsilon = 2-r^2/a^2$ ) for large  $ka$  since both approach the geometric optics solution. In fact the series  $U_m$  approaches  ${}_1F_1(\alpha, \gamma, Z)$  for large values of  $Z$ .

$$U_m = \sum_{n=0}^{\infty} A_n Z^n \quad (3.17)$$

from equations 3.18(i) to 3.18(iv) if  $Za = ka \gg 1$

$$\frac{\alpha_2 + \alpha_3}{a_2^{(\gamma+1)}} = \frac{9}{128 Za^{2(\gamma+1)}} \ll 1 \quad \text{in eqn. 3.18(ii)}$$

$$\left\{ -\frac{1}{3} \cdot \frac{1}{(\gamma+2)} \frac{(\alpha_2 + \alpha_3)}{(\gamma+1)a_2} + \frac{2\alpha_1(\alpha_2 + \alpha_3)}{\gamma a_2} + \frac{2(\alpha_2 + 2\alpha_3)}{a_2^2} \right\} \ll 1 \quad \text{in eqn. 3.18(iii)}$$

and in equation 3.18(iv) the terms not containing  $Za = ka$  can be neglected so that

$$(n+1)(n+\gamma) A_{n+1} = (\alpha_1 + n) A_n$$

$$\text{i.e.} \quad \frac{A_{n+1}}{A_n} = \frac{(\alpha_1 + n)}{(\gamma + n)} \cdot \frac{1}{(n+1)!} \quad \text{as in the hypergeometric}$$

function,  ${}_1F_1(\alpha, \gamma, Z)$  where  $\alpha_1 \rightarrow \alpha$  since  $\frac{1}{4ka} \ll 1$ . Therefore for large  $ka$  the two solutions are the same. For convenience only the hypergeometric series is used for the higher  $ka$  values ( $ka \gtrsim 10$ ).

Also for  $ka \gg 1$ ,  $\frac{2m-1}{4Za} \rightarrow \frac{m}{2Za}$  in the expression for  $Z_m$  in equation 3.23.

The behaviour of the two series  $U_m$  and  ${}_1F_1$  are very similar. If  $\alpha = (m+1-ka)$  or  $\alpha_1 = (m+1-ka + \frac{1}{4ka}) < 0$ , the terms in the series alternate in sign until approximately the  $n$ th term ( $n \simeq ka-1$ ). After the  $n$ th term ( $n \simeq ka$ ) the value of the  $n$ th term falls monotonically as  $n$  increases. Near the  $n$ th term ( $n \simeq ka-1$ ), the value of the term is approximately equal but opposite in sign to the series so far. Because of this the accuracy of the series is

suspect especially if the number of digits the computer can handle is low. The problem is not serious with the CDC 6600 which can handle approximately 14 significant digits.

In the case of the series  ${}_1F_1(\alpha, \gamma, Z)$ , if  $ka$  is an integer the series terminates at the  $l$ th term,  $l = (ka+1)$ .

If  $\alpha_1$  or  $\alpha > 0$  the terms in the series decrease monotonically.

$U(Z)$  is absolutely convergent for  $Z < a_2$  i.e.  $r < 2a$  and  ${}_1F_1(\alpha, \gamma, Z)$  is absolutely convergent.

### 3.3.2 The Output Distribution of the Lens at the Feeds

The scattering matrix for the feed system was calculated from expressions obtained in Chapter 2 - equations 2.29, 2.30, 2.31 and 2.32

$$[S] = [X][\lambda]_d [X^*] \quad (2.29)$$

$$S_{rs} = \sum_{m=1}^N \lambda_m e^{j(m-1)(r-s)\phi} \quad (2.30)$$

$$\text{where } \lambda_k = \lambda_{N-k} \quad (k = 1 \text{ to } N-1) \quad (2.31)$$

$$= \sum_{m=1}^{\frac{N'}{2}} (\lambda_0 + \lambda_n \cos(m-1)(r-s)\phi) \\ (+ \lambda_{N/2} (-1)^{N/2}, \text{ only if } N \text{ is even}) \quad (2.32)$$

$$\text{where } \frac{N'}{2} = \frac{N}{2} - 1 \text{ for } N \text{ even}$$

$$\frac{N-1}{2} \text{ for } N \text{ odd}$$

$$\phi = 2\pi/N$$

The first three rows of the matrix  $[S]$  have been computed from the expression for  $S_{rs}$  to verify the circulant properties of  $[S]$ . Later programs only compute the first row of the matrix to give the output distribution at the feeds of the lens. Details of the subroutine, SCATMX, written to compute a row of the scattering matrix  $[S]$  is given in Appendix 3.3.4.

The outputs at the feeds on the forward half of the lens are very nearly cophasal as is to be expected from a Luneburg Lens.

### 3.3.2(a) Effects of Spacing between Feeds

For a lens of fixed diameter (in wavelength) the taper on the output distribution from the  $N$  feeds of the array varies with the number of feeds used (i.e. the spacing between feeds).

With a spacing between feeds of about one wavelength there is a strong taper in the output for the forward direction, and very small outputs at the back half of the lens. As the spacing is decreased (no. of feeds increased) there is a weaker taper in the forward direction.

At the same time the outputs

adjacent to the input feed increase. Typical output distributions are

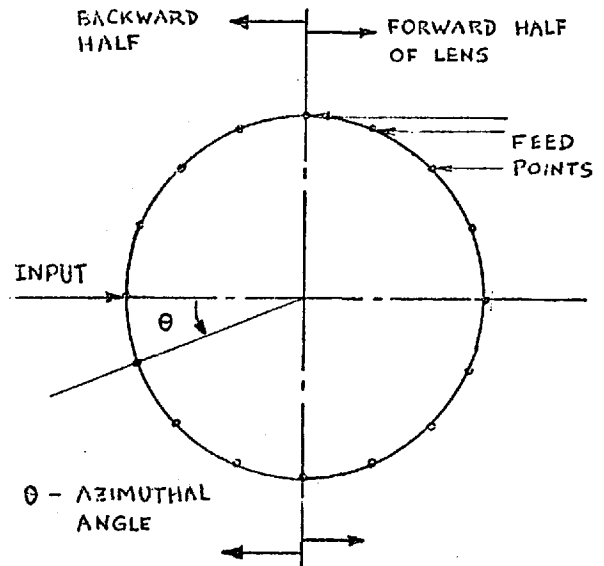


Fig. 3.3 FEED ARRANGEMENT

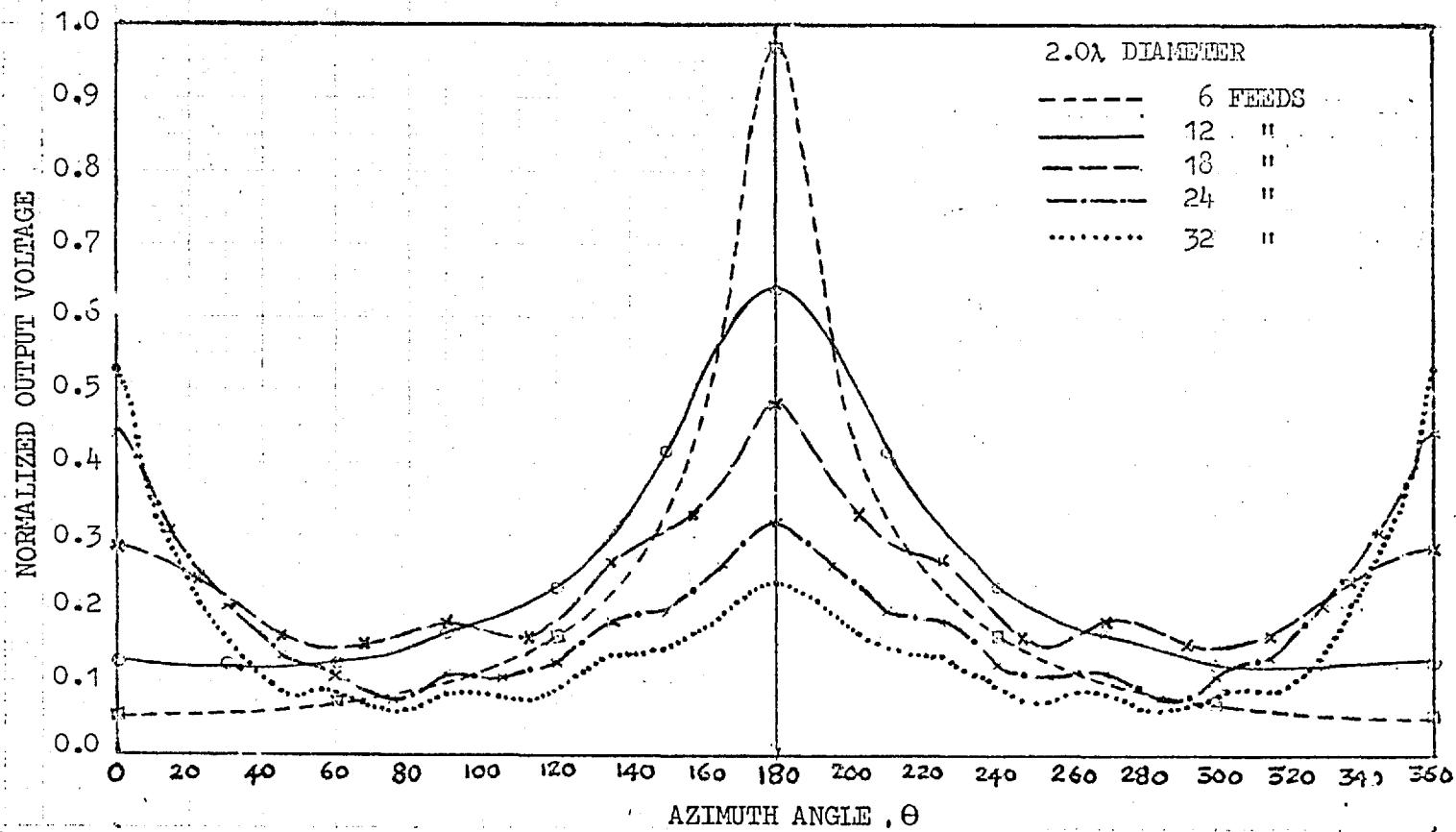


Fig. 3.4 LENS OUTPUT DISTRIBUTION



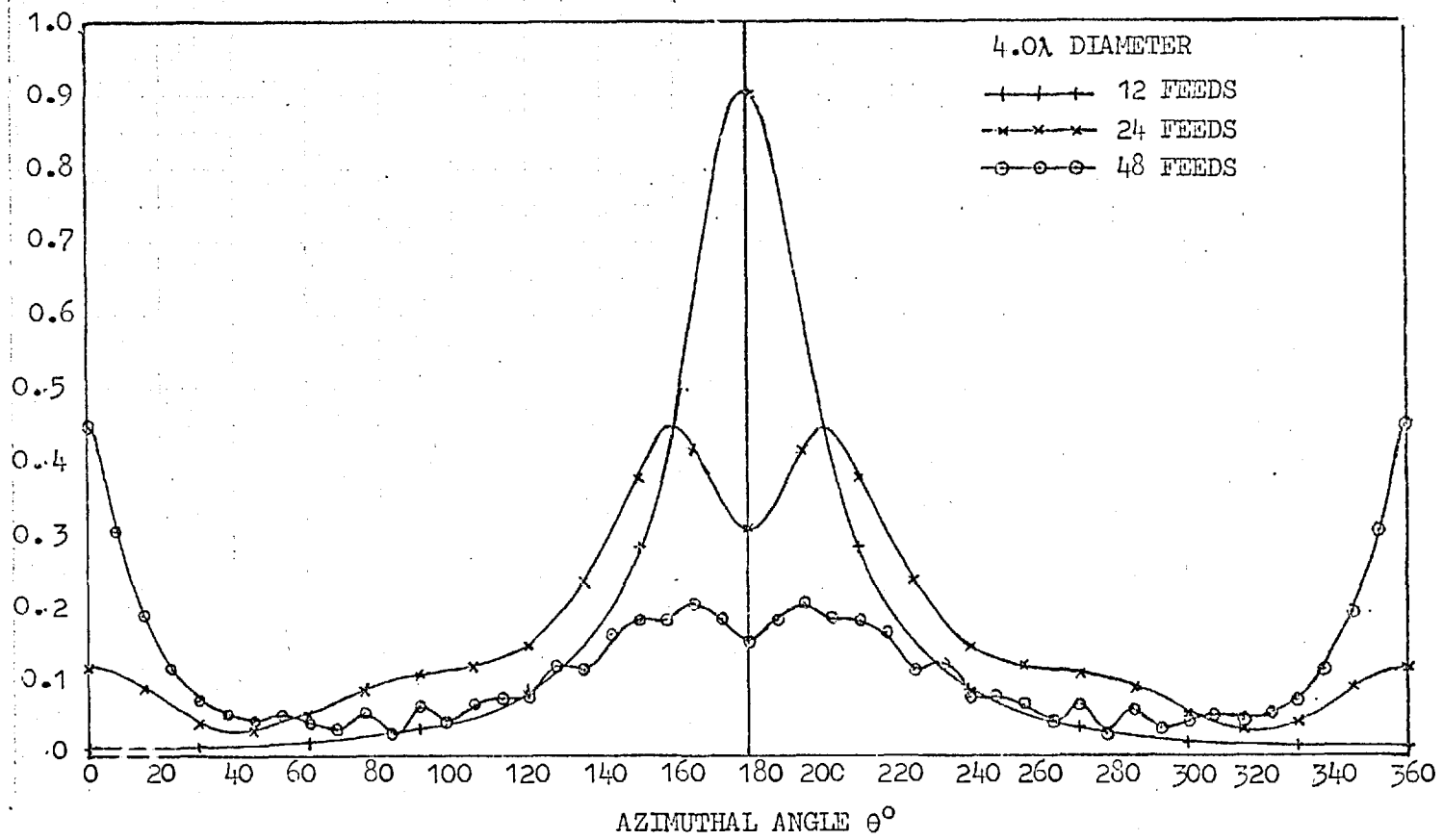


Fig. 3.5 LENS OUTPUT DISTRIBUTION

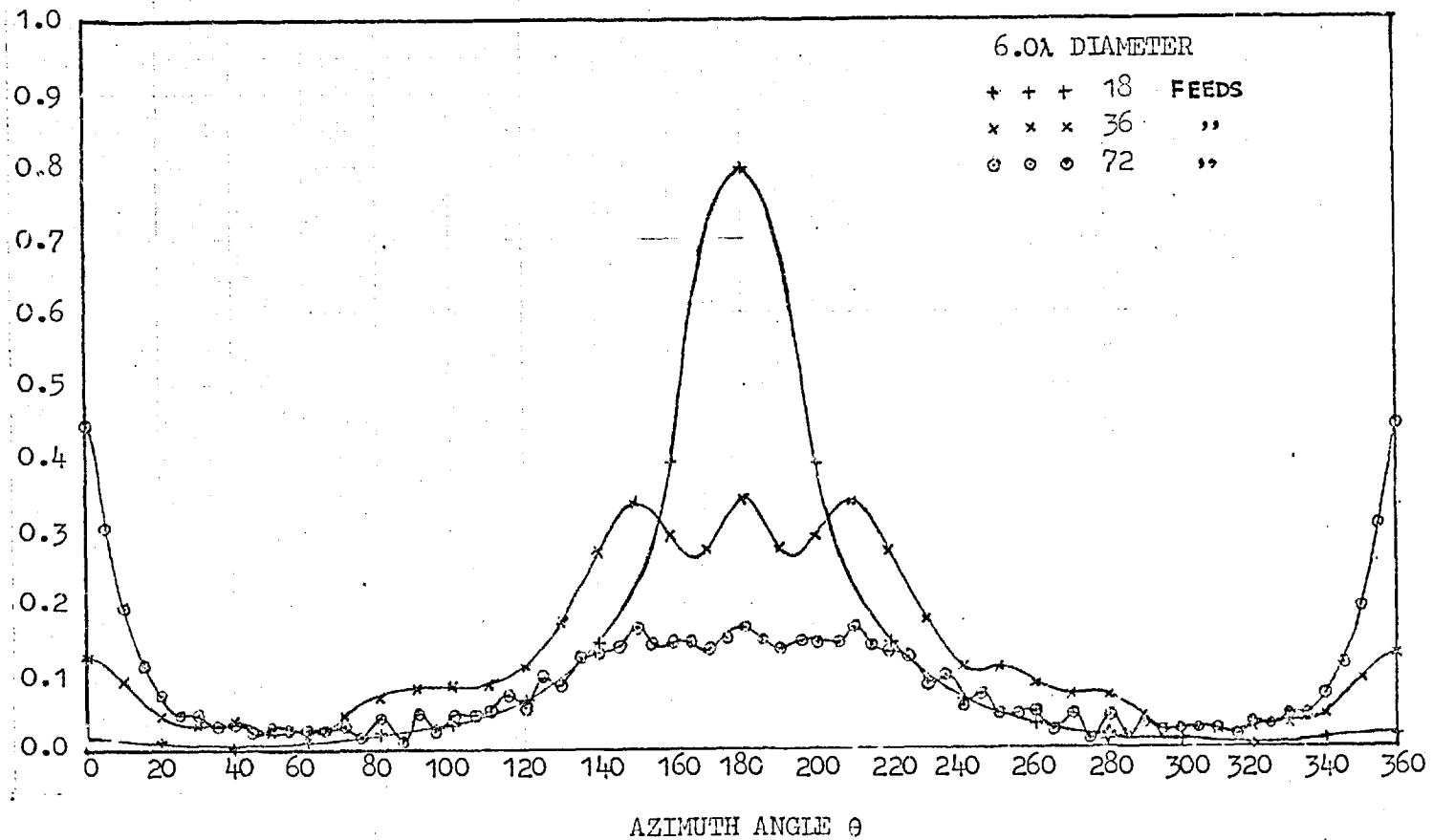


Fig. 3.6 LENS OUTPUT DISTRIBUTION

shown for various spacings for  $2.0\lambda$ ,  $4.0\lambda$  and  $6.0\lambda$  diameters in fig. 3.4, 3.5 and 3.6.

We suggest that the stronger taper when spacing is large (greater than approximately  $1.0\lambda$ ) is due to the larger effective feed aperture. Although feed directivity is not considered in the analysis its effect seems apparent. In a lens fed by horns it is apparent that the feed would have greater directivity if its aperture is larger ( $> 1.0\lambda$ ), but in an equivalent circuit lens the effect is less obvious. For smaller spacing between feeds the radiation pattern of the feed can be assumed to be approximately  $(1+\cosine)$ , giving rise to a weaker field in the forward direction and also a comparatively strong field at the feeds around the input port. The high fields at output ports adjacent to the input feeds suggest high coupling within the lens between feeds. The behaviour of  $[S]$  in relation to the reflection coefficients of the various modes is explained in the following section.

### 3.3.2(b) Effects of Mode Reflection Coefficients on Output Distribution

The modulus of the reflection coefficient for all modes is unity for a lossless structure. Only the phase ( $\rho_m$ ) varies with the mode number,  $m$ . Fig. 3.7 shows the relationship between  $\theta_m = (\rho_m - \rho_0)$  and the mode number,  $m$ , for  $2.0\lambda$ ,  $4.0\lambda$  and  $6.0\lambda$  diameter lenses.

Each of the three curves may be divided into two parts. The first region covers those values of  $\theta_m$  which increases with the mode number (mode  $\leq ka$ ). In the second region, the value  $\theta_m$  is

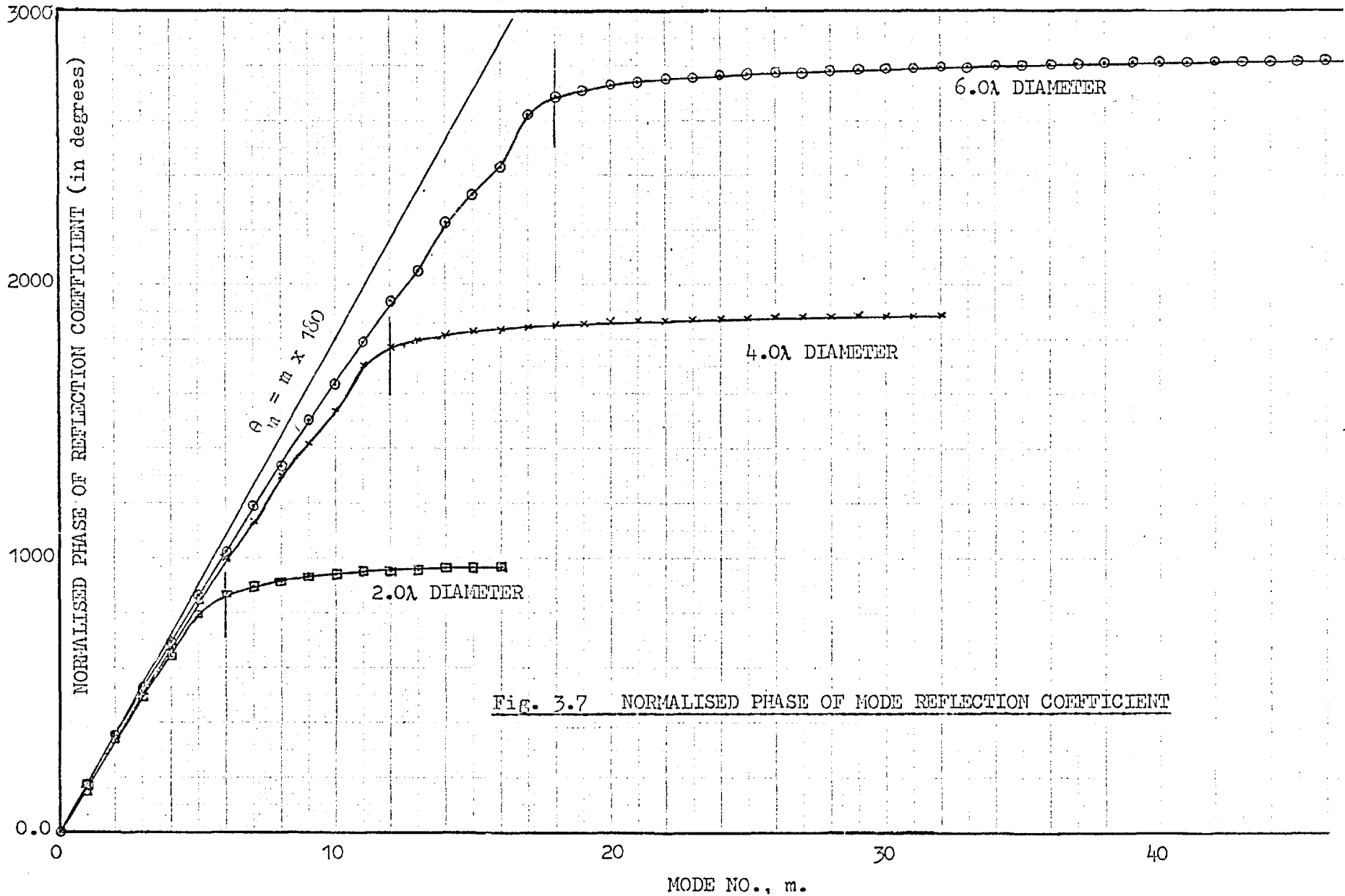


Fig. 3.7 NORMALISED PHASE OF MODE REFLECTION COEFFICIENT

approximately constant (increasing very slowly with mode number).

In the extreme, the curves in the two regions may be represented by two lines,  $\theta_m = m \times 180^\circ$  in region one and  $\theta_m = \text{constant}$  in region two.

An N-port (N even) lens system which has only eigenvalues (or reflections coefficient) represented by the line  $\theta_m = m \times 180^\circ$ , in region 1 will have all its input signal out at the output feed directly opposite the input feed. On the other hand, a lens system with only eigenvalues represented by  $\theta_m = \text{constant}$  will have all its input signals reflected back at the input feed. These results may be easily obtained from equations 3.29 to 3.32.

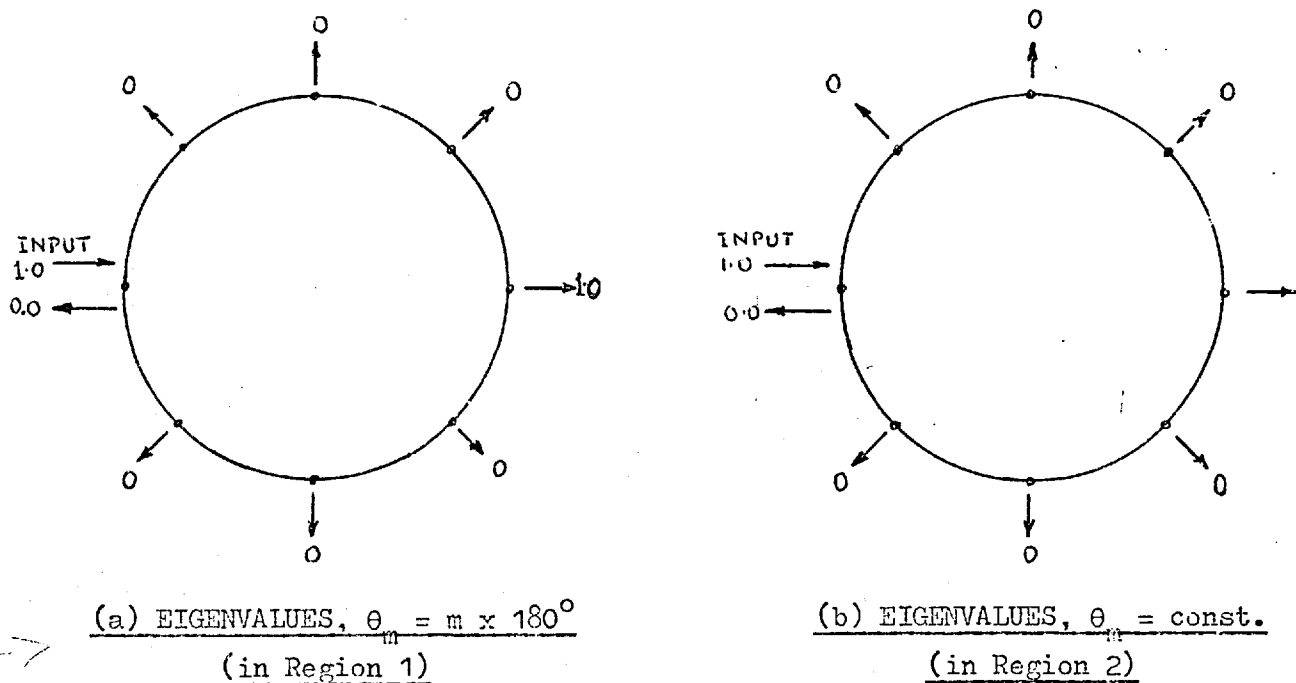


Fig. 3.7 (a)

The two curves for  $\theta_m$ ,  $\theta_m = m \times 180^\circ$  and  $\theta_m = \text{constant}$  represents

two extreme cases for output distribution for an N-port lens system. In a normal system, if most of the eigenvalues lie in region 1 a stronger taper will be obtained for the output distribution whilst, if the eigenvalues lie mainly in region 2 there is likely to be greater coupling between feeds. Fig. 3.7, together with figures 3.4, 3.5 and 3.6 supports this theory. With a decreasing number of feeds, the number of modes used decreases (number of modes used is about half the number of feeds - equation 3.32), and hence the number of eigenvalues in region 2 decreases, giving rise to a stronger taper in the output distribution.

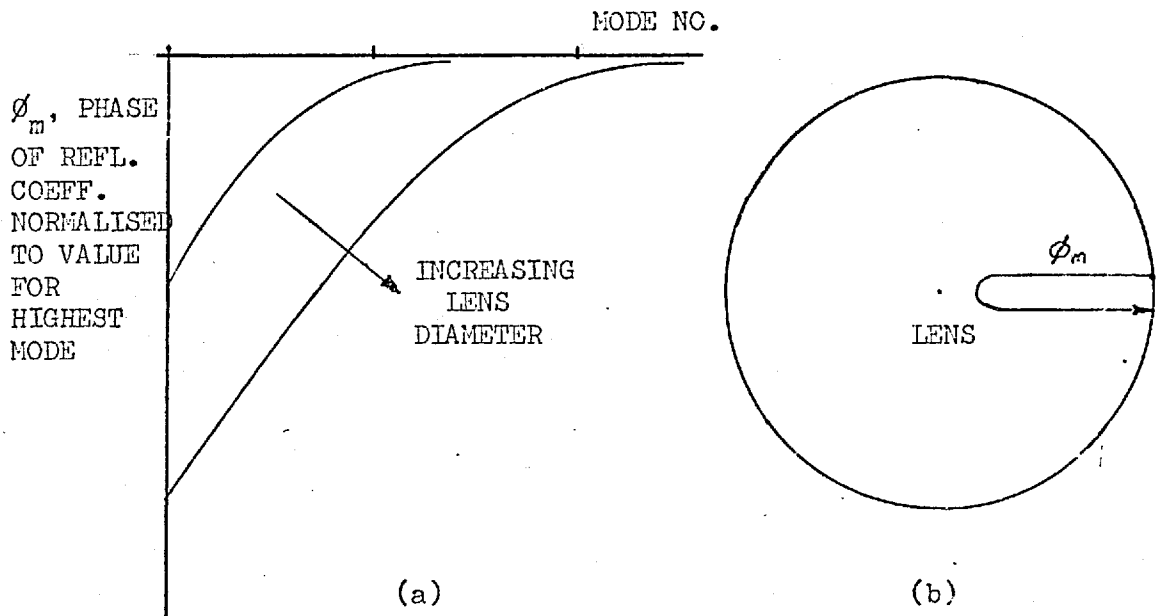


Fig. 3.8 WAVE PENETRATION INTO LENS FOR DIFFERENT MODES

The behaviour of the argument of the mode reflection coefficient suggests that a lower mode wave penetrates further into the lens

than one of a higher order. For high mode numbers ( $m \gg ka$ ) the waves are practically reflected at the lens circumference. The relative depth of the mode penetration can be estimated by looking at the arguments of the mode reflection coefficients, all normalised to the value of the highest mode, so that the arguments are negative and increasing with mode number to zero as illustrated in fig. 3.8(a). As in a reactively terminated line the phase of the reflection coefficient so normalised represents the electrical distance covered by the wave travelling into the lens and back. This discussion is particularly relevant to the equivalent circuit lens which is studied in Chapter 4.

### 3.3.3 Far-field Radiation Pattern

In an optical Luneburg Lens, the fields emerging from the lens are radiated with the aperture acting as the radiator. A lens system which feeds cardioid radiators [ (1+cosine) pattern ] will give a good approximation to this aperture for vertical polarisation. (The E-field contributes to the 1 term and the H-field, the cosine term).

To obtain the far-field pattern for the array the outputs from the lens feed system are fed into cardioid radiators. The subroutine, FARF1, programmed to compute the far-field pattern is described in appendix A3.2.6. The effect of coupling between radiators is not taken into account in this computation.

The performance of the lens system is studied under the following headings:-

- (a) Behaviour for small lens diameters for the two type of lenses.
- (b) Effect of feed spacing and lens diameter
- (c) Use of omni-directional and beverage aerials as radiators in the array.

### 3.3.3(a) Behaviour of the Lens System for Small Lens Diameters

It has been suggested early in the chapter that, for large lens diameters, the behaviour of the two types of lenses ( $\mu = \epsilon = \sqrt{2-r^2}$  and  $\mu = 1; \epsilon = 2-r^2$ ) will practically be the same. This has been confirmed by the radiation patterns obtained. Down to about  $1.5\lambda$  diameter there is very little difference between radiation patterns obtained for the two types of lens. Fig. 3.9 and 3.10 show the radiation pattern obtained for the two types of lens for feed/radiator spacing of approximately  $\lambda/2$  for lens diameters of  $0.5\lambda$ ,  $0.75\lambda$ ,  $1.0\lambda$  and  $1.5\lambda$ . The ( $\mu = \epsilon$ ) lens appears to have a marginally broader beam and slightly higher first side lobe. However the "ordinary" Luneburg lens ( $\mu = 1, \epsilon = 2-r^2$ ) has a slightly higher directivity ranging from 0.5db at  $0.5\lambda$  to about 0.1db at  $2.0\lambda$  diameter.

The beamwidth of the array has been plotted in figure 3.12 for various values of lens diameters. At the low valued end of the diameter scale the beamwidth is practically inversely proportional to the diameter. For small lens diameters there is a maximum value for the side lobe level (fig. 3.11). Because of this a minimum lens



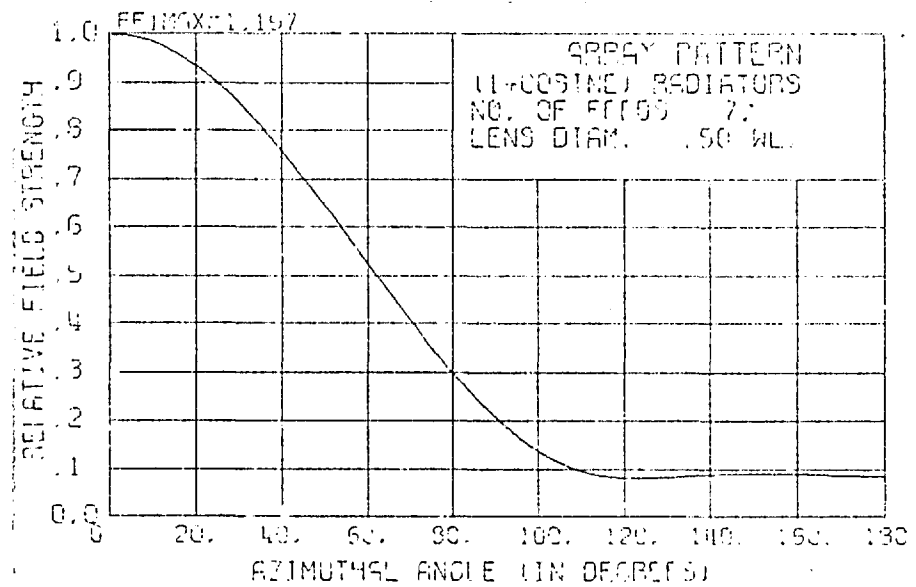
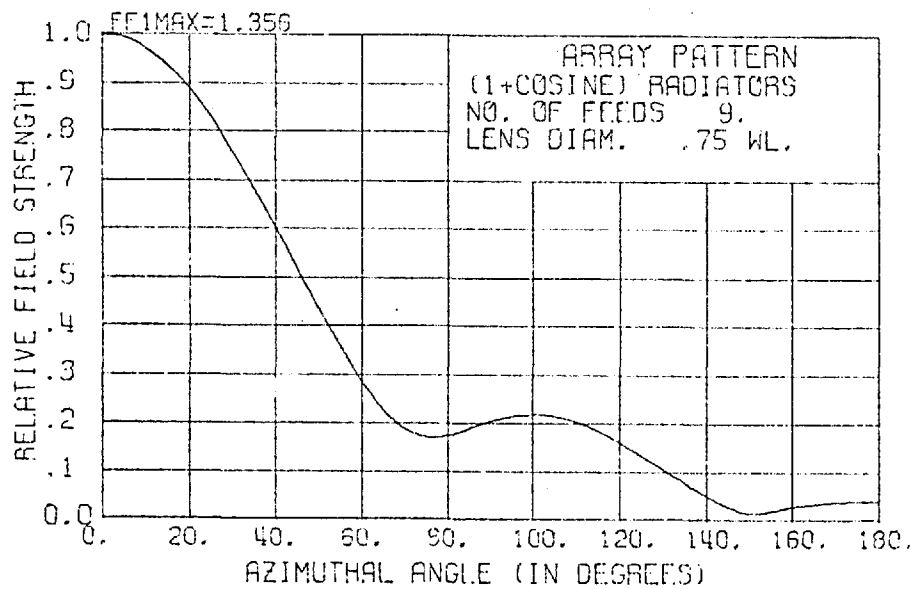
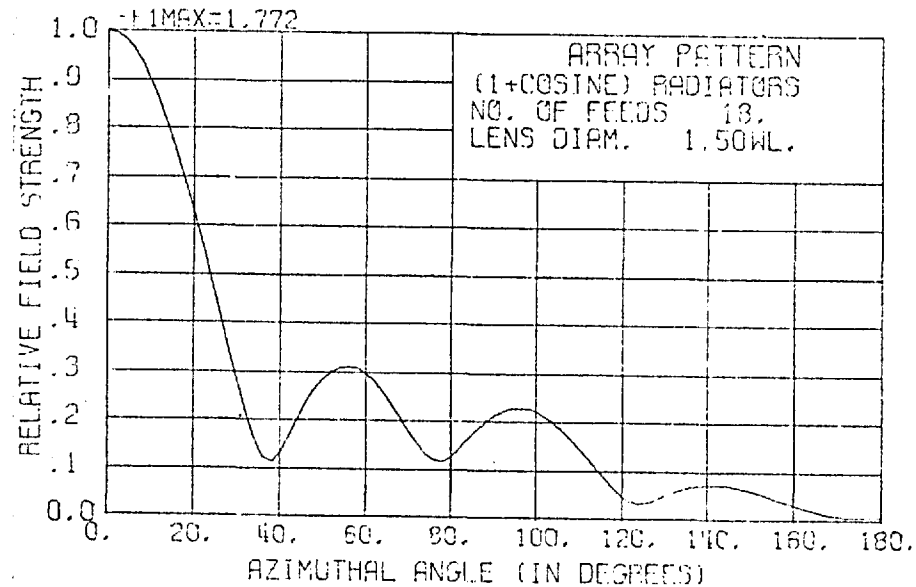
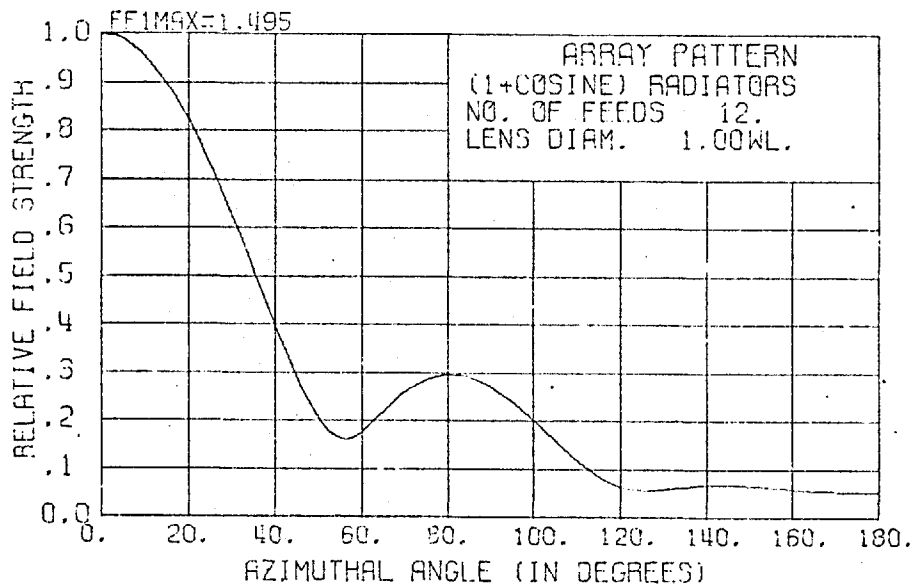


Fig. 3.9 FAR-FIELD RADIATION PATTERN OF ORDINARY LENS FOR SMALL DIAMETERS

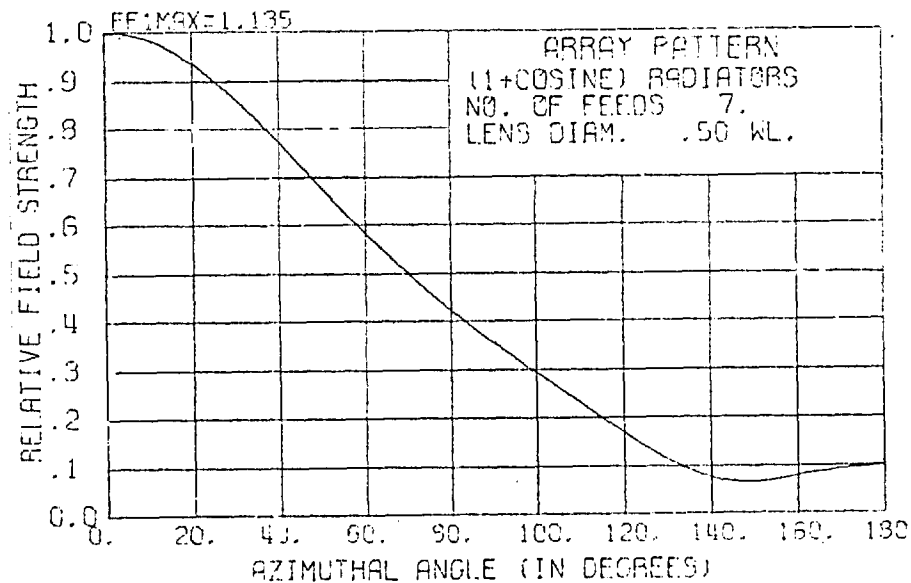
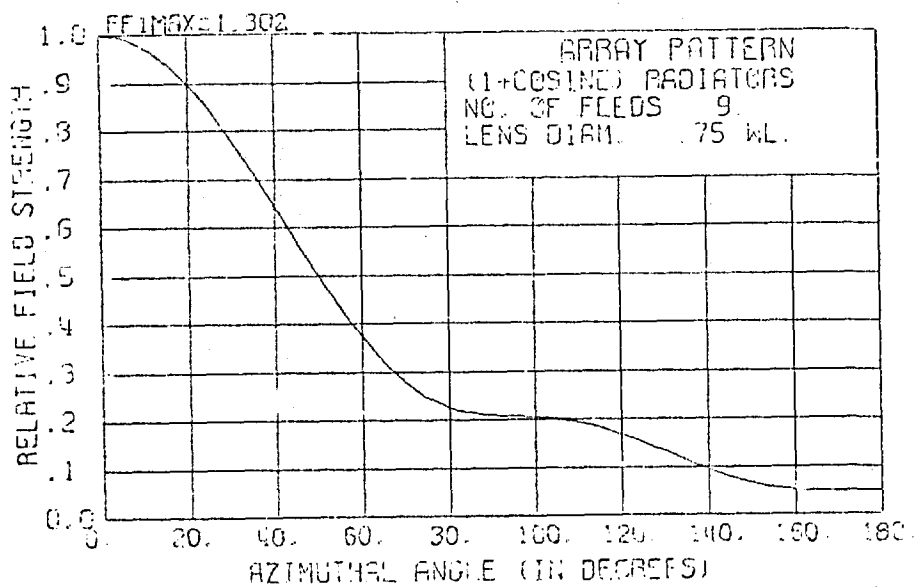
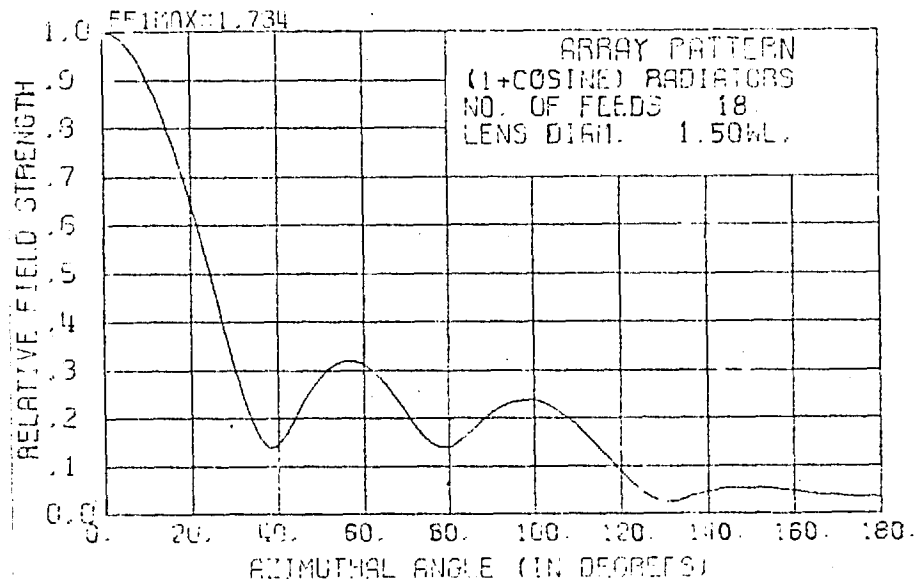
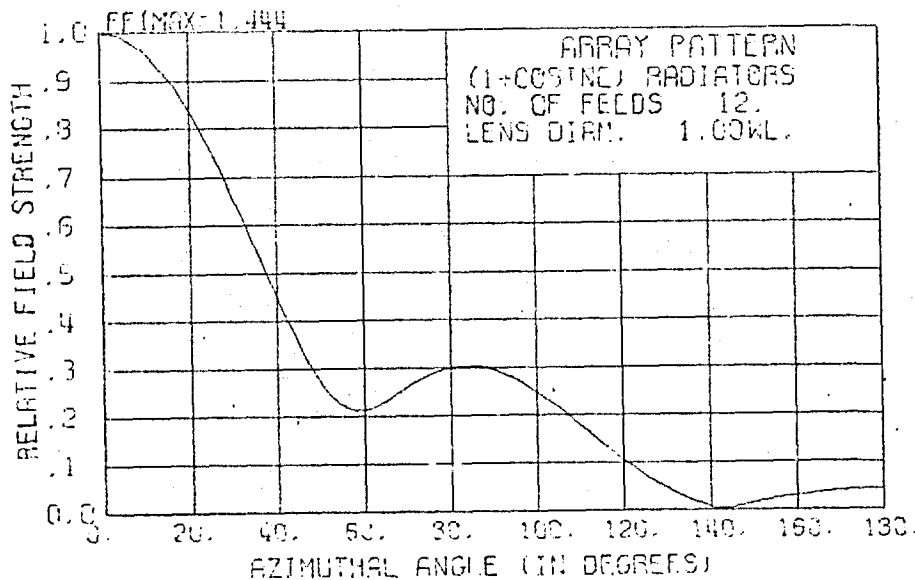


Fig. 3.10 FAR-FIELD RADIATION PATTERN OF  $\mu = e$  LENS FOR SMALL DIAMETERS

diameter of about  $2.0\lambda$  is necessary for multibeam operation. Besides, the overlap between beams will be too great if the lens diameter is too small.

### 3.3.3(b) Effect of Feed Spacing and Lens Diameter

The side lobe level relative to the main beam is plotted in fig. 3.11 for lens diameter between  $0.75\lambda$  and  $10.0\lambda$ . The beamwidth is also plotted over the same range of diameter values in fig. 3.12.

For an N-feed circular array, N far field modes are excited. The excitation of each of the modes is equivalent to that for each radiator of an N element linear array. This topic will be discussed in greater detail in Chapter 5. However, the results obtained in Chapter 5 (fig. 3.13) will be referred to in discussion in this chapter. Fig. 3.13 gives the plot of the amplitude of the far-field mode against the mode number for various values of lens diameter. This applies only to an array using cardioid ( $1+\cosine$ ) radiators.

There is a maximum value for the side lobe level at about  $1.25\lambda$  diameter. This is because below  $1.25\lambda$  diameter the amplitude distribution for the far field mode is very strongly tapered, giving rise to very low side lobe levels. Above  $1.25\lambda$  diameter, the mode amplitude distribution approaches a uniform distribution, the side lobe ratio approaching  $-13.3\text{db}$  for high values of diameters.

for N large ( $N > ka$ ; spacing between feeds  $< \lambda/2$ )

Fig. 3.13 indicates that the far field mode amplitude is negligible if the mode number is slightly greater than  $ka$ . Therefore if the

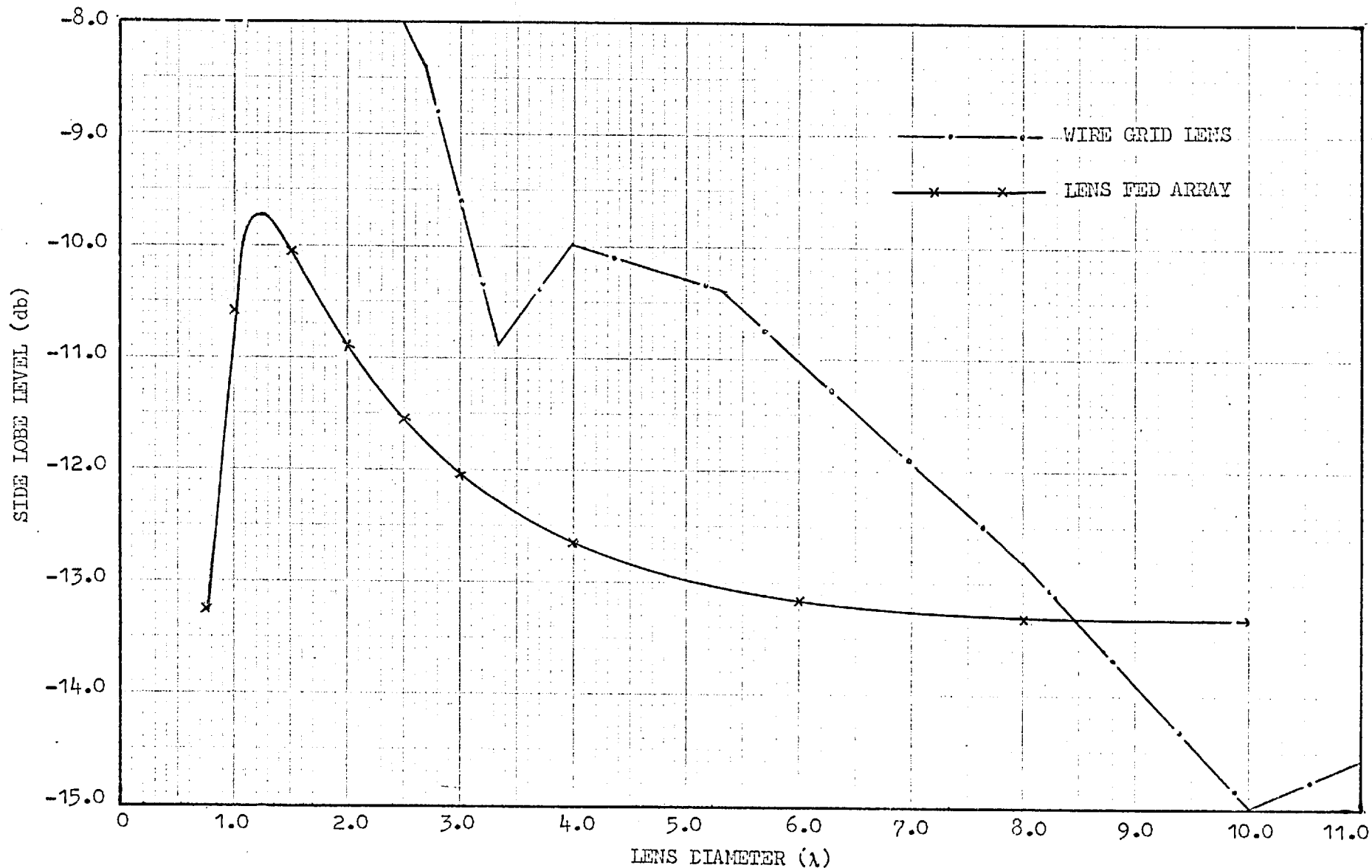


Fig. 3.11 SIDE LOBE LEVELS OF LUNTBURG LENS FED ARRAY

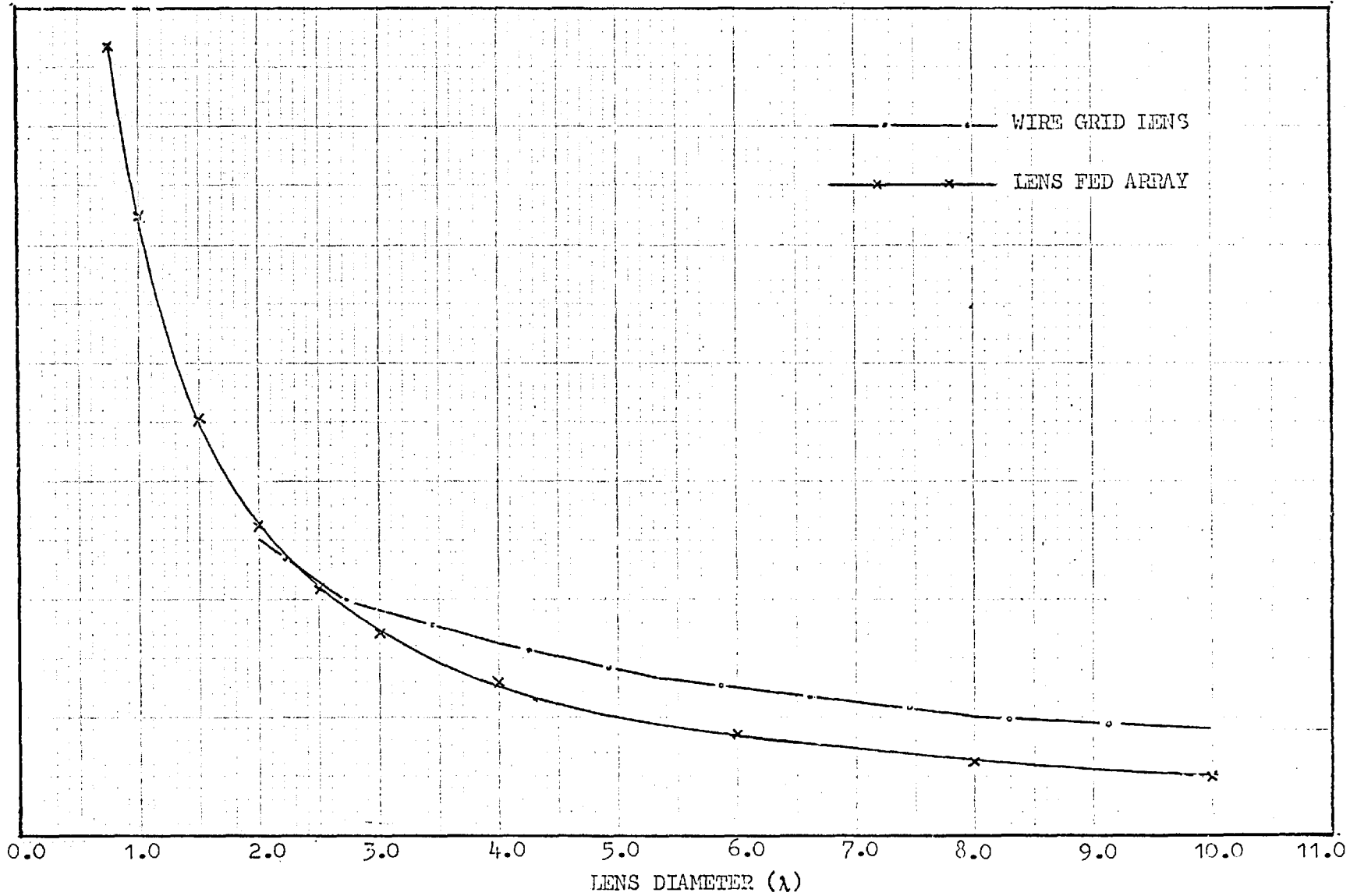


Fig. 3.12 BEAMWIDTH OF LUNEBURG LENS FED ARRAY

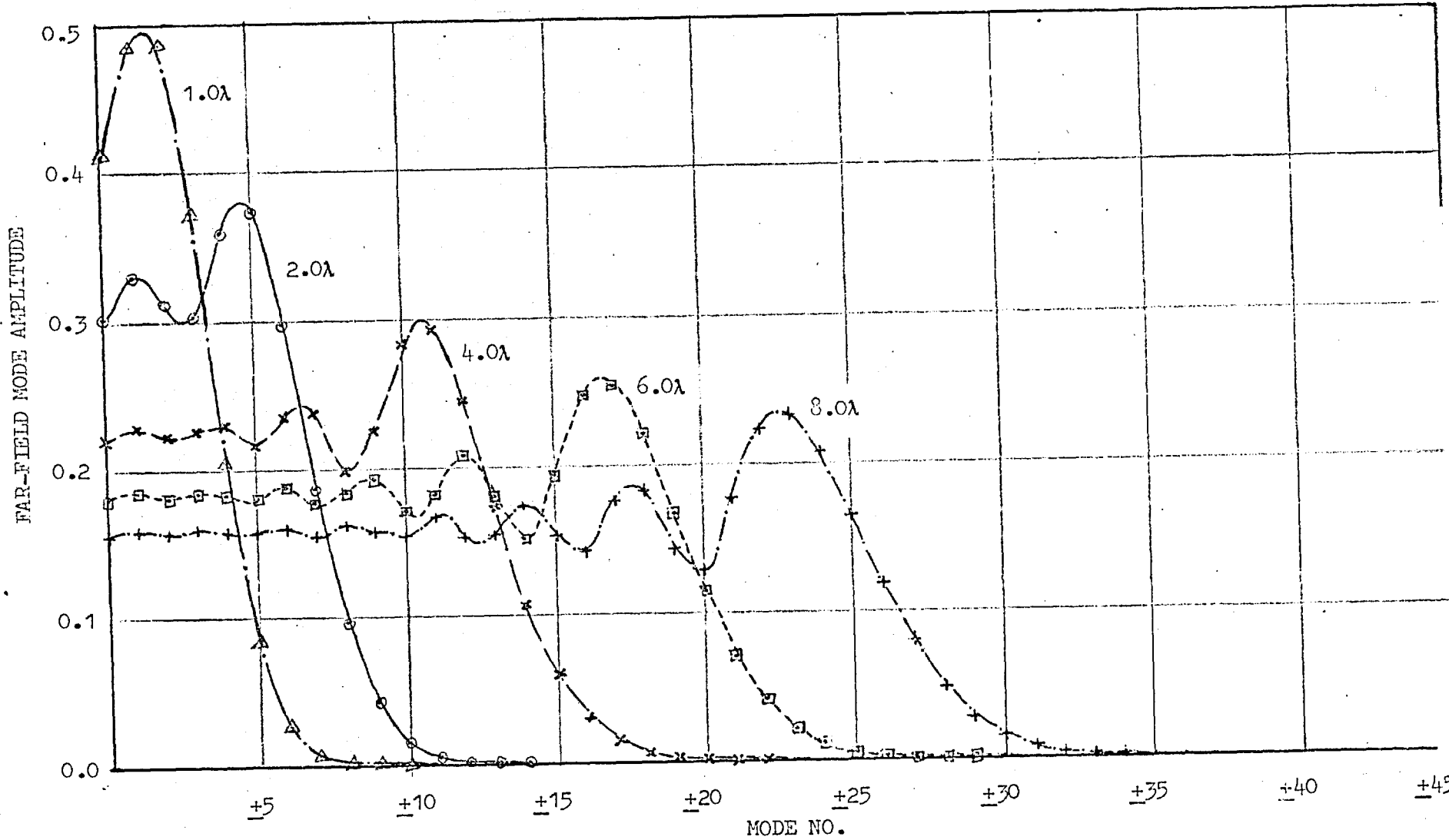


Fig. 3.13 FAR-FIELD MODE AMPLITUDE - CARDIOID (1+cosine) RADIATORS

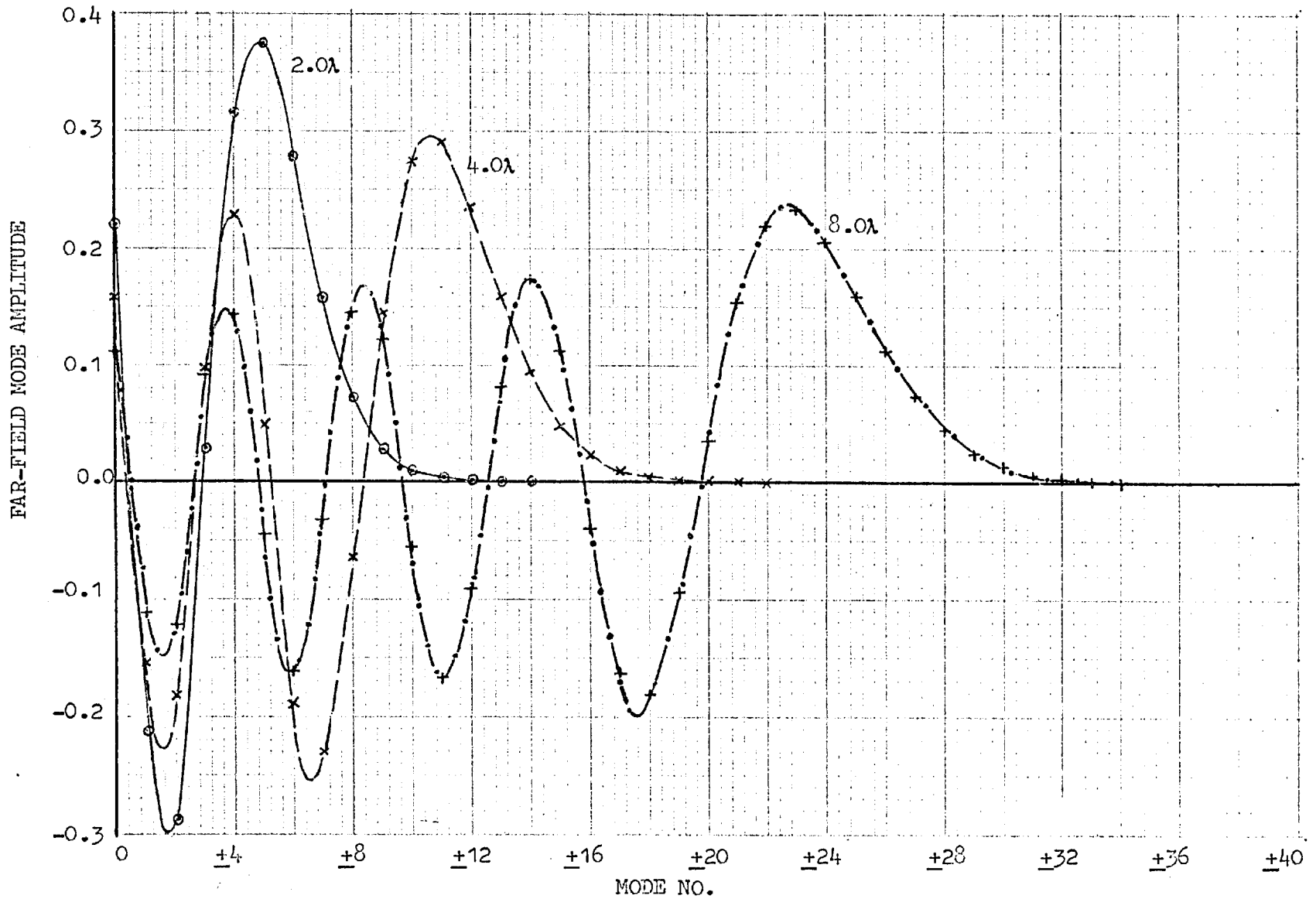


Fig. 3.13(a) FAR-FIELD MODE AMPLITUDE DISTRIBUTION (OMNI-DIRECTIONAL RADIATORS)

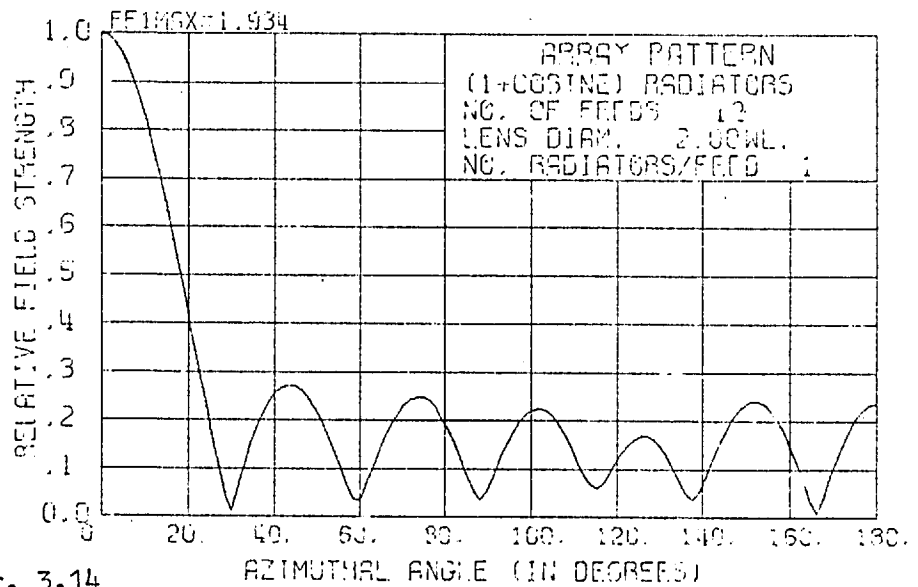
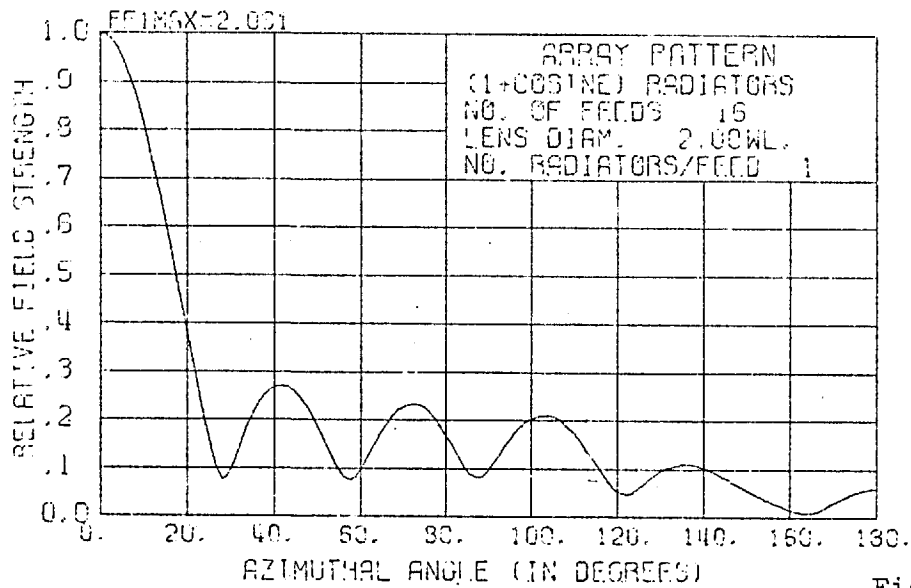
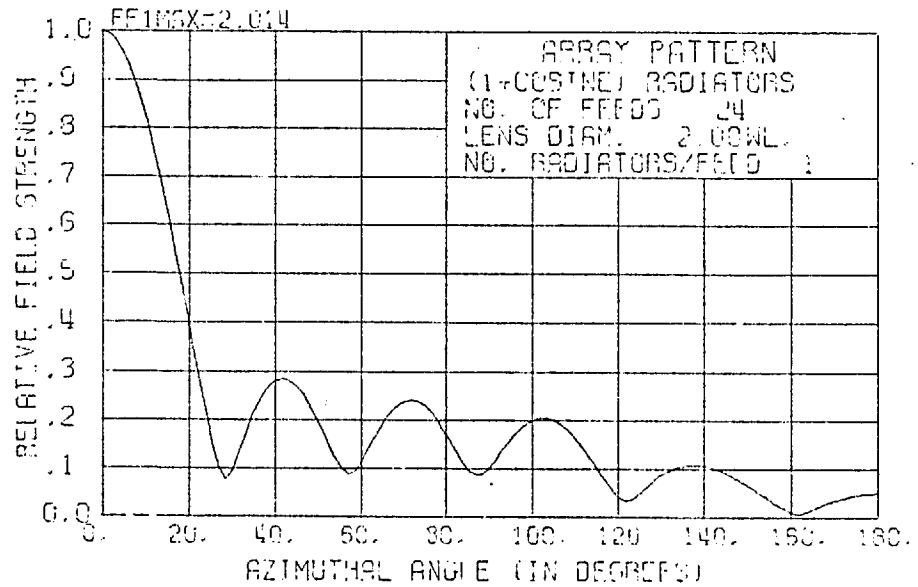
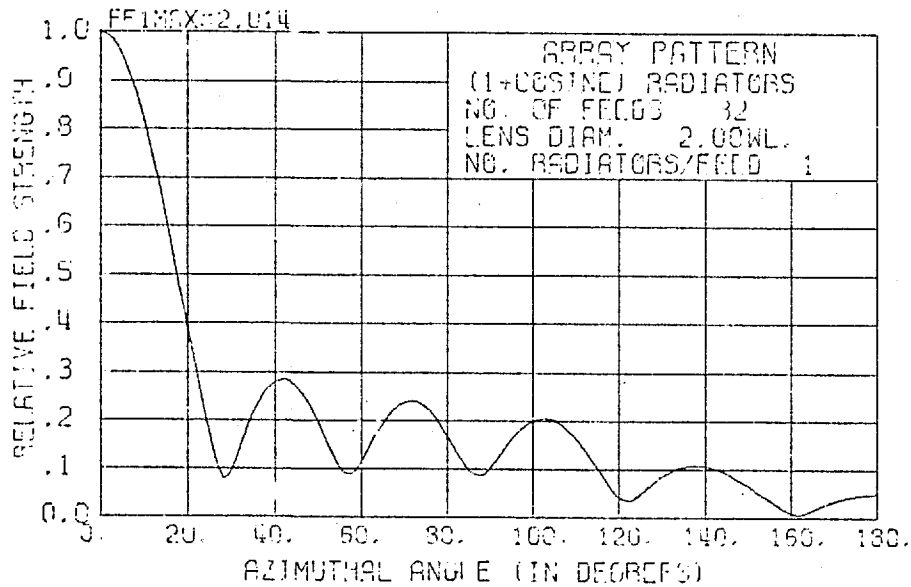


Fig. 3.14



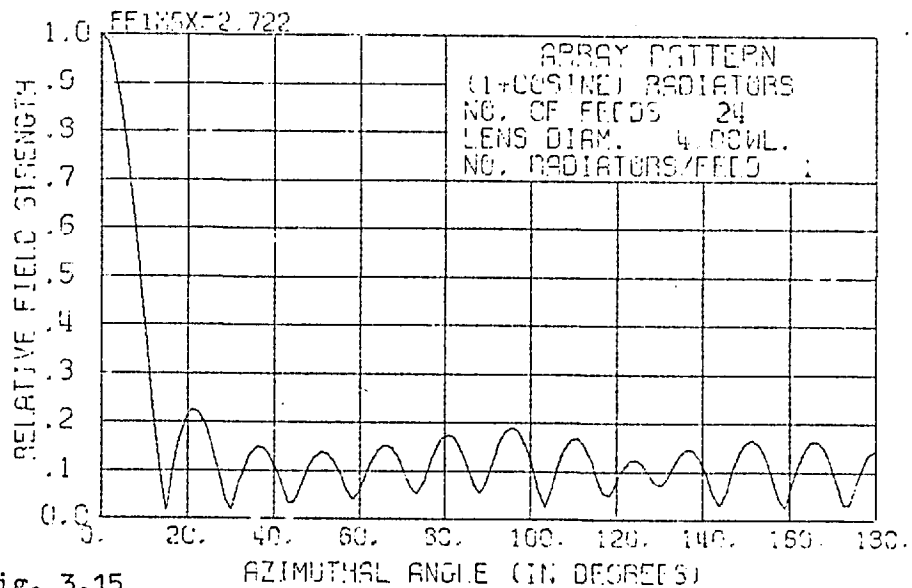
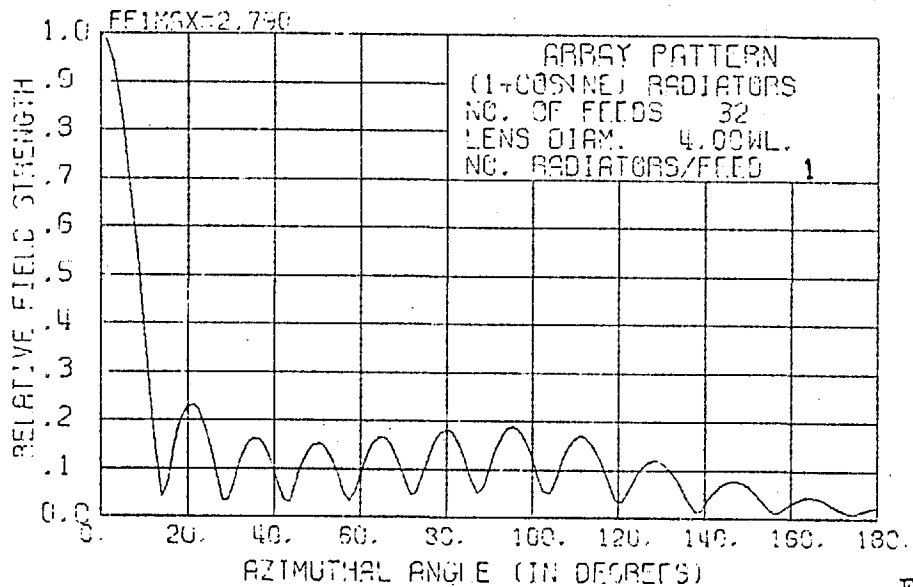
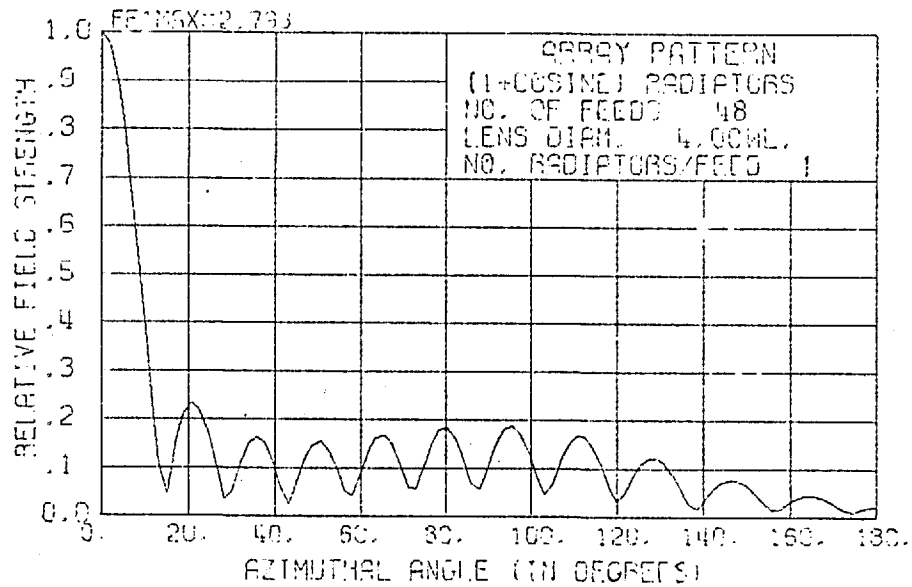
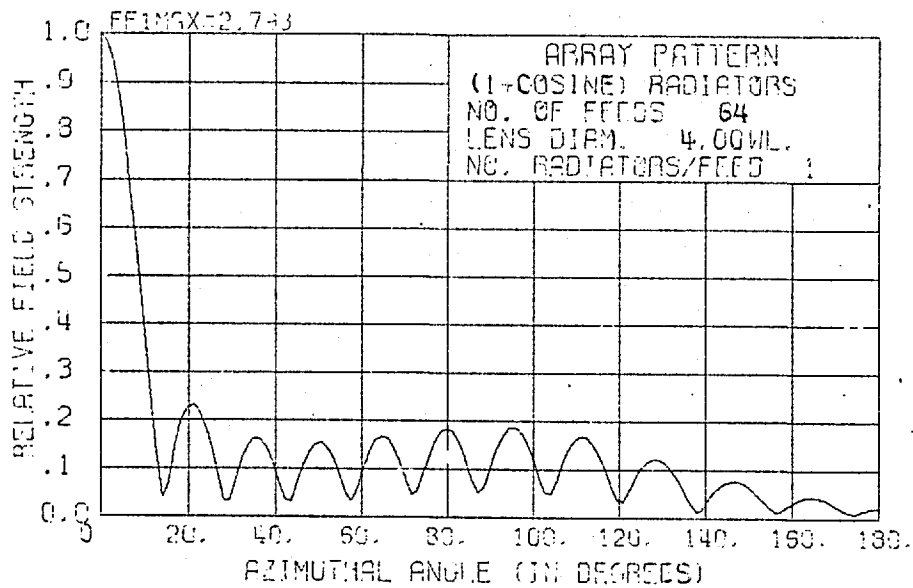


Fig. 3.15

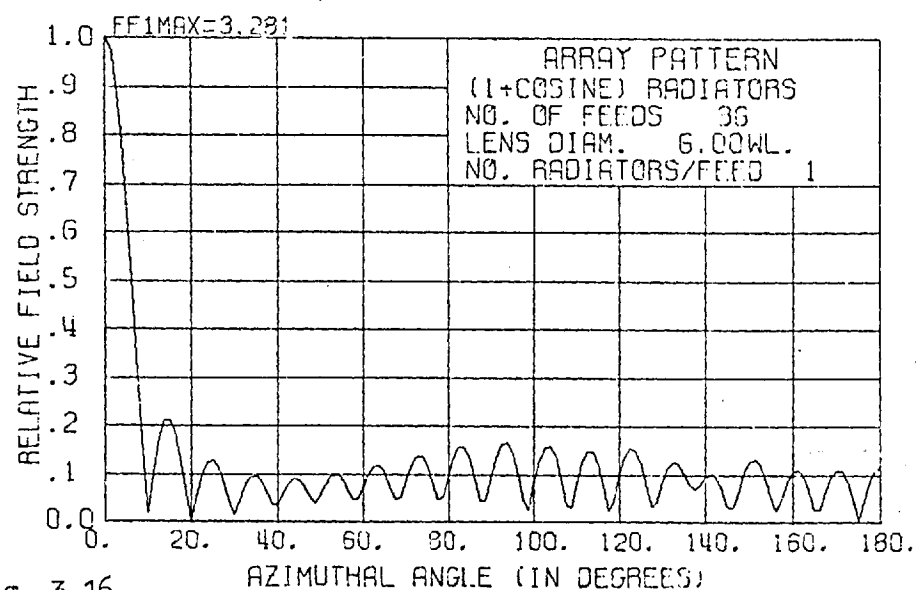
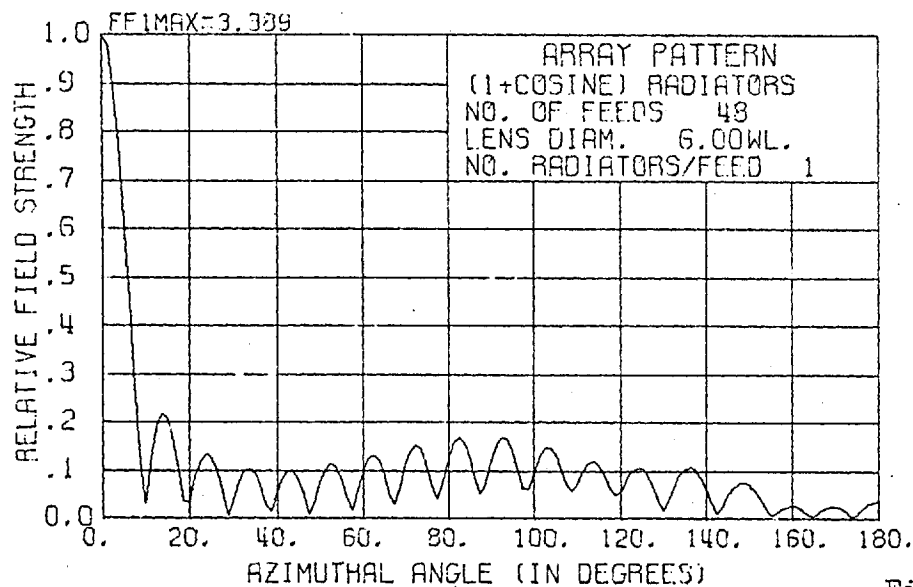
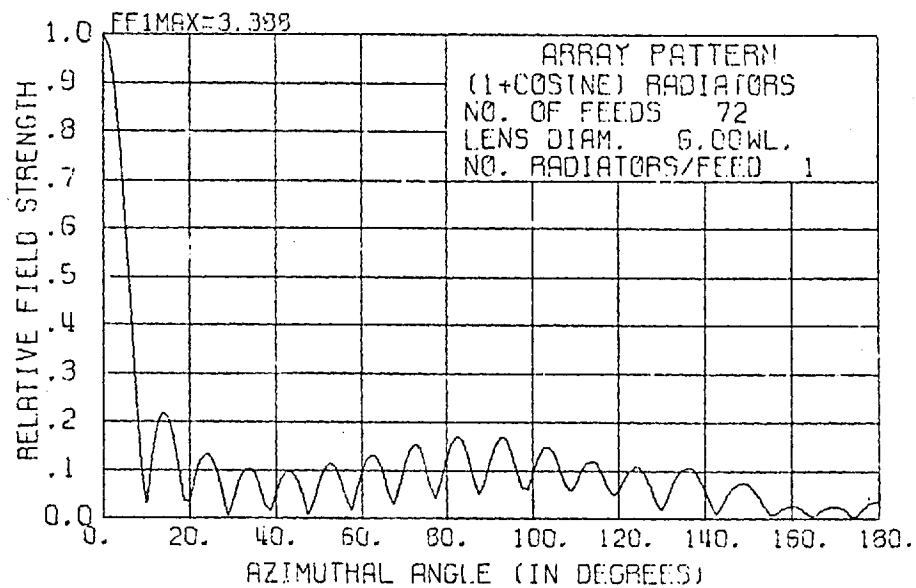
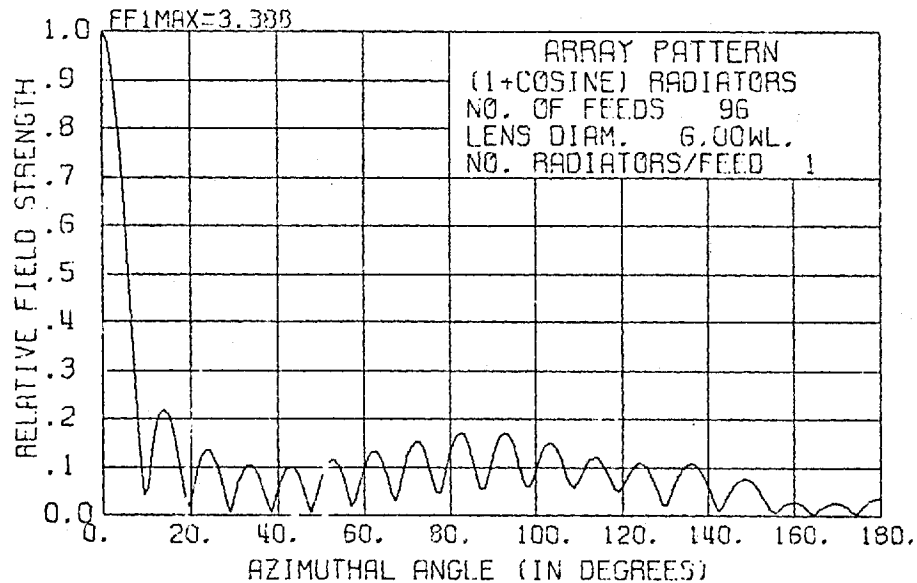


Fig. 3.16

number of feeds/radiators used in an array is greater than  $ka$  the far field pattern is quite independent of the number of feed/radiator used. This can be seen from the radiation patterns given in fig. 3.14, 3.15 and 3.16 for array diameters of  $2.0\lambda$ ,  $4.0\lambda$  and  $6.0\lambda$  respectively. The far field patterns of arrays with feed/radiator spacing of  $0.196\lambda$ ,  $0.262\lambda$ ,  $0.393\lambda$  and  $0.523\lambda$  are practically identical except for the last one which has a slightly higher side lobe.

for feed spacing less than  $\lambda/2$

The radiation pattern is made up of mode 0 to  $\frac{N-1}{2}$  (or  $\frac{N}{2}$ , if  $N$  even) where  $\frac{N}{2} < ka$ . If no grating lobes are excited (grating lobes are caused by too large spacings between radiators), then from fig. 3.13 the far field mode amplitude distribution will be nearly uniform particularly if the array diameter is large. The radiation pattern obtained will then approach a  $\sin u/u$  pattern more closely than the case with  $N > 2ka$ . But from results obtained for cardioid radiators, grating lobes begin to appear if spacings between radiators approach approximately  $0.6\lambda$ . The problem with grating lobes can be alleviated by connecting more than one radiator in parallel to each feed. Radiation patterns for arrays with spacings greater than  $\lambda/2$  are given in fig. 3.17. Fig. 3.18 shows the effect of connecting each feed to two adjacent radiators in the array.

The result of changing feed numbers in an array is tabulated in table 3.2 for a  $6.0\lambda$  diameter lens. The effects on the beamwidth, side lobes and directivity of the array can be seen. The beamwidth increases as fewer feeds are used. This is due to the use of fewer

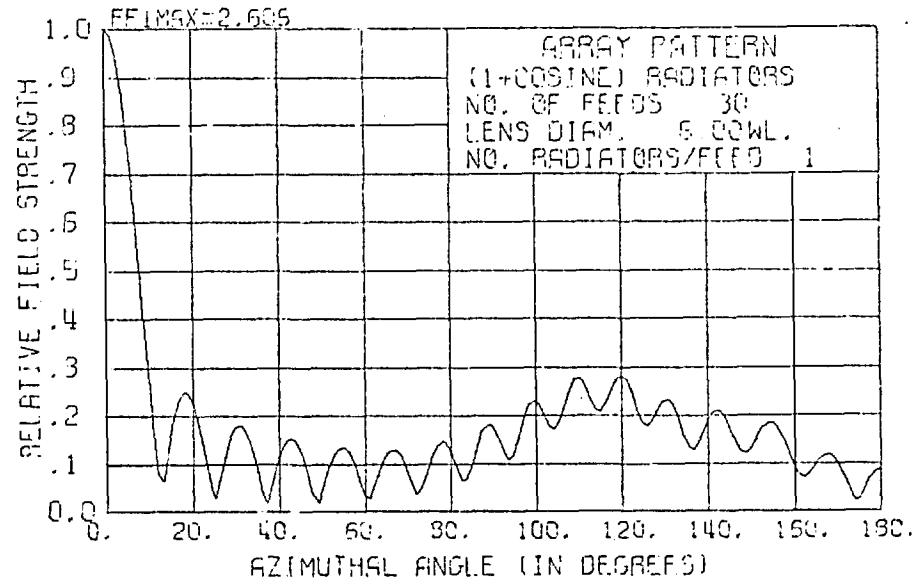
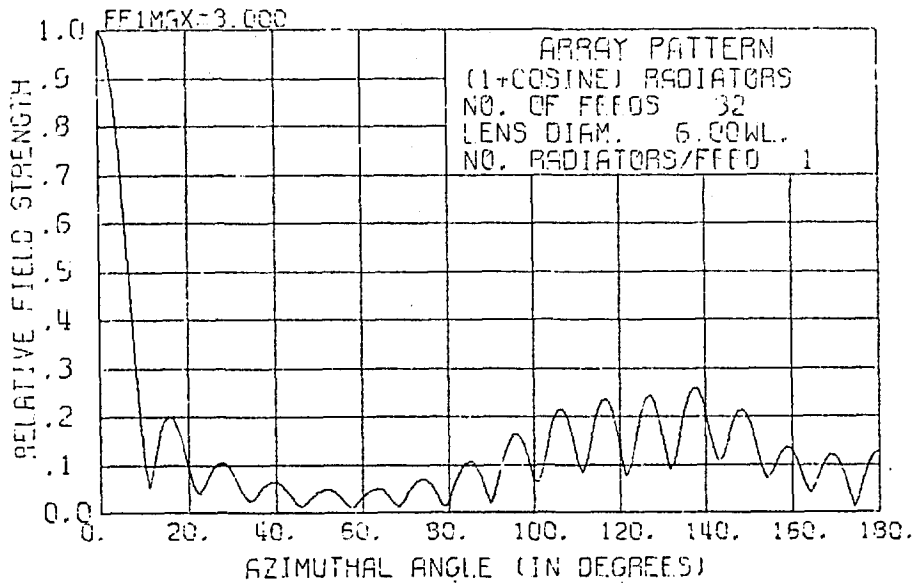
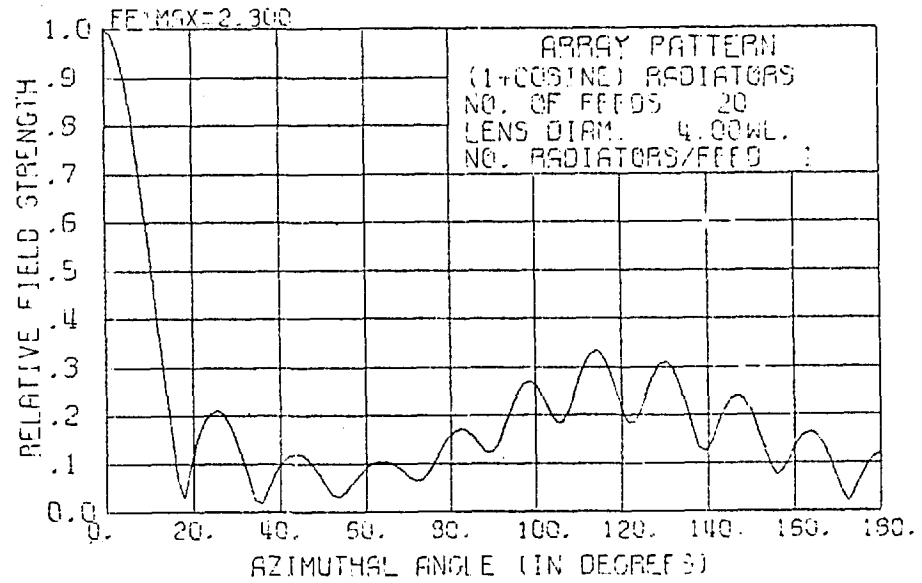
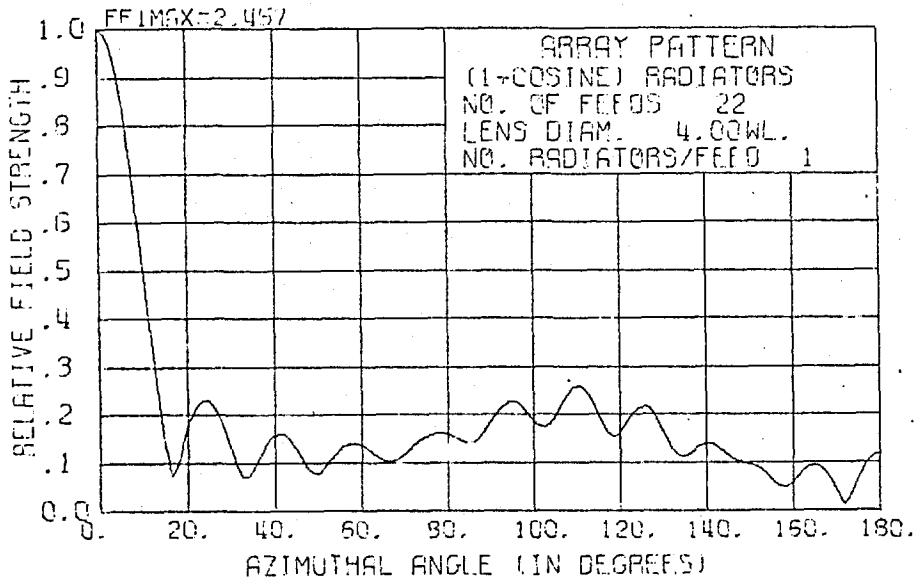


Fig. 3.17 EFFECT OF GRATING LOBES

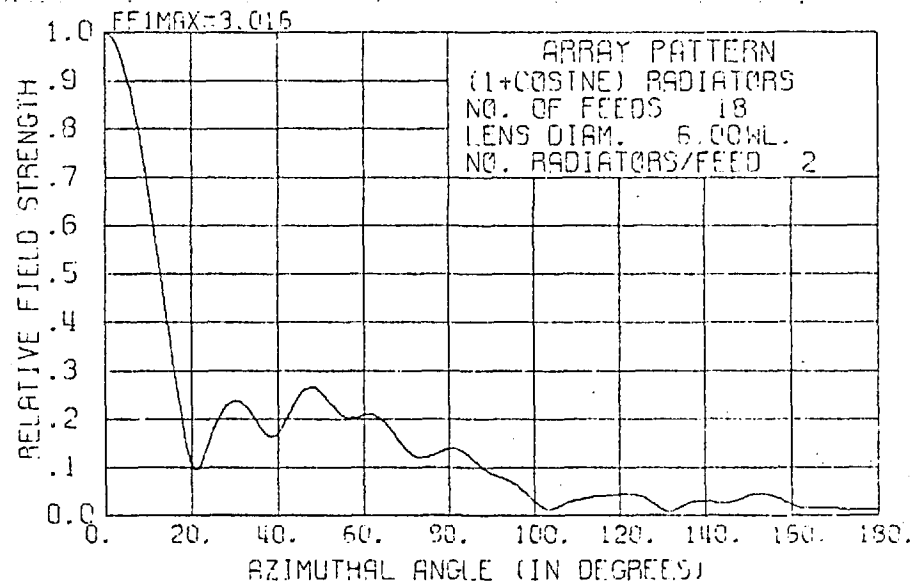
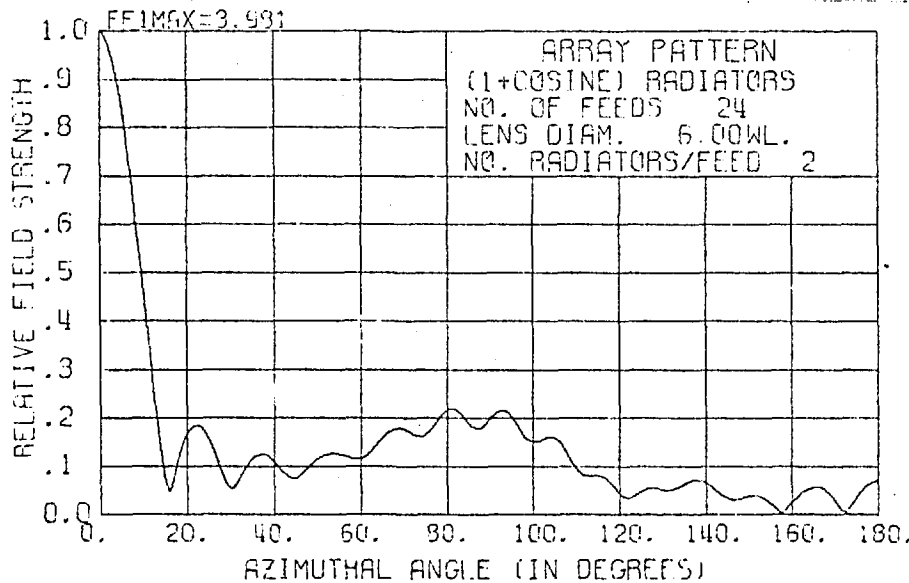
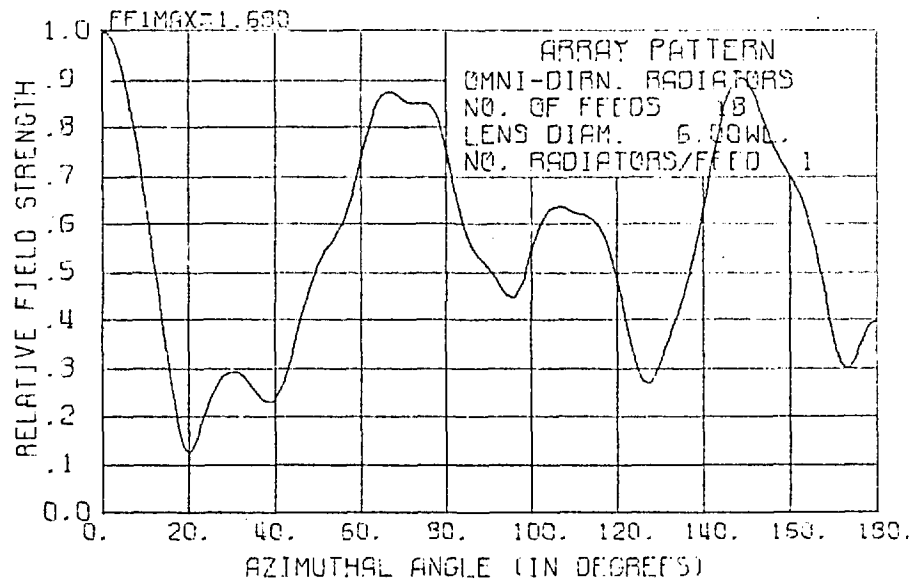
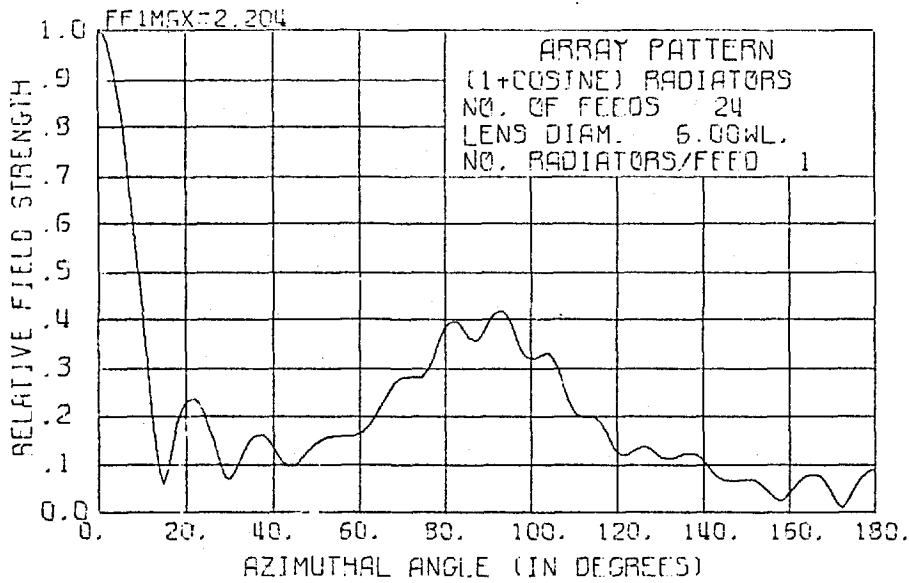


Fig. 3.18 EFFECT OF FEEDING TWO ADJACENT RADIATORS IN PARALLEL

far field mode. In fact this is equivalent to a smaller "aperture".

The beamwidth and side lobe levels for arrays of various diameters are tabulated in table 3.1. The number of feeds/radiators used is such that  $N > 2ka$ .

DIAMETER (in $\lambda$ )	BEAMWIDTH (in degrees)	FIRST SIDE LOBE (relative to main beam)	BACK LOBE	HIGHEST SIDE LOBE (beside the two already tabulated)
0.5	84.9°	0.092(-19.2db)	0.084	-
0.75	66.8	0.217(-13.3db)	0.04	-
1.0	52.5	0.296(-10.6db)	0.052	0.068
1.5	35.2	0.315(-10.0db)	0.008	0.229
2.0	26.2	0.285(-10.9db)	0.051	0.242
2.5	20.8	0.265(-11.5db)	0.047	0.226
3.0	17.2	0.250(-12.0db)	0.041	0.203
4.0	12.9	0.233(-12.7db)	0.035	0.189
6.0	8.6	0.220(-13.15db)	0.04	0.171
8.0	6.2	0.216(-13.3db)	0.034	0.148
10.0	5.0	0.217(-13.3db)	0.038	0.117

Table 3.1 Beamwidth and side lobe levels (for  $N > 2ka$ )

NO. OF FEEDS	NO. RADIATORS PER FEED	BEAMWIDTH (degrees)	FIRST SIDE- LOBE	OTHER HIGHEST SIDE LOBE	DIRECTIVITY
48	1	8.6	0.219	0.155	3.389
36	1	8.8	0.213	0.167	3.282
32	1	9.4	0.106	0.256	3.000
28	1	11.1	0.220	0.290	2.631
24	1	13.4	0.238	0.421	2.205
24	2	14.0	0.185	0.220	3.982/2
18	1	18.0	0.295	0.876	1.680
18	2	18.8	0.239	0.167	3.017/2

Table 3.2 Effects of varying feed No. for 6.0 $\lambda$  diameter array

### 3.3.3(c) Use of Omni-directional and Beverage Aerial Radiators

#### Omni-directional Radiators

If omni-directional are used in the array, the far-field mode amplitude due to a near field excitation of unit amplitude is  $J_m(ka)$  for the  $m$ th mode. The far field mode distribution corresponding to fig. 3.13 for cardioid radiators will then be given by  $A_m = J_m(ka)$  (fig. 3.13(a)). This means that the amplitude distribution changes rapidly with frequency. Fig. 3.19 shows the radiation pattern for a  $6.0\lambda$  diameter lens array with spacing between feeds/radiators of  $0.26\lambda$ ,  $0.392\lambda$ ,  $0.523\lambda$  and  $0.783\lambda$ . The grating lobe is particularly significant in the last pattern. The side lobe is of the order of  $-8$ db which is too high for our application. However, the beamwidth of this array is narrower than that using cardioid radiators. Typical beamwidth values are tabulated below in table 3.4.

DIAMETER (in $\lambda$ )	NO. OF FEEDS/ RADIATORS	BEAMWIDTH (in degrees)		
		OMNIDIRECTIONS RADIATORS	CARDIOD (1+COSINE) RADIATORS	BEVERAGE RADIATORS
4.0 $\lambda$	36	14.2	17.1	18.0
6.0 $\lambda$	72	8.0	8.8	14.3

Table 3.4 Beamwidth Comparison of Array with Omni-directional,  
Cardioid and Beverage Aerial Radiators

#### Beverage Aerial Radiators

In conjunction with this project dos Santos (5) has studied the beverage aerial and the phase compensated circular array of radially

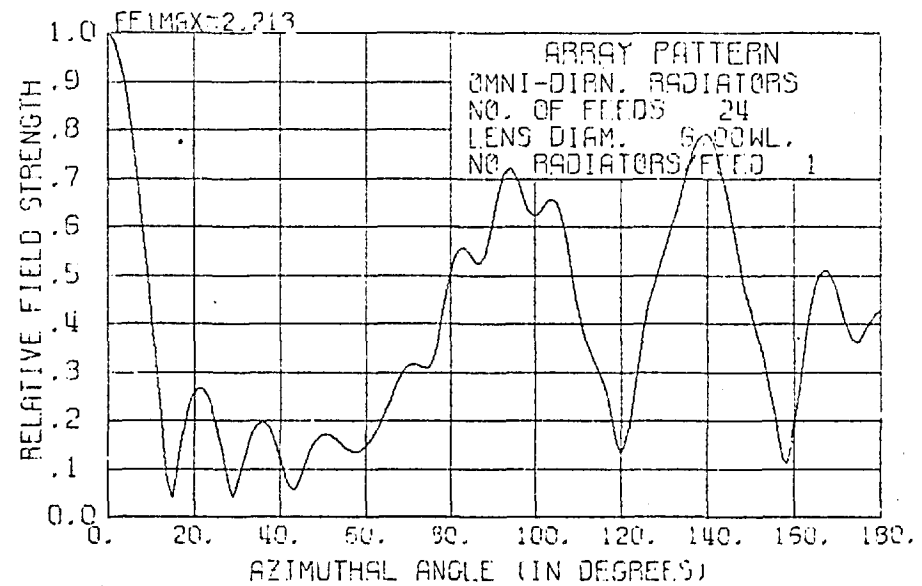
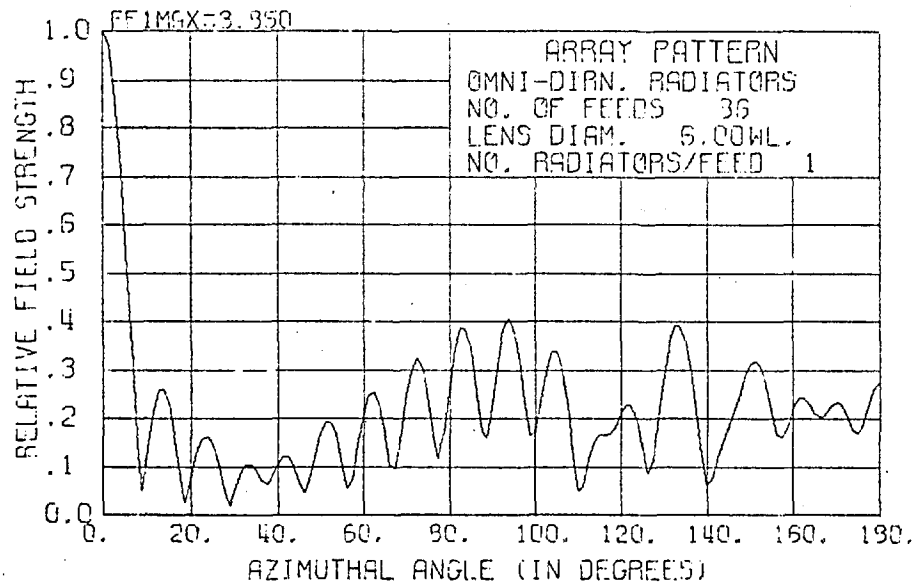
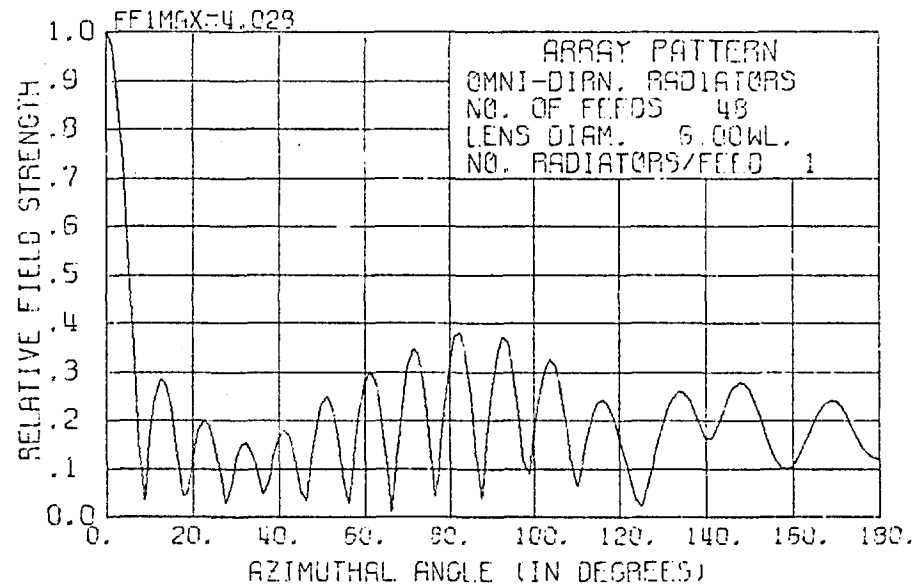
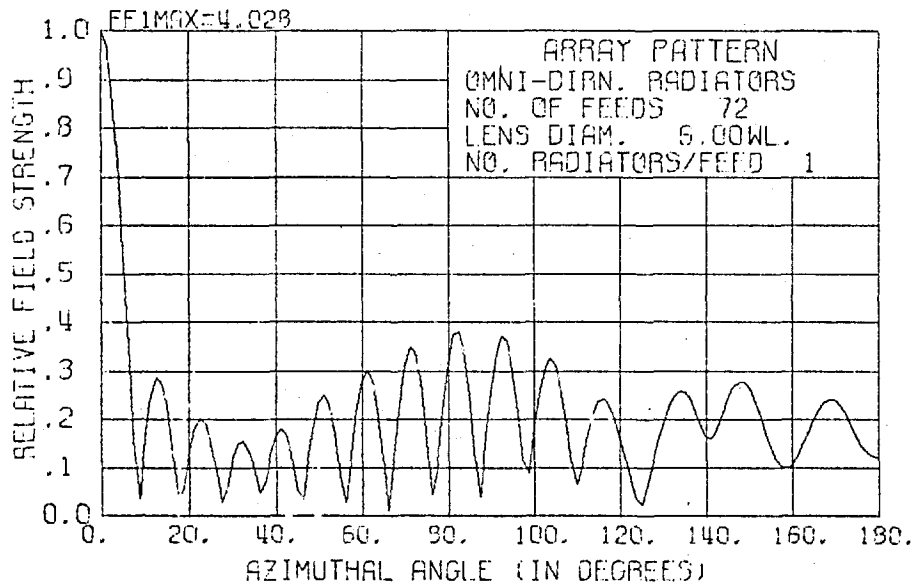
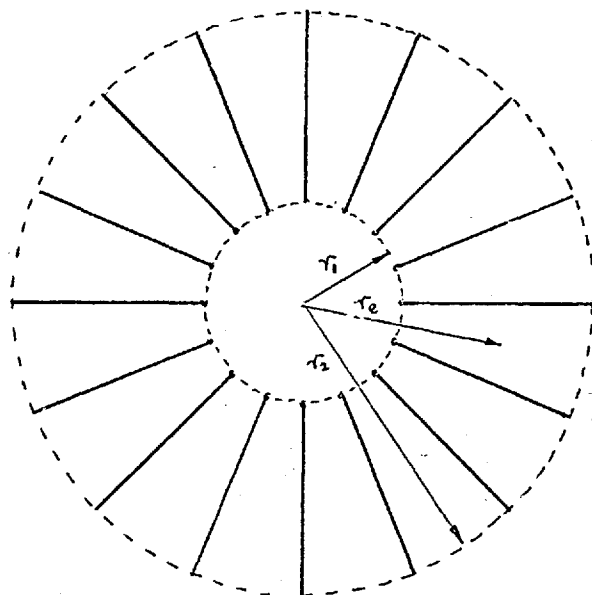


Fig. 3.19 OMNI-DIRECTIONAL RADIATORS



arranged Beverage elements.

The Luneburg Lens feed system offers a good phase compensating network for use with radial array of Beverage elements. The arrangement is illustrated in fig. 3.20.



$r_1$  - internal array radius

$r_2$  - external radius

$r_e$  - effective radius

$$= (r_1 + r_2) / 2$$

$l$  - length of beverage

$$\text{element} = (r_2 - r_1)$$

Fig. 3.20 RADIAL ARRANGEMENT OF BEVERAGE AERIALS

The beverage elements are fed at the internal radius of the array. A typical value for  $r_2/r_1$  is 1.5 i.e. the length of the beverage aerial radiator is equal to the effective radius of the array. The array of the lens fed system has the same radius as the effective radius of the array.

The radiation pattern for the beverage element is computed assuming that attenuation along the length of the element is negligible

(5, sec. 3.2)

i.e. far field

$$GP(\theta) = \frac{S \sin X}{X} \quad 3.33$$

$$\text{where } X = \frac{l}{\lambda} (1 - \cos \theta \sin \phi)$$

$\theta$  = azimuthal angle

$\phi$  = elevation angle =  $90^\circ$

$l$  = length of element

The propagation constant along the beverage element is assumed to be equal to the free space value. The far-field arc computed in subroutine BVFF (Appendix 3.2.7).

The radiation patterns shown on Fig. 3.21 are for arrays with 48, 36 and 18 feeds, one radiator per feed and for 18 feeds with two radiators per feed. The beamwidth of the array broadens with decreasing number of feed, as to be expected, since there is stronger taper in the amplitude distribution from the feed. [ as discussed in sec. 3.2(a) ]. Grating lobes are apparent in the pattern for the array with 18 feeds/radiators. In this case the spacing between phase centres of adjacent beverage elements is  $1.05\lambda$ . The closest distance between adjacent beverage element is  $0.52\lambda$ , at the internal radius of the array. However, with the use of two beverage elements per feed the side lobe is reduced.

Table 3.5 shows the variation of side lobe levels, beamwidth and directivity of a 24 feed/radiator array for diameters ranging from  $2.0\lambda$  to  $10.0\lambda$ . The beamwidth is fairly constant over the range of array diameters, but the side lobe levels increase with increase

in diameter value. The patterns are reproduced in fig. 3.22 and 3.23.

Although coupling between radiators is neglected in the computation of far-field patterns as in previous computations, coupling effects with beverage aerial radiators is likely to be smaller than with cardioid radiators. This is mainly due to the larger acceptable spacing between radiators and also due to the behaviour of the beverage aerial. Work done by dos Santos in a project parallel to this work suggests that coupling is small.

DIAMETER (in $\lambda$ )	BEAMWIDTH (degrees)	FIRST SIDE LOBE (relative to main beam)	OTHER HIGHEST SIDE LOBE	DIRECTIVITY
2.0	30.8	0.098(-20.2db)	0.172(-15.3db)	1.526
4.0	17.8	0.099(-20.1db)	0.085	1.831
6.0	15.2	0.127(-17.9db)	0.124	1.824
8.0	13.9	0.185(-14.7db)	0.186	1.714
10.0	12.3	0.270(-11.8db)	0.240	1.620

Table 3.5 Performance of a Lens fed Array of  
24 Feed/Beverage Elements

The log-periodic array with its wide bandwidth could also be used with the lens fed array. Since the log-periodic aerial is a backfire array a circular array of log-periodic aerials arranged to fire outwards will have an increasing effective array diameter with increasing frequency. This is not desirable as we required a wider

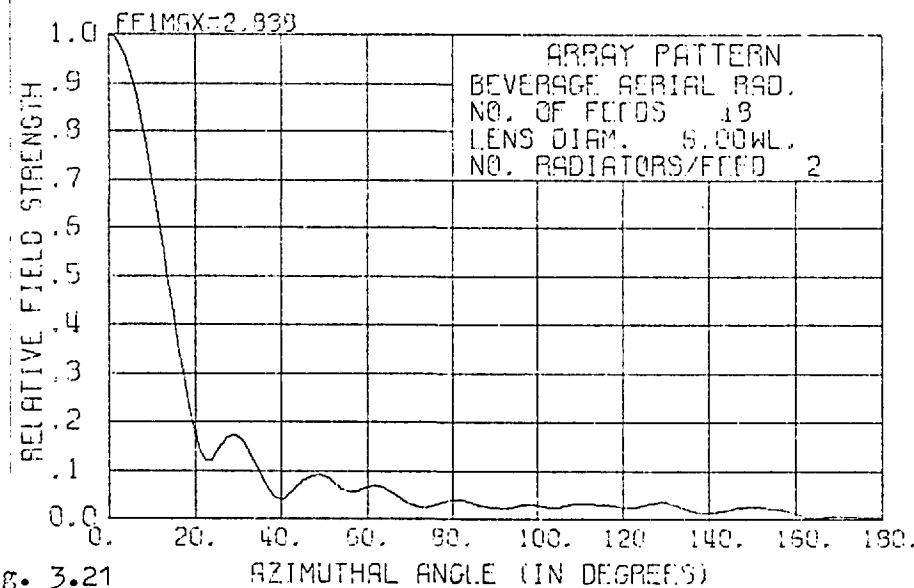
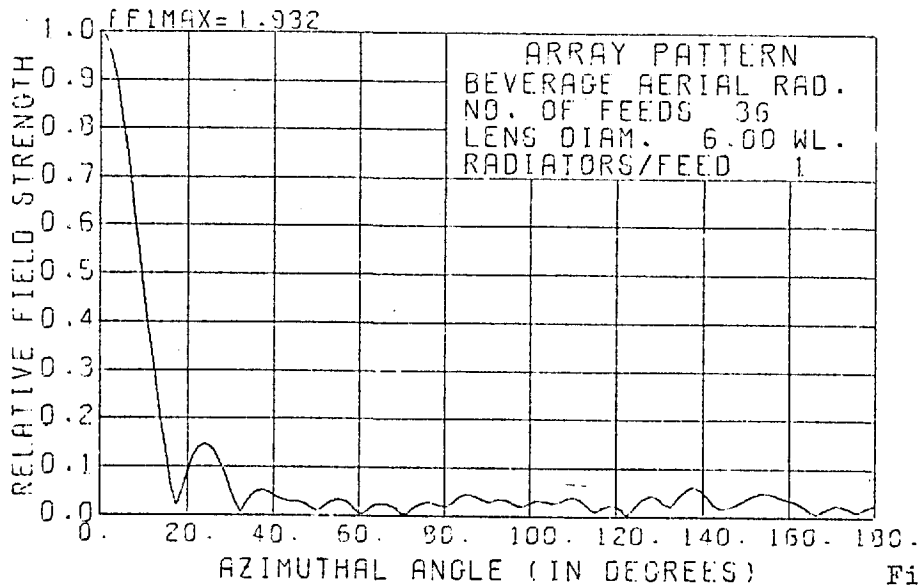
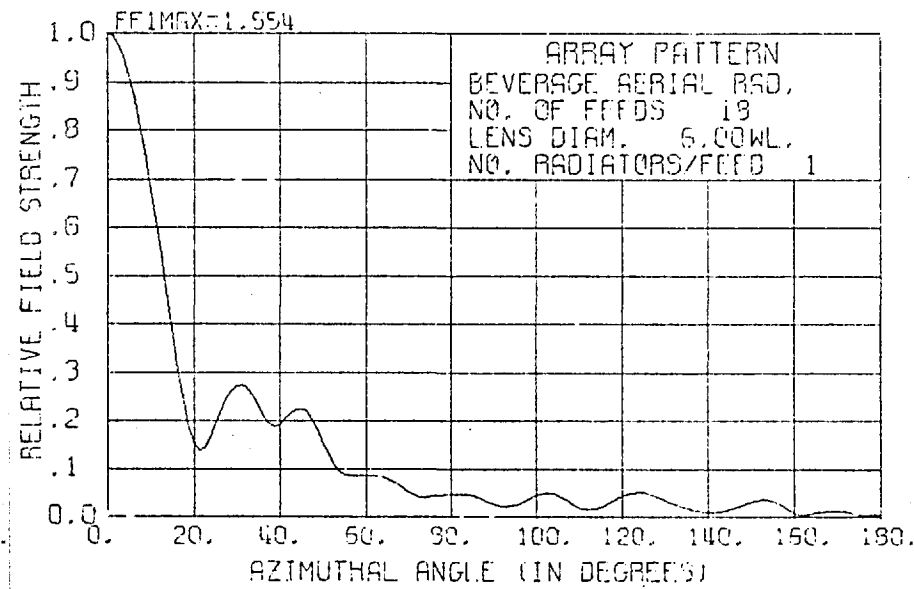
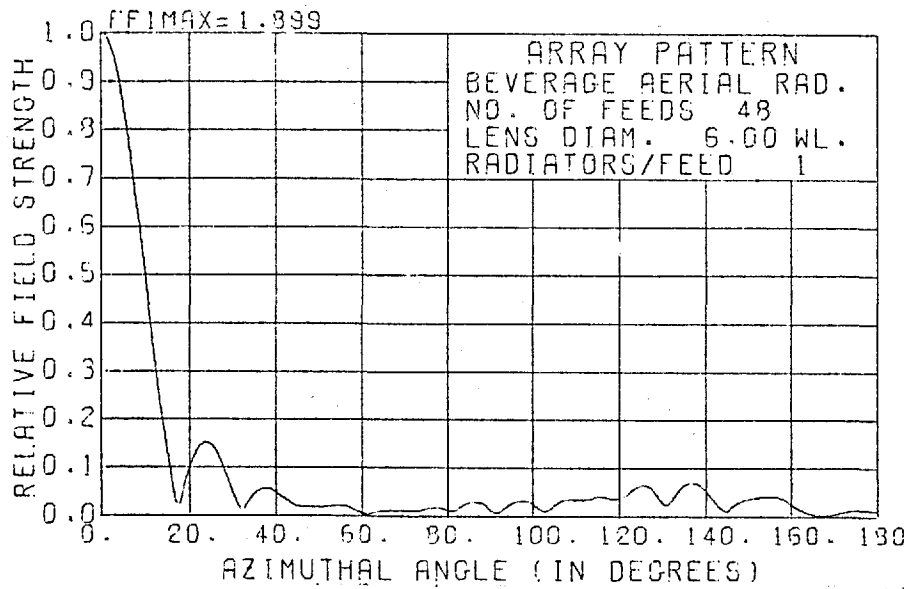


Fig. 3.21

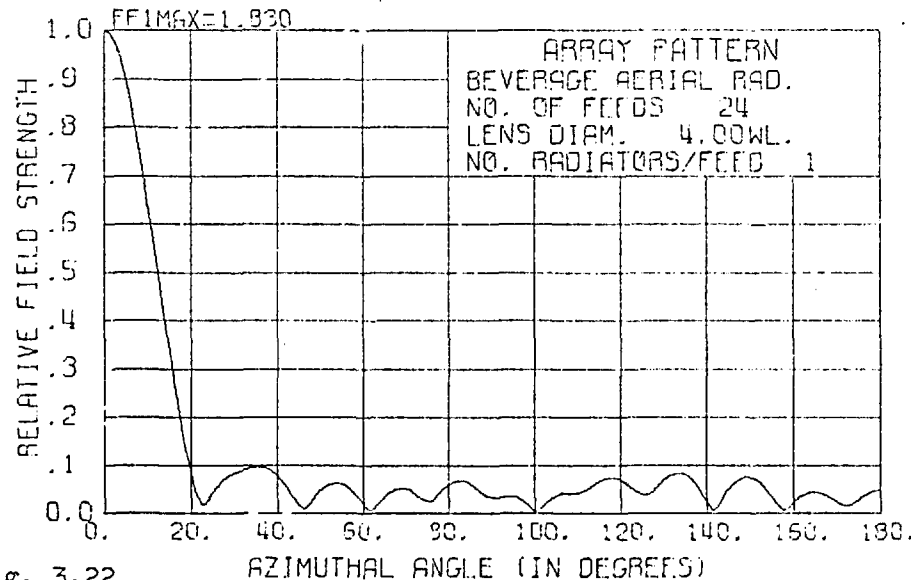
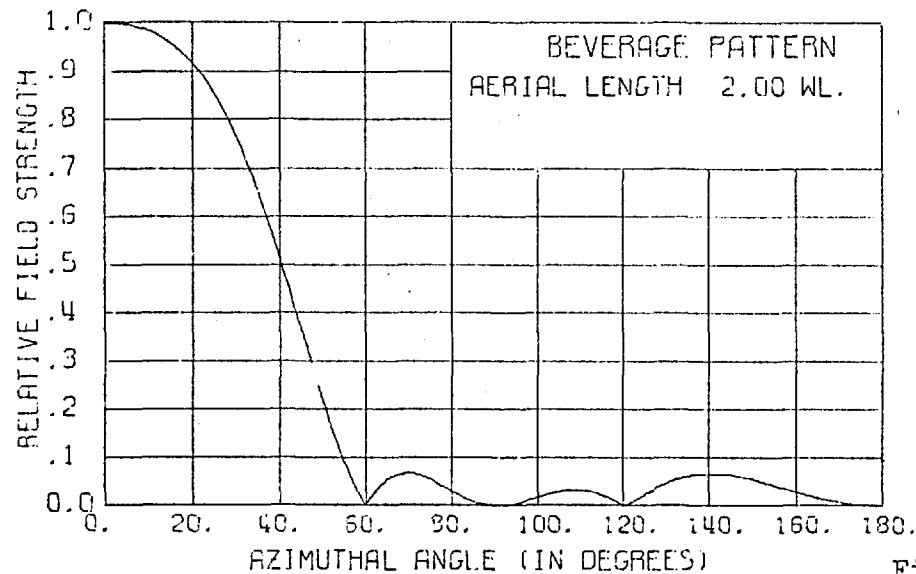
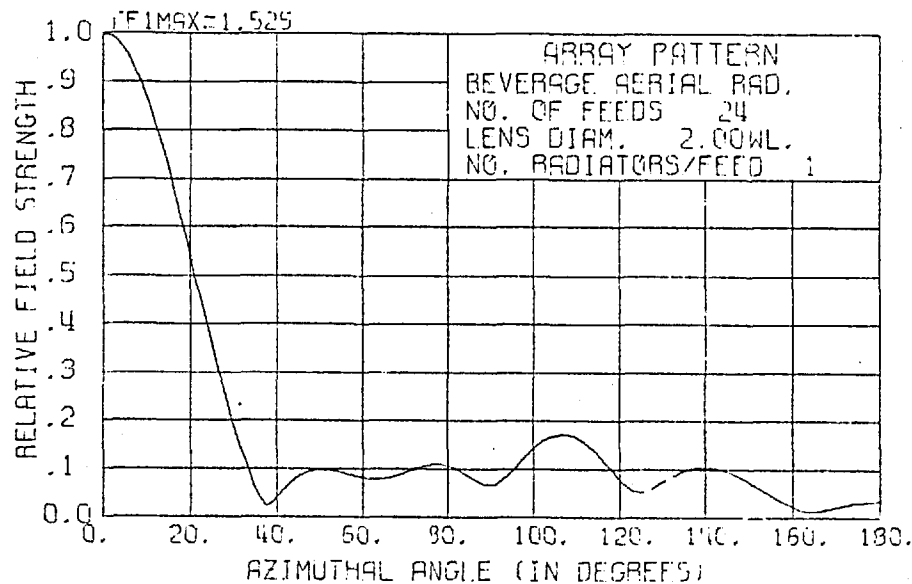
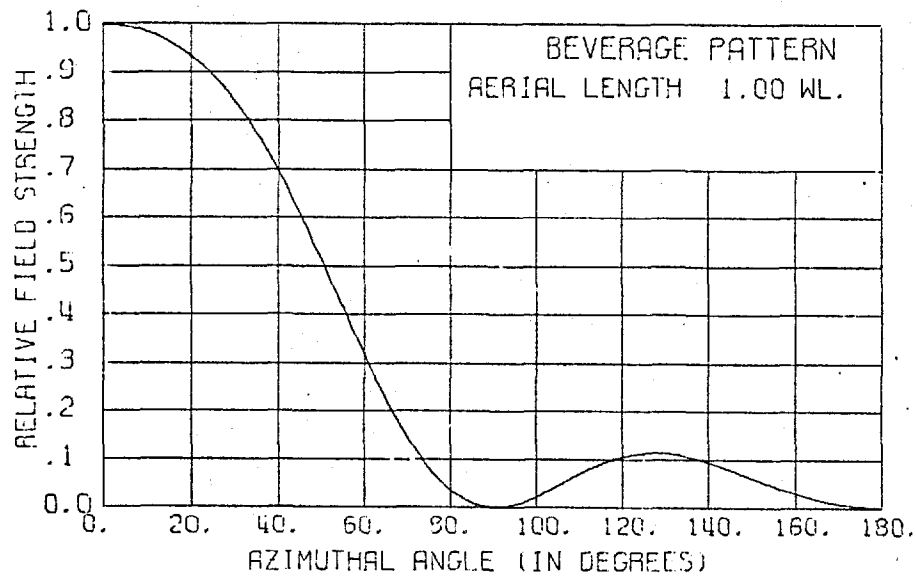


Fig. 3.22

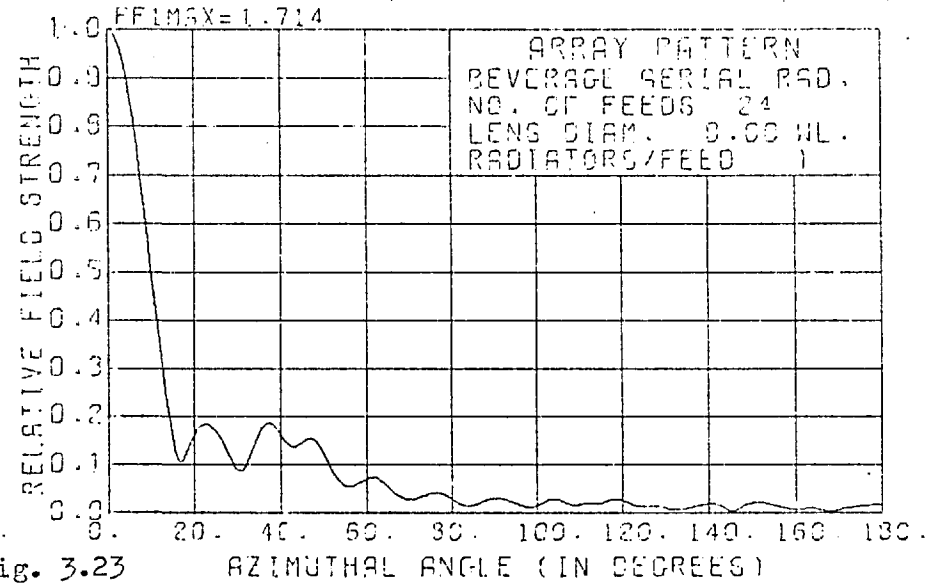
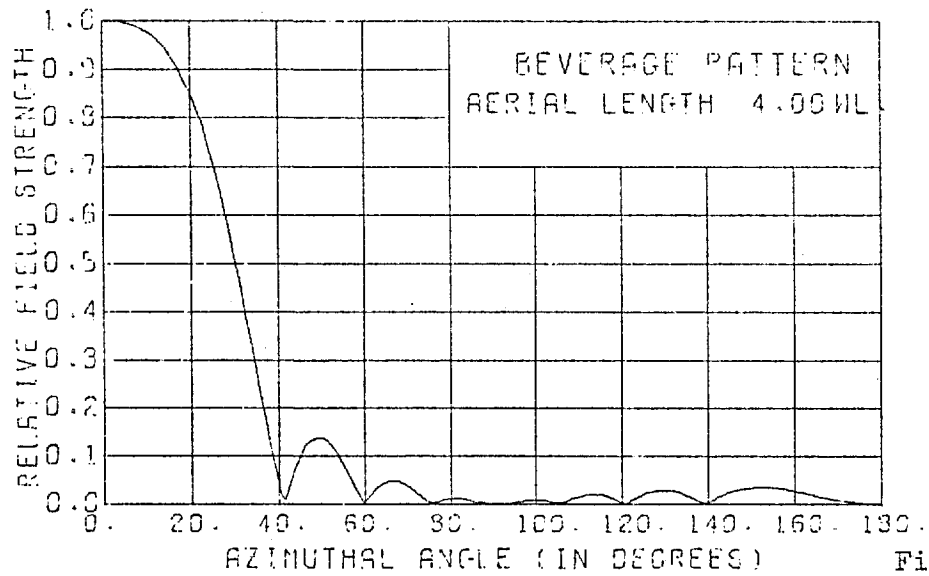
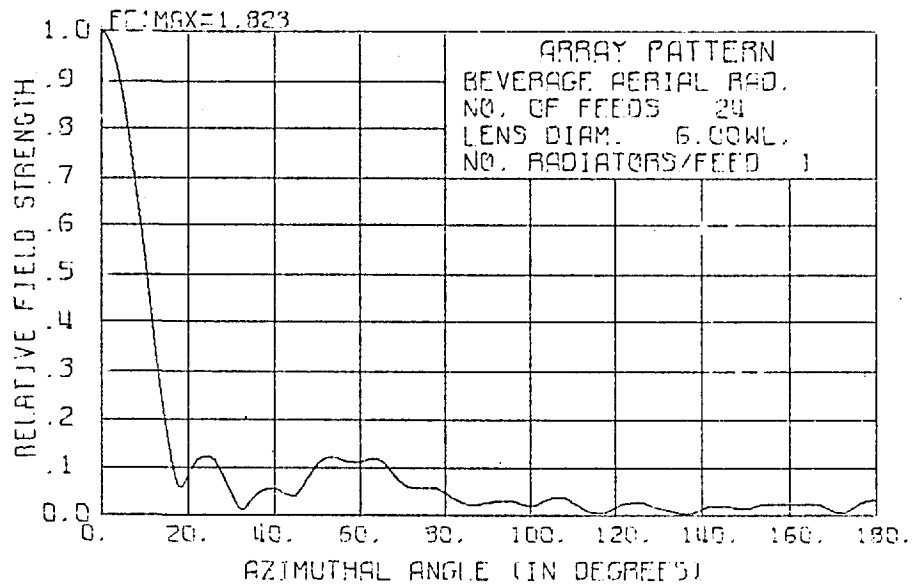
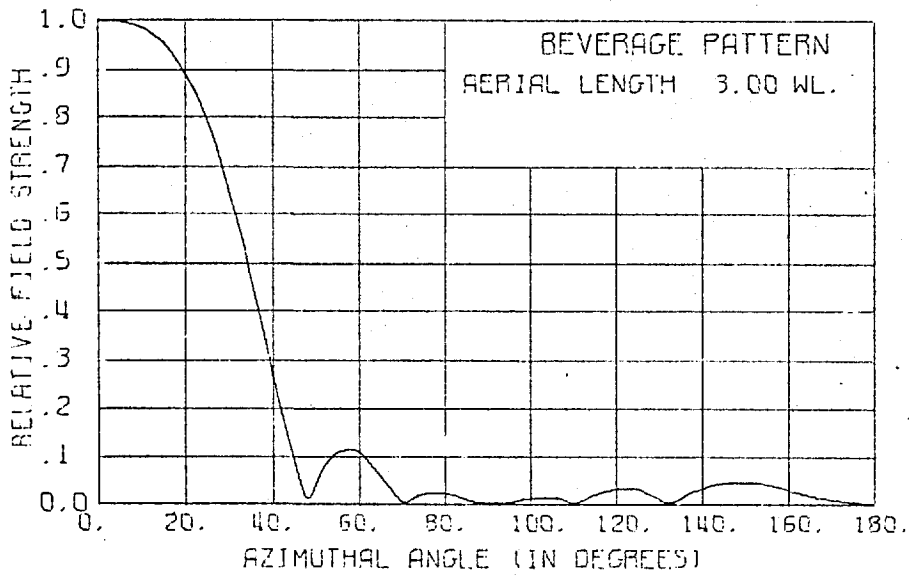


Fig. 3.23

beamwidth for the higher frequency. Problems of coupling and blockages occur if the log-periodic aeri-als were arranged to fire toward the centre of the array.

### SUMMARY

Two arrangements have been suggested to obtain a rotationally symmetric network for multibeam operation using the Luneburg Lens or its equivalent together with feeds and circulators or directional couplers.

From considerations of symmetry and by using the electromagnetic solution of the Luneburg Lens, the output from the feeds of the lens-fed system have been obtained. The taper in this output distribution becomes stronger if the number of feeds is reduced (provided that the spacing between adjacent feeds is greater than  $\lambda/2$ ).

The behaviour of the ( $\mu = \epsilon$ ) Luneburg Lens is not very different from the "ordinary" Luneburg Lens ( $\mu = 1$ ), particularly for  $ka > 10$ .

For the array using cardioid radiators the side lobe level of the array has a maximum value for an array diameter of  $1.25\lambda$  following to  $-13.3\text{db}$  as array diameter increases. The beamwidth is practically inversely proportional to the diameter of the array (as in a broad-side array).

The use of omni-directional aeri-als as radiators in the array gives rise to high side lobe levels (about  $-8\text{db}$ ) but the beamwidth obtained is narrower than that obtained using either the cardioid or beverage aerial radiators.

The pattern obtained using beverage aerial radiators proved very encouraging. Low side lobe levels have been obtained (approx. -18.0db). A 24 feed/radiator array gives beamwidths which vary from  $30.8^\circ$  at  $2.0\lambda$  diameter to  $12.3^\circ$  at  $10.0\lambda$  diameter.



APPENDIX 3

A3.1 Scattering Matrix of a 2N-Port Formed from Two N-Port Luneburg Lens Type Structures

We have shown in Chapter 2 that the required matrix for the 2N-port network is of the form:-

$$C = \begin{bmatrix} 0 & T \\ \tilde{T} & 0 \end{bmatrix} \quad \text{A3.1}$$

where T is the NxN scattering matrix of the N-port Luneburg Lens structure and

$$T \tilde{T}^* = \tilde{T} T^* = [I]$$

The arrangement for the network is illustrated in fig. 3.4 and A3.1.1 below.

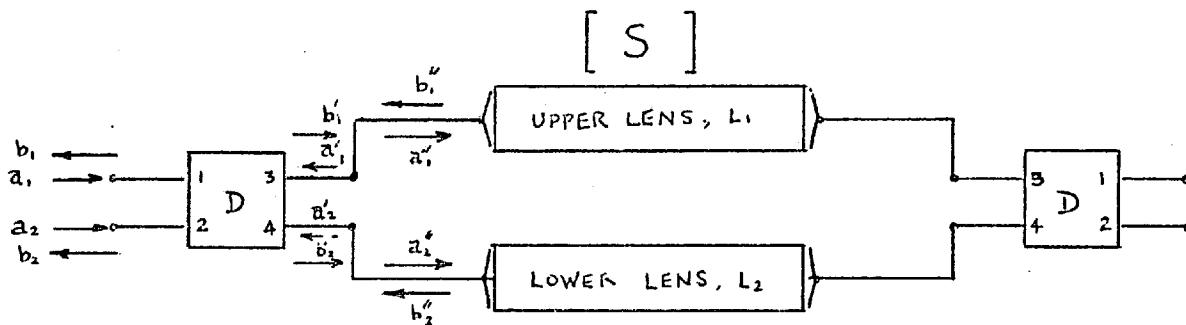


Fig.A3.1.1 USE OF DIRECTIONAL COUPLERS WITH TWO N-PORT LUNEBURG LENS TYPE STRUCTURES

The usual scattering matrix notations are used and shown in fig. A3.1.1.

Subscript 1 refers to fields in the upper ports and subscript 2, to the lower ports. The outer ports (1 and 2) of the directional couplers are numbered circumferentially 1 to N for the upper port and N+1 to 2N for the lower ports. The inner ports (3 and 4) of the directional couplers are similarly numbered, 1' to N' for the upper ports and N'+1 to 2N' for the lower ports. Port 1' to N' are connected to the N ports of the Lens, L, while ports N'+1 to 2N' are connected to Lens 2.

The scattering matrix for each of the directional couplers, D, is:-

$$D = \begin{bmatrix} 0 & 0 & 1 & j \\ 0 & 0 & j & 1 \\ 1 & j & 0 & 0 \\ j & 1 & 0 & 0 \end{bmatrix} \quad \text{A3.2}$$

At the lens feed, directional coupler junction,

$$\{a'_1\} = \{b''_1\} = S \{a''_1\} \quad \text{A3.3(i)}$$

$$\{a'_2\} = \{b''_2\} = S \{a''_2\} \quad \text{A3.3(ii)}$$

where S = scattering matrix of the N-port lens structure.

$$\{a''_1\} = \{b'_1\} = \frac{1}{2} (\{a_1\} + j\{a_2\}) \quad \text{A3.4(i)}$$

$$\{a''_2\} = \{b'_2\} = \frac{1}{2} (\{a_2\} + j\{a_1\}) \quad \text{A3.4(ii)}$$

$$\text{where } \{a_1\} = \begin{bmatrix} a_1 \\ a_2 \\ \cdot \\ \cdot \\ a_N \end{bmatrix} ; \quad \{b_2\} = \begin{bmatrix} b_N \\ b_{N+1} \\ \cdot \\ \cdot \\ b_{2N} \end{bmatrix} ,$$

similarly for  $a'_1, b'_1, a'_2$ , etc.

At the outer ports of the directional couplers (1 and 2)

$$\{b_1\} = \frac{1}{\sqrt{2}} \{a'_1\} + \frac{j}{\sqrt{2}} \{a'_2\} \quad \text{A3.5(i)}$$

$$b_2 = \frac{1}{\sqrt{2}} \{a'_2\} + \frac{j}{\sqrt{2}} \{a_1\} \quad \text{A3.5(ii)}$$

Substituting for  $\{a'_1\}$  and  $\{a'_2\}$  from equations A3.3(i) and (ii) in equations A3.5(i) and (ii)

$$\begin{pmatrix} b_1 \\ b_2 \end{pmatrix} = \frac{1}{\sqrt{2}} \begin{pmatrix} S \{a''_1\} + j S \{a''_2\} \\ S \{a''_2\} + j S \{a''_1\} \end{pmatrix} \quad \text{A3.5}$$

Substituting for  $a''_1$  and  $a''_2$  in equation A3.5

$$\begin{pmatrix} b_1 \\ b_2 \end{pmatrix} = \frac{1}{2} \begin{pmatrix} 2 S j a_2 \\ 2 S j a_1 \end{pmatrix}$$

$$\text{i.e.} \quad \begin{pmatrix} b_1 \\ b_2 \end{pmatrix} = j \begin{bmatrix} 0 & S \\ S & 0 \end{bmatrix} \begin{pmatrix} a_1 \\ a_2 \end{pmatrix}$$

Since  $S$  is symmetrical

$$\begin{pmatrix} b_1 \\ b_2 \end{pmatrix} = j \begin{bmatrix} 0 & S \\ \tilde{S} & 0 \end{bmatrix} \begin{pmatrix} a_1 \\ a_2 \end{pmatrix} \quad \text{A3.6}$$

A3.2.1 Solution of Equation 3.11

$$r^2 R''(r) + \frac{2a^2 r}{(2a^2 - r^2)} R' - [m^2 - k^2 r^2 (2 - r^2/a^2)] R = 0 \quad 3.10$$

The solutions of similar differential equation by Tai (15) and Jasik (14) suggest a transformation of the form

$$R(r) = Z^\beta (2Za - Z)^\nu e^{-Z/2} U(Z) \quad A3.7$$

where  $\rho = kr$

$$\rho_a = ka$$

$$Z = \frac{\rho^2}{\rho_a^2}$$

$Za = \rho_a$  and  $\beta$  and  $\nu$  are constants to be chosen

1. put  $\rho = kr$  in eqn. 3.10

$$\begin{aligned} \text{i.e. } R''(\rho) + \frac{2\rho_a^2}{(2\rho_a^2 - \rho^2)} R'(\rho) - \left[ \frac{m^2}{\rho^2} - \left( 2 - \frac{\rho^2}{\rho_a^2} \right) \right] R(\rho) \\ = 0 \end{aligned} \quad A3.8$$

2. put  $Z = \frac{\rho^2}{\rho_a^2}$

$$\begin{aligned} \text{i.e. } 4Z R''(Z) + \frac{(8Za - 2Z)}{(2Za - Z)} R'(Z) - \left[ \frac{m^2}{Z} - (2Za - Z) \right] R(Z) \\ = 0 \end{aligned} \quad A3.9$$

3. put  $R(Z) = Z^\beta S(Z)$

$$\begin{aligned} \text{i.e. } 4Z S''(Z) + \left[ \frac{8(2\beta+1)Za - 2(4\beta+1)Z}{(2Za - Z)} \right] S'(Z) \\ + \left[ \frac{(4\beta^2 - m^2)}{Z} + \frac{2\beta}{(2Za - Z)} + (2Za - Z) \right] S(Z) = 0 \end{aligned} \quad A3.10$$

4. put  $S(Z) = e^{-Z/2} T(Z)$

$$\begin{aligned} \text{i.e. } 4Z T''(Z) + \left[ \frac{8(2\beta+1)Za - 2(4\beta+1)Z}{(2Za-Z)} - 4Z \right] T'(Z) \\ + \left[ \frac{(4\beta^2 - m^2)}{Z} + \frac{2\beta - 4(2\beta+1)Za - (4\beta+1)Z}{(2Za-Z)} + 2Za \right] T(Z) \\ = 0 \end{aligned} \quad \text{A3.11}$$

5. put  $T(Z) = (2Za-Z)^\nu U(Z)$

$$\begin{aligned} \text{i.e. } U''(Z) + \left[ \frac{8(2\beta+1)Za - (8\beta+8\nu+2)Z}{4Z(2Za-Z)} - 1 \right] U'(Z) \\ + \left[ \frac{\nu(\nu-1)}{(2Za-Z)^2} - \frac{\{8(2\beta+1)Za - 2(4\beta+1)Z\}\nu}{4Z(2Za-Z)^2} + \frac{\nu}{(2Za-Z)} \right. \\ \left. + \frac{4\beta^2 - m^2}{4Z^2} + \frac{2\beta - \{4(2\beta+1)Za - (4\beta+1)Z\}}{4Z(2Za-Z)} + \frac{Za}{2Z} \right] U(Z) \\ = 0 \end{aligned} \quad \text{A3.12}$$

$$\begin{aligned} \text{i.e. } U''(Z) + \left[ \frac{(2\beta+1)}{Z} - \frac{(2\nu-\frac{1}{2})}{(2Za-Z)} - 1 \right] U'(Z) \\ + \left[ \frac{(\nu^2 - \frac{3}{2}\nu)}{(2Za-Z)^2} + \frac{(4\beta^2 - m^2)}{4Z^2} + \frac{(\nu - \frac{1}{4} + \{-2\nu(2\beta+1) + \beta\}/4Za)}{(2Za-Z)} \right. \\ \left. + \frac{-(2\beta+1)/2 + Za/2 + \{-2\nu(2\beta+1) + \beta\}/4Za}{Z} \right] U(Z) \\ = 0 \end{aligned} \quad \text{A3.13}$$

To simplify equation A3.13

$$\text{put } \frac{(2\nu - \frac{1}{2})}{(2Za-Z)} = 0 \quad \text{and} \quad 4\beta^2 - m^2 = 0$$

$$\text{i.e. } \nu = \frac{1}{4} \quad \text{and} \quad \beta = \frac{m}{2}, \text{ taking positive sign.}$$

Hence equation A3.13 becomes

$$U''(Z) + \left(\frac{\gamma}{Z} - 1\right) U'(Z) + \frac{\alpha_1}{Z} + \frac{2\alpha_2}{(Z-2Za)} - \frac{2\alpha_2 \alpha_3}{(Z-2Za)^2} U(Z) = 0 \quad A3.14$$

where  $\gamma = m+1$

$$\alpha_1 = \frac{1}{2}\left(m+1-Za+\frac{1}{4Za}\right)$$

$$\alpha_2 = -\frac{1}{16Za} \quad A3.15$$

$$\alpha_3 = -\frac{5}{64Za}$$

$$a_2 = 2Za$$

$$\text{i.e. } R(r) = Z^{m/2} (2Za-Z)^{\frac{1}{4}} e^{-Z/2} U(Z) \quad A3.16$$

The function  $U(Z)$  which satisfies equation 3.14 is similar in form to that obtained by Tai (15) for the transverse magnetic solution of the spherical Luneburg Lens. The constants  $\gamma$ ,  $\alpha_1$ ,  $\alpha_2$ ,  $\alpha_3$  differ slightly. The equation has a regular singularity at  $Z=0$  with exponent 0, and  $1-\gamma$ . It also has an irregular singularity at  $\infty$  and a regular singularity at  $Z = a_2$ .

The solution of interest must be finite at the origin. The following series solution is assumed:-

$$U_m = \sum_{n=0}^{\infty} A_n Z^n \quad A3.17$$

The constants are obtained in the following section.

### A3.2.2 Series Solution for $U_m(Z)$

$$U_m(Z) = \sum_{n=0}^{\infty} A_n Z^n \quad \text{A3.17}$$

Substituting for  $U_m$ ,

$$U'_m = \sum_{n=0}^{\infty} n A_n Z^{n-1},$$

and  $U''_m = \sum_{n=0}^{\infty} n(n-1) A_n Z^{n-2}$  in equation 3.14,

$$\begin{aligned} & \sum_{n=0}^{\infty} \left\{ Z^{n-2} A_n [a_2^2 n(n+\gamma-1)] \right. \\ & - Z^{n-1} A_n a_2 [a_2 (n + \alpha_1 + 2n(n+\gamma-1))] \\ & + Z^n A_n [n(n+\gamma-1) + 2a_2(n + \alpha_1 + \alpha_2 + \alpha_3)] \\ & \left. - Z^{n-1} A_n [n + \alpha_1 + 2\alpha_2] \right\} = 0 \end{aligned} \quad \text{A3.18}$$

Coeff. of  $Z^{-1}$

$$A_2^2 (1) \gamma A_1 - \alpha_2 (\alpha_1 a_2) A_0 = 0$$

$$\text{i.e. } \frac{A_1}{A_0} = \frac{\alpha_1}{\gamma} \quad \text{A3.19}$$

Coeff. of  $Z^0$

$$2a_2^2 (\gamma+1)A_2 = [2\gamma + (1+\alpha_1)a_2] A_1 - 2(\alpha_1+\alpha_2+\alpha_3) A_0$$

$$\text{i.e. } \frac{A_2}{A_0} = \frac{\alpha_1(\alpha_1+1)}{2\gamma(\gamma+1)} - \frac{(\alpha_2+\alpha_3)}{a_2(\gamma+1)} \quad \text{A3.20}$$

Coeff of Z

$$3a_2^2 (\gamma+2) A_3 - a_2 [ 4(\gamma+1) + (2+\alpha) a_2 ] A_2$$

$$+ [ \gamma + 2a_2(1+\alpha_1+\alpha_2+\alpha_3) ] A_1 - (\alpha_1+\alpha_2) A_0 = 0$$

Substituting for  $A_1$  and  $A_2$

$$\frac{A_3}{A_0} = \frac{1}{3!} \frac{\alpha(\alpha_1+1)(\alpha_1+2)}{\gamma(\gamma+1)(\gamma+2)} - \frac{1}{3(\gamma+2)} \frac{(\alpha_1+2)(\alpha_2+\alpha_3)}{(\gamma+1)a_2}$$

$$+ \frac{2\alpha_1(\alpha_2+\alpha_3)}{\gamma a_2} + \frac{2(\alpha_2+2\alpha_3)}{a_2}$$

A3.21

Coeff. of  $Z^{n-1}$ ,  $n \geq 3$

from equation A3.8,

$$a_2^2(n+1)(n+\gamma)A_{n+1} - a_2 [ a_2(n+\alpha_1) + 2n(n+\gamma-1) ] A_n$$

$$+ [ (n-1)(n+\gamma-2) + 2a_2(\alpha_1+\alpha_2+\alpha_3+n-1) ] A_{n-1}$$

$$- [ (n-2+\alpha_1+2\alpha_2) ] A_{n-2} = 0$$

A3.22

There appears to be an error in Tai's equation corresponding to equation A3.2.2. The series is absolutely convergent for  $Z < 2Za$ .



### A3.3 Description of Program and Subroutines

The following programs and subroutines are described with the aid of flow charts where necessary:-

#### 3.3.1 Main Program

The main program reads in the relevant data and calls the other subroutines to calculate the output from the NN feeds of the Luneburg Lens Feed system. The far-field pattern can also be computed (put IFF = 1) for the array using either omni-directional, cardioid (1 + cosine), or beverage aerial radiators.

The parameters read into the program are:-

- NN - no. of feed used
- DIAM - diameter of lens array in wavelength
- LPATDR - this parameter defines type of radiator used
- LP - no. of far-field point in azimuth per radiator
- L - no. of radiator per feed.

The flow chart is illustrated in fig. 3.2.1.

#### 3.3.2(a) Subroutine LEU(ZA, U, DF1U, NCT, MODE, NCOEFF)

This subroutine sums the confluent hypergeometric function series  $U(M1) = {}_1F_1(\alpha, \gamma, Z)$  and its derivative,  $DF1U(M1)$  for the (M1-1) mode

$$\begin{aligned} {}_1F_1(\alpha, \gamma, Z) &= 1 + \frac{\alpha}{\gamma} Z + \frac{\alpha(\alpha+1)}{\gamma(\gamma+1)} \frac{Z^2}{2} + \frac{\alpha(\alpha+1)(\alpha+2)}{\gamma(\gamma+1)(\gamma+2)} \frac{Z^3}{3!} + \dots \\ &= U(M1) \end{aligned}$$

where  $\alpha = (m + 1.0 - Za)/2 = XALPHA$

$\gamma = (m+1) = XGAMMA$

$$m = \text{mode} = (M1-1)$$

$$Z = Z_a = ka = ZA$$

The "accuracy" (ACC) is defined as  $ANZ/U$ , U being the series up to the Nth term. If ACC is less than  $10^{-4}$  the series is terminated.

Otherwise if the number of terms in a series reaches NCOEFF, an error message is printed. The flow chart for this subroutine is given in fig. 3.2.2(a).

3.3.2(b) Subroutine NCFU2(ZA, NCOEFF, U, MODE, ALPHA3, ALPHA2, A, NCT, DF1U)

This subroutine sums the series,  $U(M1) = \sum_n^{\infty} A_n Z^n$  and its derivative, DF1U(M1) (see appendix 3.1) The first three terms of the series are calculated separately. The other terms in the series are calculated using the four term recurrence series:-

$$\begin{aligned} \text{CANP1} * A(N+1) - \text{CANO} * A(N) + \text{CANL2} * A(N-1) - \text{CANL2} * A(N-2) \\ = 0 \end{aligned}$$

In the program

$$A_n = A(n)$$

$$Z = ZA$$

$$M1 = \text{mode number} + 1$$

The accuracy of the series is tested after the addition of every term as in subroutine LEU. The flow chart is given in fig. 3.2.2(b).

3.3.3 Subroutine ETALAM(ALAMDA, LAMDA, ETA, ETAO, MODE, ZA, U, DF1U)

The characteristic impedance, ETA(M1) for the (M1-1) mode and the reflection coefficient, LAMDA(M1) is computed from expression given in eqn. 3.23 and 3.28.

### 3.3.4 Subroutine SCATMX(LAMDA, S, NN, ETAO, ALAMDA, ARG, AMP)

This subroutine calculates the KP1 row (normally = 1) of the scattering matrix  $S(KP1, LP1)$  of a circularly symmetric structure given the eigenvalues (or the mode reflection coefficients),  $LAMDA(I)$ .  $S(KP1, LP1)$  is complex but  $S(LP1)$  is converted to its amplitude  $AMP(LP1)$  and its phase  $ARG(LP1)$ , in radians.

The expression for  $S$  is given in equation 3.31 and 3.32. The flow chart for this subroutine is illustrated in Fig. 3.2.4.

### 3.3.5 Subroutine ID1S(NN, L, AMP, ARG)

This subroutine reads NN outputs (amplitude,  $AMP(I)$ , and argument,  $ARG(I)$ ) into a new array with L radiators fed in parallel to each of the NN feeds.

### 3.3.6 Subroutine FARF1(NN, L, LPATDR, DIAM, AMP, ARG, FF1, LP, IX, KP)

The far-field pattern for the array is computed and plotted on "calcomp" paper by this routine. Instead of computing cosines for angles which are multiples of  $2\pi/(NN*L*LP*2)$  several times in the routine, the cosines are stored in array  $CS(I)$ . The function  $\exp\{jka \cos(\theta - \theta_0)\}$  is also computed and stored as  $EJKACS(I)$  for values of  $(\theta - \theta_0)$  which are multiples of  $2\pi/(NN*L*LP*2)$ .

If beverage aerial radiators are used for the array subroutine BVFF is called to calculate the beverage aerial pattern.

Each far-field value for a particular azimuth angle is calculated in the subroutine SUMFF.

Where the radiation pattern plots are required subroutine GRPLT1/2 is called. The "calcomp" packet is used for plotting on

calcomp paper. The flow chart for this subroutine is given in fig. 3.2.6.

### 3.3.7 Subroutine BVFF(NN, LP, GP, ALW, CS, FF1)

The radiation pattern of a beverage aerial of length, ALW, is computed using this subroutine. The pattern is stored in array GP(I). The absolute value of GP(I) is stored in FF1(I) and plotted. The expression used for the far-field value is given by equation 3.33.

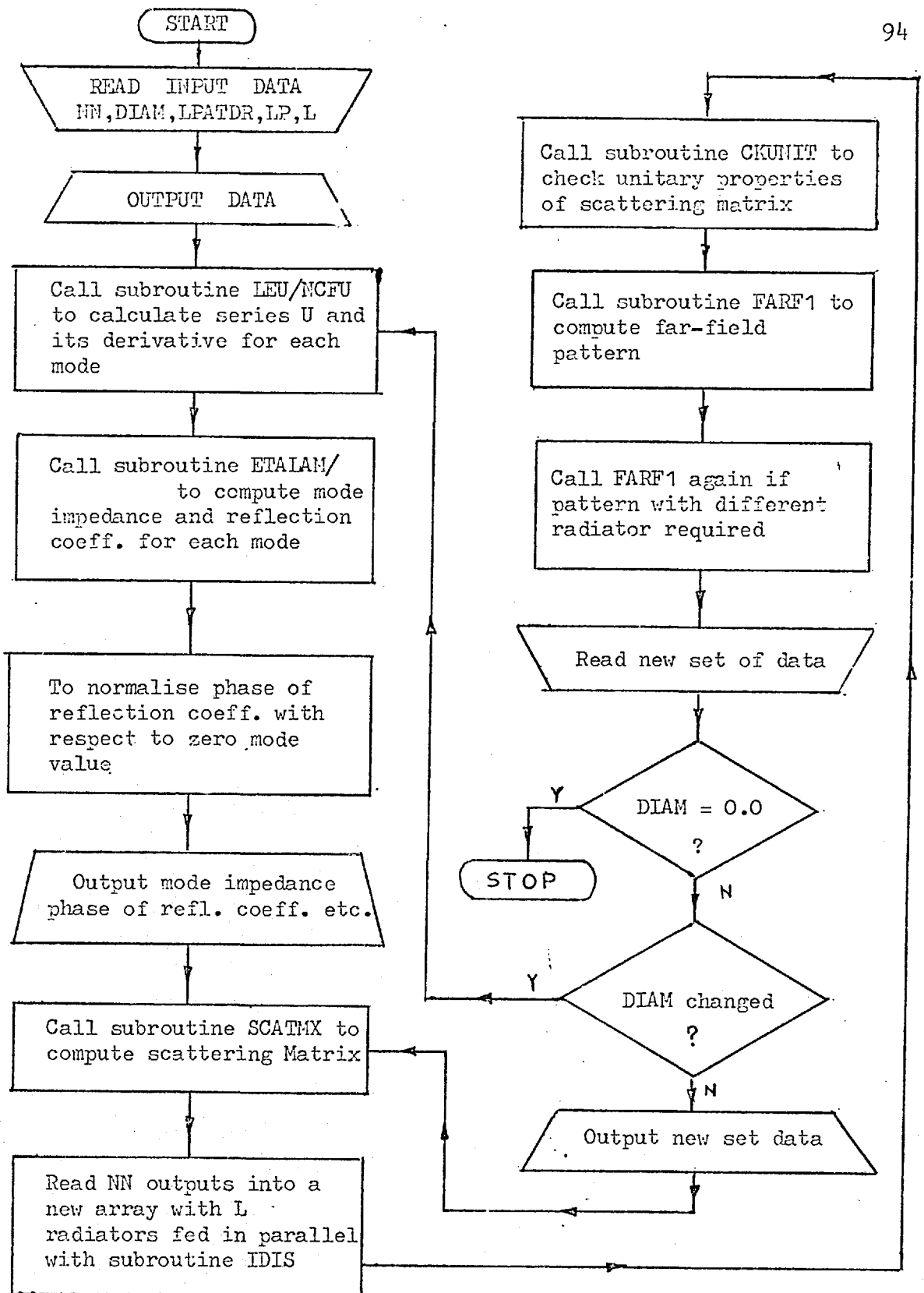
The flow chart for BVFF is shown in fig. 3.2.7.

### 3.3.8 Subroutine SUMFF1(NN, L, DIAM, LPATDR, AMP, ARG, IAZFC, IAZ, GP, FF2, EXPARG, LP, EJKACS, CS)

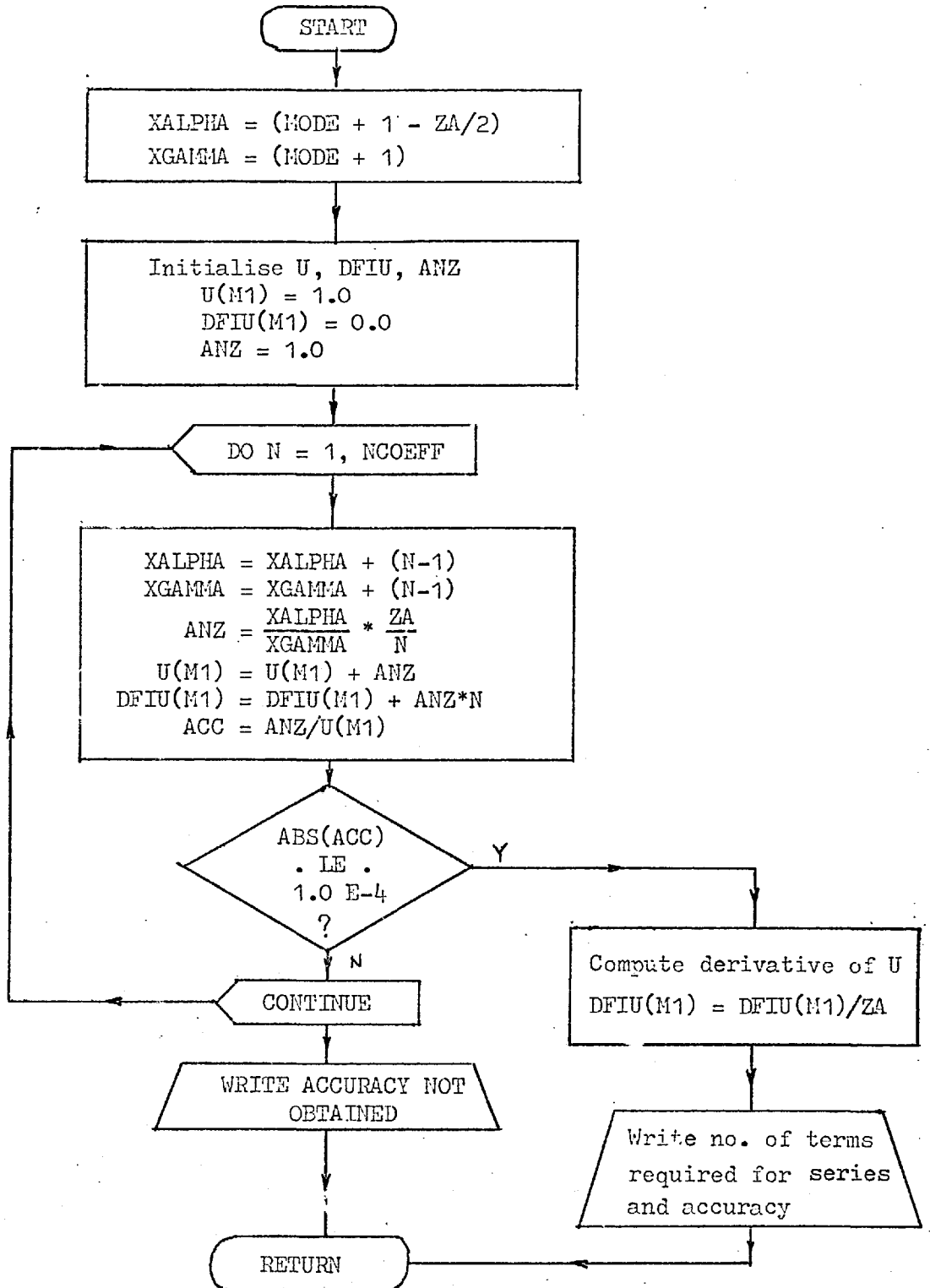
This subroutine sums up the far-field strength for a particular angle in azimuth. The subroutine sums up the field contributions from all the radiators (NN\*L). The routine could be used for omnidirectional, cardioid (1 + cosine) or beverage aerial radiators.

### 3.3.9 Subroutine GRPLT1/2(FF1, NP, KP, LPATDR, NN, DIAMWL, NELR, FF1MAX)

The flow chart for the subroutine is shown in fig. 3.2.9. This subroutine uses the "calcomp" package. It plots the radiation patterns on a quarto size frame. Four graphs can be plotted on each quarto frame. Each graph frame has dimensions 22" by 4". Some details of the array are also written on the plot.

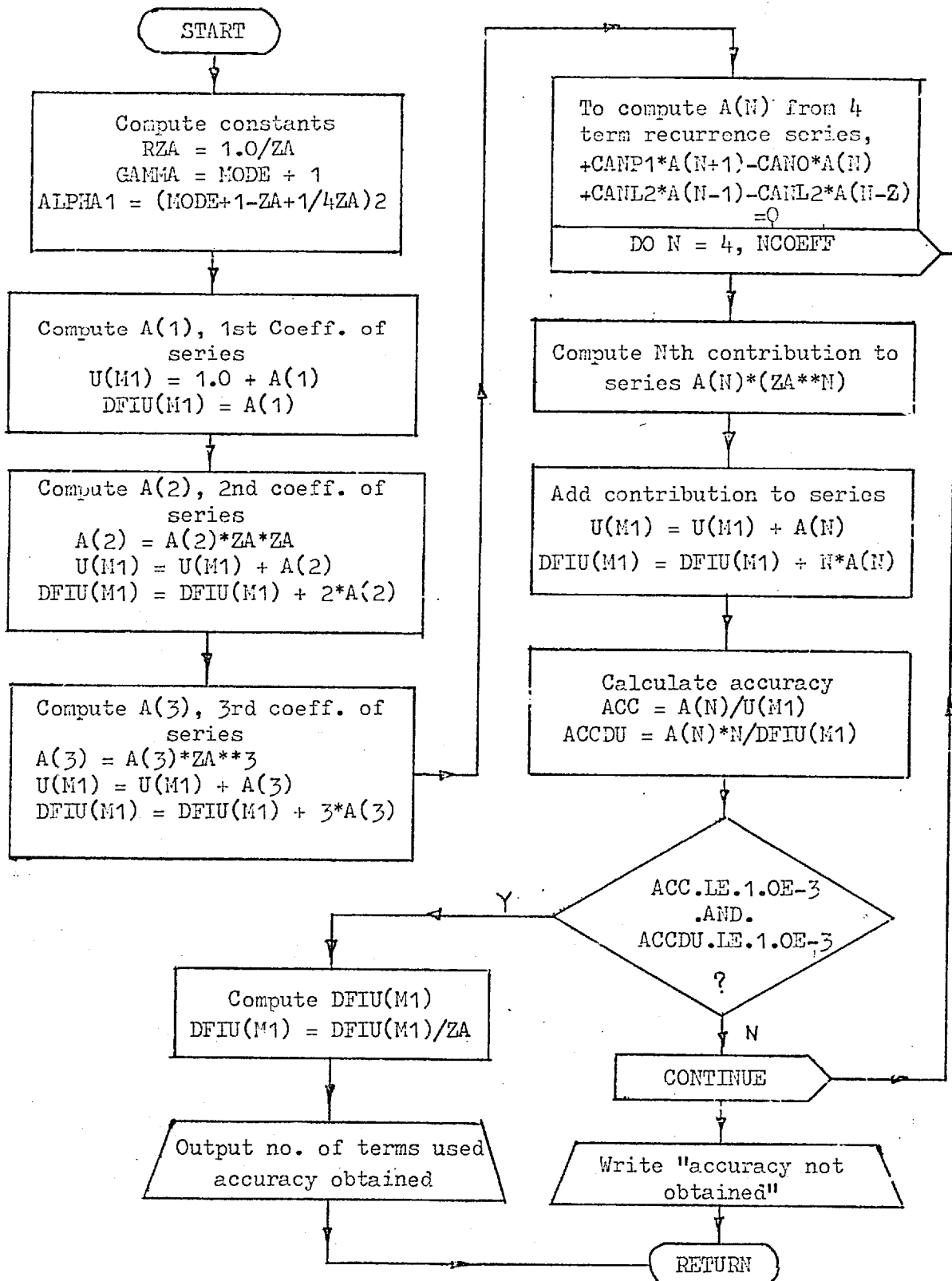


3.2.1 FLOW CHART OF MAIN PROGRAM

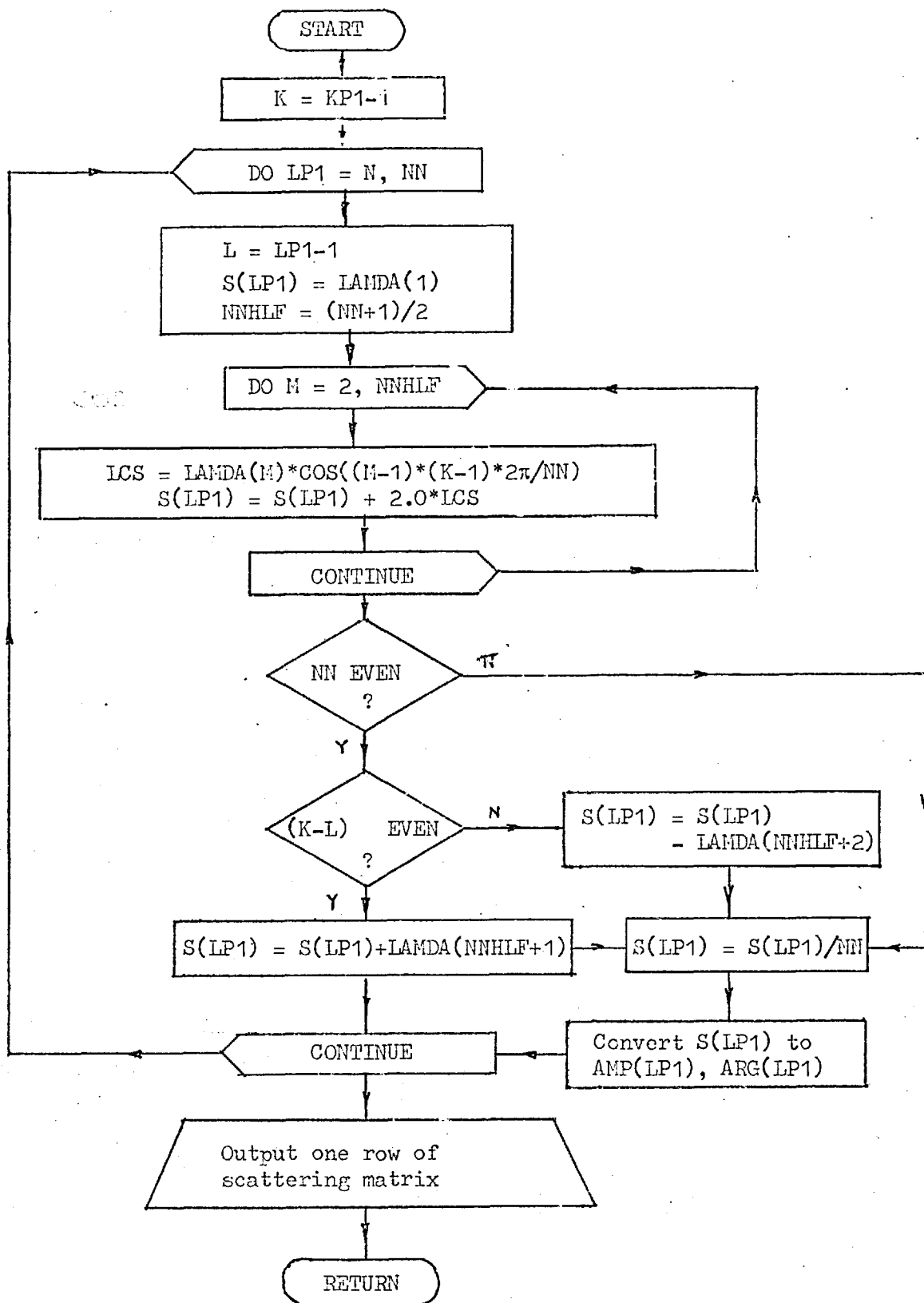


3.2.2(a) FLOW CHART OF SUBROUTINE LEU

(to sum Hypergeometric function and its derivative, m=MODE)

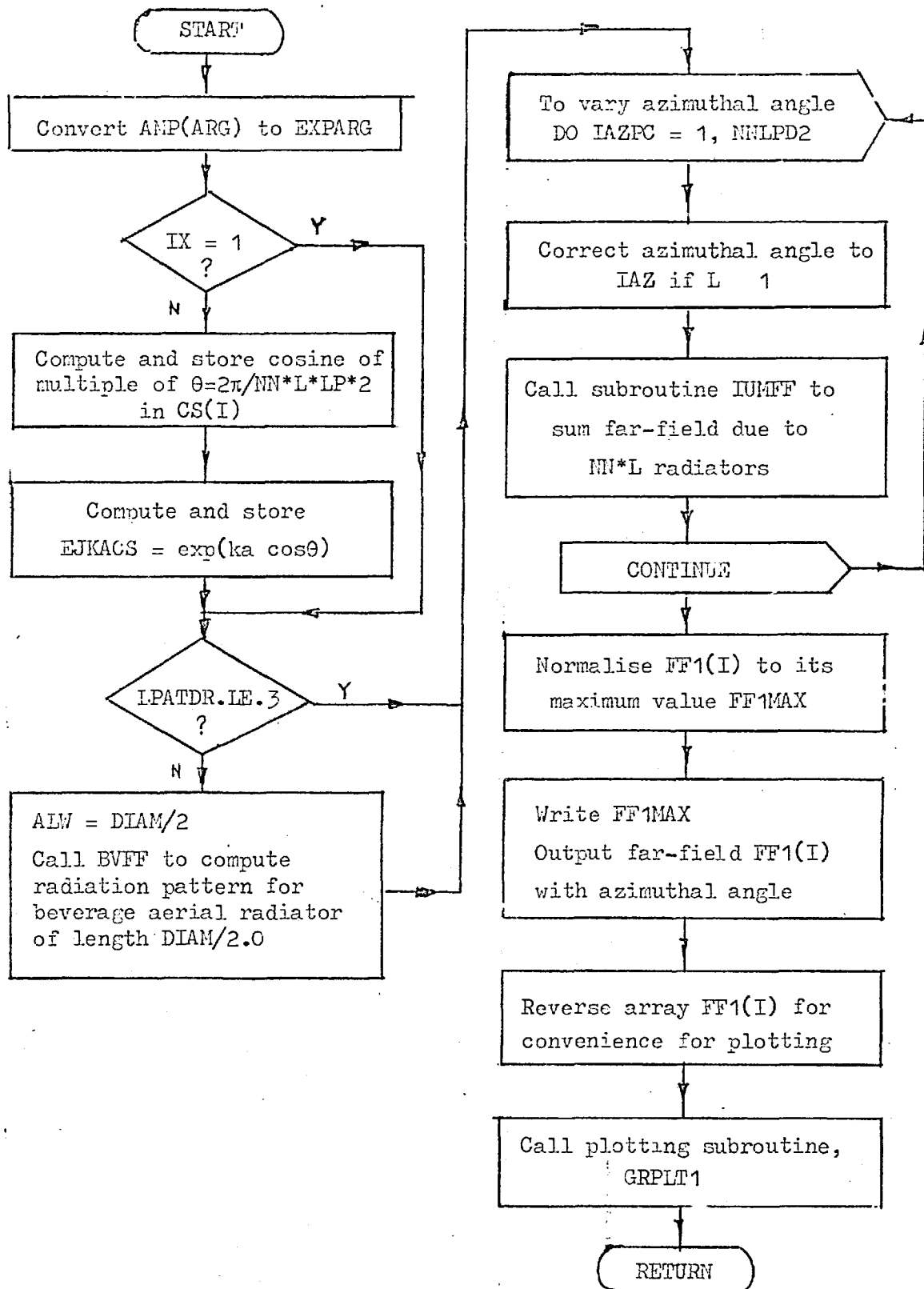


3.2.2(b) FLOW CHART OF SUBROUTINE NCFU2

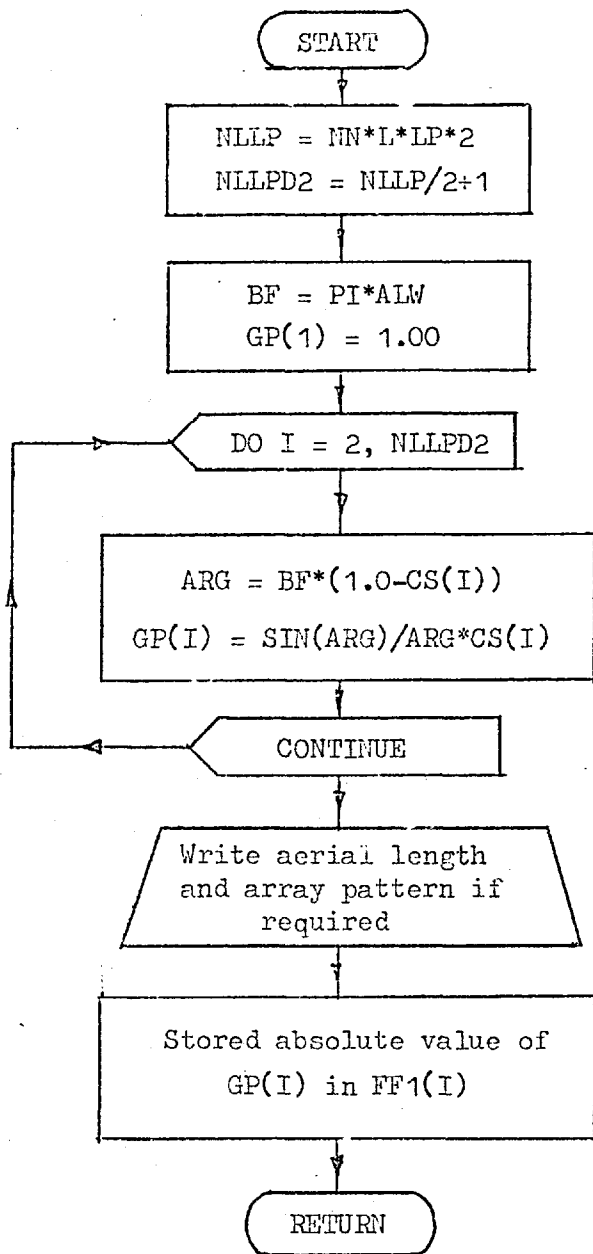


3.2.4 FLOW CHART OF SUBROUTINE SCATMX

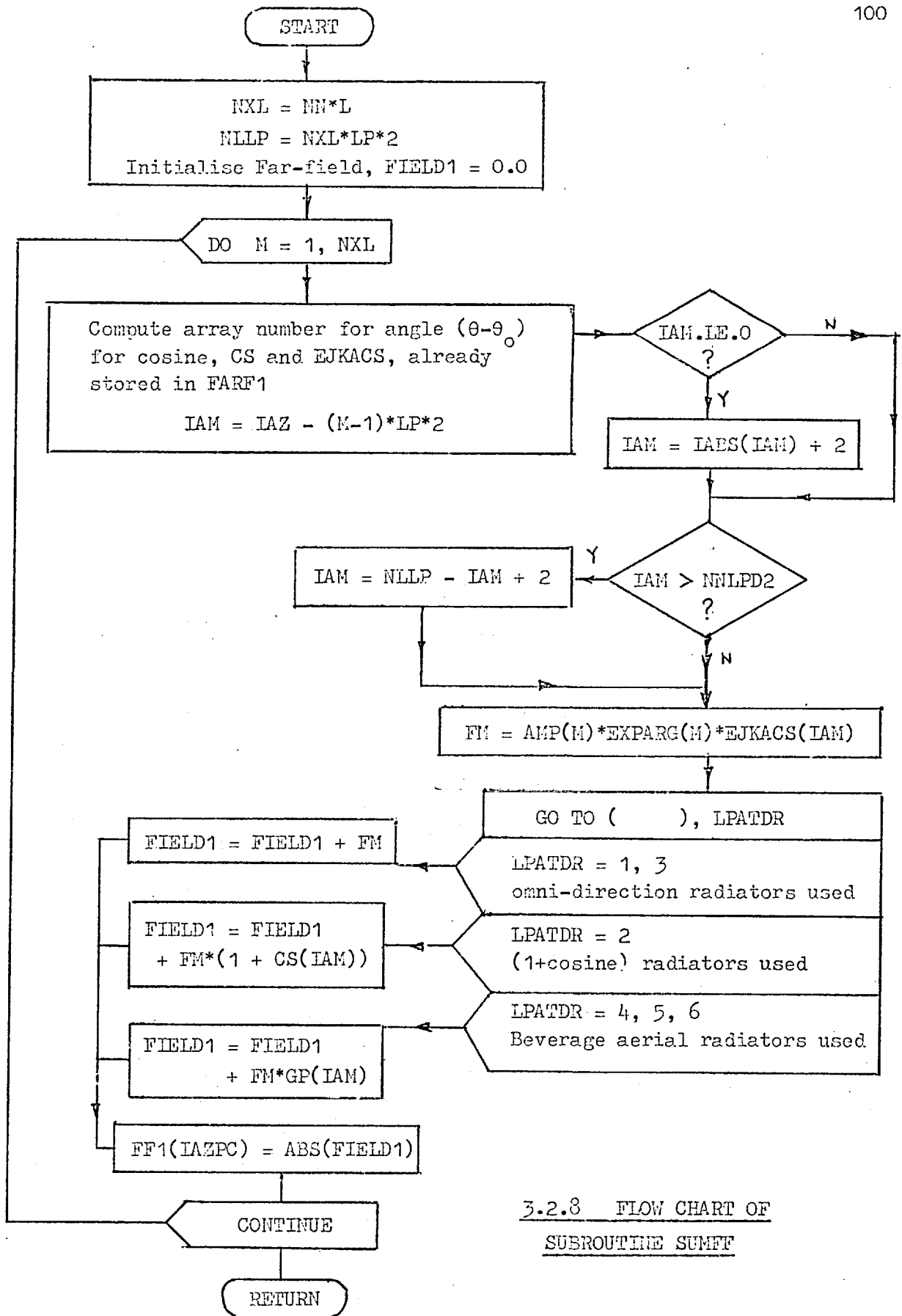




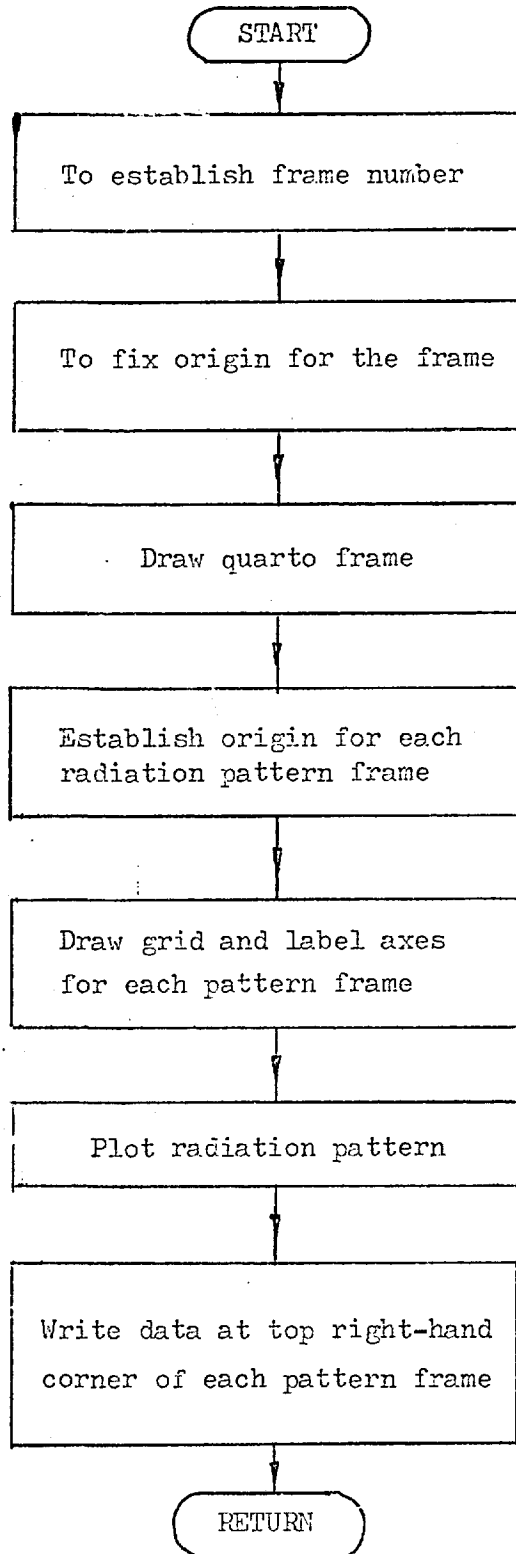
3.2.6 FLOW CHART OF SUBROUTINE FARF1/2



3.2.7 FLOW CHART OF SUBROUTINE BVFF



3.2.8 FLOW CHART OF  
 SUBROUTINE SUMFF



## CHAPTER 4

### 4. THE EQUIVALENT CIRCUIT LUNEBURG LENS

In chapter 3 we showed the feasibility of using the Luneburg Lens to feed an array. At H.F., however, the physical size of the lens is large and therefore the cost is high. A lumped element equivalent circuit for the lens is envisaged. If the number of elements used in the circuit is unlimited the performance of the lumped circuit is expected to be no different from an ideal lens. It is obviously desirable to determine the minimum number of elements that can be used to simulate the performance of the lens without significant deterioration in its behaviour. Towards this end the values of the lumped elements of the equivalent circuit are computed.

The values of the equivalent lumped elements for the equivalent circuit for a TE Mode Luneburg Lens are obtained by converting the TE solution of Maxwell's equations to finite difference equations. By replacing electric field by voltages and magnetic fields by currents, we obtain three equations which satisfy Kirchoff voltage and current laws. From these equations the expressions for the lumped elements are deduced.

The equivalent circuit structure (with its circular symmetry - see fig. 4.5) may be decomposed into a ladder network for each mode. For mode,  $m$ , the reflection coefficient,  $\rho_m$ , looking into the ladder

network is calculated. Each of these reflection coefficients corresponds to the reflection coefficients or eigenvalues worked out in chapter 3. The scattering matrix of the structure is computed as is done in chapter 3. The far-field pattern is similarly obtained.

The far-field pattern obtained is compared with that for the continuously-varied-refractive-index lens to determine the acceptability of the equivalent lens circuit.

#### 4.2 Equivalent Circuit for the TE Mode Luneburg Lens (More Generally for TE Mode in Cylindrical Co-ordinates)<sup>21, 31</sup>

Maxwell's Equations for the TE mode in cylindrical co-ordinates are written down as differential equations, and are then converted into finite difference equations. If the electric field,  $E$ , and the magnetic field,  $H$  are expressed in terms of voltage,  $V$  and current,  $I$ , respectively, a set of equations which satisfy Kirchoff's current and voltage laws, are obtained. The values of the equivalent lumped components, L's and C's can then be deduced from Kirchoff's equations.

Maxwell's Equation (TE Mode —  $H_z, H_r, H_\phi$  only)

$$\text{Curl } \bar{E} = - \frac{\partial \bar{B}}{\partial t} \left\{ \begin{array}{l} \frac{1}{r} \frac{\partial E_z}{\partial \phi} = - \frac{\partial B_r}{\partial t} \\ - \frac{\partial E_z}{\partial r} = - \frac{\partial B_\phi}{\partial t} \end{array} \right. \quad (4.1)$$

$$(4.2)$$

$$\text{Curl } \bar{H} = \frac{\partial \bar{D}}{\partial t} \left\{ \begin{array}{l} \frac{1}{r} \frac{\partial}{\partial r} (r H_\phi) - \frac{1}{r} \frac{\partial H_r}{\partial \phi} = \frac{\partial D_z}{\partial t} \end{array} \right. \quad (4.3)$$

Equations (4.1) to (4.3) are converted to finite difference

equations using the following relationships. In converting these equations to finite difference form it is convenient to treat  $rH_\phi$  as a variable rather than  $H_\phi$ . Let  $H'_\phi = rH_\phi$  (Kron [21])

$$\frac{\partial E_z}{\partial \phi} \Big|_{r, \phi + \Delta\phi/2} = \left[ E_z \Big|_{r, \phi + \Delta\phi} - E_z \Big|_{r, \phi} \right] / \Delta\phi \quad (4.4(i))$$

$$\frac{\partial E_z}{\partial r} \Big|_{r + \Delta r/2, \phi} = \left[ E_z \Big|_{r + \Delta r, \phi} - E_z \Big|_{r, \phi} \right] / \Delta r \quad (4.4(ii))$$

$$\frac{\partial H'_\phi}{\partial r} \Big|_{r, \phi} = \left[ H'_\phi \Big|_{r + \Delta r/2, \phi} - H'_\phi \Big|_{r - \Delta r/2, \phi} \right] / \Delta r \quad (4.4(iii))$$

$$\text{and } \frac{\partial H_r}{\partial \phi} \Big|_{r, \phi} = \left[ H_r \Big|_{r, \phi + \Delta\phi/2} - H_r \Big|_{r, \phi - \Delta\phi/2} \right] / \Delta\phi \quad (4.4(iv))$$

We get

$$\left[ E_z \Big|_{r, \phi + \Delta\phi} - E_z \Big|_{r, \phi} \right] / (r\Delta\phi) = -j\omega\mu H_r \Big|_{r, \phi + \Delta\phi/2} \quad (4.1)$$

$$\left[ E_z \Big|_{r + \Delta r, \phi} - E_z \Big|_{r, \phi} \right] / \Delta r = \frac{j\omega\mu H'_\phi}{r} \Big|_{r + \Delta r/2, \phi} \quad (4.2)$$

$$\left[ H'_\phi \Big|_{r + \Delta r/2, \phi} - H'_\phi \Big|_{r - \Delta r/2, \phi} \right] / (r\Delta r) - \left[ H_r \Big|_{r, \phi + \Delta\phi/2} - H_r \Big|_{r, \phi - \Delta\phi/2} \right] / (r\Delta\phi) = j\omega \epsilon E_z \Big|_{r, \phi} \quad (4.3)$$

Multiplying the equations above by  $\Delta\phi \Delta r$  and rearranging

$$\left[ E_z \Big|_{r, \phi + \Delta\phi} - E_z \Big|_{r, \phi} \right] \cdot \Delta r = -j\omega\mu r \Delta\phi H_r \Big|_{r, \phi + \Delta\phi/2} \quad (4.1)$$

$$\left[ E_z \Big|_{r + \Delta r, \phi} - E_z \Big|_{r, \phi} \right] \cdot \Delta r = j\omega\mu \frac{\Delta r}{r} H'_\phi \Big|_{r + \Delta r/2, \phi} \quad (4.2)$$

$$\left[ H'_\phi \Big|_{r + \Delta r/2, \phi} - H'_\phi \Big|_{r - \Delta r/2, \phi} \right] \cdot \Delta\phi - \left[ H_r \Big|_{r, \phi + \Delta\phi/2} - H_r \Big|_{r, \phi - \Delta\phi/2} \right] \cdot \Delta r = j\omega \epsilon r \Delta r \Delta\phi E_z \Big|_{r, \phi} \quad (4.3)$$

Replacing  $\Delta r H_r$  by  $-I_\phi$

$\Delta\phi H'_\phi$  by  $I_r$  and

$\Delta z E_z$  by  $V_z$  in equations 4.1 to 4.3

$$\left\{ V_z \Big|_{r, \phi + \Delta\phi} - V_z \Big|_{r, \phi} \right\} = j\omega \left[ \mu r \frac{\Delta\phi \Delta z}{\Delta r} \right] I_\phi \Big|_{r, \phi + \Delta\phi/2} \quad (4.5)$$

$$\left\{ V_z \Big|_{r + \Delta r, \phi} - V_z \Big|_{r, \phi} \right\} = j\omega \left[ \mu \frac{\Delta r \Delta z}{r \Delta\phi} \right] I_r \Big|_{r + \Delta r/2, \phi} \quad (4.6)$$

$$\left\{ I_r \Big|_{r + \Delta r/2, \phi} - I_r \Big|_{r - \Delta r/2, \phi} \right\} + \left\{ I_\phi \Big|_{r, \phi + \Delta\phi/2} - I_\phi \Big|_{r, \phi - \Delta\phi/2} \right\} \\ = j\omega \left[ \epsilon r \frac{\Delta\phi \Delta r}{\Delta z} \right] V_z \Big|_{r, \phi} \quad (4.7)$$

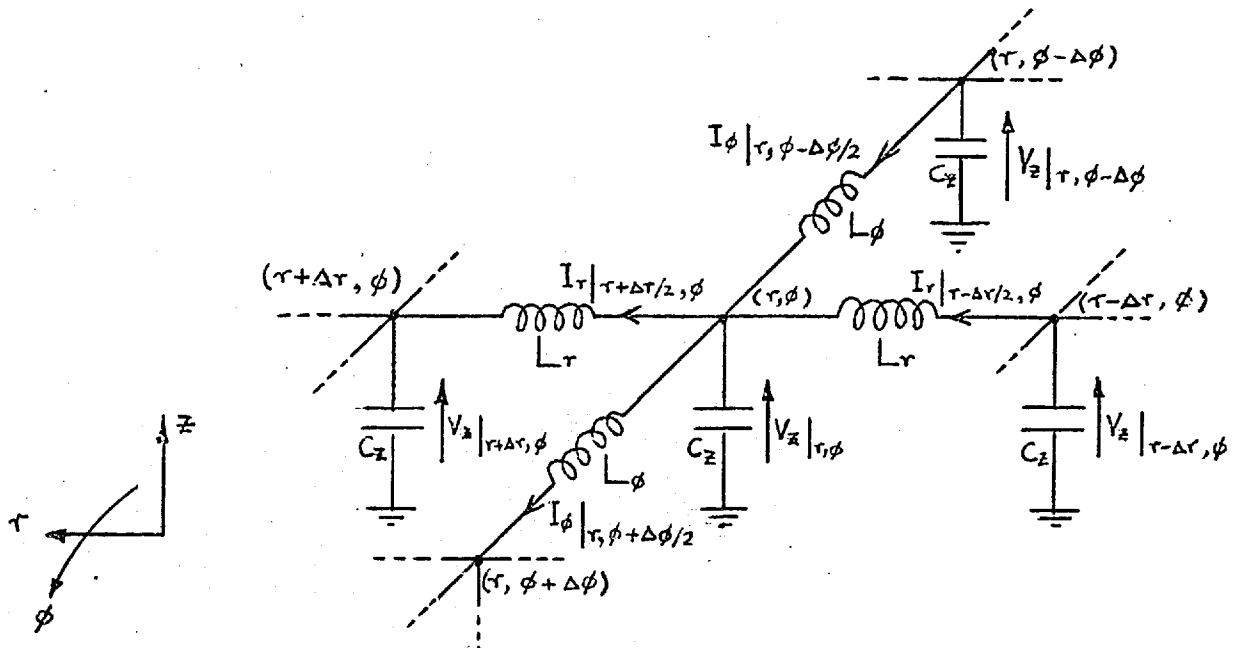


Fig. 4.1 EQUIVALENT CIRCUIT FOR TE MODE

The three equations above satisfy Kirchoff's voltage and current laws for the network shown in fig. 4.1. The quantities within the square brackets in equations 4.5 to 4.7 represent respectively the inductance  $L_\phi$ ,  $L_r$  and the capacitance  $C_z$ .



$$\text{Hence } L_{\phi} = \mu \cdot r \cdot \frac{\Delta\phi\Delta z}{\Delta r} \text{ H} \quad (4.8)$$

$$L_r = \mu \cdot \frac{\Delta r\Delta z}{r\Delta\phi} \text{ H} \quad (4.9)$$

$$C_z = \epsilon \cdot \frac{r\Delta\phi\Delta r}{\Delta z} \text{ F} \quad (4.10)$$

$C_z$  represents the capacitance of a parallel plate of area  $r\Delta\phi\Delta r$ , separation,  $\Delta z$ , filled with material of dielectric constant  $\epsilon$ .

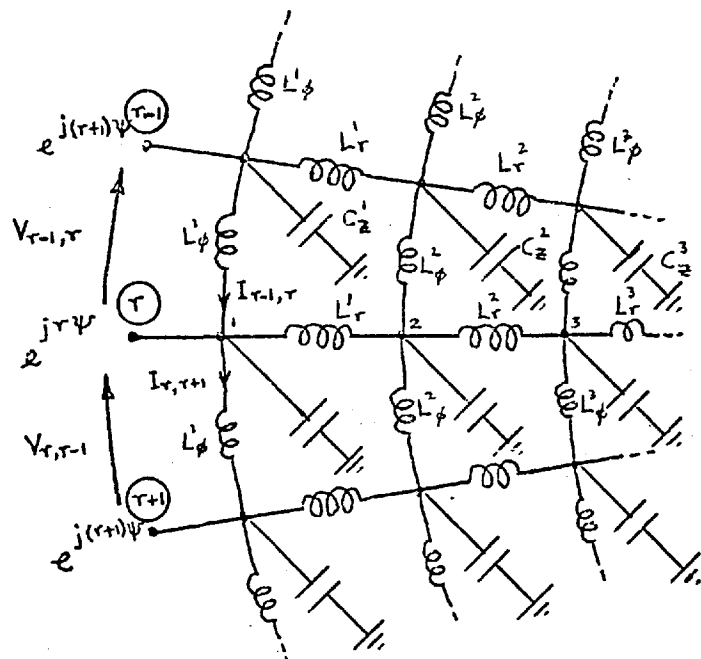
$L_r$  is the inductance associated with two conductors of width  $r\Delta\phi$ , length  $\Delta r$  and separation  $\Delta z$ , filled with material of permeability  $\mu$ .

$L_{\phi}$  is the inductance associated with two conductors of width  $\Delta r$ , length  $r\Delta\phi$  and separation,  $\Delta z$ , filled with material of permeability,  $\mu$ .

The equivalent circuit for a lens has been obtained. To compute the scattering matrix for the equivalent circuit the reflection coefficient for each of the  $N$  modes is required. The circular network can be decomposed to a ladder network for each mode by replacing the circumferential currents by currents flowing through an admittance to ground.

#### 4.2.1 Decomposition of Circular Network into a Ladder Network for Each Mode

If all the  $N$  feeds of the structure are excited with equal amplitude and phase we describe this as the zero mode excitation. The  $m$ th mode is excited if there is a phase progression between adjacent feeds of  $2\pi \ m/N$  radians



$N$  = No. of feeds along circumference

$$= 2\pi m/N$$

$m$  = mode

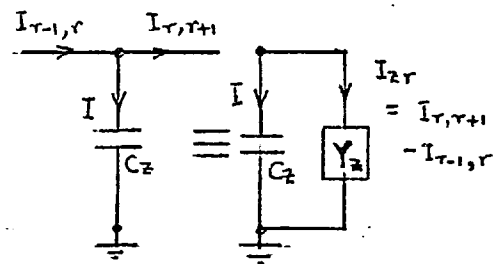


Fig. 4.2 DECOMPOSITION INTO LADDER NETWORK

The voltage distribution along the radial lines on the lens is shown in fig. 4.2. For the  $r$ th line,

$$V_{r-1,r} = e^{j(r-1)\psi} - e^{jr\psi} = e^{j(r-\frac{1}{2})\psi} (e^{-j\frac{\psi}{2}} - e^{j\frac{\psi}{2}})$$

$$\text{i.e. } V_{r-1,r} = -j2e^{j(r-\frac{1}{2})\psi} \sin \frac{\psi}{2} \quad (4.11)$$

$$\text{and } V_{r,r+1} = e^{jr\psi} - e^{j(r+1)\psi} = e^{j(r+\frac{1}{2})\psi} (e^{-j\frac{\psi}{2}} - e^{j\frac{\psi}{2}})$$

$$\text{i.e. } V_{r,r+1} = -j2e^{j(r+\frac{1}{2})\psi} \sin \frac{\psi}{2} \quad (4.12)$$

∴ circumferential currents for radial line,  $r$  at mode 1 are:-

$$I_{r-1,r} = \left\{ -2j \sin \frac{\psi}{2} \cdot \exp [j(r-\frac{1}{2})\psi] \right\} / j\omega L_{\phi}^1 \quad (4.13)$$

$$I_{r,r+1} = \left\{ -2j \sin \frac{\psi}{2} \cdot \exp [j(r+\frac{1}{2})\psi] \right\} / j\omega L_{\phi}^1 \quad (4.14)$$

replacing these two currents by a current flowing into an inductance,  $L_z^1$  for radial line,  $r$ , at mode 1.

$$\begin{aligned} I_{z_r} &= I_{r,r+1} - I_{r-1,r} \\ &= -2j \sin \frac{\psi}{2} \left\{ \exp [j(r+\frac{1}{2})\psi] - \exp [j(r-\frac{1}{2})\psi] \right\} / j\omega L_{\phi}^1 \\ I_{z_r} &= -\exp(jr\psi) \cdot (2j \sin \frac{\psi}{2})^2 / j\omega L_{\phi}^1 \end{aligned} \quad (4.15)$$

$$\text{i.e. } \frac{I_{z_r}}{\exp(jr\psi)} = (4 \sin^2 \frac{\psi}{2}) / j\omega L_{\phi}^1 = Y_{z_1} \quad (4.16)$$

Hence the circumferential inductances,  $L_{\phi}^1$  can be replaced by an inductance  $L_z^1$  in a ladder network. The analysis can be repeated for other nodes so that  $L_{\phi}^n$  can be replaced by  $L_z^n$  in a ladder network where

$$L_z^n = \frac{L_{\phi}^n}{4 \sin^2 \frac{\psi}{2}} \quad (4.17)$$

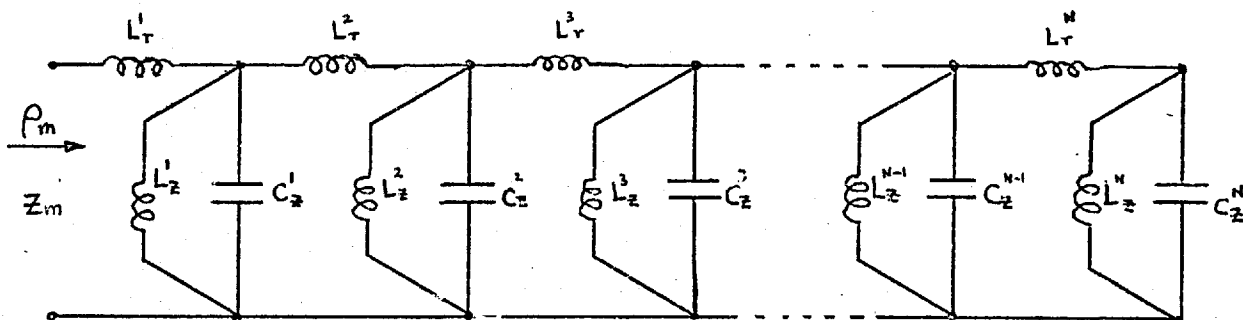


Fig. 4.3 EQUIVALENT LADDER NETWORK FOR MODE, m

The network is terminated by  $Z_o$  the characteristic at the edge of the lens.

Characteristic Impedance,  $Z_o$ , at Edge of Lens

$$Z_o = \sqrt{\frac{L}{C}} = \sqrt{\left\{ \frac{\mu \Delta r \Delta z}{r \Delta \phi} / \frac{e \cdot r \Delta \phi \Delta r}{\Delta z} \right\}} \quad \Omega$$

(from equations 4.8, 4.9 and 4.10)

i.e. 
$$Z_o = \frac{\Delta z}{r \Delta \phi} \sqrt{\frac{\mu}{\epsilon}} \quad (4.18)$$

Mode Reflection Coefficient,  $\rho_m$

If  $Z_m$  is the input impedance of the ladder network for mode;  $m$  the reflection coefficient for the  $m$ th mode is

$$\rho_m = \frac{Z_m - Z_o}{Z_m + Z_o} \quad (4.19)$$

#### 4.2.2 Behaviour of the Equivalent Ladder Network for Different Modes

Figure 4.4 shows the phase of the reflection coefficient for the various modes for different lens diameters. These reflection coefficients are those obtained for the ideal lens studied in chapter 4. All phases are normalised to the value of the highest mode value so that the phases are negative and decrease numerically with mode number. In chapter 4 we suggest that the higher modes do not penetrate the lens as much as the lower modes. This supposition is confirmed by the equivalent transmission line type equivalent ladder network obtained for each mode.

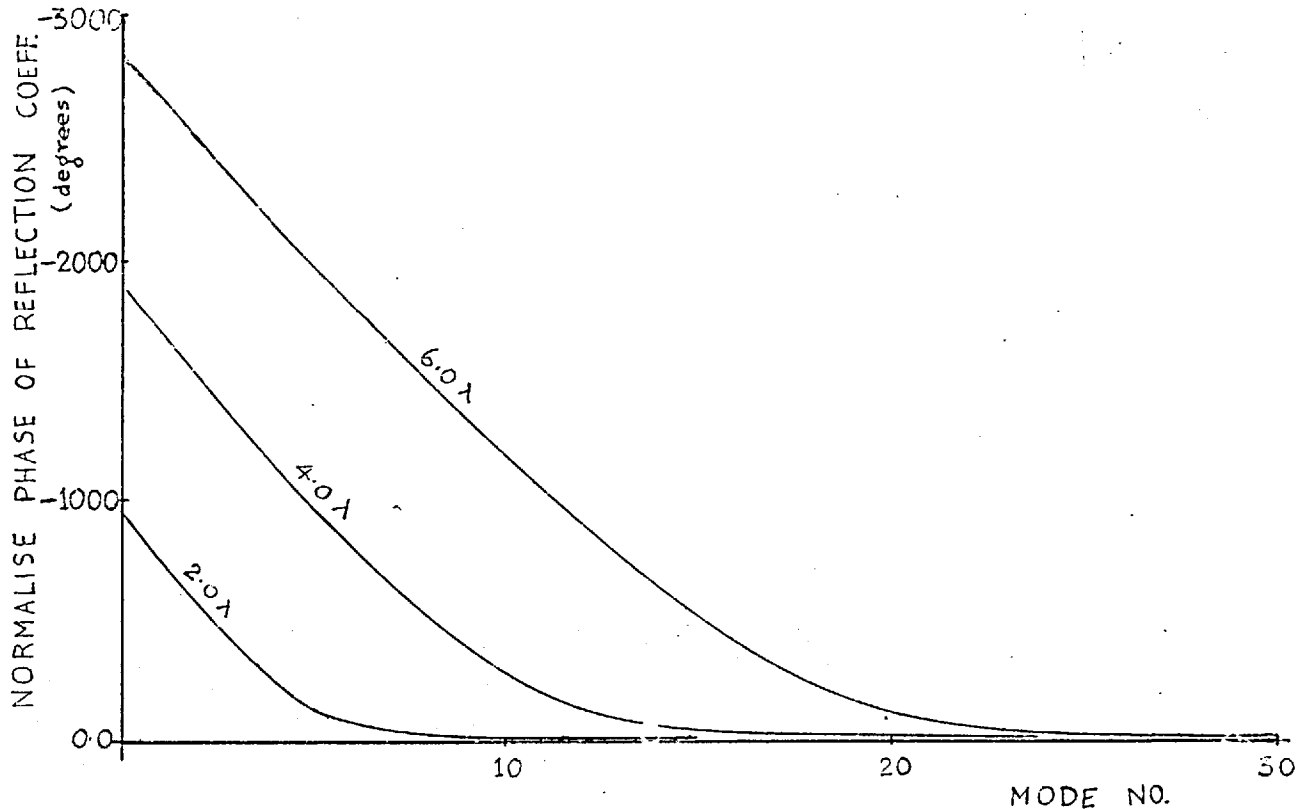


Fig. 4.4 NORMALISED PHASE OF MODE REFLECTION COEFFICIENT  
(for Luneburg Lens)

Each of the shunt elements of the ladder network in fig. 4.3 consist of the capacitance,  $C_z$  in parallel with the inductance,  $L_z = L_\phi / 4 \sin^2 \psi$ . Since both  $C_z$  and  $L_\phi$  are directly proportioned to  $r$ , (the distance from the centre of the lens), the inductance,  $L_z$  and capacitance,  $C_z$  decreases towards the centre of the lens. Thus the reactance of the shunt inductor,  $L_z$ , decreases towards the centre of the lens while the capacitive reactance increases. Therefore the reactance of the shunt elements is capacitive at the feed end of

the ladder network, decreasing in value toward the lens centre. At a point distance,  $l$  from the feed, the reactance becomes zero and beyond  $l$  the reactance is inductive. Since the series elements in the ladder network is inductive, beyond  $l$  the mode does not propagate appreciably further into the lens.

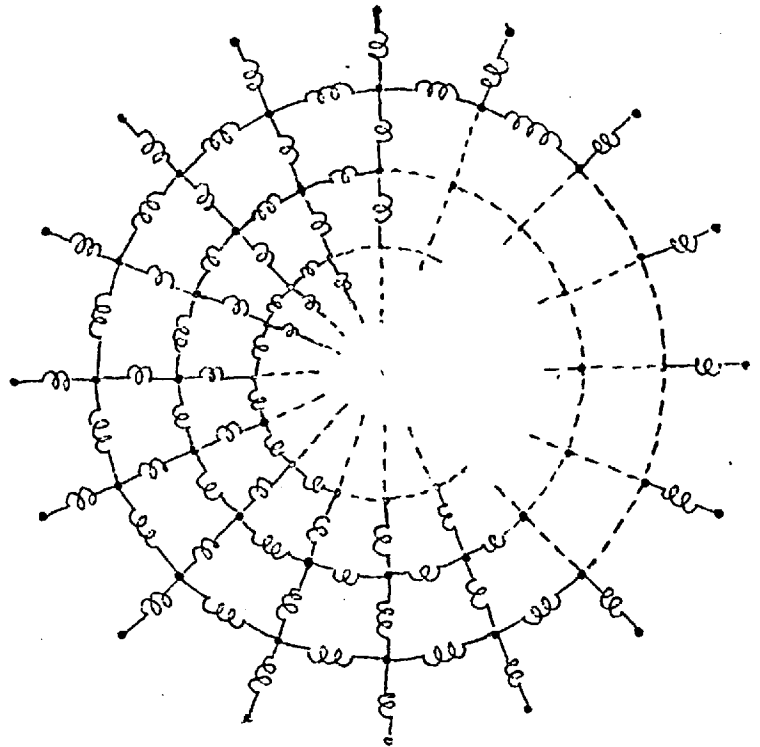
Each section of the ladder network can be viewed as a filter. Where the shunt element is inductive, this corresponds to the stop band. In fact these filters have a high-pass behaviour. At a higher frequency the reactance of the shunt elements could be capacitive, so that for the same mode number the waves penetrate further into the lens.

With a higher mode number, the value of the shunt inductance, ( $L_z = L_\phi / 4 \sin^2 \psi$ ) decreases so that the stop band region in the ladder network moves towards the feed away from the centre of the lens. We see in figure 4.4 that the higher modes barely penetrate the lens.

#### 4.3 Minimum Number of Elements Required for the Equivalent Circuit

##### Lens

The criteria for judging the acceptability of an equivalent circuit is the far-field pattern obtained by feeding its outputs to a ring array of cardioid  $(1 + \cos \theta)$  radiators. The radiation pattern obtained is compared with that obtained using the continuously varied dielectric lens.



There is a capacitance,  
 $C_z$  down to earth at  
 every node

Fig. 4.5 THE EQUIVALENT CIRCUIT LUNEBURG LENS

The relative phase of the various mode reflection coefficients also gives a good indication of the behaviour of the far-field radiation pattern. The phase values obtained for the ideal lens (in chapter 3) is used as the standard reference values.

The radiation patterns for the array and the relationship between reflection coefficients of different modes are investigated for equivalent circuit lenses with varying number of components.

The two important parameters are:-

(a) the number of elements used per radial line for the equivalent circuit. In this context one element represents one

section of the lens, viz, one shunt capacitor,  $C_z$ , one radial inductor,  $L_r$  and one circumferential inductor,  $L_\phi$ .

(b)  $N$ , the number of radial lines used for the circuit. Each radial line corresponds to a feed point at the circumference of the lens. The maximum order mode excited is  $N/2$  if  $N$  is even ( $(N-1)/2$ , if  $N$ , odd).

A computer program has been written to calculate the values of the components of the equivalent circuit lens (subroutine EQCCT, described in Appendix A4.1). The mode reflection coefficient is computed from the equivalent ladder network by the subroutine RFLCCT (Appendix A4.1). The scattering matrix for the structure and the far-field pattern for the array is calculated using the subroutines already described in Appendix A3.3 in chapter 3.

The program was run principally for three values of lens diameters -  $2.0\lambda$ ,  $4.0\lambda$  and  $6.0\lambda$ , i.e. 200.0 metres at 3.0, 6.0 and 9.0 MHz. The number of radial lines were varied. Side lobe levels are given in tables 4.5, 4.6 and 4.7.

#### 4.3.1 Component Values for Equivalent Circuit Lens

Some typical values of the components used in the equivalent circuit is tabulated in table 4.1 & 4.2 for a 200.0 metre diameter lens. Table 4.1 shows the component values for a lens with 24 radial lines and 8 elements per radial line (i.e.  $N = 24$ ,  $NELR = 8$ ). Two types of lenses are indicated - the  $\mu = 1$ ,  $\epsilon = (2-r^2)$  ordinary lens and the  $\mu = \epsilon = \sqrt{2-r^2}$  lens.



200.0 Metre Lens ; 24 Radial Lines ; $Z_0 = 14.39 \Omega$							
$\mu = 1$ ORDINARY LENS				$\mu =$ LENS			
No.	$L_\phi$ $\mu\text{H}$	$C_z$ nF	$L_r$ $\mu\text{H}$	No.	$L_\phi$ $\mu\text{H}$	$C_z$ nF	$L_r$ $\mu\text{H}$
1	2.467	3.045	0.300	1	2.612	2.876	0.300
2	2.138	3.154	0.686	2	2.475	2.725	0.762
3	1.809	3.042	0.800	3	2.236	2.462	0.959
4	1.480	2.744	0.960	4	1.921	2.115	1.218
5	1.151	2.293	1.200	5	1.548	1.705	1.587
6	0.822	1.722	1.600	6	1.134	1.249	2.182
7	0.493	1.067	2.400	7	0.692	0.762	3.341
8	0.164	0.361	4.800	8	0.232	0.256	6.762

Table 4.1 Component Values for Lens Type Indicated

200.0 Metre Lens ; 60 Radial Lines ; $Z_0 = 35.98 \Omega$							
No.	$L_\phi$ $\mu\text{H}$	$C_z$ nF	$L_r$ $\mu\text{H}$	No.	$L_\phi$ $\mu\text{H}$	$C_z$ nF	$L_r$ $\mu\text{H}$
1	2.303	5.282	0.333	10	1.119	4.322	1.333
2	2.171	5.476	0.7059	11	0.987	3.920	1.500
3	2.040	5.582	0.750	12	0.855	3.478	1.714
4	1.908	5.606	0.800	13	0.724	3.001	2.000
5	1.776	5.555	0.857	14	0.592	2.495	2.400
6	1.645	5.429	0.923	15	0.460	1.965	3.000
7	1.513	5.239	1.000	16	0.329	1.417	4.000
8	1.382	4.987	1.091	17	0.197	0.856	6.000
9	1.250	4.680	1.200	18	0.0658	0.286	12.000

Table 4.2 Component Values for Ordinary Lens

Table 4.2 shows the component values for a lens capable of working below 6MHz (i.e. a maximum lens diameter of  $4.0\lambda$ ) with 60 radial lines and 18 elements per radial line.

The height of the equivalent lens is one metre. This value can be varied to match the aerial or to vary component values, as long as the lens height is less than  $\lambda/2$  at the highest frequency of operation. Otherwise higher order TE modes and TM modes can also exist in the lens. The values of the components of the equivalent circuit lens will vary in accordance with the expression given in equations 4.8, 4.9 and 4.10.

The radiation patterns obtained using the ordinary lens ( $\mu = 1$ ) and the  $\mu = \epsilon$  lens do differ significantly, particularly for the larger lens. The  $\mu = \epsilon$  lens tend to have a very slightly high side lobe.

All following results and discussions apply to the ordinary  $\mu = 1$ ,  $\epsilon = (2-r^2)$  lens.

#### 4.3.2 Equivalent Circuit Lens Behaviour

In the next two sections the behaviour of the phases of the mode reflection coefficient is studied. The two parameter, NELR, the number of elements per radial line and N, the number of radial lines are varied separately.

##### 4.3.2 (a) Effect <sup>of</sup> Variation of NELR on the Behaviour of Mode Reflection Coefficient

The lens diameter (in wavelength) and N, the number of radial

lines are fixed while the number of elements per line, NELR is varied. The phase of the mode reflection coefficient is plotted against  $N$ , the number of elements per line used for mode 0 to 12 in fig. 4.6 and 4.7 for a  $2.0\lambda$  diameter lens. Similar results for a  $4.0\lambda$  diameter lens are tabulated in table 4.3 for the more significant modes. The corresponding phases for the ideal lenses are also shown.

It is clear that the higher modes are unaffected by the change in the number of radial elements, NELR, used. For low order modes the phase changes rapidly with an increase in NELR, reaching an asymptotic value below that of the ideal lens. As the mode number increases the deviation of the asymptotic value from the ideal lens value increases. However, if  $N$ , the number of radial lines used is larger the phase deviation decreases. This can be seen in the next section.

#### 4.3.2 (b) Effect of Variation of $N$ (, Number of Radial Lines) on the Phase Behaviour of Mode Reflection Coefficient

The phases of the mode reflection coefficients are plotted against  $N$  in fig. 4.9 and 4.10 for a  $2.0\lambda$  diameter lens. (200.0 metres at 3MHz). The same parameters are tabulated in table 4.4 for a representative selection of mode numbers for a  $4.0\lambda$  diameter lens (200.0 metres at 6.0MHz). The corresponding phases of the modes reflection coefficients for the ideal lens (discussed in chapter 3) are also shown in fig. 4.8 and 4.9 and table 4.4.

We see that the lower order modes are unaffected by the change in the number of radial lines used. In fig. 4.8 the phase of the mode reflection coefficient for mode 0, 1 and 2 are practically

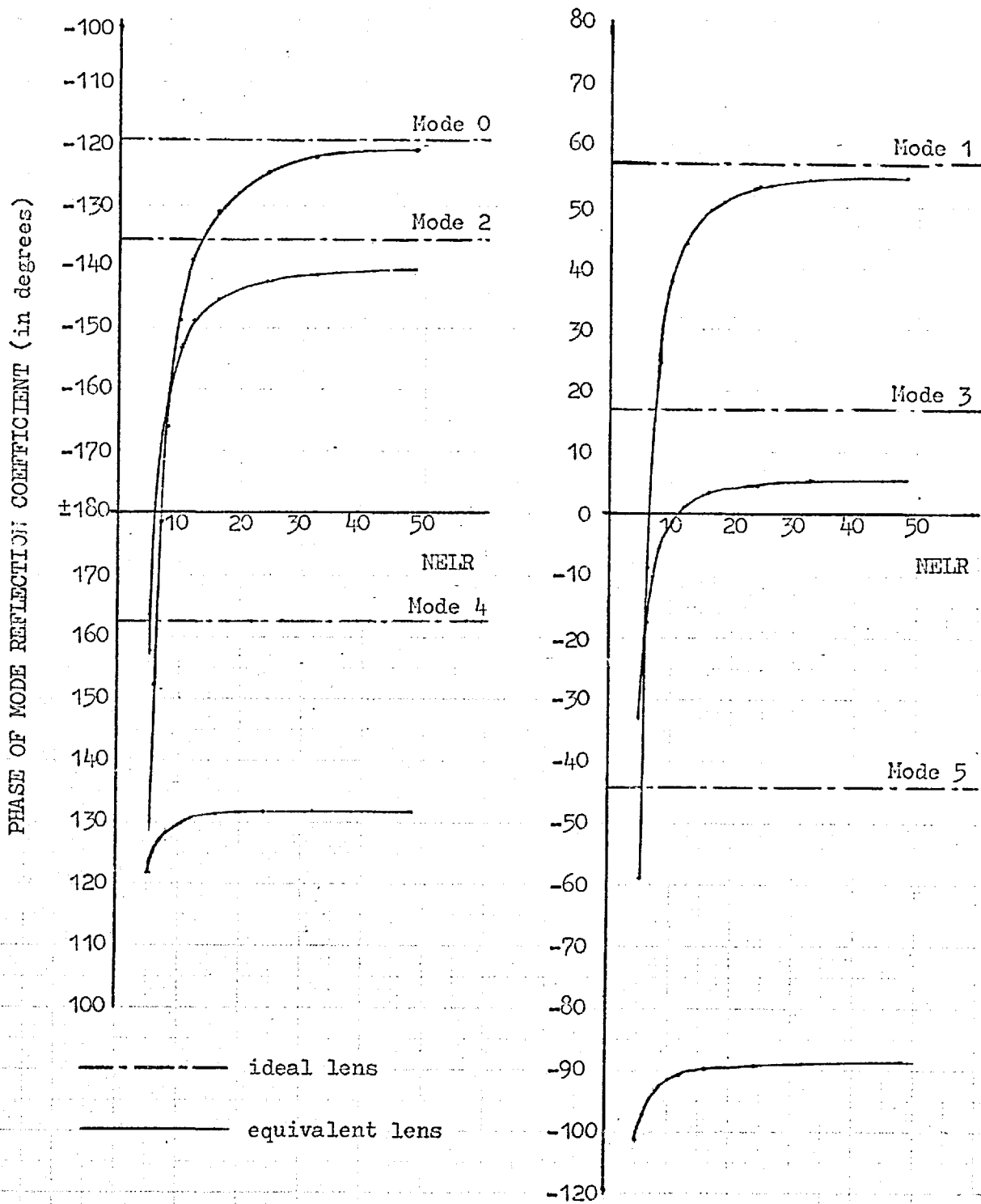


Fig. 4.6 BEHAVIOUR OF MODE REFLECTION COEFFICIENT FOR VARYING VALUE FOR NELR (2.0λ Lens)

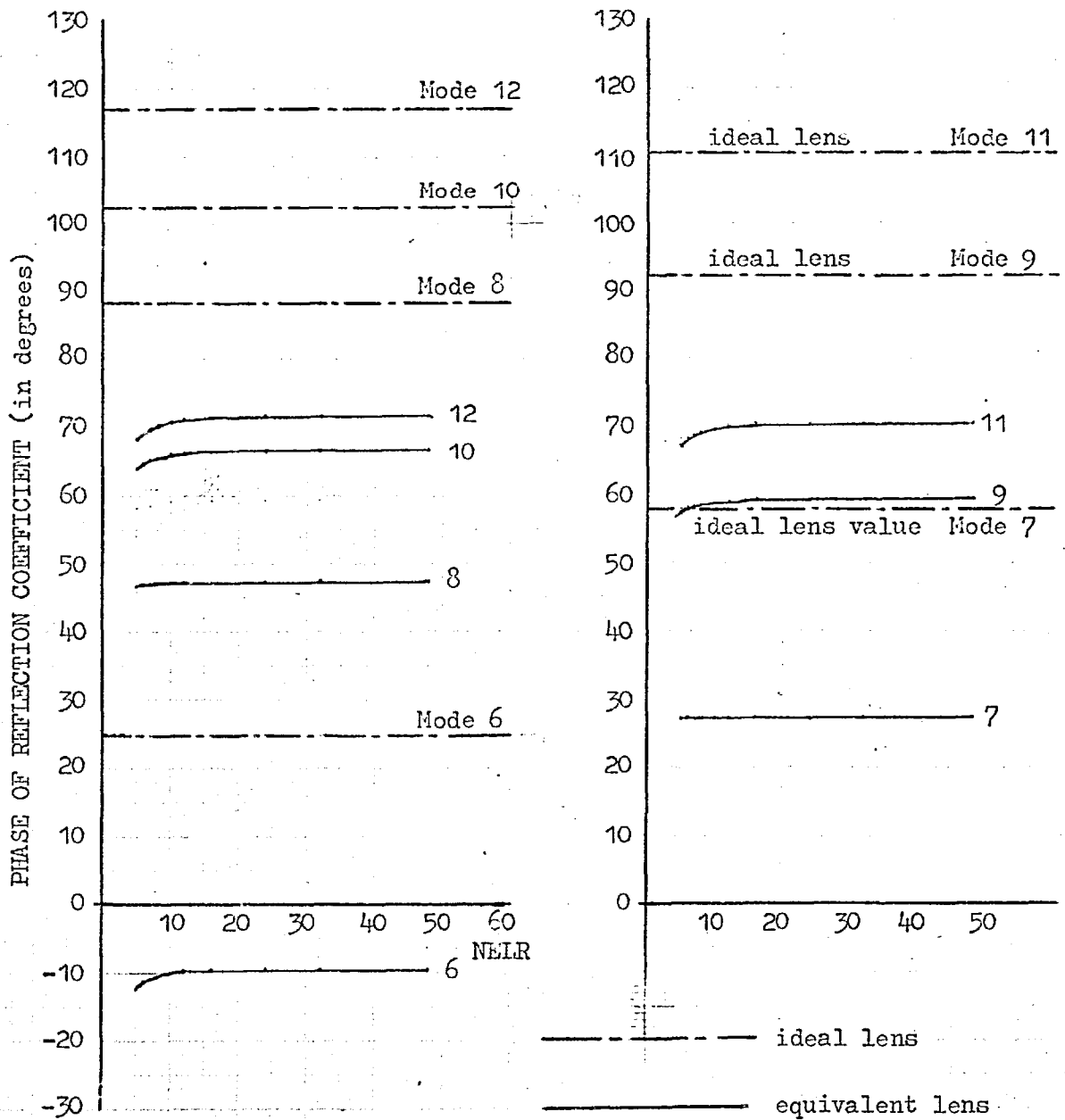


Fig. 4.7 BEHAVIOUR OF MODE REFLECTION COEFFICIENT FOR VARYING VALUE OF NELR (2.0λ Lens)

MODE NO.	PHASE OF MODE REFLECTION COEFFICIENT FOR VARYING NO. OF ELEMENTS PER RADIUS								
	12	14	16	18	24	32	48	64	IDEAL LENS
0	-156.3	-97.9	-61.3	-37.5	-2.2	15.6	27.4	31.4	37.7
1	69.5	116.3	141.3	157.2	-177.6	-163.7	-153.9	-150.5	-144.8
2	-105.6	-64.0	-39.0	-23.2	0.3	12.2	20.1	22.8	28.1
3	103.2	130.2	145.9	156.3	173.0	-177.8	-171.3	-169.0	-162.7
4	-86.5	-61.0	-45.9	-36.3	-21.7	-14.2	-9.1	-7.4	-0.5
5	95.7	110.6	119.6	125.6	135.2	140.5	144.3	145.6	158.1
6	-104.4	-90.4	-81.8	-76.1	-67.3	-62.7	-59.4	-58.3	-41.7
7	45.8	52.9	57.0	59.8	64.1	66.4	68.0	68.5	92.5
8	-165.7	-158.9	-154.6	-151.6	-146.8	-144.1	-142.2	-141.5	-101.1
9	-29.2	-25.7	-23.5	-22.1	-19.9	-18.7	-17.9	-17.6	16.1
-	-	-	-	-	-	-	-	-	-
20	76.8	78.0	78.8	79.3	80.3	80.8	81.2	81.3	102.3
21	79.7	81.0	81.9	82.6	83.7	84.3	84.7	84.9	106.6
22	82.1	83.6	84.6	85.3	86.5	87.2	87.7	87.9	110.4
-	-	-	-	-	-	-	-	-	-
28	89.1	91.1	92.4	93.4	95.0	96.0	96.5	96.9	126.7
29	89.4	91.4	92.8	93.7	95.4	96.4	97.1	97.3	128.7
30	89.5	91.5	92.9	93.9	95.5	96.5	97.2	97.5	130.5

Table 4.3 Phase of Reflection Coefficient for Varying No. of Elements per Radius  
(for 60 radial lines -  $4.0\lambda$  diameter)

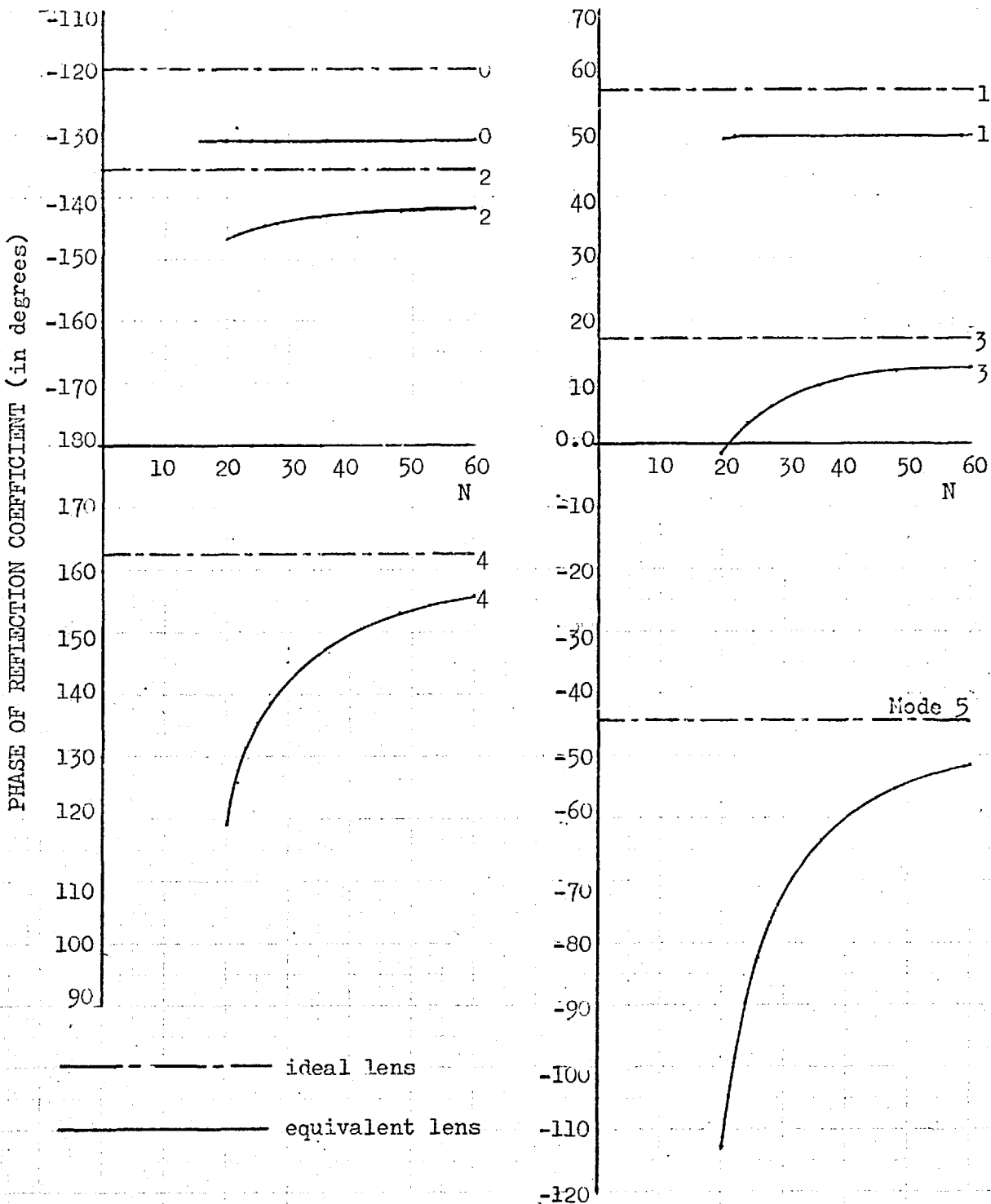


Fig. 4.8 BEHAVIOUR OF MODE REFLECTION COEFFICIENT FOR VARYING NUMBER OF RADIAL LINES (N)

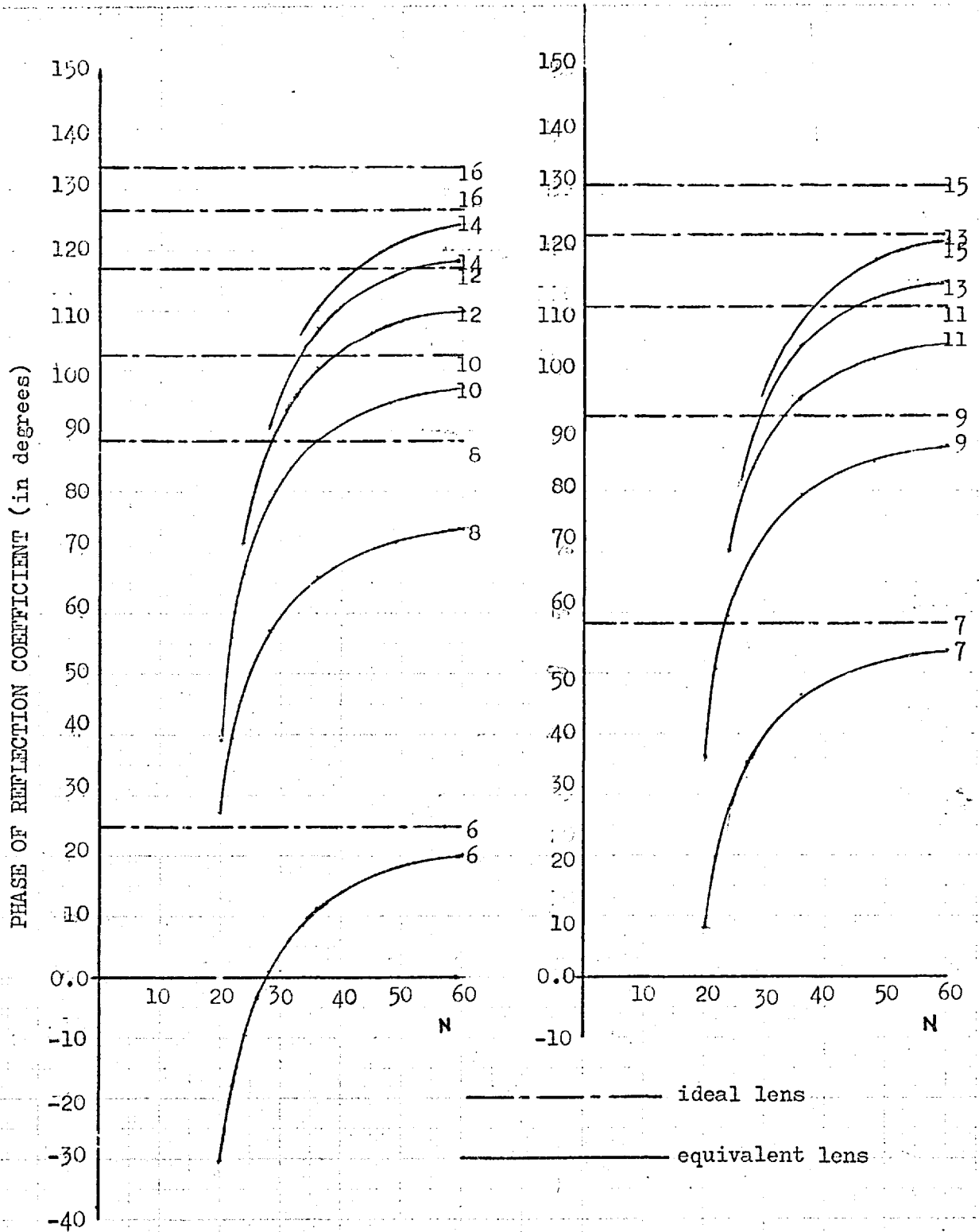


Fig. 4.9 BEHAVIOUR OF MODE REFLECTION COEFFICIENT FOR VARYING NUMBER OF RADIAL LINES (N)



MODE NO.	PHASE OF MODE REFLECTION COEFFICIENT FOR DIFFERENT NO. OF RADIAL LINES									
	40	44	48	52	56	60	64	72	96	LENS
0	15.6	15.6	15.6	15.6	15.6	15.6	15.6	15.6	15.6	37.7
1	-163.8	-163.8	-163.7	-163.7	-163.7	-163.7	-163.7	-163.7	-163.7	-144.8
2	11.4	11.6	11.8	12.0	12.1	12.2	12.2	12.4	12.6	28.1
3	179.6	-179.6	-179.0	-178.5	-178.1	-177.8	-177.5	-177.2	-176.5	-162.7
-	-	-	-	-	-	-	-	-	-	-
9	-66.2	-50.3	-38.9	-30.4	-23.8	-18.7	-14.5	-8.3	1.7	16.1
10	14.7	31.1	44.0	54.6	63.5	71.0	77.5	88.1	107.5	139.1
11	87.6	120.3	150.7	177.5	-160.3	-142.5	-128.4	-108.3	-79.7	-50.2
-	-	-	-	-	-	-	-	-	-	-
18	27.3	45.6	56.1	63.0	67.6	71.5	74.2	78.2	84.0	91.7
20	31.2	52.5	64.2	71.7	76.9	80.8	83.7	87.9	93.9	102.3
22		54.5	68.4	77.0	82.9	87.2	90.4	94.9	101.3	110.4
24			69.8	80.0	86.7	91.5	95.1	100.0	107.0	116.9
26				80.9	88.8	94.4	98.4	103.9	111.5	122.2
28					89.5	96.0	100.6	106.8	115.1	126.7
30						96.5	101.9	108.8	118.0	130.5
32							102.3	110.3	120.4	133.8
34								111.8	122.3	136.6

Table 4.4 Phase of Mode Reflection Coefficient for Different No. of Radial Lines

(32 elements per radial line -  $4.0\lambda$  diameter)

constant. The same applies to mode 0, 1, 2 and 3 in table 4.4 for the  $4.0\lambda$  lens.

As the mode order increases the mode reflection coefficient becomes increasingly dependent on N, the number of radial lines used in the equivalent circuit lens; the phase approaching the ideal lens values as the number of radial lines used is increased. However, the phase does not approach the ideal lens values. An asymptotic value below the ideal lens value is reached. For the lower order modes where the phases are practically independent of N, the constant values may also be considered as the asymptotic value. Other results obtained indicate that this asymptotic value approaches the ideal lens value as the number of elements used per line, NELR, is increased.

Results obtained in section 4.3.2(a) and (b) thus indicate that if N and NELR are sufficiently large the equivalent lens circuit will behave exactly like the ideal lens as is to be expected.

The unchanged behaviour of the higher order modes in section 4.3.2(a) and of the lower order modes in section 4.3.2(b) is consistent with the equivalent ladder network discussed in section 4.2.2. Where the number of elements per radial line is fixed, the shunt inductive elements are large for the lower order mode ( $L_z = L_\phi / 4 \sin^2 \psi$ ,  $\psi = (2\pi * \text{Mode})/N$ ) and hence mode behaviour is fairly independent of N, the number of radial lines used.

### 4.3.3 Far-Field Pattern from the Equivalent Circuit Lens (Using Cardioid (1+cosine) Radiators)

We have suggested that the criteria for judging the acceptability of the equivalent circuit lens is the radiation pattern obtained by feeding the outputs from the lens to radiating elements in an array. As in chapter 3 cardioid (1+cosine) radiators are used. The use of Beverage Aerial radiators will be discussed in a later section.

A representative selection of radiation patterns obtained using equivalent circuit lens of varying  $N$ , and  $NELR$  are shown in fig. 4.10 for a  $2.0\lambda$  lens and fig. 4.11 and 4.12 for a  $4.0\lambda$  lens.

The radiation patterns obtained indicate that in most cases the first or second side lobes are higher than that obtained using the ideal lens. In extreme cases the main beam is bifurcated. In table 4.5, 4.6 and 4.7 we show the side lobe levels obtained for 3 lens,  $2.0\lambda$ ,  $4.0\lambda$  and  $6.0\lambda$  diameters (i.e. at 3.0, 6.0 and 9.0MHz for a 200.0 metre lens) for different values of  $N$  and  $NELR$ .

We see that for a fixed number of  $N$  (, the number of radial lines used) or a fixed value of  $NELR$  (, the number of elements used per radial line) there is an optimum side lobe level. For example, in table 4.6, for  $NELR = 16$ , the minimum side lobe level is obtained for  $N = 56$  (side lobe level of 0.260). The corresponding value for  $NELR = 18$  is for  $N = 60$  (0.241 side lobe level). As  $NELR$  is increased the value of  $N$  required to give a minimum side lobe level increases so that the minimum side lobe level in tables will be roughly along the non-leading diagonal. As both  $NN$  and  $NELR$  become large the side

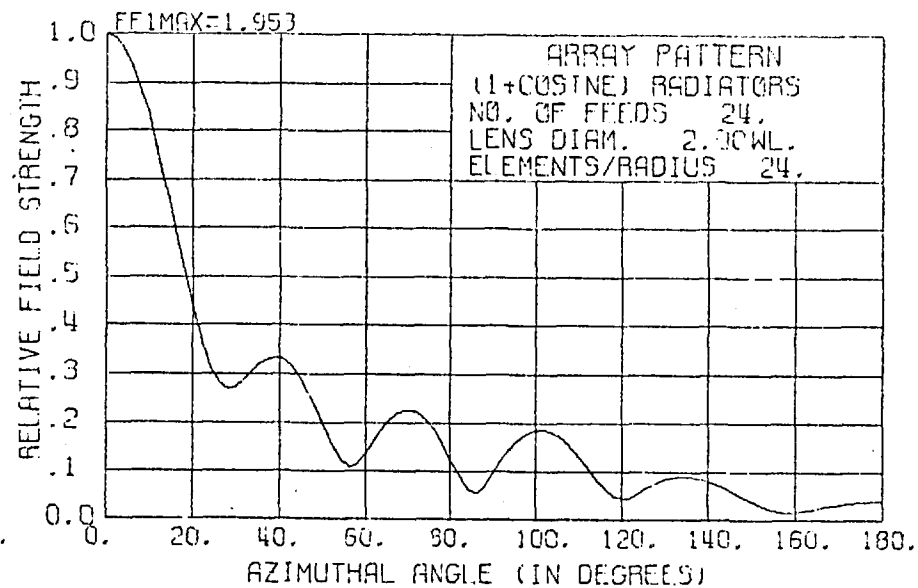
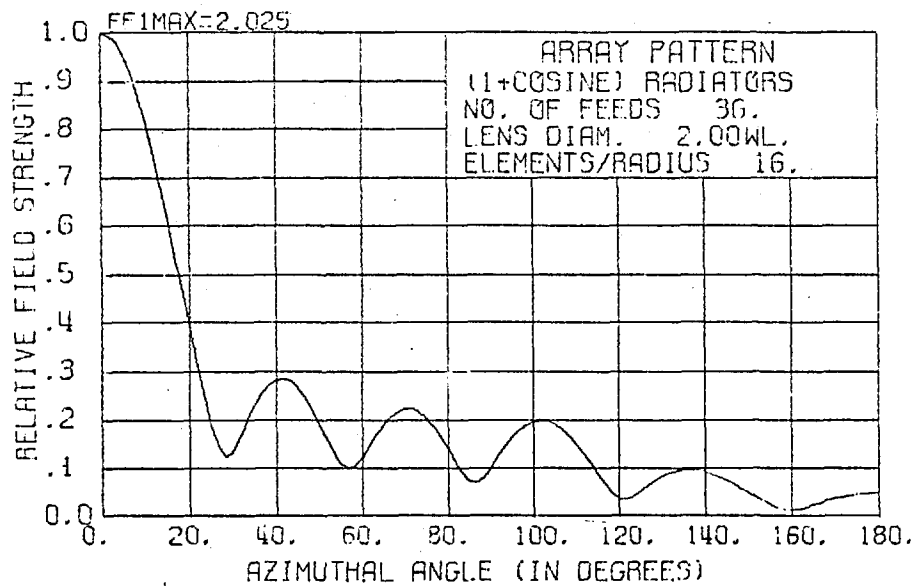
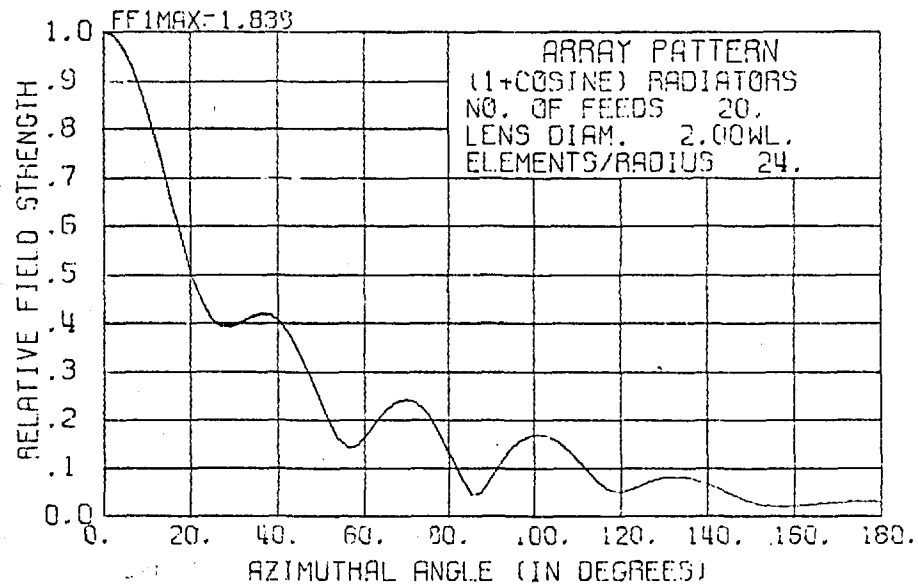
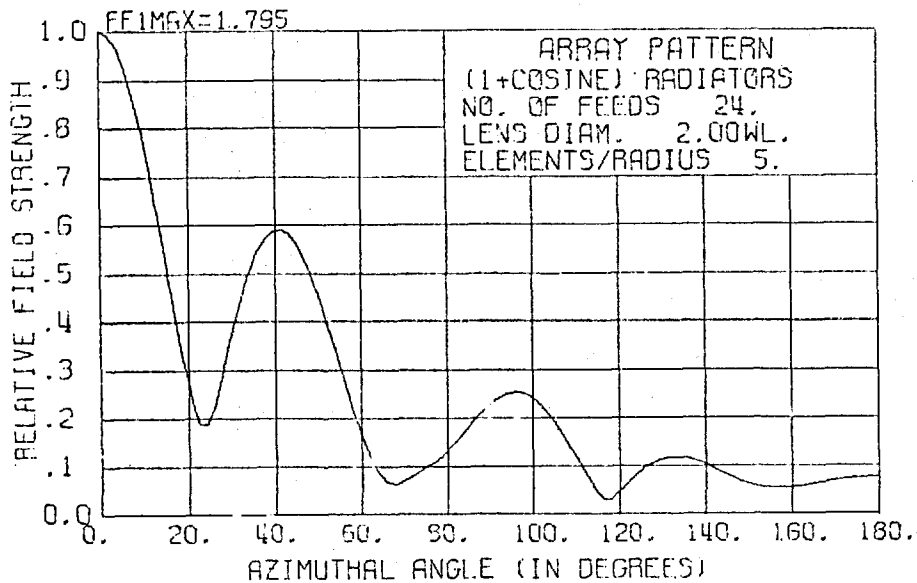


Fig. 4.10

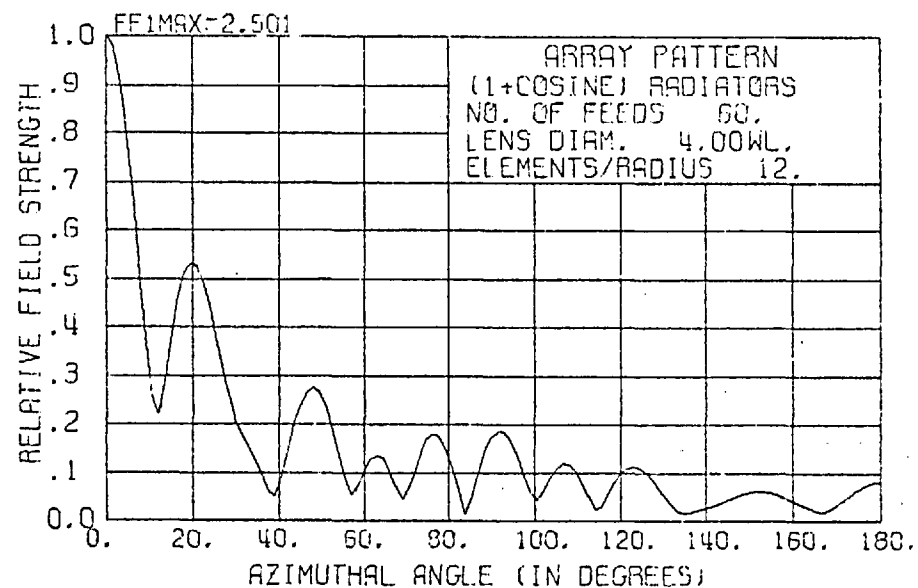
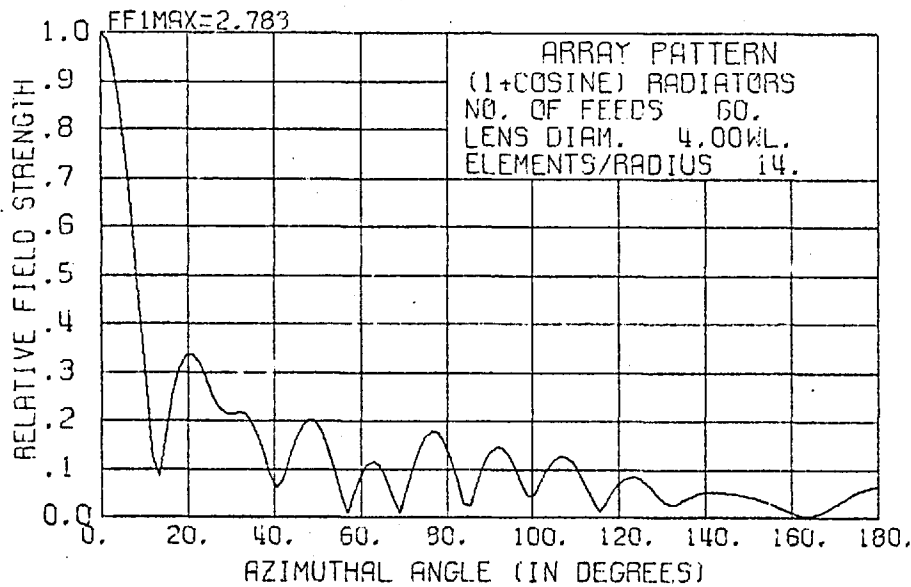
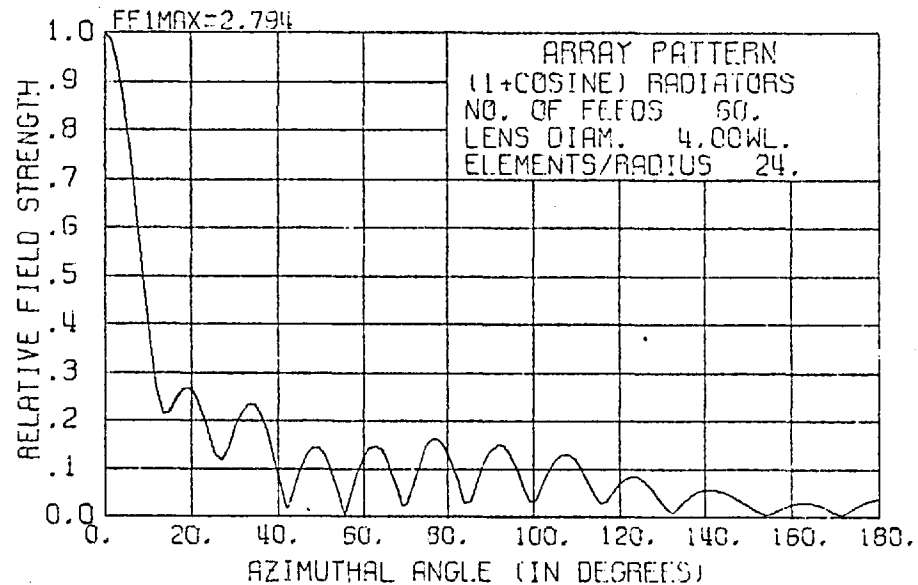
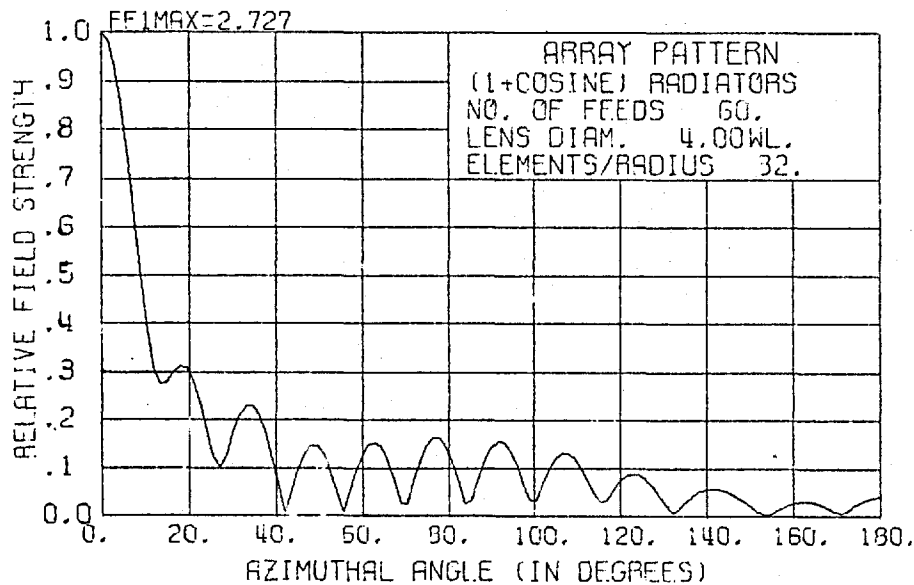


Fig. 4.11

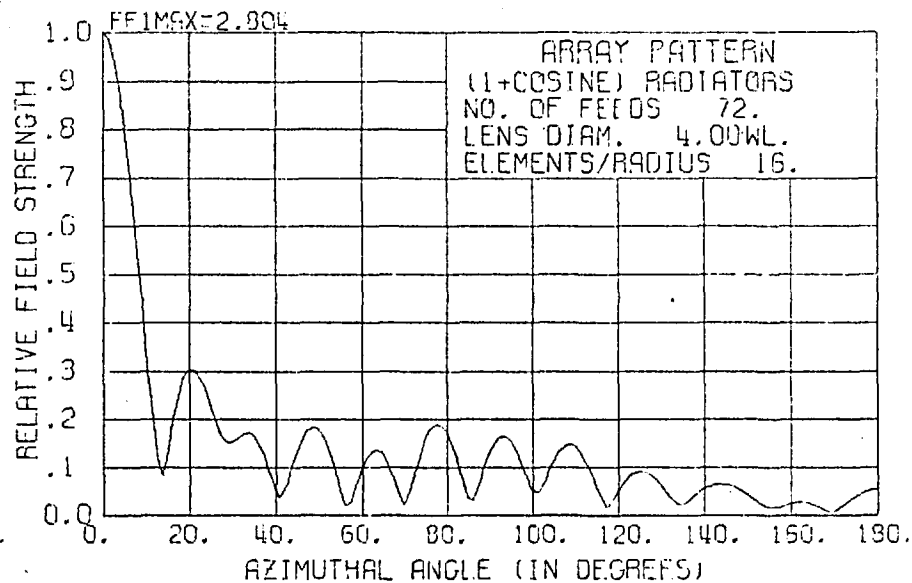
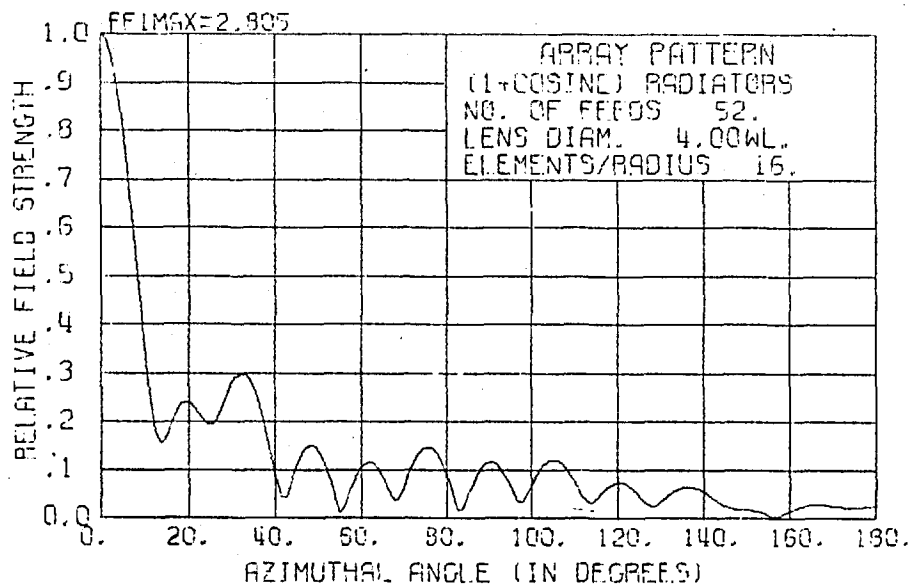
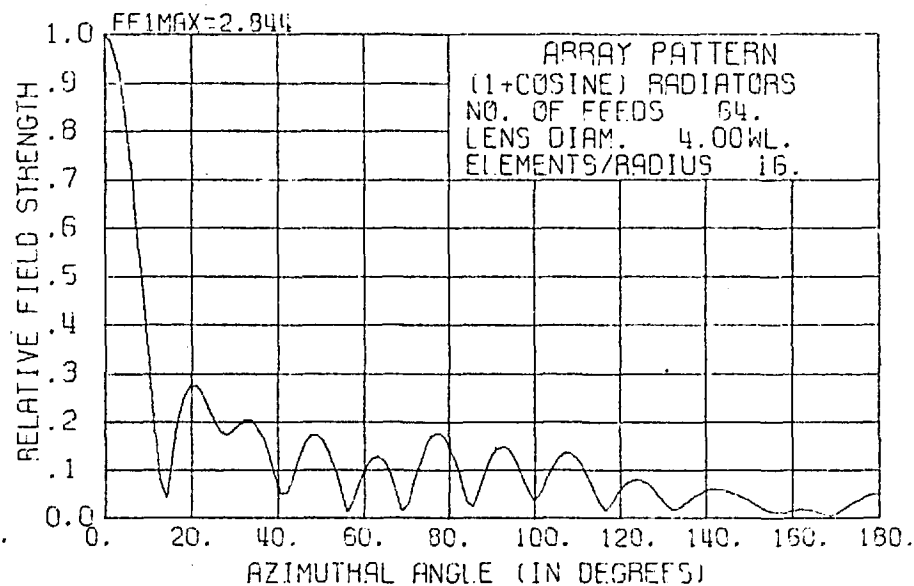
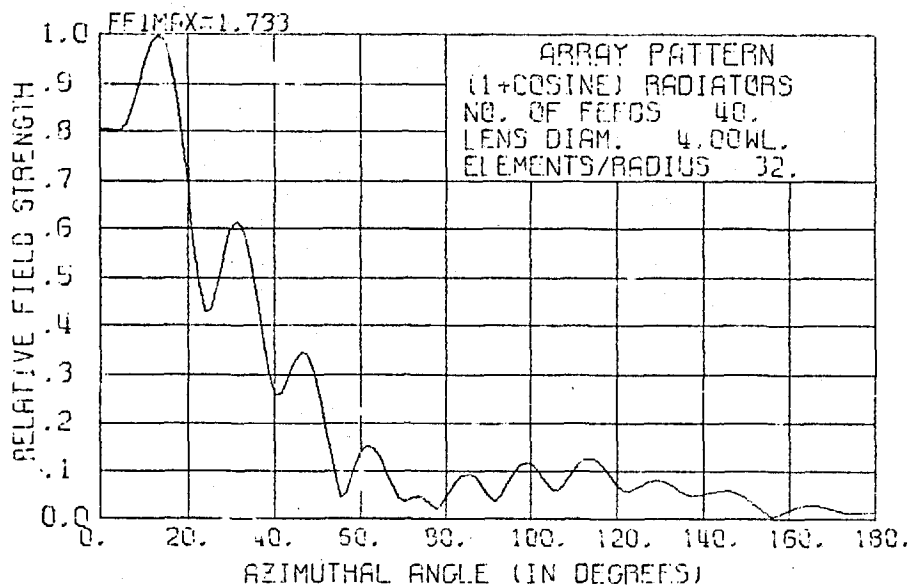


Fig. 4.12

NN	48	36	28	26	24	22	20
NELR							
5					0.593		
6					0.358		
7					0.304		
8	0.329		0.298	0.294	0.291		0.307
10					0.295		
12	0.290		0.290		0.306		
14					0.315	0.339	0.386
16	0.285	0.286	0.297	0.306	0.321	0.348	0.398
24	0.285	0.288	0.304		0.334		0.420
32	0.285	0.289	0.339				
48	0.285						
IDEAL LENS	0.285				0.285		

Table 4.5 Highest Side Lobe Level for 2.0λ Diameter Equivalent  
Circuit Lens (Cardioid Radiators)

NN	72	68	64	60	56	52	48	44	40
NELR									
12				0.532			0.384		
14				0.338	0.312		0.356		
16	0.305	0.291	0.277	0.262	0.248 / 0.260	0.243 / 0.301	0.267 / 0.355	0.398 / 0.436	0.74 / 0.597
18			0.245	0.241	0.244 / 0.263	0.264 / 0.299			
20	0.242				0.260 / 0.263				
24	0.238	0.243	0.252	0.268	0.303		0.476 / 0.349	0.675 / 0.453	Bifurcated
28	0.245			0.29			0.527 / 0.351		
32	0.254		0.283	0.314	0.360 / 0.258	0.436 / 0.297	0.561 / 0.357	0.778 / 0.474	Bifurcated main beam
48				0.353			0.624 / 0.364		
64							0.646 / 0.367		
IDEAL LENS			0.233				0.234		

Table 4.6 Highest Side Lobe Level for 4.0λ Diameter Equivalent Circuit Lens

(Cardioid Radiators)



NN	108	104	100	98	96	92	88	84	78	72	66
NELR											
20					0.534	0.503	0.465			0.62	
22										0.596	
24		0.331			0.295 0.299	0.334	0.354	0.392	0.474	0.584	
26	0.287 0.241	0.225 0.259					0.354			0.582	0.776
28	0.250	0.241 0.259	0.231 0.277		0.222 0.297						
30	0.229 0.244	0.225 0.259			0.255 0.286					0.603	
32	0.226 0.243	0.224 0.258		0.230 0.283	0.236 0.292	0.258 0.313	0.341				
34				0.245 0.281							
36				0.263 0.280						0.642	
40											
48					0.370 0.283						
IDEAL LENS					0.220					0.220	

Table 4.7 Highest Side Lobe Levels for 6.0λ Diameter Equivalent Circuit Lens  
(Cardioid Radiators)

lobes level tend towards the value obtained using the ideal lens.

We see that the equivalent circuit does not work properly if one of the parameters,  $N$  or  $NELR$  is too small even though the other parameter is large.

Typical combined optimum values for  $N$  and  $NELR$  are given below:-

For a  $2.0\lambda$  lens,  $N = 24$  and  $NELR = 8$  gives a side lobe level of 0.291 compared with the ideal lens value of 0.285.

For a  $4.0\lambda$  lens,  $N = 60$  and  $NELR = 18$  gives a side lobe of 0.241 compared with the ideal lens value of 0.233.

With a  $6.0\lambda$  lens  $N = 108$  and  $NELR = 28$  produces a side lobe level of 0.25. The corresponding side lobe level for an ideal lens is 0.220.

The radiation patterns for the examples quoted are given in fig. 4.16 and 4.19 for the  $2.0\lambda$  and  $4.0\lambda$  lenses. The radiation patterns obtained using the  $6.0\lambda$  lens circuit is shown in fig. 4.15 for 9.0, 7.5, 6.0 and 3.0 MHz (corresponding to  $6.0\lambda$ ,  $5.0\lambda$ ,  $4.0\lambda$  and  $2.0\lambda$  diameters).

It is evident that the relative value of the phase of the mode reflection coefficient is more important than each individual value. In fig. 4.13 and 4.14 the relative phases of the mode reflection coefficients are plotted against the mode number,  $m$ , for different values of  $N$  and  $NELR$ . The phases have been normalised to the zero order value. The corresponding curve for the ideal lens is also shown.

We see that if the normalised phase of mode reflection coefficient deviates from the ideal lens value by greater than approximately  $50^\circ$  we get high side lobes appearing in the radiation pattern. In the

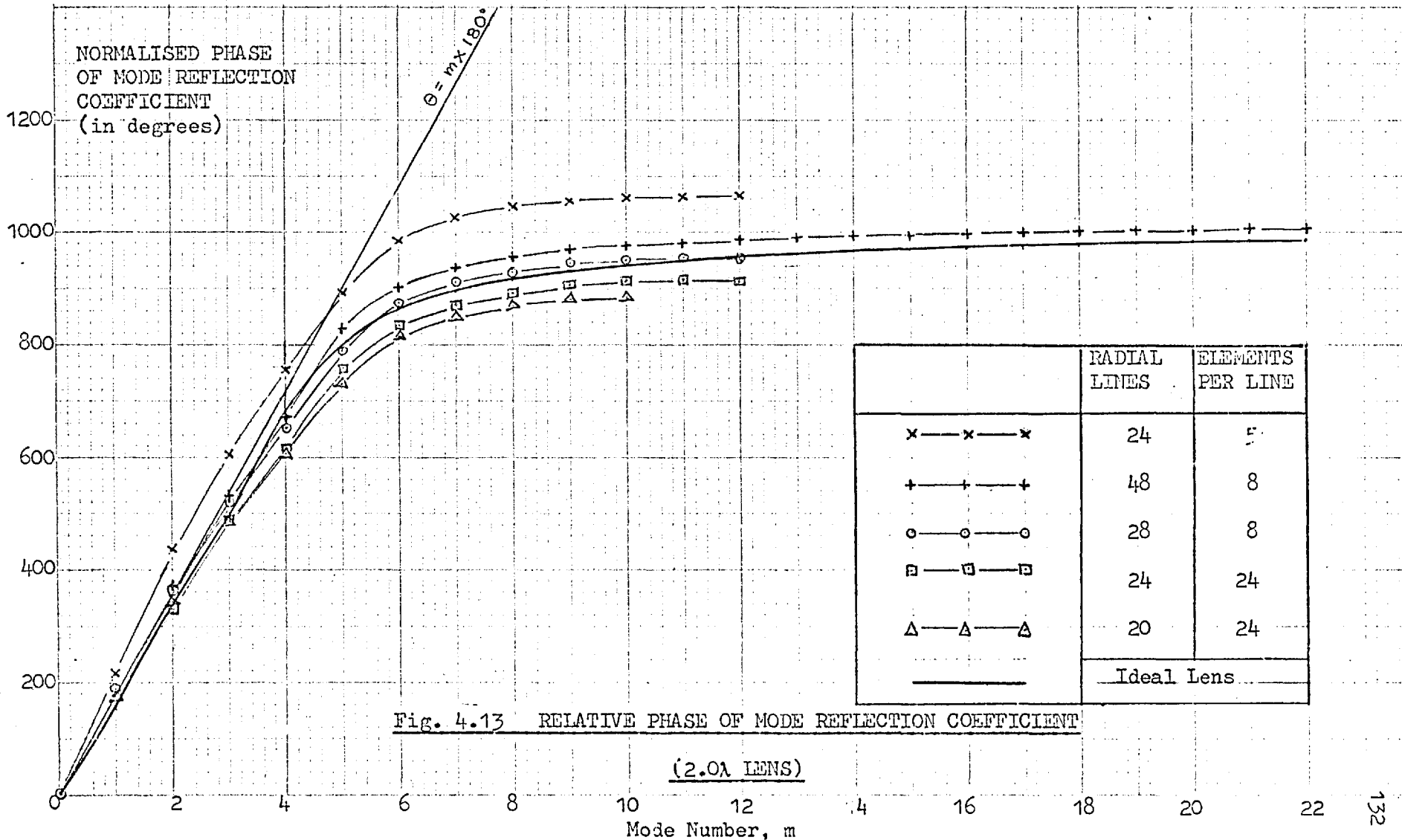


Fig. 4.13 RELATIVE PHASE OF MODE REFLECTION COEFFICIENT

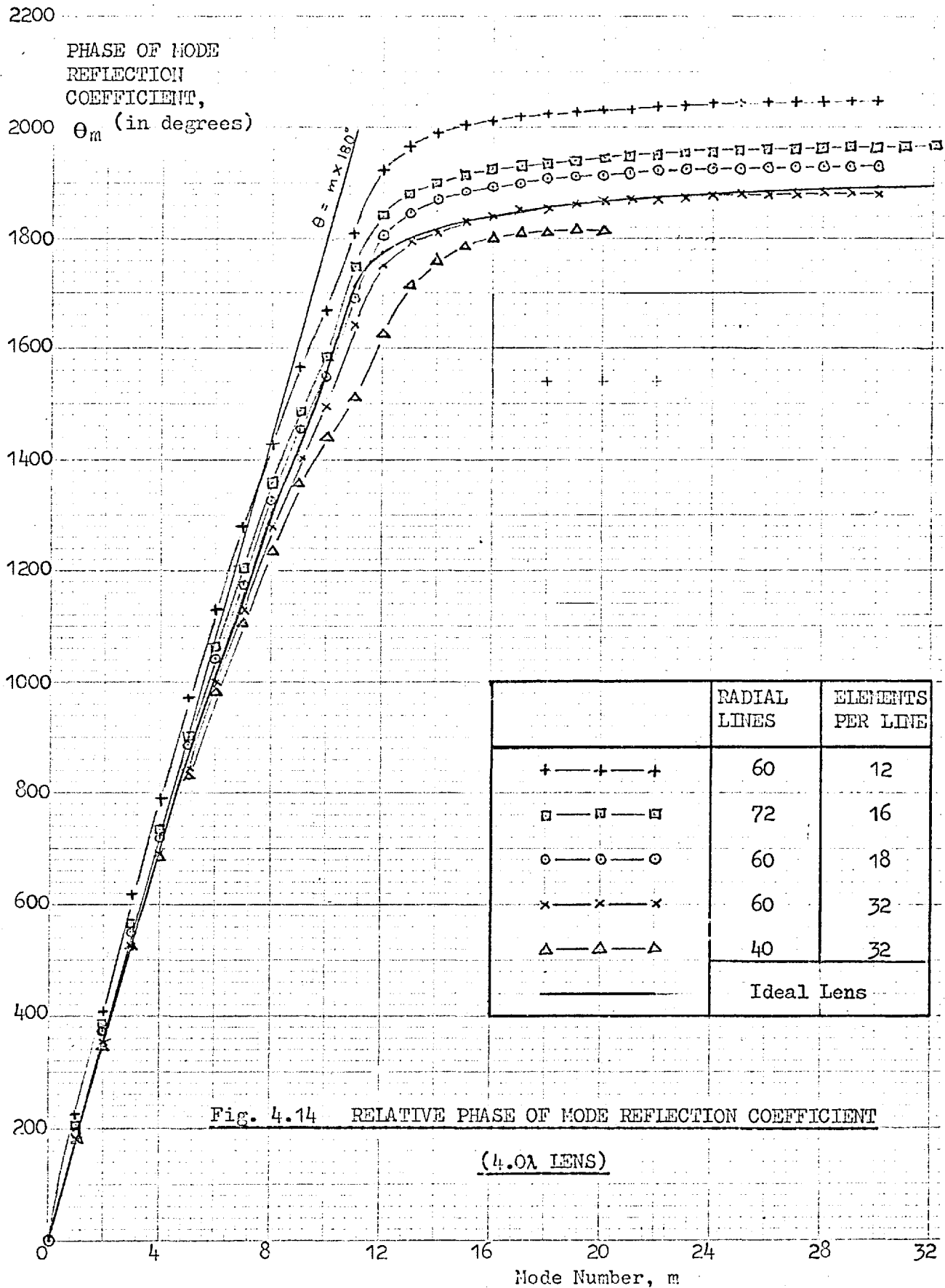


Fig. 4.14 RELATIVE PHASE OF MODE REFLECTION COEFFICIENT

(4.0λ LENS)

equivalent lens with  $N = 20$ ,  $NELR = 24$ , the maximum deviation from the ideal lens value occurs for mode 6. The deterioration in the radiation pattern will be worst if the large deviation occurs for modes which have high far-field mode amplitudes (fig. 3.13) in chapter 3). On the other hand, if the far-field mode amplitude is negligible large phase deviation from the ideal lens figure is unimportant since the particular mode does not contribute significantly to the far-field.

In general if  $NELR$  is large, the relative phases of the mode reflection coefficients for the low modes closely follow the behaviour of the ideal lens. However, for the higher modes, the phases tend to be lower than the ideal lens value, e.g.  $N = 20$ ,  $NELR = 24$  for the  $2.0\lambda$  lens and  $N = 40$ ,  $NELR = 32$  for the  $4.0\lambda$  lens. As  $N$  increases the equivalent lens behaviour approaches that of the ideal lens. On the other hand, if  $NELR$  is small (less than about six elements per wavelength of radial line), the relative phase values for the mode reflection coefficient tend to be higher than the ideal lens value, e.g. for  $N = 24$  and  $NELR = 5$  for the  $2.0\lambda$  lens in fig. 4.13 and for  $N = 60$  and  $NELR = 12$  for the  $4.0\lambda$  lens in fig. 4.14. But as  $NELR$  increases the phase behaviour of the equivalent lens approaches that of the ideal lens.

These results seem to suggest that a minimum value for  $N$  of 24 in a  $2.0\lambda$  lens, 60 in a  $4.0\lambda$  lens and 108 in a  $6.0\lambda$  lens. The spacings between feeds at the circumference are for the three lenses respectively  $0.262\lambda$ ,  $0.21\lambda$  and  $0.174\lambda$ . The corresponding values for

NELR, for the three lenses are 8, 18 and 28 respectively, equivalent to about 9 elements per wavelength of radial line.

The behaviour of a 200.0 metre lens with  $N = 108$  and  $NELR = 28$  is shown in fig. 4.15 for 3.0, 6.0, 7.5 and 9.0 MHz, (i.e. lens diameters of  $2.0\lambda$ ,  $4.0\lambda$ ,  $5.0\lambda$  and  $6.0\lambda$  respectively). The radiation pattern obtained for the lower frequencies is practically the same as that obtainable using the ideal lens.

#### 4.3.4 The Effect of Losses in the Equivalent Circuit due to Losses in the Inductors

All inductors used in the equivalent circuit are assumed to have the same  $Q$  value. The effect of finite  $Q$  values for the inductors is not significant as far as the radiation patterns are concerned. This can be seen from the radiation patterns in fig. 4.16 and 4.17 where patterns using circuits with  $Q = \infty$ , 200, 100 and 50 are used.

The effect of finite  $Q$  for the circuit is a decrease in the amplitude of the mode phase reflection coefficient. In a lossless circuit the amplitudes of the reflection coefficients are all unity. With  $Q = 200$ , the amplitude of the reflection coefficient could fall to about 0.9 for a  $4.0\lambda$  diameter lens ( $N = 60$ ,  $NELR = 18$ ). For  $Q = 100$  the mode amplitude fall to approximately 0.85. At  $Q = 50$  the figure is approximately 0.7. However, the phases of the mode reflection coefficients are quite independent of  $Q$  values, explaining the practically unchanged radiation patterns for different values for  $Q$ .

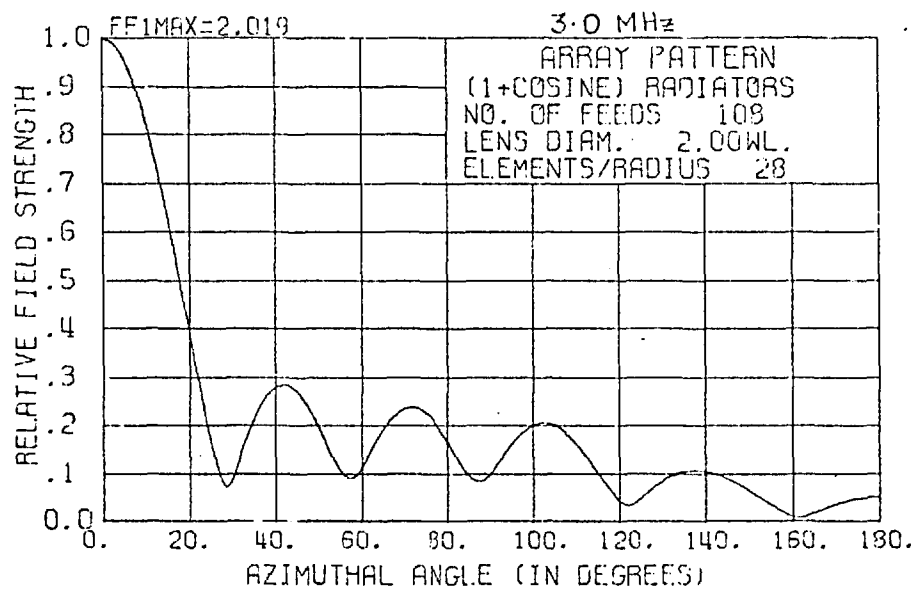
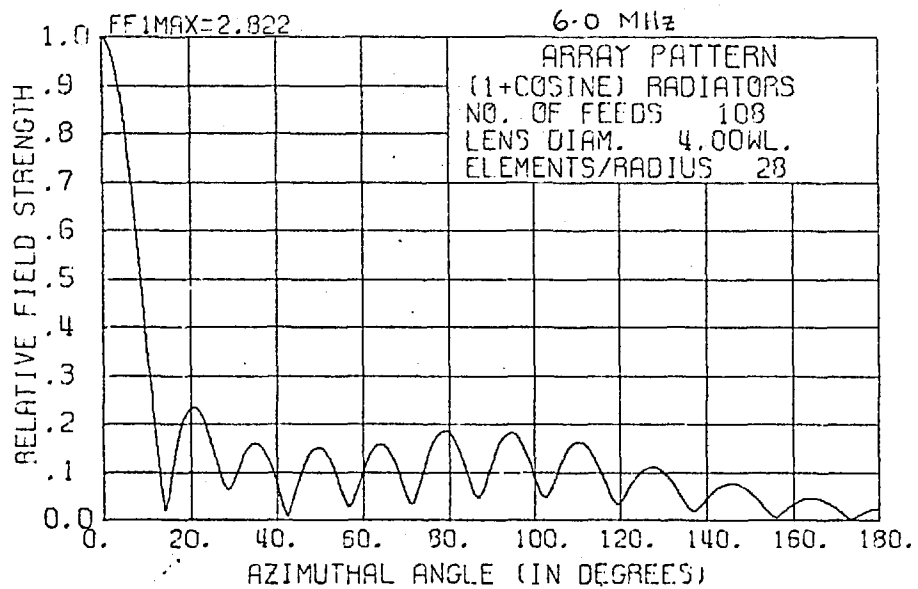
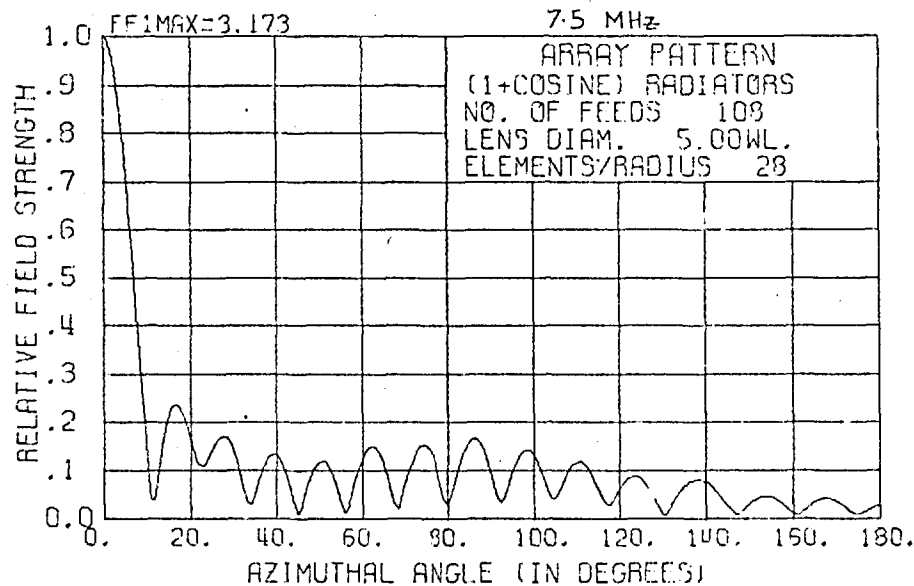
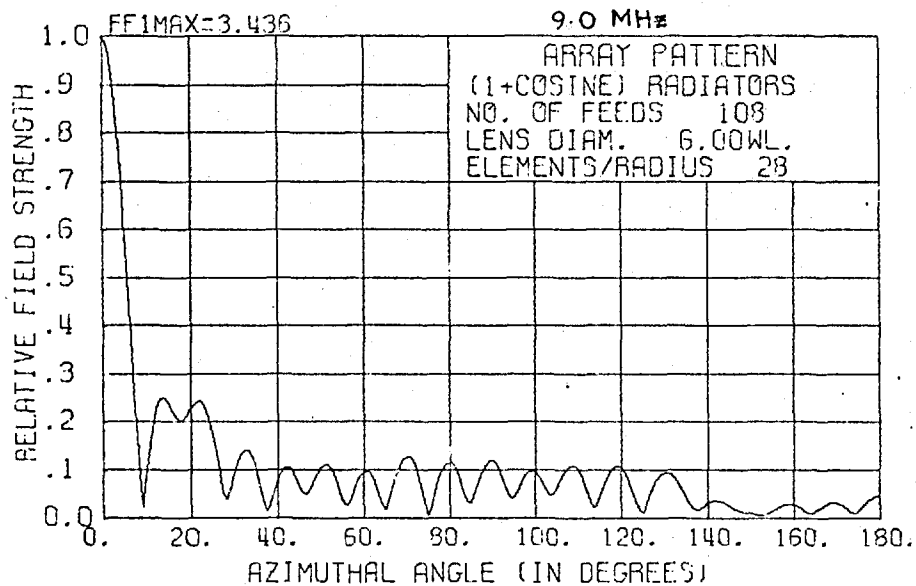


Fig. 4.15

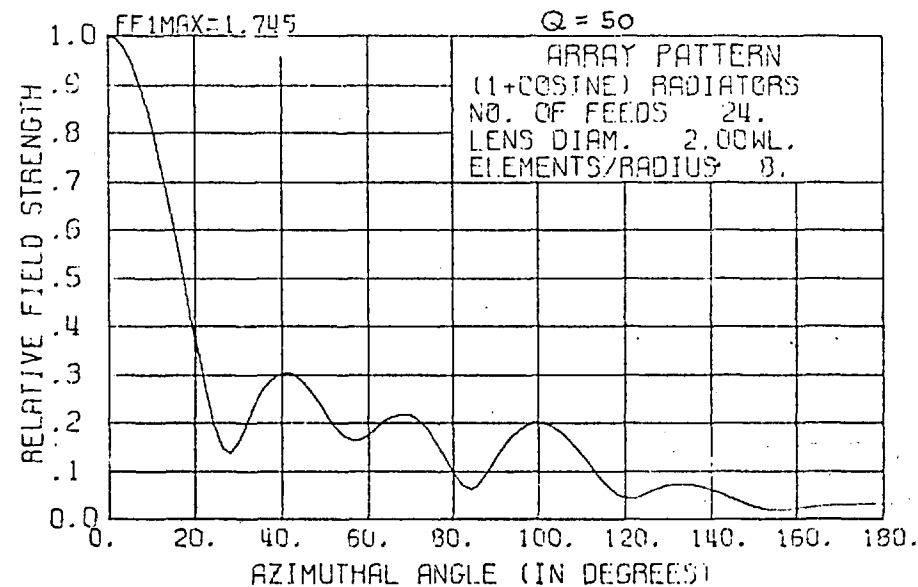
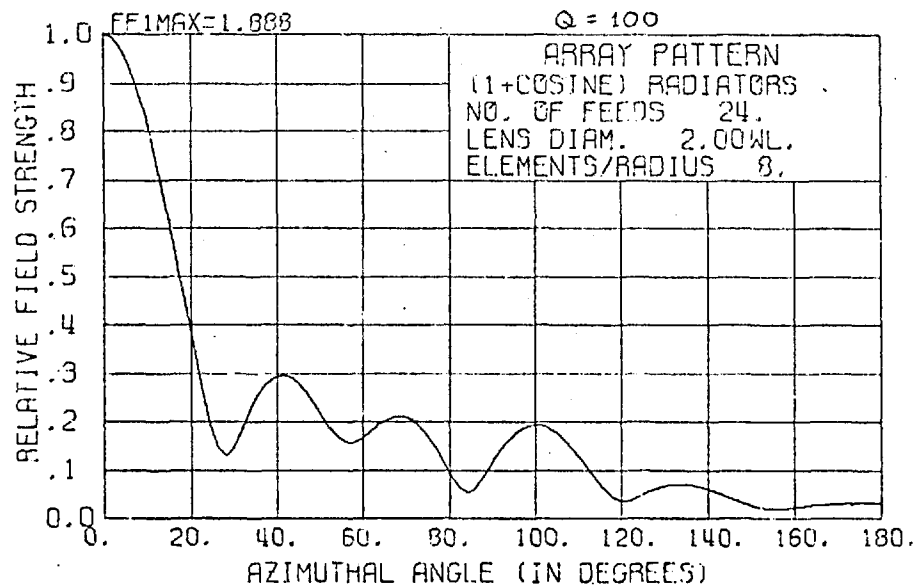
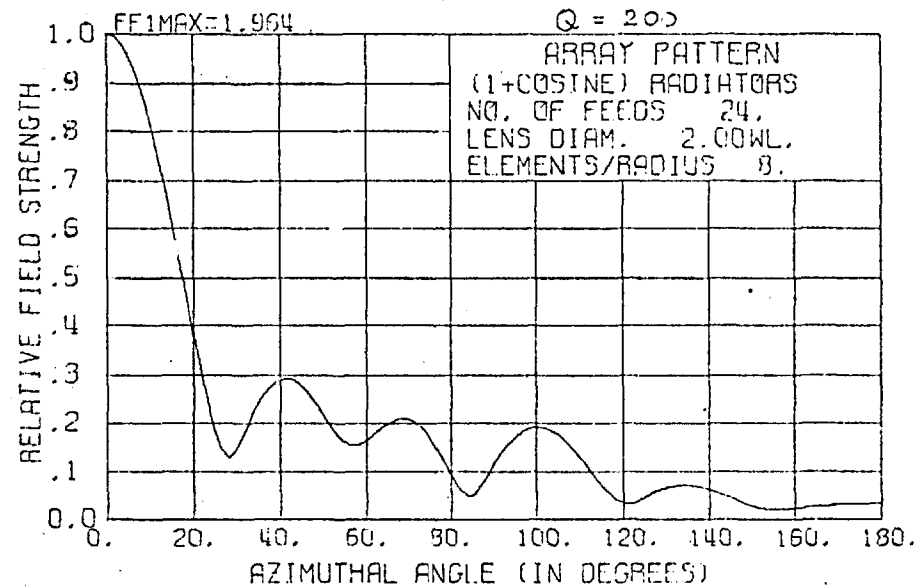
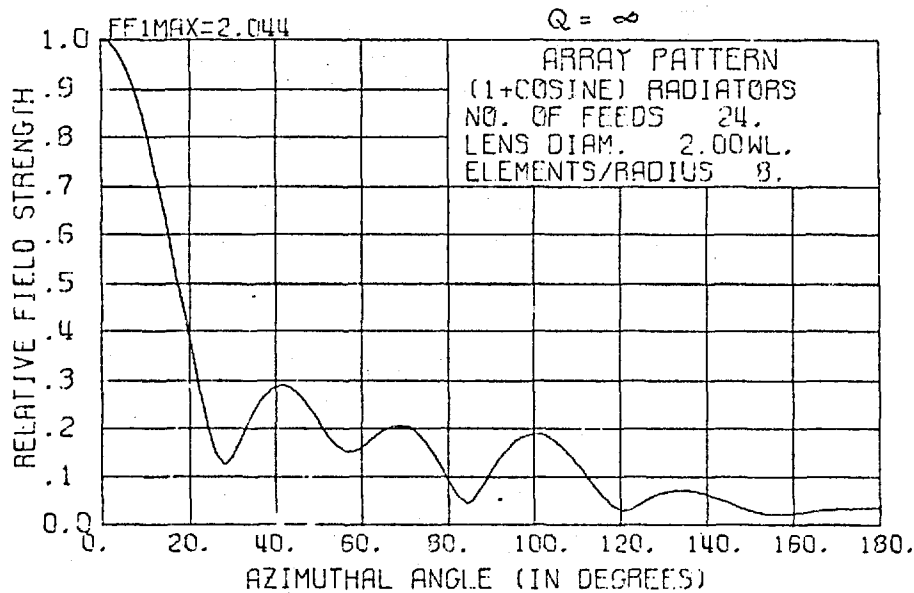


Fig. 4.16 EFFECT OF LOSSES



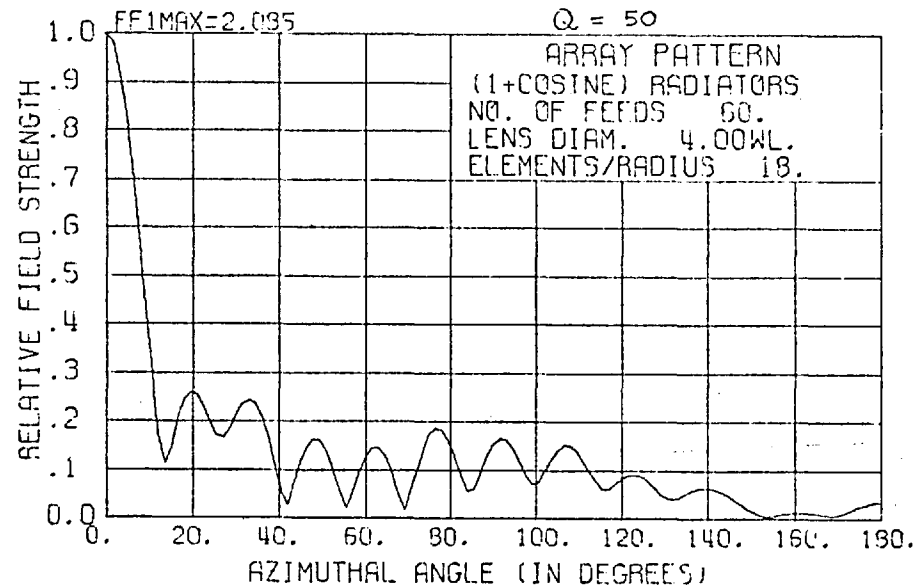
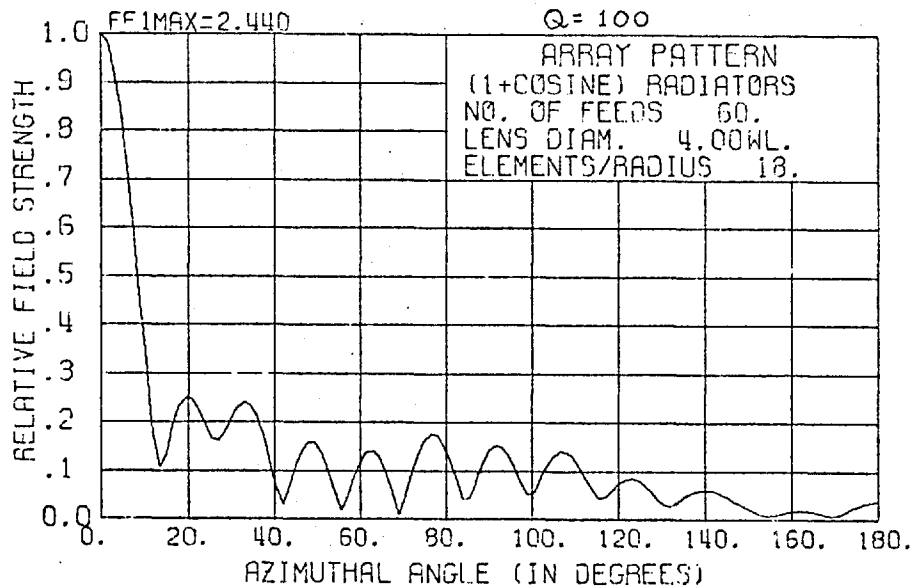
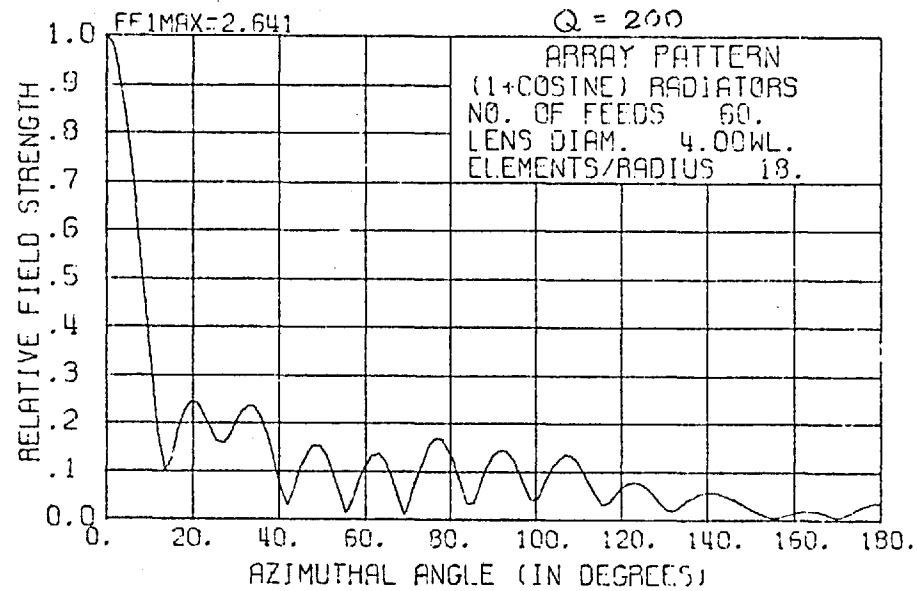
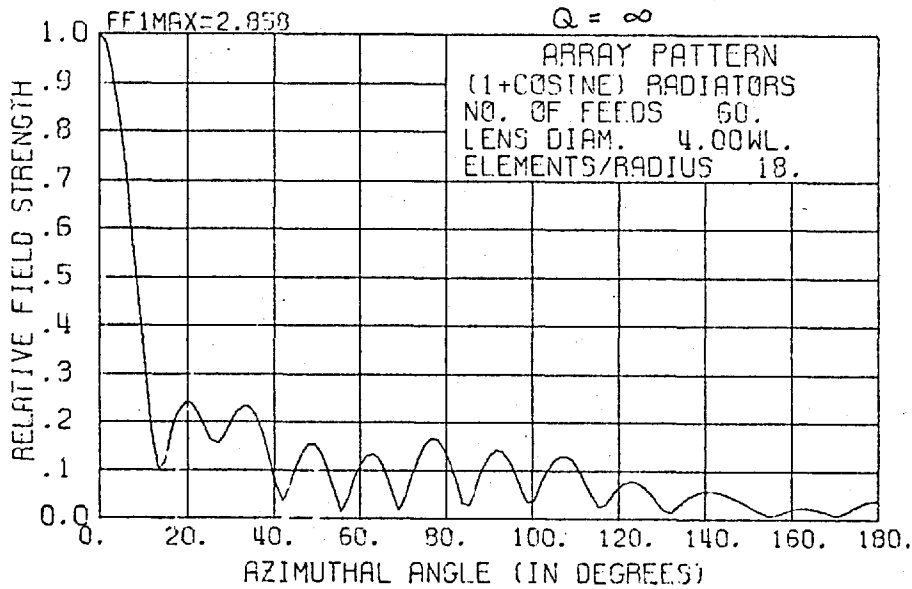


Fig. 4.17 EFFECT OF LOSSES

The result of the lower value for the amplitude reflection coefficients is a loss in gain for the array. This is discussed in the following paragraphs.

The far-field in the maximum direction is calculated using equivalent circuits of varying  $Q$  values and varying values of  $N$  and  $NELR$ .

We find that losses due to finite  $Q$  values are independent of the value of  $N$  or  $NELR$ . The results are summarised in tables 4.8(a) to 4.8(d). The losses are also independent of the physical size of the lens but are proportional to the size of the lens in wavelength. For  $Q = 100$ , for example, the losses are  $-0.69\text{db}$ ,  $-1.35\text{db}$  and  $-2.0\text{db}$  for a  $2.0\lambda$ ,  $4.0\lambda$  and  $6.0\lambda$  diameter lens, respectively. The losses in db are also roughly inversely proportional to the  $Q$  value. For the  $6.0\lambda$  diameter lens for example the losses for  $Q = 200$ ,  $100$  and  $50$  are  $-1.04\text{db}$ ,  $-2.0\text{db}$  and  $-4.0\text{db}$  respectively.

Since the loss in an equivalent circuit lens is proportional to the frequency of operation, the effect of losses is not expected to be serious, since the gain of the array increases with frequency.

#### 4.4

In section 4.3 we assume that at the circumference of the lens each radial line corresponds to a feed. Further, we assume that each feed is connected to a radiator. A maximum spacing of between  $0.175\lambda$  and  $0.25\lambda$  at the circumference between radial lines has been suggested.

Table 4.8(a) 2.0λ LENS 24 RADIAL LINES

No. of elements per radius	FARFIELD IN MAXIMUM DIRECTION FOR Q =			
		200	100	50
8	2.044(0db)	1.964(0.34db)	1.888(0.69db)	1.745(1.37db)
16	1.972(0db)	1.899(0.33db)	1.822(0.69db)	1.695(1.36db)
24	1.954(0db)	1.881(0.33db)	1.812(0.66db)	1.681(1.37db)

Table 4.8(b) 4.0λ LENS 60 RADIAL LINES

No. of elements per radius	FARFIELD IN MAXIMUM DIRECTION FOR Q =			
		200	100	50
18	2.858(0.0db)	2.641(0.68db)	2.440(1.37db)	2.085(2.74db)
24	2.794(0.0db)	2.585(0.68db)	2.391(1.35db)	2.048(2.70db)
32	2.728(0.0db)	2.525(0.68db)	2.337(1.34db)	2.004(2.68db)

Table 4.8(c) 2.0λ LENS 16 ELEMENTS PER RADIUS

No. of radial lines	FARFIELD IN MAXIMUM DIRECTION FOR Q =			
		200	100	50
24	1.972(0db)	1.889(0.33db)	1.822(0.69db)	1.695(1.36db)
36	2.025(0db)	1.953(0.32db)	1.883(0.63db)	1.751(1.26db)
48	2.028(0db)	1.956(0.31db)	1.887(0.63db)	1.757(1.24db)

Table 4.8(d) 4.0λ LENS 24 ELEMENTS PER RADIUS

No. of radial lines	FARFIELD IN MAXIMUM DIRECTION FOR Q =			
		200	100	50
52	2.627(0.0db)	2.427(0.69db)	2.243(1.37db)	1.916(2.74db)
60	2.794(0.0db)	2.585(0.68db)	2.391(1.35db)	2.048(2.70db)
72	2.845(0.0db)	2.637(0.66db)	2.444(1.32db)	2.100(2.63db)

This condition is rather restricting. It has already been shown in chapter 3 that if feed spacing is small outputs from feeds adjacent to the input port is large. Also a tapering in the output distribution is desirable to reduce beamwidth at the high frequency end of the scale. A tapered output can only be achieved if spacing between feeds is greater than  $\lambda/2$ .

It is therefore desirable to reduce the number of feed by half or a third. One solution was briefly studied. Only every second, third or kth feed is connected to a radiator. The other feeds are left open-circuited. This is equivalent to a reduction in the number of modes used.

#### 4.4.1 Reduction of Mode

If only one out of every k radiator is fed to a radiator while the other feeds are left open-circuited the number of modes used will be reduced by k. The equivalent circuit lens has been analysed using as many modes as there are radial lines. If every feed except the kth are left open-circuited the impedance of each mode and therefore the reflection coefficient has to be recalculated. This is done in Appendix A4.2.

The impedance of the Mth mode (new) is given by:-

$$\mathcal{Z}'_M = \frac{1}{k} \sum_{s=0}^{k-1} \mathcal{Z}_{M+(N.s)/k} \quad (4.20)$$

where  $\mathcal{Z}'_M$  - impedance for the new mode, M

$\mathcal{Z}_r$  - impedance for the old mode, r

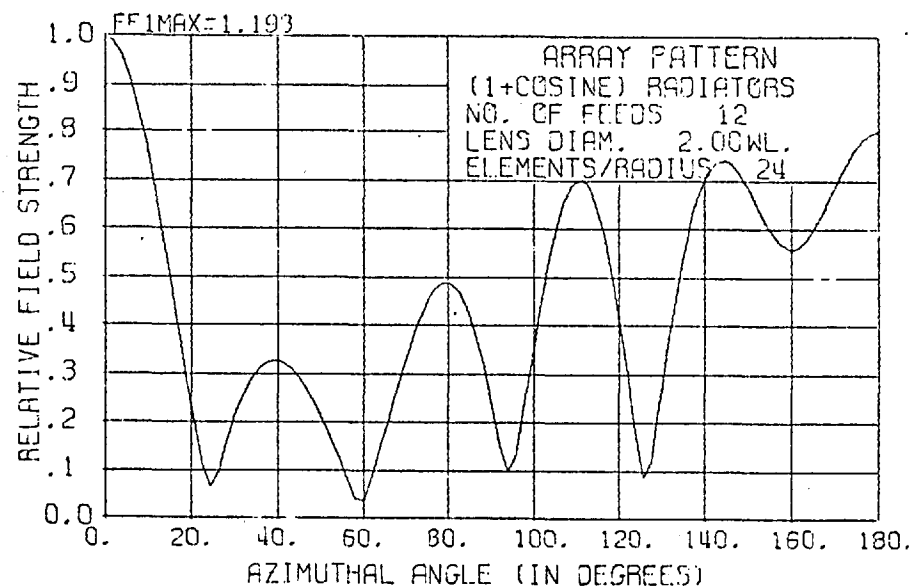
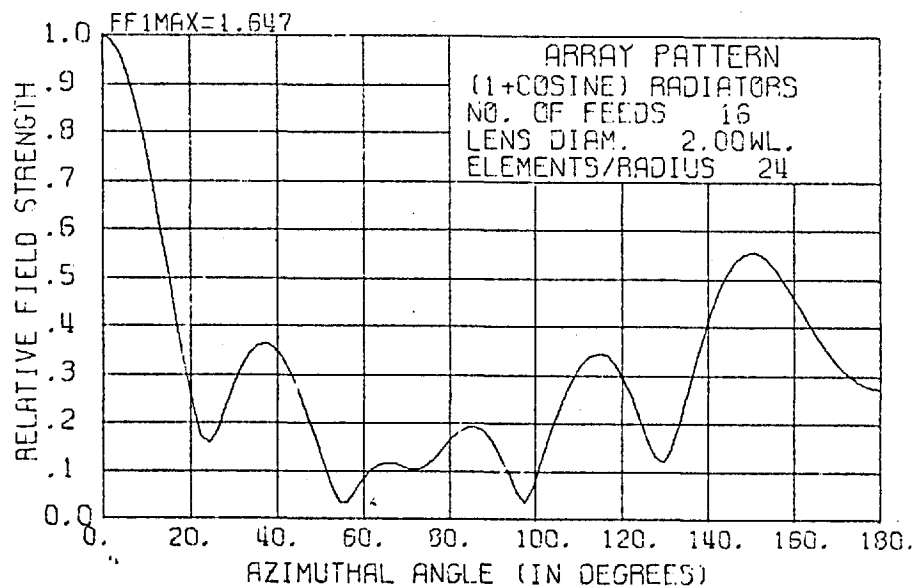
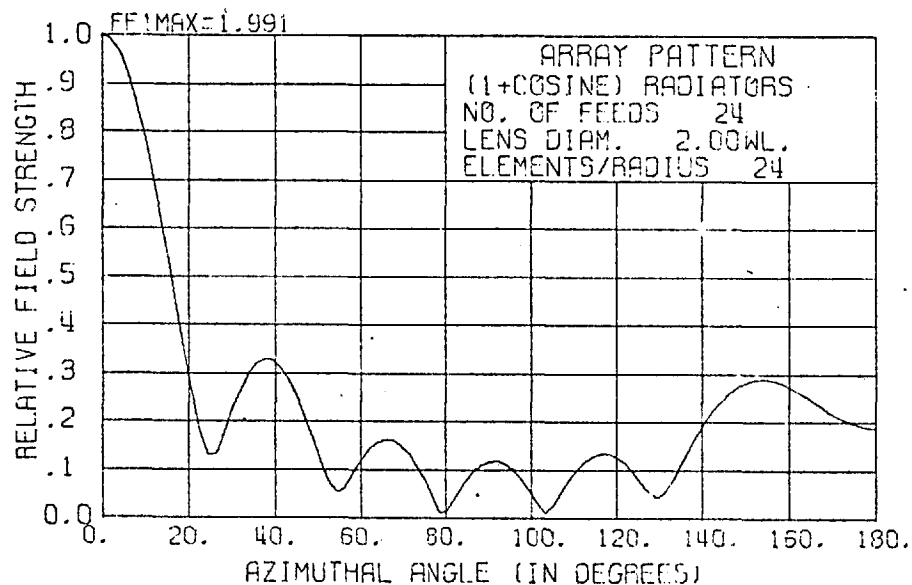
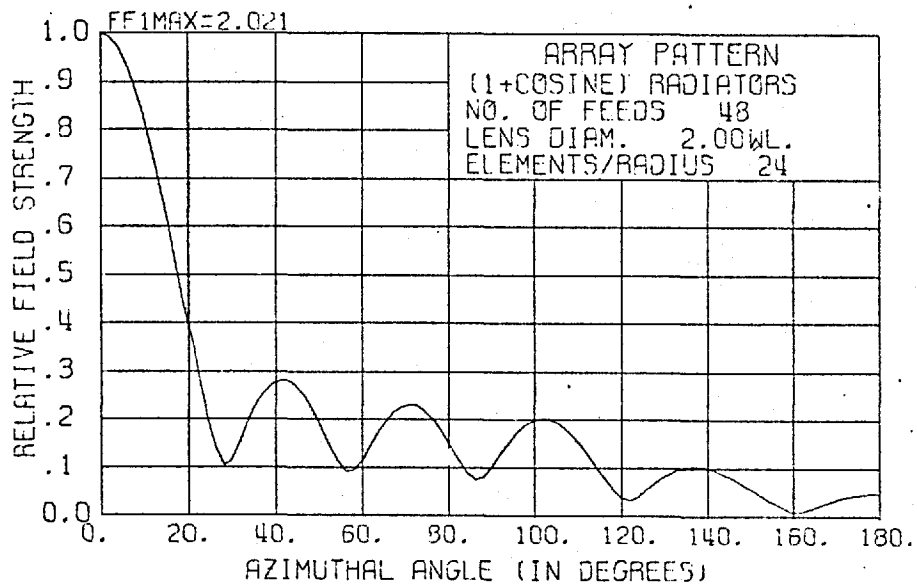


Fig. 4.18 EFFECT OF MODE REDUCTION

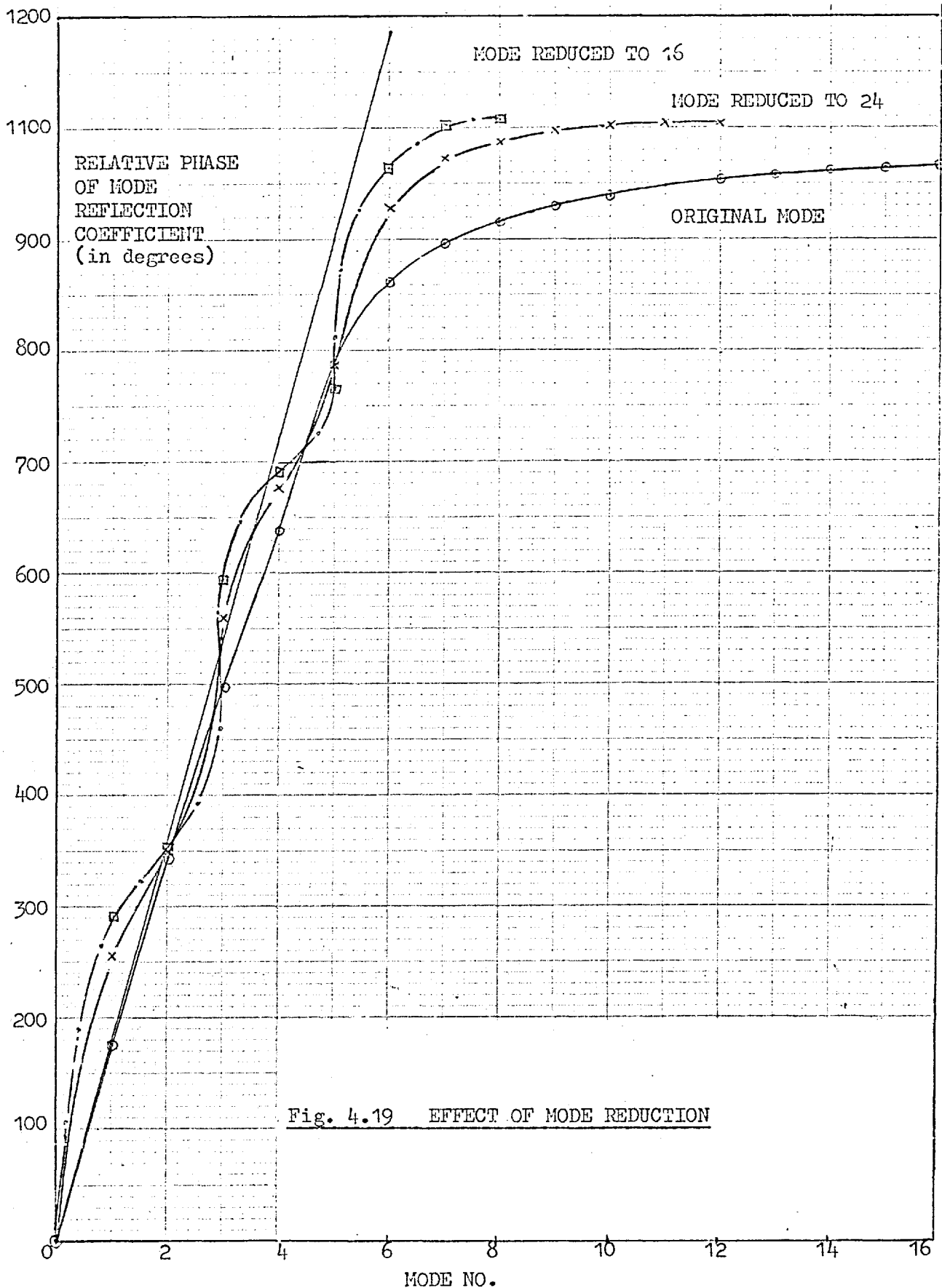


Fig. 4.19 EFFECT OF MODE REDUCTION

The new reflection coefficient  $\rho_m'$  is calculated accordingly. This is done by the subroutine RMODE described in Appendix 4.1.

Fig. 4.18 shows the radiation pattern obtained for the equivalent circuits with modes reduced by 2, 3 and 4. The values of N and NEIR used are 48 and 24 respectively. The effect of reducing the modes is an increase in the back lobe of the radiation pattern.

The relative phase of the new and old mode reflection coefficients are shown in fig. 4.19. This is a fairly large oscillation of the relative phase values about those of the original mode values.

Because of the undesirable high side lobe levels obtained if some radial lines at the lens circumference are short circuited, this method of reducing the feed number is not suitable.

#### 4.4.2 Other Methods of Reducing Feed Numbers

Essentially, a matching type network is needed to combine 2 or more adjacent radial lines near the circumference to form each feed point.

A technique used by Spangenberg, Walter or Schott (22) on the solution of electromagnetic field problems using electrical analogue networks is briefly discussed. In their work the fields at some points are required more accurately than for other points. To obtain the better accuracy required for the analogue network, the number of elements used at the particular part of the network is increased. The transition between the two regions of fine and coarse meshes is shown in fig. 4.20.

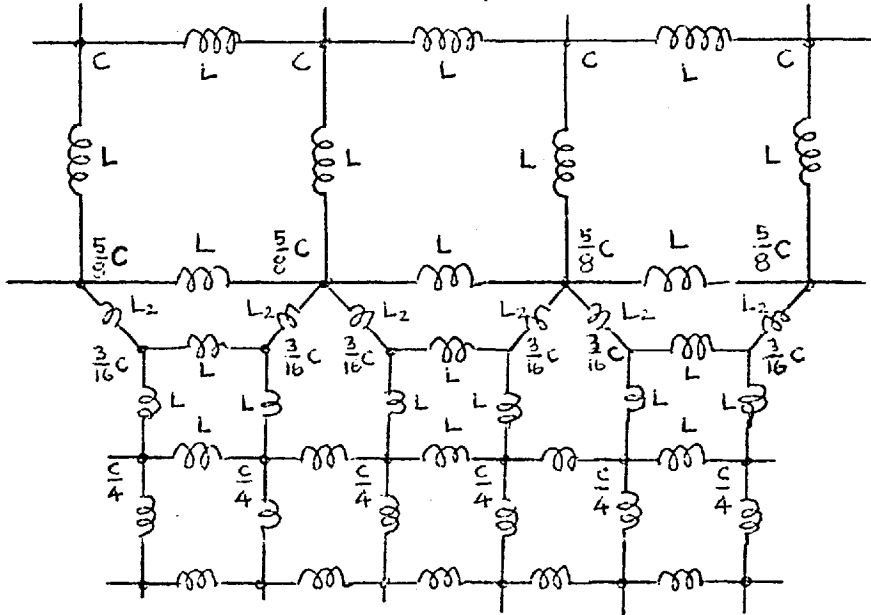


Fig. 4.20 ARRANGEMENT FOR HALVING NO. OF RADIAL LINES  
NEAR THE LENS CIRCUMFERENCE

#### 4.5 Use of the Equivalent Circuit Lens with Beverage Aerial Radiators

It was thought that an equivalent lens which was judged to be acceptable for use with cardioid radiators would be suitable for use with beverage aerial radiators. This was not the case at the higher frequencies, when the length of the beverage radiating elements in wavelength is large so that the radiators are more directive.

Compare the far-field pattern obtained using the circuit with  $N = 108$  and  $NELR = 28$  for cardioid radiator in fig. 4.15 and that obtained with beverage radiators in fig. 4.21 for operation at 9.0



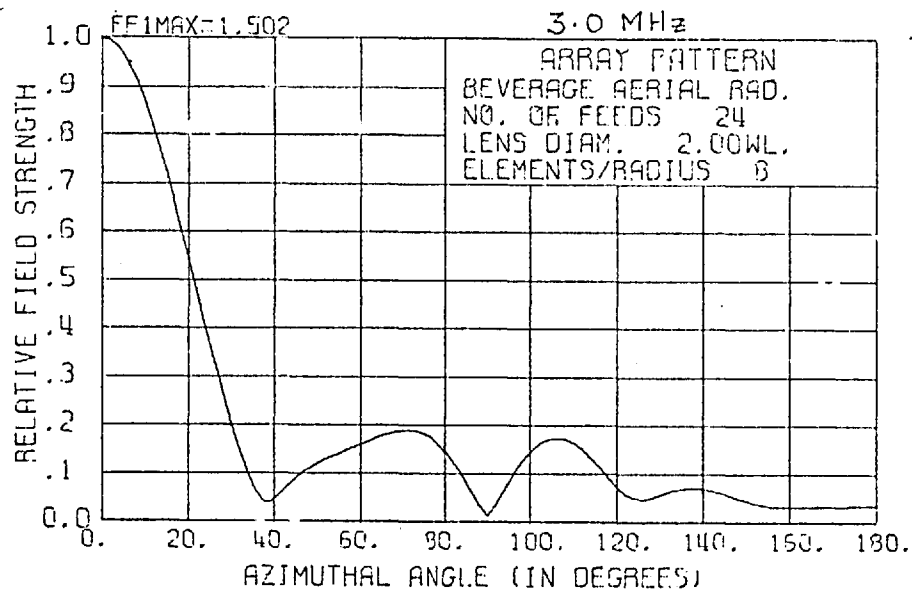
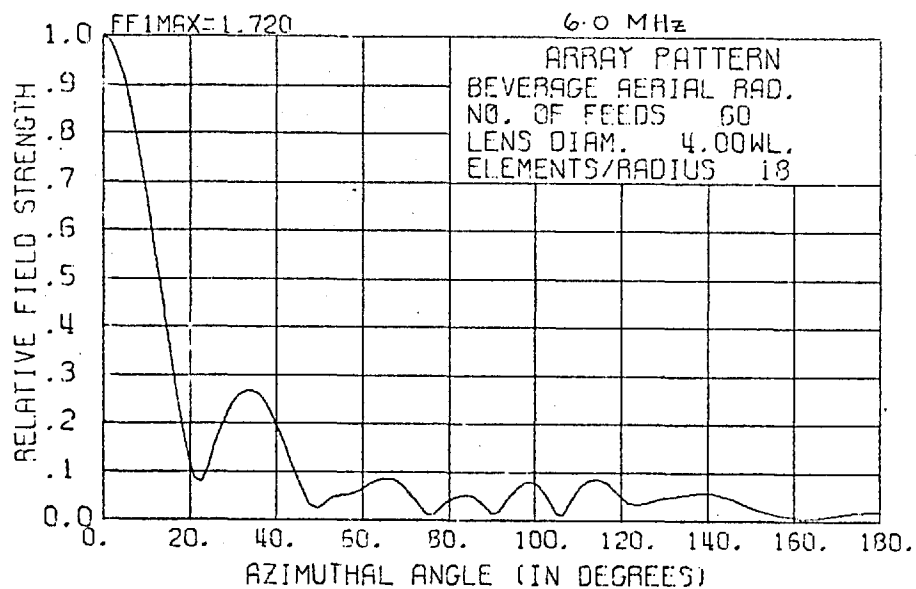
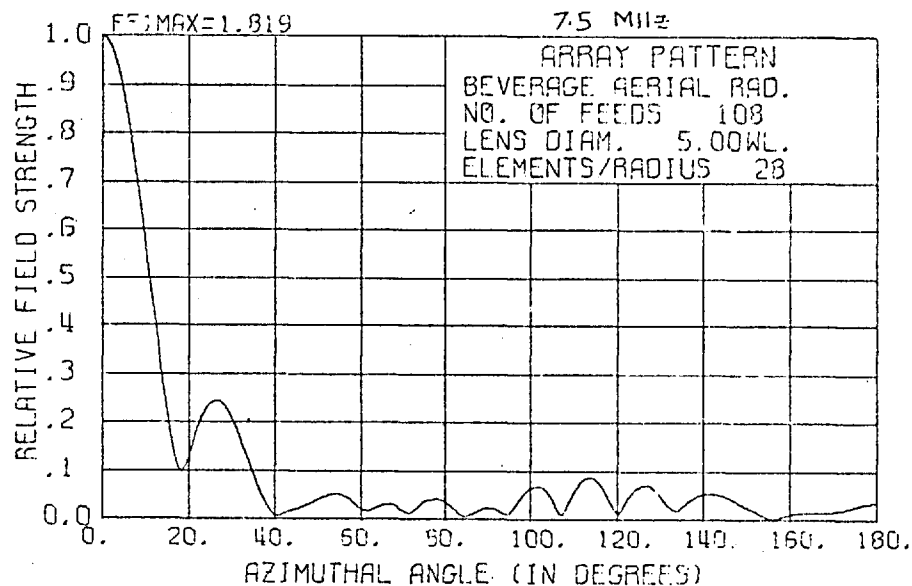
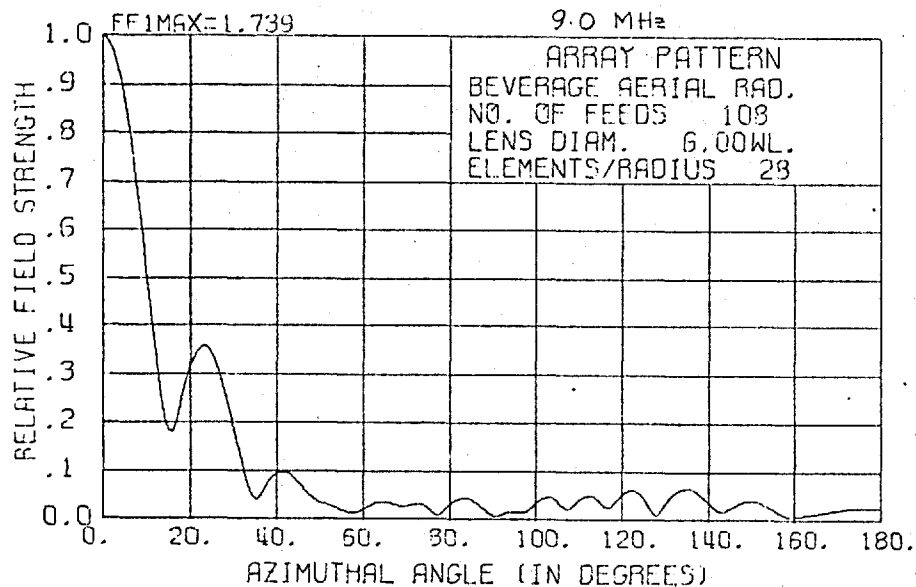


Fig. 4.21

and 7.5 MHz. The side lobe level for the beverage array is unacceptably high compared with that obtained using the ideal lens. On the other hand, with a smaller lens  $4.0\lambda$  diameter,  $N = 60$ ,  $NELR = 18$  and  $2.0\lambda$  diameter,  $N = 24$ ,  $NELR = 8$  the patterns obtained using beverage radiators is quite acceptable (fig. 4.21). However, for the  $4.0\lambda$  diameter lens the side lobe level is high compared with the level that can be achieved with an ideal lens.

We found in chapter 3 that with the use of beverage aerial elements in the lens fed array the side lobes are lower and the beamwidth, wider. This tends to suggest that the far-field mode amplitude distribution (equivalent to amplitude distribution for a linear array) is tapered; the taper is more marked if the radiator becomes more directive. If this is the case the behaviour of the lower order modes of the equivalent circuit lens becomes much more important.

We observed in section 4.3.2(a) that the behaviour of the lower order modes is mainly dependent on  $NELR$ , the number of elements used per radial line in the lens circuit. If  $NELR$  is sufficiently large the relative phases of the mode reflection coefficient approach very closely that of the ideal lens. In table 4.9 the deviation for various equivalent lenses from the relative phase of the mode reflection coefficient of the ideal lens is tabulated for a  $6.0\lambda$  lens (see also fig. 4.13 and 4.14 for  $2.0\lambda$  and  $4.0\lambda$  diameter lenses). We see that for fairly low values of  $N$ , the behaviour of the relative phases between mode reflection coefficients is similar to that of the ideal

MODE NO.	DEVIATION OF RELATIVE PHASE FROM IDEAL LENS VALUE FOR THE FOLLOWING N/NELR VALUES					
	108/28	60/48	48/48	48/36	60/36	72/36
0	0.0	0.0	0.0	0.0	0.0	0.0
1	4.5	1.5	2.4	3.2	3.3	3.3
2	21.2	6.0	5.6	10.6	11.4	11.2
3	24.7	7.5	5.7	13.9	12.0	10.5
4	37.9	6.9	4.7	21.4	17.6	19.1
5	40.4	7.5	-0.1	4.1	16.1	19.0
6	50.2	5.2	-7.5	-3.7	15.7	20.7
7	49.5	1.5	-20.4	-23.8	8.2	16.0
8	58.0	-6.2	-31.5	-37.9	5.1	15.8
9	51.0	-33.3	-64.2	-82.6	-15.8	1.1
10	60.5	-33.4	-68.8	-97.0	-14.0	4.9
11	46.4	-71.4	-116.1	-147.6	-50.4	-23.7
12	53.2	-86.6	-158.0	-213.7	-54.3	-25.2
13	51.4	-82.8	-154.5	-241.7	-60.7	-27.1
14	17.4	-170.0	-243.5	-329.6	-147.9	-99.9
15	51.1	-168.3	-286.0	-372.0	-145.8	-63.2
16	31.5	-146.0	-312.5	-425.5	-92.9	-64.0
17	-41.8	-271.5	-420.5	-588.4	-247.5	-195.7
18	48.5	-282.6	-415.8	-632.8	-264.3	-168.9
19	71.4	-252.2	-398.2	-645.9	-227.8	-51.2
20	77.9	-160.5	-386.7	-657.5	-136.5	-5.8
21	80.4	-87.1	-379.7	-	-62.8	9.0
22	81.7	-57.7	-376.1	-	-33.2	15.4

Table 4.9    Relative Phase Behaviour of Equivalent  
Circuit Lenses (6.0λ Diameter Lens)

2.0λ

NN	48	36	24	20	16
NELR					
12	0.176	0.174	0.177	0.215	0.312
14			0.175		
16	0.173	0.171	0.173	0.213	0.311
24	0.120	0.169	0.171	0.210	0.311

4.0λ

NN	72	60	48	44	40	36
NELR						
24	0.195	0.215	0.242	0.246	0.258	0.266
28	0.179	0.200	0.231	0.235	0.250	0.260
32	0.170	0.192	0.225	0.232	0.246	0.258

6.0λ

NN	96	72	60	54	48	40
NELR						
32	0.299	0.304	0.258	0.295	0.263	
36	0.266	0.280	0.240	0.281	0.248	0.288
48	0.225	0.250	0.223	0.266	0.239	

Table 4.10 Side Lobe Levels for Array of Beverage Aerials

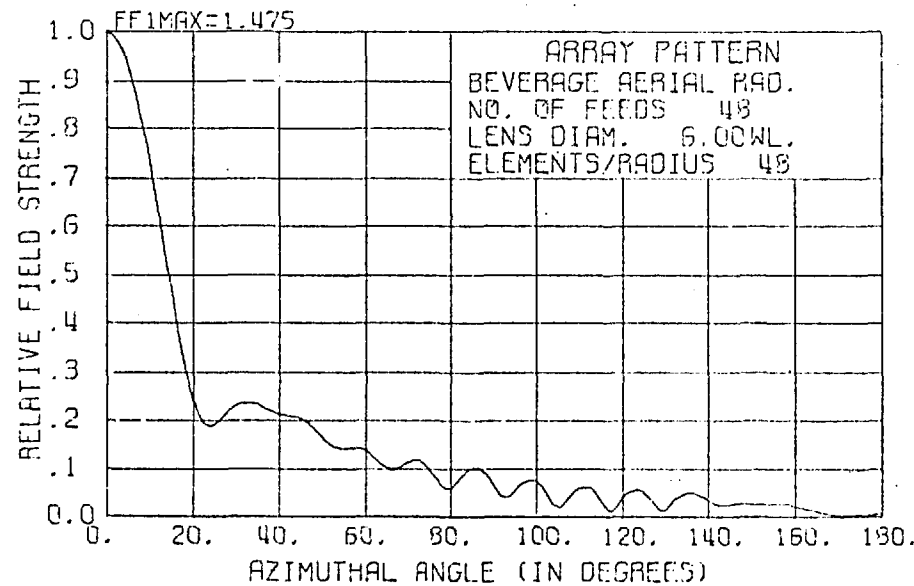
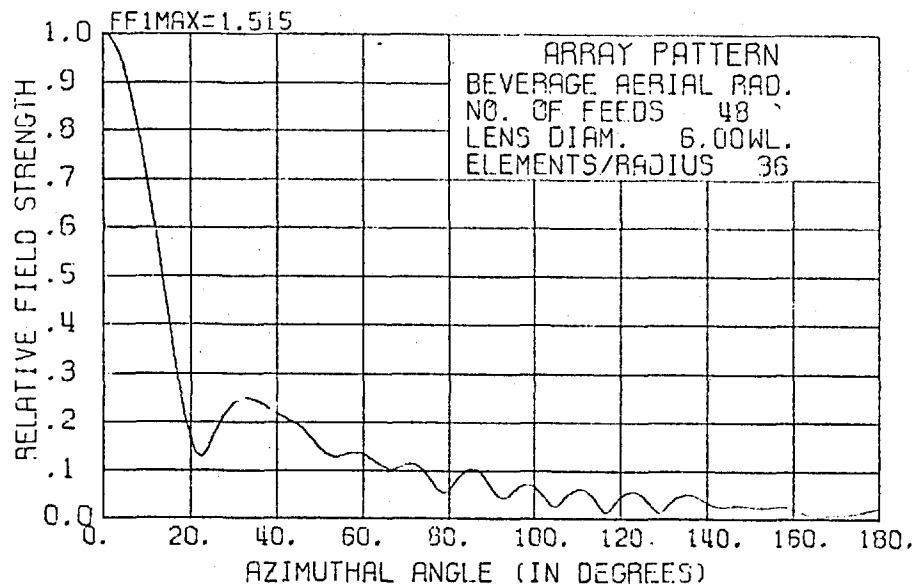
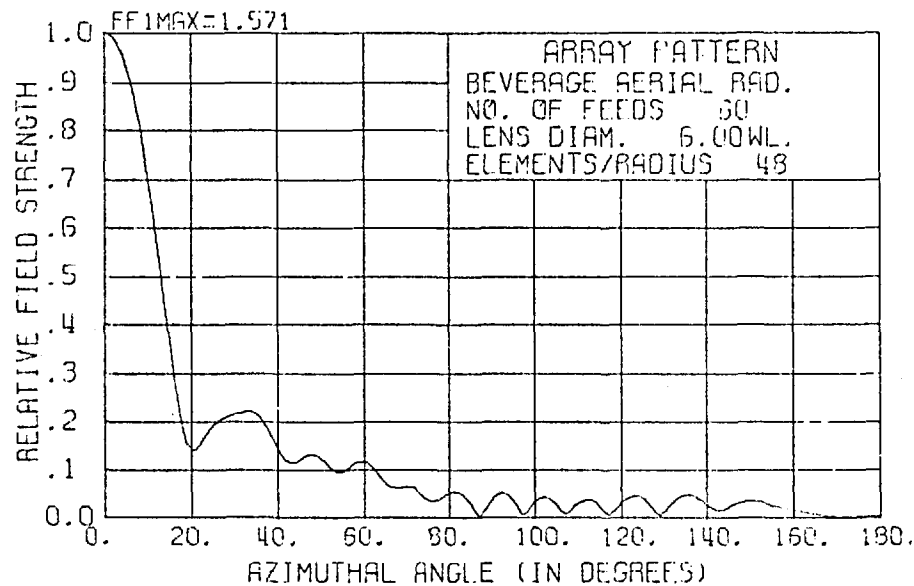
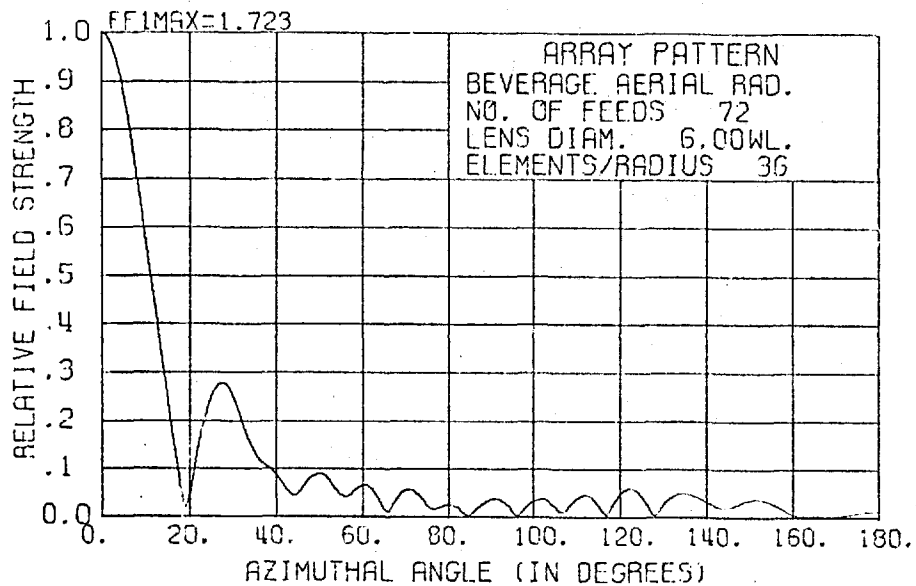


Fig. 4.22

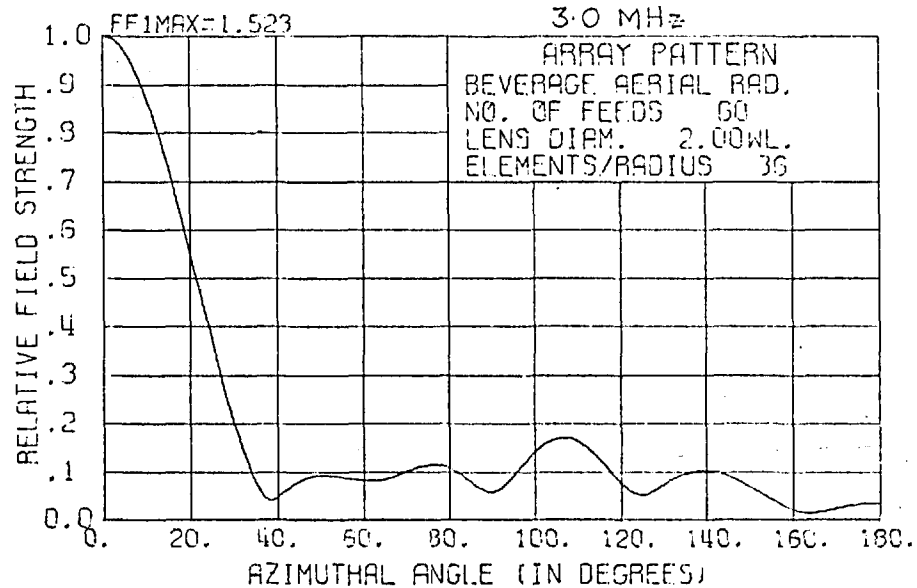
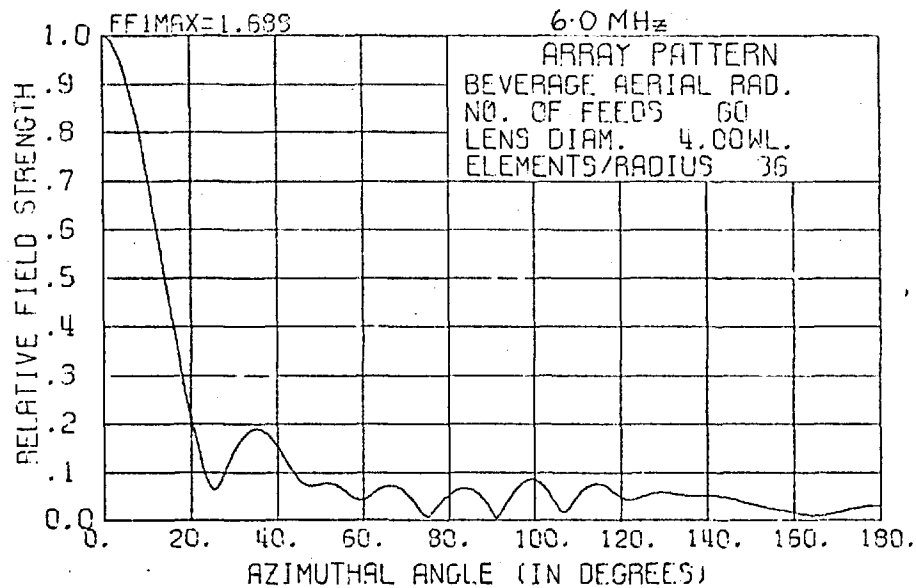
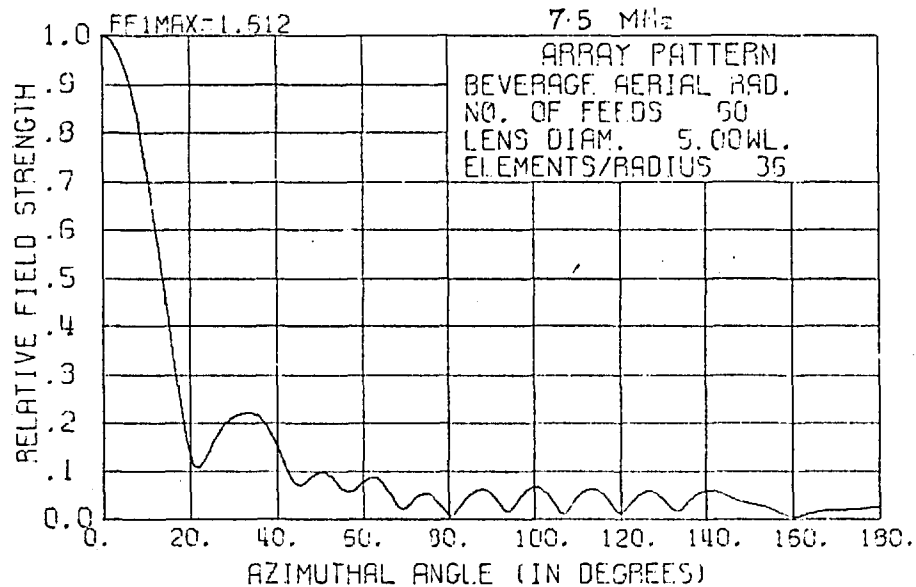
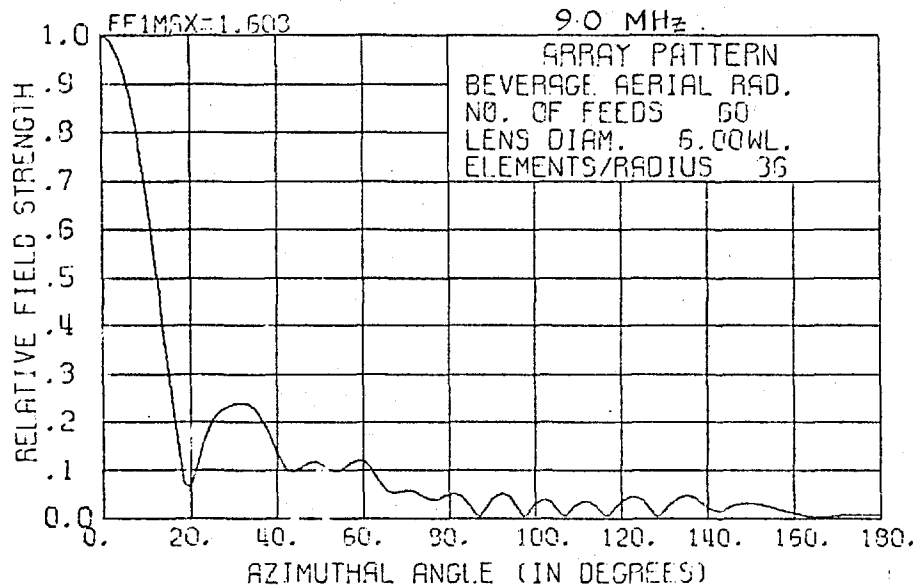


Fig. 4.23

lens. Hence an equivalent circuit lens used with directive radiators will need a lower value for  $N$  but a slightly higher value for  $NELR$  as compared to values for the lens used in conjunction with cardioid radiators.

Whereas a  $6.0\lambda$  equivalent lens used in conjunction with cardioid radiators requires a minimum of about 108 radial lines and  $NELR$  of about 28 a corresponding lens for use with beverage radiators need an  $N$  value of about 60 or even fewer (48). The value for  $NELR$  need is, however, higher.

The side lobe levels obtained from an equivalent lens with different  $N$  and  $NELR$  values for beverage radiators are shown in table 4.10. A representative selection of radiation patterns is shown in fig. 4.22.

In fig. 4.23 the radiation patterns of a suitable equivalent lens ( $N = 60$ ,  $NELR = 36$ ) for 9.0, 7.5, 6.0 and 3.0 MHz are shown.

#### 4.6 Summary

The equivalent circuit for the Luneburg Lens has been obtained. From the equivalent ladder network obtained from each mode and from the results obtained we conclude that the higher modes do not penetrate the lens as much as the lower modes. We find that the lower order mode behaviour is largely dependent on the number of elements used per radial line, while the higher order modes are dependent mainly on the number of radial lines used. The behaviour of the equivalent lens circuit is influenced by the relationship between phases of the mode

reflection coefficients and not by individual phase values.

Used in conjunction with cardioid radiators the equivalent circuit will need a larger value of  $N$  as compared with one to be used with more directive radiators. We suggest that with the use of more directive radiators in the array, the far-field mode amplitude distribution (equivalent to amplitude distribution in a linear array) is more tapered. This effect is an advantage in a multibeam system where a fairly constant beamwidth is desirable.

The idea of leaving some radial lines open-circuited to reduce the number of radiators needed to be used has not proved to be a good one. A higher side lobe level is obtained for the radiation pattern if this were done. We suggest a form of matching network could be designed to combine every two or three adjacent radial lines to form a feed point.

Although only two types of Luneburg Lenses were studied, the technique of obtaining equivalent circuits could be applied for other types of lenses. In particular the constant beamwidth Luneburg Lens (De Size and Woodward, 20) is probably worth studying.



## APPENDIX A4.1

### Description of Program Subroutines

In addition to the programs described in the appendix of chapter 3 the following additional subroutines are used in the program for the equivalent circuit lens:-

#### A4.1.1 Subroutine EQCCT(XLO,XLR,CZ,NELR,DIAM,F,DR,DO,ZO)

This subroutine calculates the values of the components  $L_{\phi}$ ,  $L_r$ , and  $C_z$  for the equivalent circuit Luneburg Lens and also for the characteristic impedance,  $ZO$  for the space outside the lens. By changing the value of  $U1$ ,  $U2$  and  $E$  the program can be converted to calculate the component values for the  $\mu = \epsilon$  Luneburg Lens.

EO = free space permittivity

UO = free space permeability

DIAM = diameter of lens in metres

DR = element spacing in r-direction =  $DIAM/(2*NELR)$

DO = element spacing in  $\theta$ -direction =  $2\pi/N$

XLO =  $L_{\phi}$

XLR =  $L_r$

CZ =  $C_z$

Elements values are numbered 1 to NELR starting at the lens circumference.

The flow chart for this subroutine is given in fig. A4.1.1.

#### A4.1.2 Subroutine RTLCCT(XLZ,XLR,CZ,YT,NELR,M1,ZO,CXRHO,Q,W,ARGRHO,ZTT)

This subroutine calculates the reflection coefficient of a ladder network terminated by an impedance, ZT for the (M1-1) mode. The Q of the coils used in the network can be specified.

The subroutine starts at the end of the line, calculating the input impedance as it moves toward the feed point

CXRHO(M1) = Complex reflection coefficient of (M1-1) the mode

ARGRHO(M1) = its argument

ABSRHO(M1) = its modulus

$$L_z = L_\phi / 4 \sin^2 \psi, \text{ where } \psi = 2\pi * \text{Mode}/N,$$

is computed in the main program. The subroutine prints the values of the phase reflection coefficient normalised to the zero value so that the phase angle increases with mode number. The normalised input impedance for each equivalent circuit is also printed.

#### A4.1.3 Subroutine RMODE(ZTT,ZTM,IN,CXRHO,ARGRHO,M)

This subroutine is programmed to calculate the New mode reflection coefficients for an N line equivalent lens but with all but every Mth ports are open circuited. Hence the number of new modes is reduced from the number of old modes by M

$ZTT(M1) = \mathcal{Z}_m$  = normalised old mode input impedance

$ZTM(M1) = \mathcal{Z}'_m$  = new mode input impedance

The expression obtained in Appendix 4.2 is used for the computation

$$\zeta'_{\text{New}} = \frac{1}{M} \sum_s \zeta_{M + NN \cdot s/M}$$

There are  $M$  terms in this summation.

In the computation the old modes are arranged so that Mode  $ZTT(I)$  is the same for  $I = 0$  to  $NN/2$  and mode  $NN$  to  $NN/2 + 1$ .

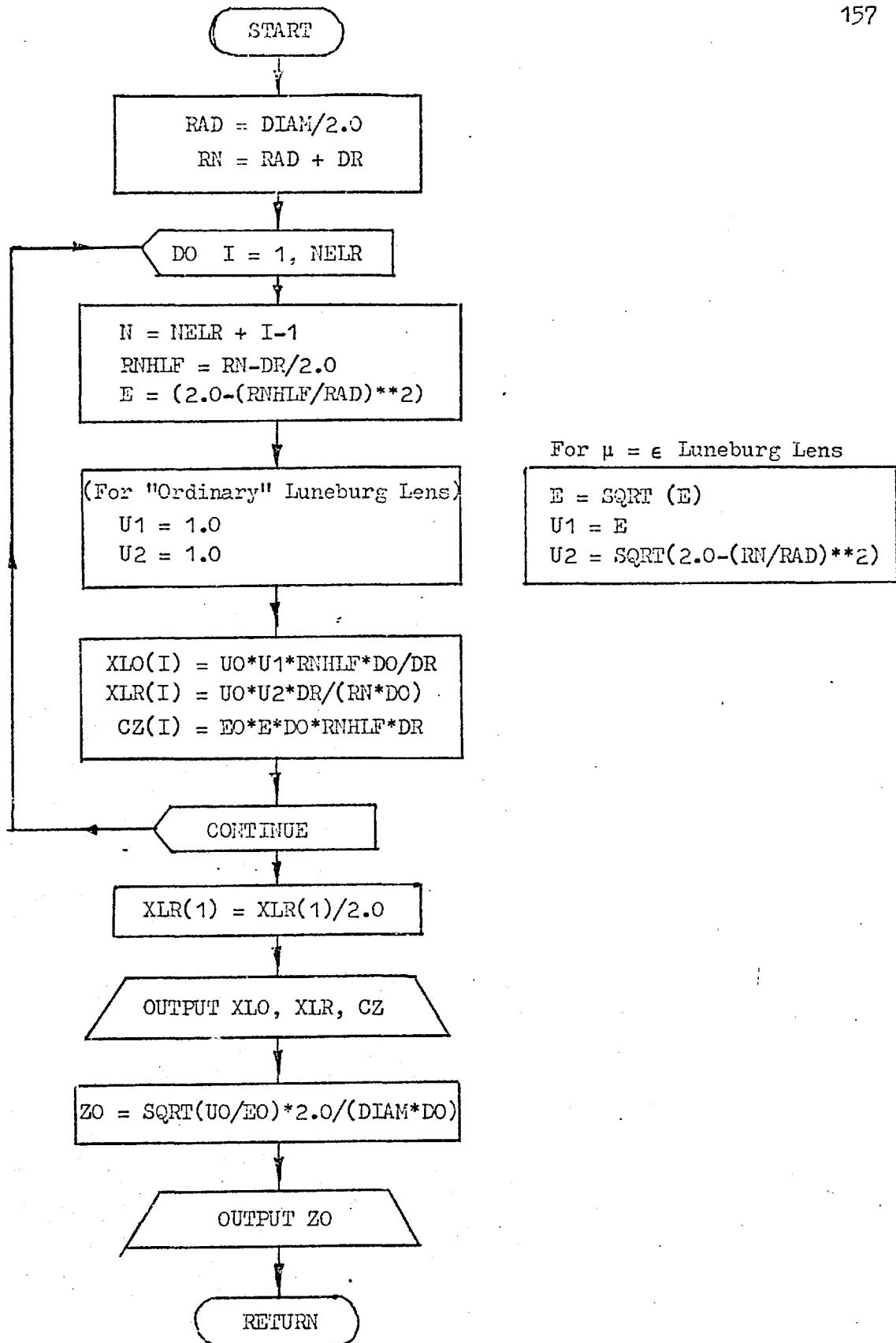


Fig. A4.1.1 FLOW CHART FOR SUBROUTINE EQCCT

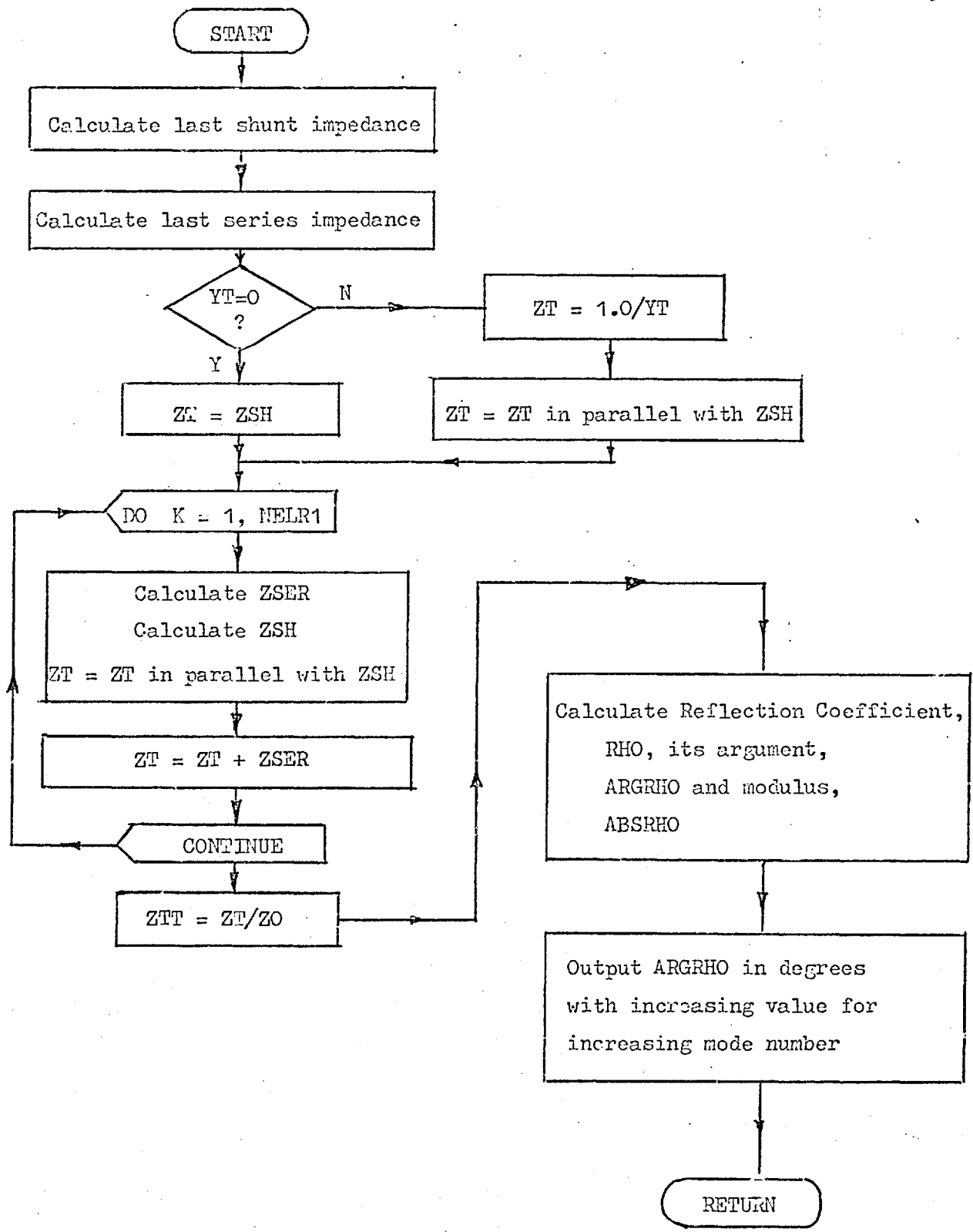


Fig. A4.1.2 FLOW CHART OF SUBROUTINE RTLCTT

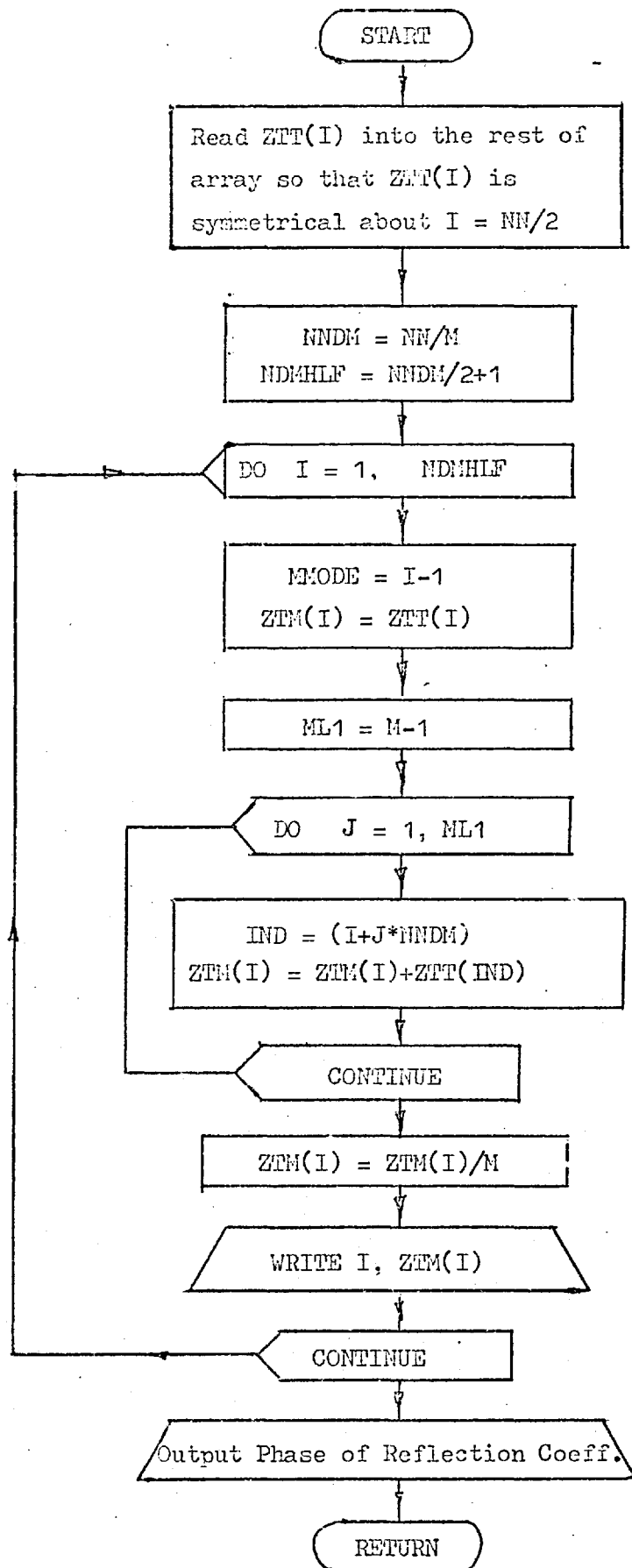


Fig. A4.1.3  
 FLOW CHART OF  
 SUBROUTINE RMODE

APPENDIX A4.2

Mode Reduction by a Factor, k

For an equivalent circuit structure of N radial lines if all except every kth radiator is left open circuited then current only flows out from every kth line. Instead of N modes the number of new modes will be reduced by a factor k. The impedance for each new mode is calculated below.

For the Old Modes, m

Zero order

$$\begin{aligned}
 & I_1^0 = I_{1+k}^0 = I_{1+2k}^0 = \dots = I^0 \\
 \text{and } & I_r^0 = 0, \text{ for } r \neq 1 + kq ; q = 0, 1, 2, \dots \\
 & V_1^0 = V_{1+k}^0 = V_{1+2k}^0 = \dots = V^0
 \end{aligned}
 \left. \vphantom{\begin{aligned} I_1^0 = I_{1+k}^0 = I_{1+2k}^0 = \dots = I^0 \\ I_r^0 = 0, \text{ for } r \neq 1 + kq ; q = 0, 1, 2, \dots \\ V_1^0 = V_{1+k}^0 = V_{1+2k}^0 = \dots = V^0 \end{aligned}} \right\} \text{A4.1(a)}$$

First Mode

$$\begin{aligned}
 & I_1^1 = I_{1+k}^1 \exp(-j 2\pi k/N) = I_{1+2k}^1 \exp(-j 2\pi k/N) = \dots = I^1 \\
 \text{and } & I_r^1 = 0, \text{ for } r \neq 1 + kq ; q = 0, 1, 2, \dots \\
 & V_1^1 = V_{1+k}^1 \exp(-j 2\pi k/N) = V_{1+2k}^1 \exp(-j 2\pi k/N) = \dots = V^1
 \end{aligned}
 \left. \vphantom{\begin{aligned} I_1^1 = I_{1+k}^1 \exp(-j 2\pi k/N) = I_{1+2k}^1 \exp(-j 2\pi k/N) = \dots = I^1 \\ I_r^1 = 0, \text{ for } r \neq 1 + kq ; q = 0, 1, 2, \dots \\ V_1^1 = V_{1+k}^1 \exp(-j 2\pi k/N) = V_{1+2k}^1 \exp(-j 2\pi k/N) = \dots = V^1 \end{aligned}} \right\} \text{A4.1(b)}$$

more generally for the mth mode ( $m = 1-N/2$  to  $N/2$ , N even)

$$\begin{aligned}
 I_1^m &= I_{1+k}^m \exp(-j 2\pi km/N) = I_{1+2k}^m \exp(-j 2\pi km/N) = \dots = I^m \\
 I_r^m &= 0 \text{ for } r \neq 1 + kq ; q = 0, 1, 2, \dots \\
 V_1^m &= V_{1+k}^m \exp(-j 2\pi km/N) = I_{1+2k}^m \exp(-j 2\pi km/N) = \dots = V^m
 \end{aligned}
 \tag{A4.1(c)}$$

For the New Mode, M (= 1-N/2k to N/2k)

$$I_r^M = \sum_m p_m \exp(j r m \alpha) \tag{A4.2}$$

where  $p_m$  = constant for each mode

$m$  = old mode

$r$  = feed position number

$\alpha = 2\pi/N$

$$\text{Also } V_r^M = \sum_m p_m \mathcal{Z}_m \exp(j r m \alpha) \tag{A4.3}$$

where  $\mathcal{Z}_m$  = old mode impedance

Replacing  $r$  by  $r+k$  in equation A4.2

$$I_{r+k}^M = \sum_m p_m \exp(j m (r+k) \alpha) \tag{A4.4}$$

But for new mode, M

$$\begin{aligned}
 I_{r+k}^M &= I_r^M \exp(j 2\pi kM/N) \\
 &= I_r^M \exp(j k M \alpha)
 \end{aligned}$$

substituting for  $I_r^M$  from equation A4.2

$$I_{r+k}^M = \sum p_m \exp(j r m \alpha) \cdot \exp(j k M \alpha) \tag{A4.5}$$

Equating A4.2 to A4.5



$$\sum_m p_m \exp(j m (r+k) \alpha) = \sum_m p_m \exp(j r m \alpha) \exp(j k M \alpha)$$

$$\text{i.e. } p_m \exp(j m k \alpha) = p_m \exp(j k M \alpha)$$

$$\text{i.e. } \exp(j (m-M)k \alpha) = \exp(j 2\pi s),$$

$$s = 0, 1, 2, \dots$$

∴

$$m = M + Ns/k$$

A4.6

but for  $m < N$ ,

∴ from equation A4.2

$$I_r^M = \sum_s p_n \exp(j r n \alpha) \quad \text{A4.7}$$

where  $n = M + Ns/k$

and  $|n| < N$

Taking  $I_r^M$  for  $k$  consecutive values of  $r$  ( $r = 1$  to  $k$ , say)

$$I_1^M = I_1^M = \exp(j M \alpha) \left[ p_{M+N \cdot 0/k} + p_{M+N \cdot 1/k} \exp(j 2\pi \cdot 1/k) + \dots \right]$$

$$I_2^M = 0 = \exp(j 2M \alpha) \left[ p_{M+N \cdot 0/k} + p_{M+N \cdot 1/k} \exp(j 4\pi \cdot 1/k) + \dots \right]$$

$$I_k^M = 0 = \exp(j k M \alpha) \left[ p_{M+N \cdot 0/k} + p_{M+N \cdot 1/k} \exp(j 2(k) \cdot 1/k) + \dots \right]$$

Rearranging in matrix form

$$\begin{pmatrix} 0 \\ I_1^M \\ 0 \\ \cdot \\ 0 \end{pmatrix} = \begin{bmatrix} \exp(j M k \alpha) \\ \exp(j M \alpha) \\ \exp(j 2M \alpha) \\ \cdot \\ \exp(j (k-1) M \alpha) \end{bmatrix} \begin{bmatrix} 1 & 1 & \cdot & \cdot & 1 \\ 1 & \exp(j \beta) & \cdot & \cdot & \exp(j (k-1) \beta) \\ \cdot & \cdot & \cdot & \cdot & \cdot \\ \cdot & \cdot & \cdot & \cdot & \cdot \\ 1 & \exp(j (k-1) \beta) & \cdot & \cdot & \exp(j (k-1)^2 \beta) \end{bmatrix}$$

$$x \begin{bmatrix} p_M \\ \\ \\ \\ \\ p_{M+N(k-1)/k} \end{bmatrix}$$

$$\text{where } \beta = \frac{2\pi}{k}$$

$$\text{i.e. } \begin{bmatrix} p_M \\ \cdot \\ \cdot \\ \cdot \\ p_{M+N(k-1)/k} \end{bmatrix} = \frac{1}{k} \begin{bmatrix} 1 & 1 & \cdot & \cdot & 1 \\ 1 & \exp(-j\beta) & \cdot & \cdot & \exp(-j(k-1)\beta) \\ \cdot & \cdot & \cdot & \cdot & \cdot \\ \cdot & \cdot & \cdot & \cdot & \cdot \\ 1 & \exp(-j(k-1)\beta) & \cdot & \cdot & \exp(-j(k-1)^2\beta) \end{bmatrix}$$

$$x \begin{bmatrix} \exp(-jkM\alpha) \\ \exp(-jM\alpha) \\ \cdot \\ \cdot \\ \exp(-j(k-1)M\alpha) \end{bmatrix} \begin{Bmatrix} 0 \\ I_1^M \\ 0 \\ \cdot \\ 0 \end{Bmatrix}$$

$$= \frac{1}{k} \begin{bmatrix} 1 & 1 & \cdot & \cdot & 1 \\ 1 & \exp(-j\beta) & \cdot & \cdot & \exp(-j(k-1)\beta) \\ \cdot & \cdot & \cdot & \cdot & \cdot \\ \cdot & \cdot & \cdot & \cdot & \cdot \\ 1 & \exp(-j(k-1)\beta) & \cdot & \cdot & \exp(-j(k-1)^2\beta) \end{bmatrix} \begin{Bmatrix} 0 \\ I_1^M \exp(-jM\alpha) \\ 0 \\ \cdot \\ 0 \end{Bmatrix}$$

$$= \frac{I_1^M}{k} \begin{bmatrix} 1 \\ \exp(-j\beta) \\ \cdot \\ \cdot \\ \exp(-j(k-1)\beta) \end{bmatrix} \exp(-jM\alpha)$$

$$\text{i.e. } p_{M+N_s/k} = \frac{I_1^M}{k} \exp(-jM\alpha) \cdot \exp(-js\beta) \quad \text{A4.8}$$

From equation A4.3

$$V_r^M = \sum_m p_m \exp(j r m \alpha) \mathcal{Z}_m$$

$$V_1^M = \sum_m p_m \exp(j m \alpha) \mathcal{Z}_m$$

$$= \sum_s p_{M+N_s/k} \mathcal{Z}_m \exp(j (M+N_s/k) \alpha)$$

Substituting for  $p_{M+N_s/k}$  from equation A4.8

$$\begin{aligned} V_1^M &= \sum_s \mathcal{Z}_m \frac{I_1^M}{k} \exp(-jM\alpha) \cdot \exp(-js\beta) \cdot \exp(jM\alpha + jN_s\alpha/k) \\ &= \frac{I_1^M}{k} \sum_s \mathcal{Z}_{M+N_s/k} \end{aligned}$$

i.e.  $\mathcal{Z}'_M$ , the new mode impedance

$$= \frac{V_1^M}{I_1^M} = \frac{1}{k} \sum_s \mathcal{Z}_{M+N_s/k} \quad \text{A4.9}$$

i.e.  $\mathcal{Z}'_M = \frac{1}{k} \sum \mathcal{Z}_m$ , where  $|m| < NN$

## CHAPTER 5

### 5. THE OPTIMUM LENS AND ITS DESIGN

#### 5.1 Introduction

Although the behaviour of the Luneburg Lens is fairly optimum we feel that there may be other rotationally symmetrical networks (RSN) which have characteristics better than that of the Luneburg Lens. In obtaining the equivalent circuit Luneburg Lens we have no control over its characteristics. In this chapter we explore the possibilities of obtaining a technique for the design of an optimum Luneburg type lens.

In chapter 2 we showed that a RSN can be built by cascading two Butler type networks via  $N$  phase shifters. The only parameters involved in such a network are the values of the  $N$  phase-shifters (whose phase values correspond to the phases of the mode reflection coefficients or eigenvalues of the RSN structure). Therefore, in any design technique the values of the  $N$  phase shifters need to be known.

Chadwick and Glass (23), Davis (12) and Sheleg (24) have established the equivalence between the linear and circular array. In the two-Butler-type matrix network one of the matrix network acts as the mode forming network and the other, as the beam forming network, much like the network used to feed  $N$  radiators in a linear array.

There is a relationship between the mode in the near field (the output from the network) and the mode in the far-field. This transformation factor depends on the radiation pattern of the radiators used in the array. The correspondence between linear and circular array and the relationship between modes in the near and far-field will be treated in section 5.2.

In the design of the optimum lens we maximise the field in the direction of the main beam. This is done by choosing the appropriate values for the  $N$  phase shifter (i.e. phases of the mode reflection coefficients), so that the phase of all the modes in the far-field is equal.

We proposed to construct the RSN by interconnecting 2-port networks between the  $N$  feeds points of the RSN structure as shown in fig. 5.9. The expression for the  $Y_{12}$  parameter for the two ports is derived in section 5.4.

In section 5.5 we explore the possibility of realising the 2-port network from the  $Y_{12}$  parameters already obtained.

## 5.2 Equivalences Between Linear and Circular Arrays

The equivalence between the circular and linear array was established by Chadwick and Glass (23), Davis (12) and later by Sheleg (24).

We have shown this equivalence purely from consideration of rotational symmetry. Figure 5.1 shows the equivalent circuit for a rotationally symmetric network for multibeam operation obtained in

chapter 2. The second Butler Matrix  $[B^*]$  acts as the mode forming network, while the first matrix network  $[B]$  acts as the beam forming network much like the Butler Matrix use in a linear array for multi-beam operation.

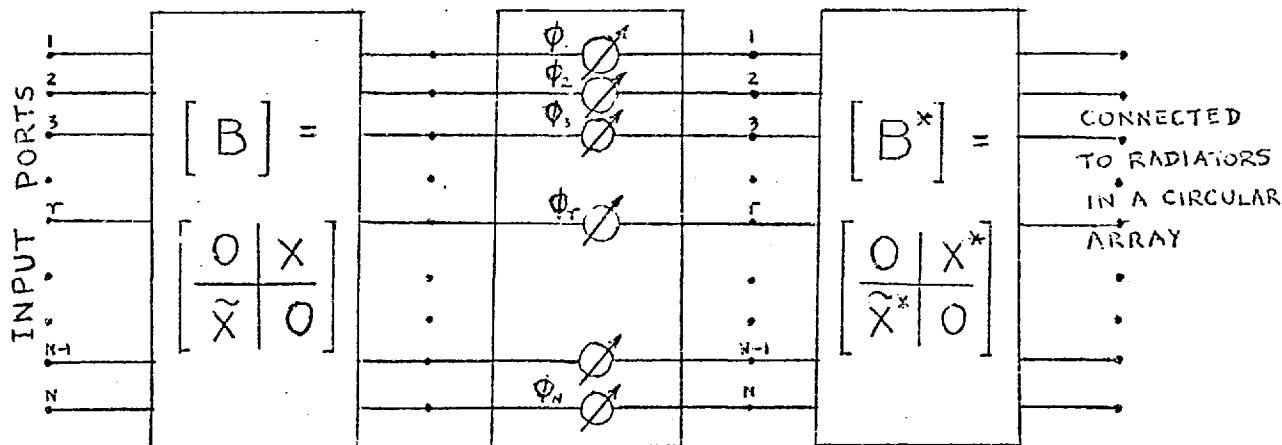


Fig. 5.1 ROTATIONALLY SYMMETRIC NETWORK FROM TWO BUTLER-TYPE NETWORKS

If the  $r$ th input port of the beam-forming network is excited the outputs from the  $N$  output ports (inputs to the radiators) are equal in amplitude but have a phase progression between adjacent ports of  $2\pi r/N$  radians. This excitation corresponds to the  $r$ th mode. For clarity in this discussion we assume that this is equivalent to a continuous current distribution,  $\exp(j r \theta)$  where  $\theta =$  array azimuthal angle. This assumption is justified if the spacing between radiators is less than  $\lambda/2$ . The  $r$ th mode in the near field gives rise to radiation in the far-field (Appendix A5.1), given by

$$F_r(\theta') = B_r \exp(j r \theta') \quad 5.1$$

where  $\theta'$  = azimuthal angle in far-field

$B_r$  = constant (dependent of the pattern of the radiator used in the array.

Hence the excitation of the  $r$ th input port of the second matrix network,  $[B^*]$  gives rise to a far-field mode,  $r$ . Taking into account the phase shift,  $\phi_r$  the far-field becomes

$$F_r(\theta') = B_r \exp(j\phi_r) \exp(jr\theta') \quad 5.2$$

Compare this with the expression for the far-field contribution of the  $r$ th element in a linear array

$$F_{lr}(\theta') = L_r \exp(jru)$$

$$\text{where } u = (kd/\lambda) \sin \theta'$$

$d$  = spacing between radiators

$L_r$  = excitation at the  $r$ th radiator.

Whereas  $F_{lr}(\theta')$  is a function of  $(kd/\lambda) \sin \theta'$  in a linear array,  $F_r(\theta')$  is a function  $\theta'$  only. We see, therefore, that the first Butler Matrix Network,  $[B]$  acts as the usual beam forming network in a linear array ([11], [29], [30]). Consequently, the restrictions applicable for a lossless Butler-Matrix used with the linear array applies, i.e. the output amplitudes from the beam forming network must all be equal. Therefore, the mode amplitude for a lossless RSN (in the near field) must be equal. Hence, in the near field the total field in direction,  $\theta$  is given by

$$F_{\text{near}}(\theta) = \sum_m A_m \exp(jm\theta) \quad 5.3$$

$A_m = 1$  for lossless network considered

In the far field

$$F(\theta') = \sum_m B_m \exp(j \phi_m) \exp(j m \theta') \quad 5.4$$

The constants  $B_m \exp(+j \phi_m)$  corresponds to current excitation for the  $m$ th radiator for a corresponding linear array.  $B_m$  (a complex value) is investigated in the next section.

### 5.2.1 Relationship Between Near and Far-field Mode Excitations

It has been shown (Longstaff, Chow and Davis [25] Knudsen [26]) that for the  $m$ th mode the far-field  $F_m(\theta')$  has the same form as the current distribution along the circumference of the array but modified by an  $m$ th order Bessel function and  $(j)^m$  for omni-directional radiators.

$$\text{i.e. for } I_z(\theta) = I_r \exp(j m \theta) \quad 5.5$$

$$F_m(\theta') = (j)^m J_m(ka) \exp(j m \theta') \quad 5.6$$

where  $a$  = radius of the array

For certain value of  $a$   $J_m(ka) = 0$  so that some modes are not excited, suggesting that the system is frequency sensitive. The mode amplitude distribution ( $|B_m| = b_m$ ) is plotted in fig. 5.2 for omni-directional radiators for a  $2.0\lambda$ ,  $4.0\lambda$  and  $8.0\lambda$  diameter array. We can neglect the effects of the higher order modes which are also excited if the spacing between feeds is less than about  $\lambda/2$ . Otherwise equation 5.6 becomes

$$F_m(\theta') = \sum_{q=-\infty}^{\infty} (j)^{m-Nq} J_{n-Nq}(ka) \exp(j(n-Nq)\theta) \quad 5.7$$



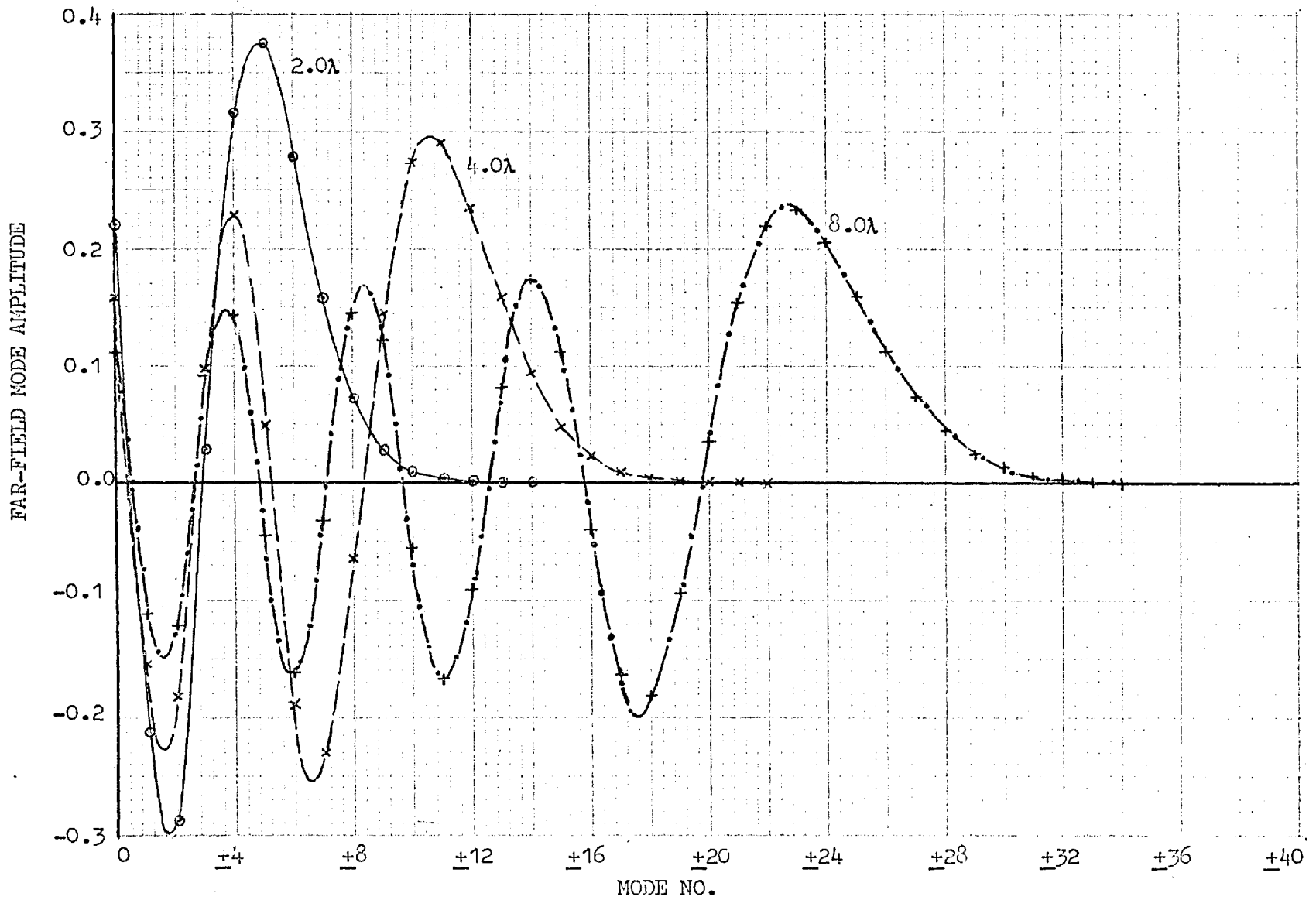


Fig. 5.2

FAR-FIELD MODE AMPLITUDE DISTRIBUTION (OMNI-DIRECTIONAL RADIATORS)

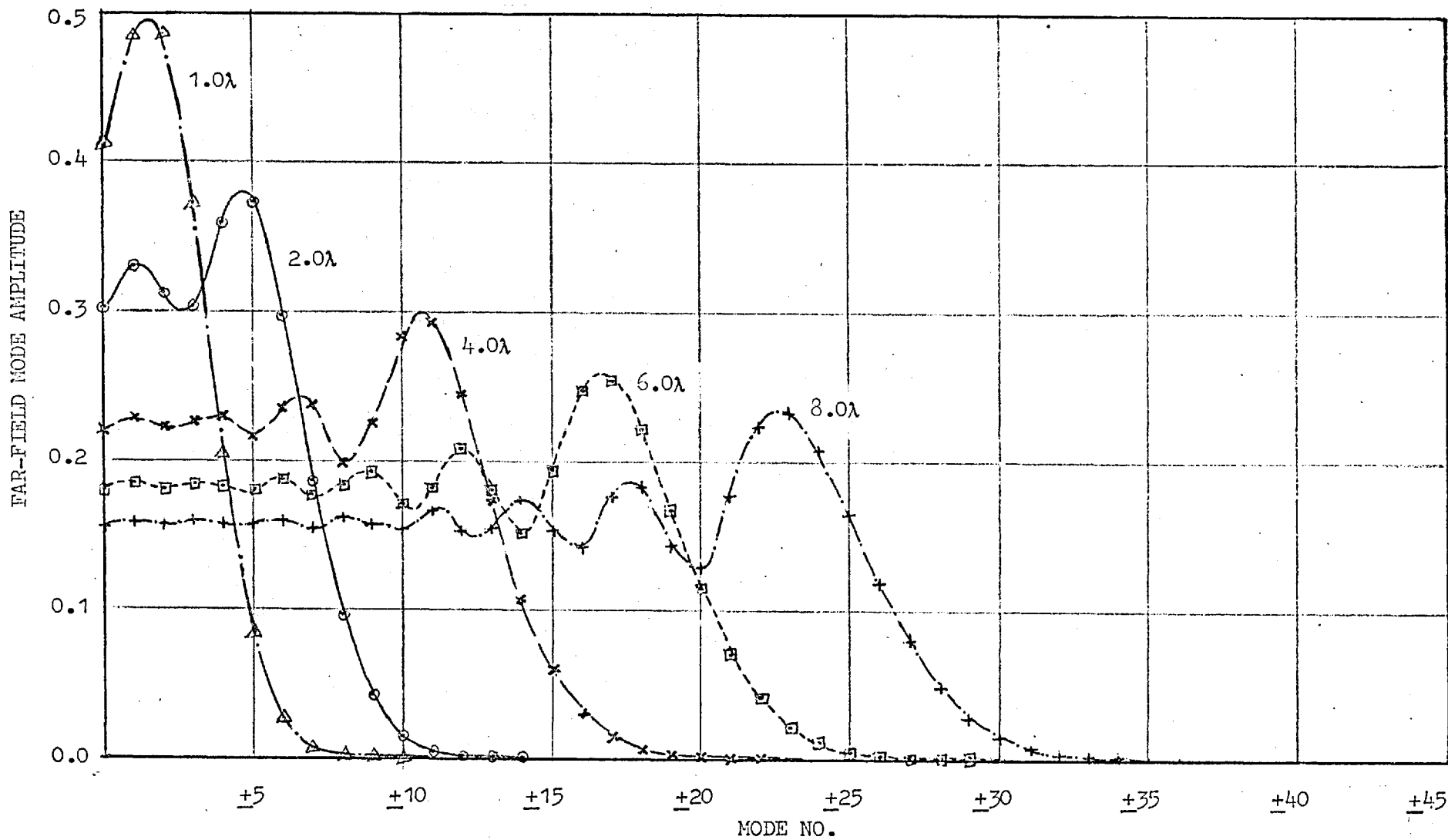


Fig. 5.3 FAR-FIELD MODE AMPLITUDE - CARDIOID (1+cosine) RADIATORS

If cardioid  $\frac{(1+\cos\theta)}{2}$  radiators are used (Appendix 5.1)

$$B_m = \frac{1}{2} \left\{ (j)^m J_m(ka) - j \left[ J_{m+1}(ka) - J_{m-1}(ka) \right] / 2 \right\}$$

$$= \frac{1}{2} (j)^m \left[ J_r(ka) - J_r'(ka) \right], \text{ neglecting the}$$

effects of grating lobes.

$B_m = b_m / \sqrt{V_r}$  is calculated using a digital computer by the subroutine AMPARG (described in Appendix 5.2). For the cardioid radiators the far-field mode amplitude distribution is plotted in fig. 5.3 for  $1.0\lambda$ ,  $2.0\lambda$ ,  $4.0\lambda$ ,  $6.0\lambda$  and  $8.0\lambda$  diameter arrays.

Whereas the far-field mode amplitude changes rapidly with mode number for an array of omni-directional radiators, that for cardioid radiators is fairly constant, increasing in value, reaching a peak value when  $m \approx ka$ . For  $m > ka$  the mode amplitude falls off rapidly to a very low value. The effect of the far-field mode amplitude distribution of the far-field pattern has already been discussed in chapter 3 for the Luneburg Lens. For cardioid radiators if all the significant modes are used the side lobe level obtained approaches  $-13.3\text{db}$  - a figure very close to that for an array with uniform amplitude.

Judging from the radiation patterns obtained using beverage aerial radiators we are led to believe that far-field mode amplitude distribution is more tapered if more directive radiators are used in the array. Equation A5.7 in appendix A5.1 supports this theory. A more directive radiator will contain a higher number of cosine harmonics in the expression for its radiation pattern.

The phase,  $\psi_m$ , of  $B_m$  has been computed for the (1+cosine) radiator array.

### 5.3 The Optimum Lens

We define the optimum lens as one which has maximum gain in the forward direction of the array ( $\theta' = \pi$  for feed at  $\theta = 0$ ). To maximise gain we maximise  $F(\theta')$ .

#### 5.3.1 Behaviour of Mode Reflection Coefficient

From equation 5.4 the far-field excited by the RSN is given by

$$\begin{aligned} F(\theta') &= \sum_m B_m \exp(j\phi_m) \exp(jm\theta') \\ &= \sum_m b_m \exp(j(\phi_m + \psi_m)) \exp(jm\theta') \end{aligned} \quad 5.4$$

To maximise  $F(\theta')$  we put the phase of all the terms in the summation equal to a constant, zero for convenience, i.e.

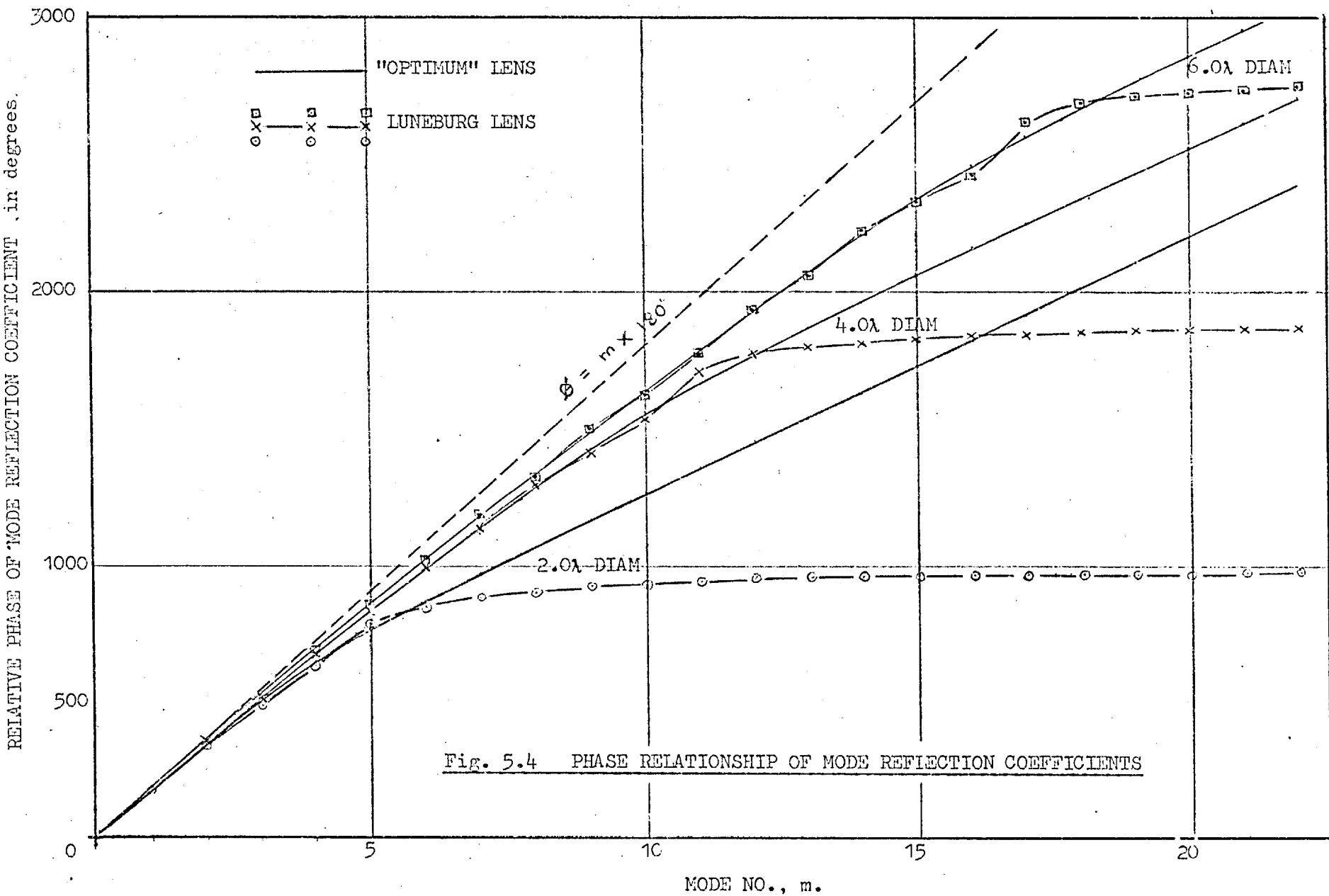
$$\begin{aligned} \phi_m + \psi_m + m\theta'_{\max} &= 0 \\ \phi_m &= -\psi_m - m\theta'_{\max} \end{aligned} \quad 5.5$$

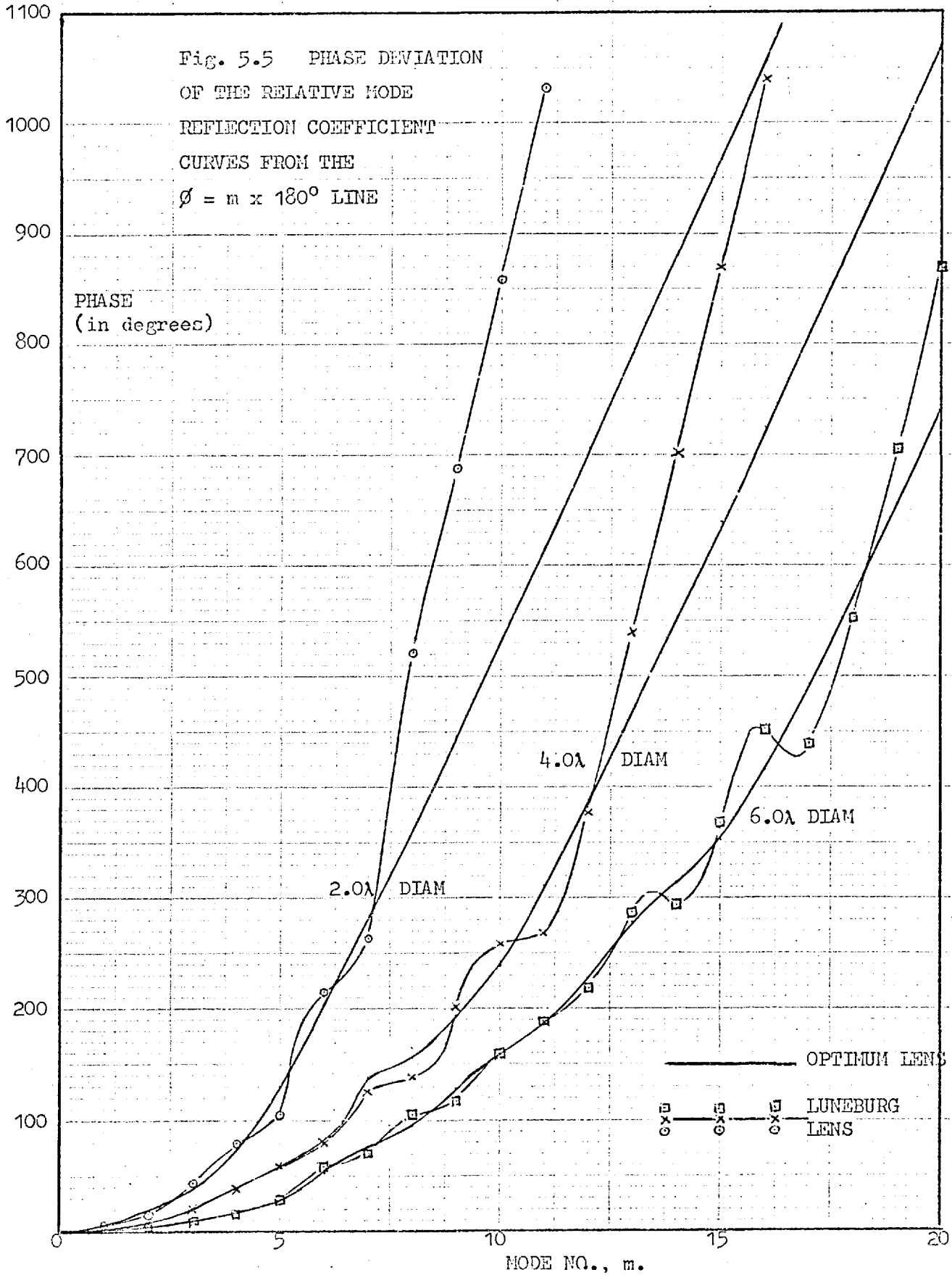
We had established that  $\phi_m$  is the phase of the mode reflection coefficient for the RSN. For optimum lens design  $\theta'_{\max} = 180^\circ$

$$\text{i.e.} \quad \phi_m = -\psi_m - m\pi \quad 5.6$$

The relative value of  $\phi_m$  has been plotted in fig. 5.4 for the  $2.0\lambda$ ,  $4.0\lambda$  and  $6.0\lambda$  diameter lenses. The corresponding curves for the Luneburg Lens are also shown.

Like the Luneburg Lens the phase of the mode reflection coefficient





increases at a rate of less than  $180^\circ$  per mode, for mode numbers less than  $ka$ . For modes greater than  $ka$  the phase increases at a rate of nearly  $90^\circ$  per mode. The phases are fairly constant for the corresponding modes for the Luneburg Lens. Since the far-field mode amplitudes for  $m$  greater than  $ka$  are not very significant the behaviour of the two lenses should be similar as far as the far-field patterns are concerned, particularly for low values for feed numbers. Since the relative phase of the mode reflection coefficient curve deviates slightly from the  $\phi(m) = m \times 180^\circ$  line for  $m$  less than  $ka$ , we have plotted the difference between the two curves in fig. 5.5 for both type of lenses.

### 5.3.2 Feed Output Distribution

The output distribution from the feeds of the optimum lens is shown in fig. 5.6 for a  $4.0\lambda$  diameter lens for 48, 24 and 12 feeds. The corresponding distribution for the Luneburg Lens is given in fig. 3.5 (sec. 3.2.2(a) of chapter 3). The significant differences between the two output distributions are:-

- (i) the lower amplitude of outputs at feeds adjacent to input port especially if feed numbers are small, for the optimum lens.
- (ii) for high number feeds used the amplitude output is high at the side of the array (around  $\theta = 90^\circ$  and  $270^\circ$ ) for the optimum lens.

### 5.3.3 Far-field Patterns

The radiation pattern for the array fed by the optimum lens is shown in fig. 5.7 and 5.8 for a  $2.0\lambda$  and  $4.0\lambda$  diameter lens, for

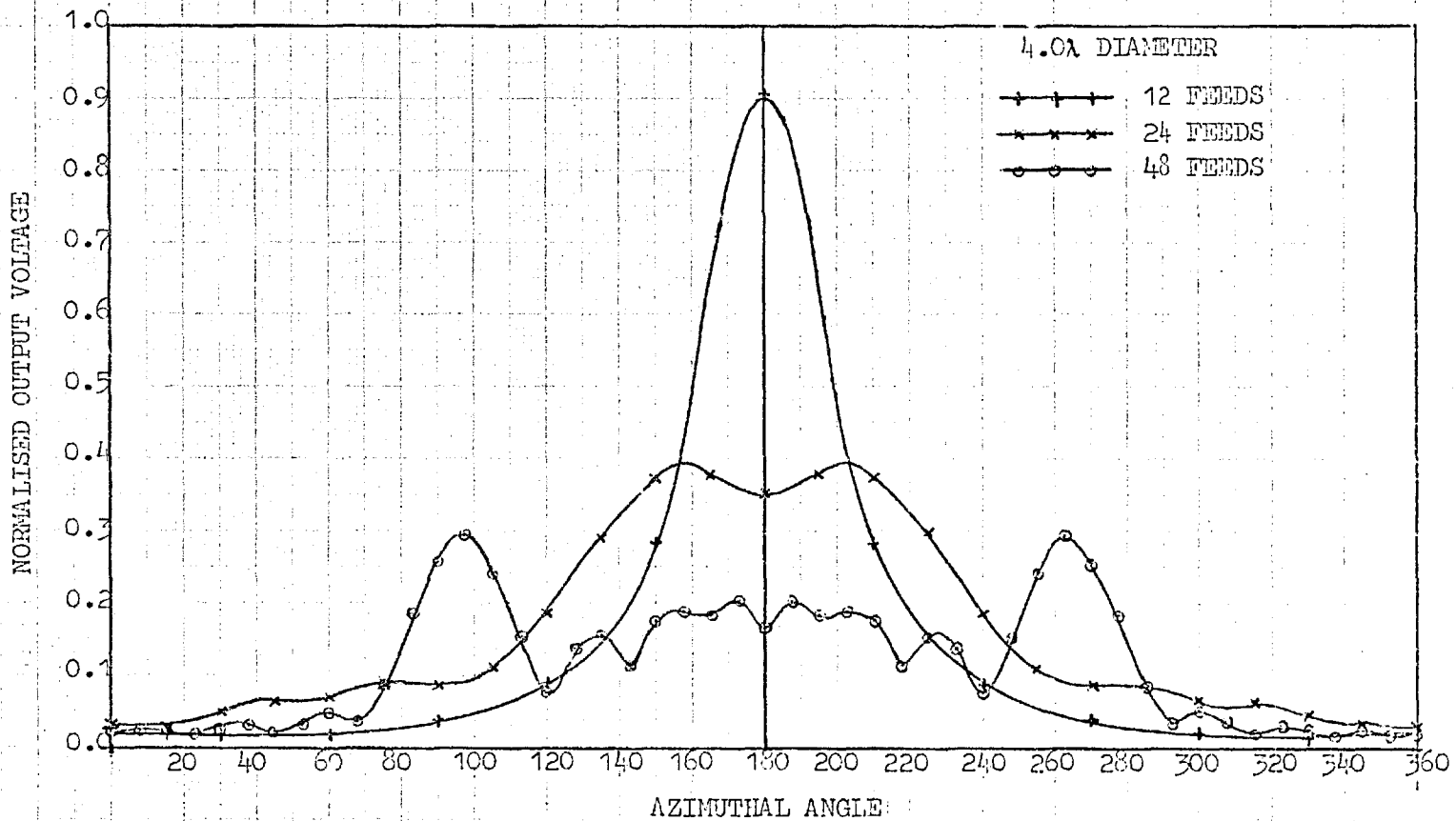


Fig. 5.6 OUTPUT DISTRIBUTION FROM OPTIMUM LENS  
(4.0λ DIAMETER LENS)



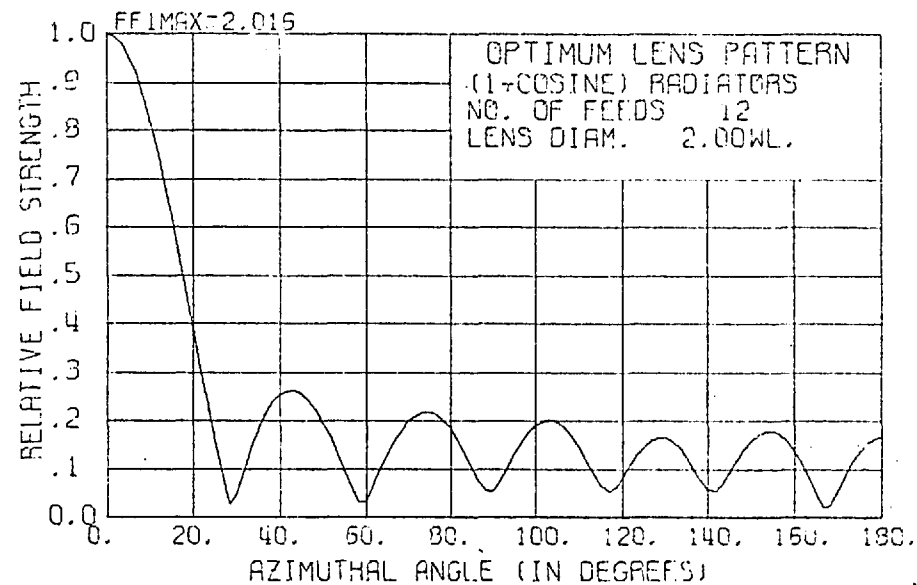
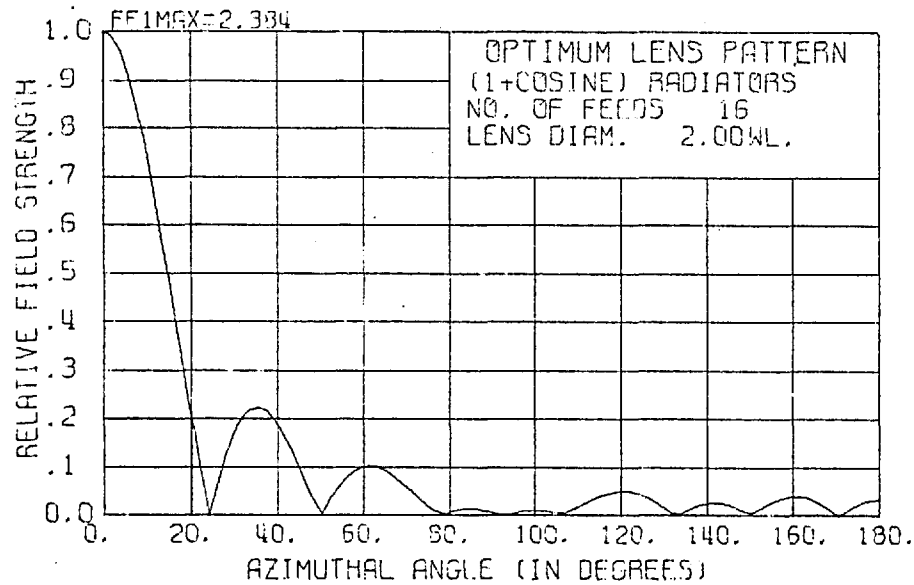
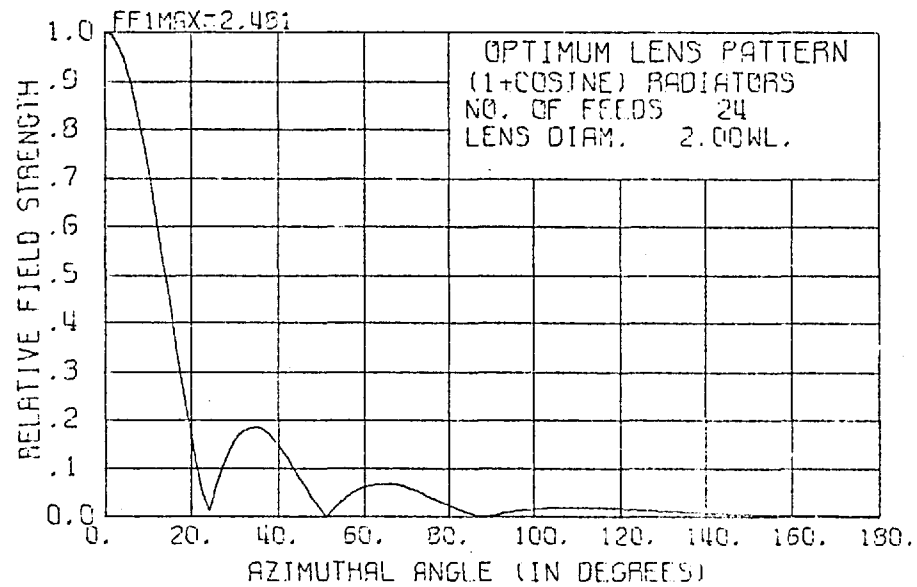
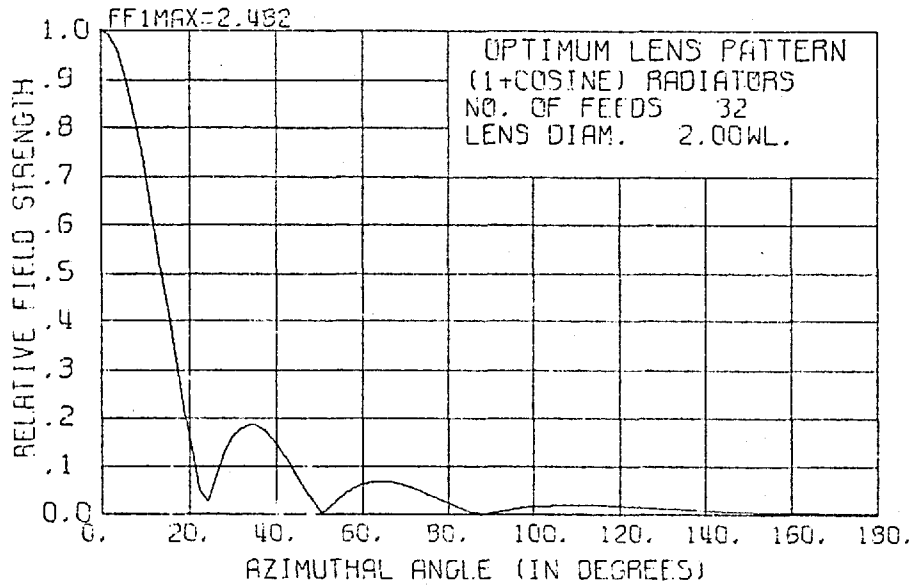


Fig. 5.7

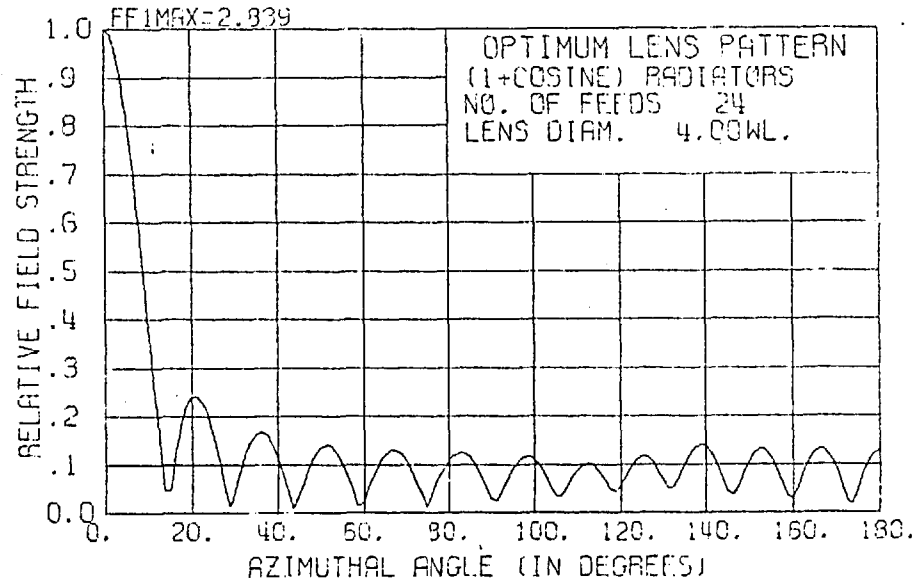
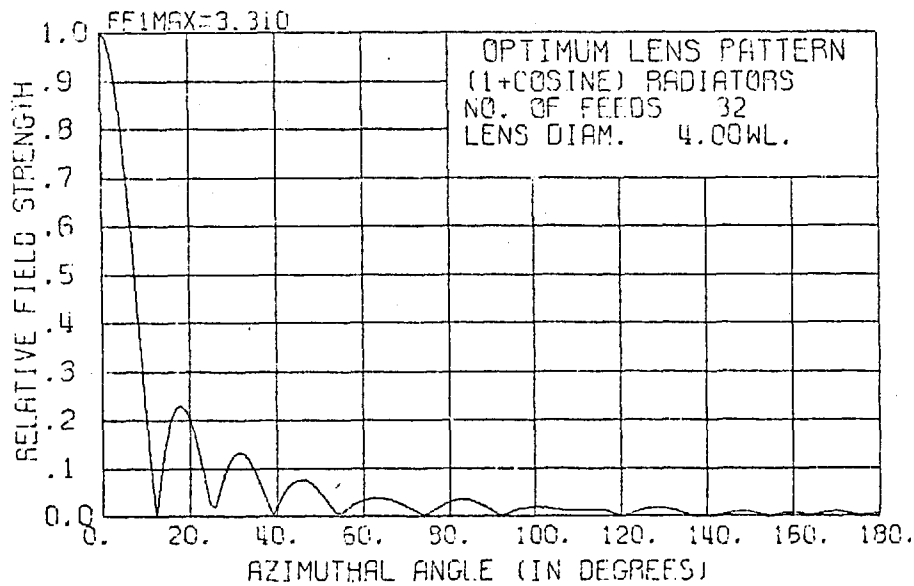
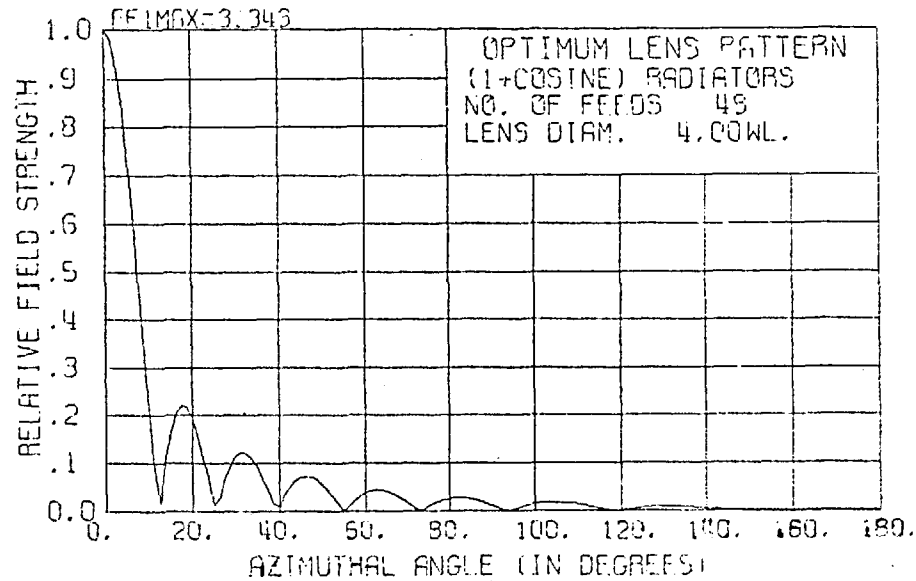
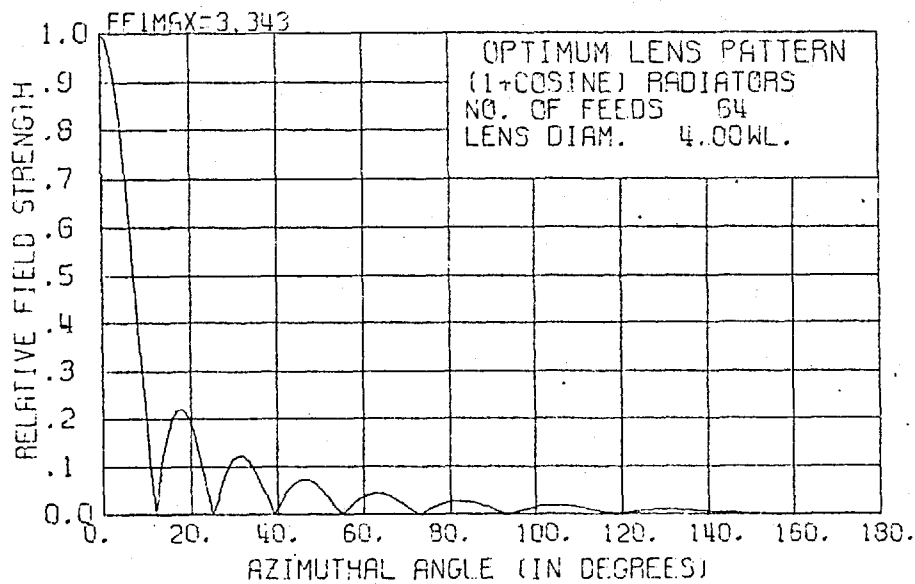


Fig. 5.8

various numbers of modes (or feeds) used. The corresponding patterns for the Luneburg Lens, shown in fig. 3.14 and 3.15 have already been dismissed in sec. 3.3.3 in chapter 3.

On the whole, where the spacing between feeds is large (lower number of feeds) the patterns obtained for the two lenses are nearly the same. But for higher feed numbers the side lobe levels in the optimum lens array tend to fall away from the main lobe, so that back lobe levels are very low. The higher side lobe levels for arrays with feed spacing of about  $\lambda/2$  is mainly to grating lobes which are also excited. The optimum lens array has narrower beamwidth.

If the RSN is viewed as a lens fed at  $\theta = 0$ , with maximum field in  $\theta' = \pi$ , this corresponds to radiation in the forward direction. Such a lens belongs to the class to which the Luneburg Lens belongs. If, however, we maximise the far-field in the direction  $\theta' = 0$  instead of  $\pi$  we obtain a lens which radiates in the backward direction. Such a lens belongs to the class referred to as Eaton-Lippman Lenses (Kay [27])

$$\text{For } F_{\max}(\pi) = \phi_m = -\psi_m - m\pi \quad (\text{forward direction}) \quad 5.6$$

$$\text{For } F_{\max}(0) = \phi_m = -\psi_m \quad (\text{backward direction}) \quad 5.7$$

#### 5.4 Synthesis of the Optimum Lens Network

The phase of the mode reflection for the optimum lens network has been obtained in the previous section. We propose to construct the lens network by connecting 2-port networks between the  $N$  output

feed points as shown in fig. 5.9. Let  $N = 2M+1$ .

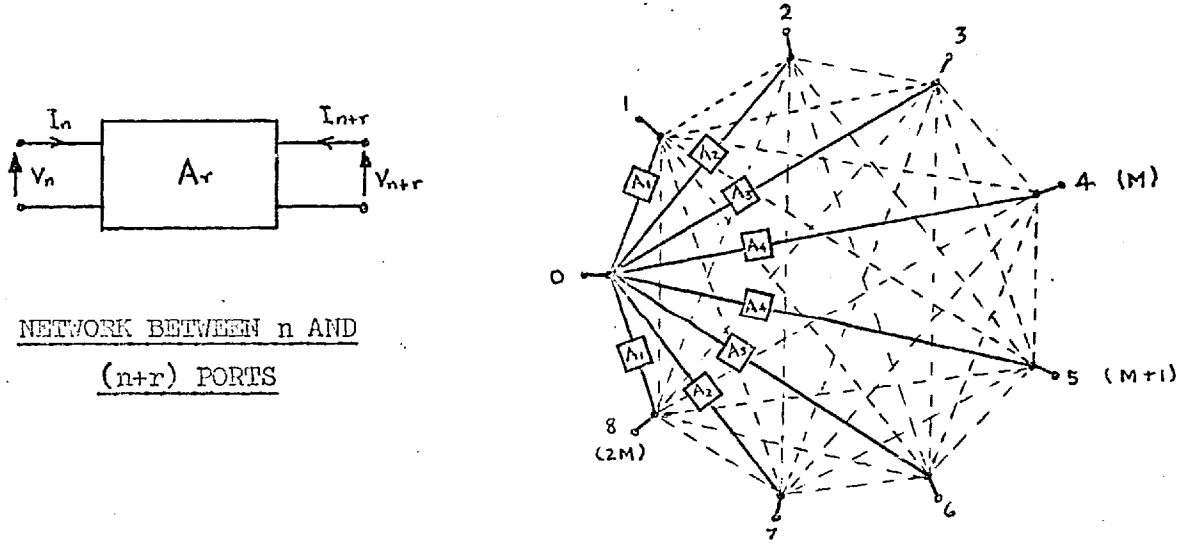


Fig. 5.9 THE LENS CIRCUIT

In the following paragraphs we obtain the relationship between the  $Y_{12}^r$  parameters for the  $r$ th 2-port network and the reflection coefficients obtained in section 5.3.

For the  $r$ th 2-port network itself,

$$\begin{Bmatrix} I_n \\ I_{n+r} \end{Bmatrix} = \begin{bmatrix} Y_1^r & Y_{12}^r \\ Y_{12}^r & Y_1^r \end{bmatrix} \begin{Bmatrix} V_n \\ V_{n+r} \end{Bmatrix} \tag{5.8}$$

where  $Y_1^r = Y_{11}$  parameter

$Y_2^r = Y_{12}$  parameter

For the Whole  $N$ -port Structure ( $N = 2M+1$ ),

at the  $n$ th port for  $m$ th mode,

$$I_n^m = \sum_{r=1}^M [Y_1^r V_n + Y_2^r V_{n+r}] + \sum_{r=M+1}^{2M} [Y_1^{2M+1-r} V_n + Y_2^{2M+1-r} V_{n+r}] \tag{5.9}$$

But  $V_n = \exp(j m n \phi)$

5.10

where  $\phi = 2\pi/N$

$$\begin{aligned} \therefore I_n^m &= \sum_{r=1}^M \left[ Y_1^r \exp(j m n \phi) + Y_2^r \exp\{j m(n+r)\phi\} \right] \\ &+ \sum_{r=M+1}^{2M} \left[ Y_1^{2M+1-r} \exp(j m n \phi) + Y_2^{2M+1-r} \exp\{j m(n+r)\phi\} \right] \\ &= \exp(j m n \phi) \left[ 2 \sum_{r=1}^M Y_1^r + \sum_{r=1}^M Y_2^r \{ \exp(j m r \phi) - \exp(-j m r \phi) \} \right] \\ \text{i.e. } I_n^m &= \exp(j m n \phi) \left[ 2 \sum_{r=1}^M Y_1^r + 2 \sum_{r=1}^M Y_2^r \cos m r \phi \right] \quad 5.11 \end{aligned}$$

If a shunt element exists in the  $n$ th port

$$I_n^m = \exp(j m n \phi) \left[ \sum_{r=1}^M (2 - \delta_{r0}) Y_1^r + 2 \sum_{r=1}^M Y_2^r \cos m r \phi \right] \quad 5.12$$

$$\text{i.e. } B_m = \frac{I_n^m}{V_n^m} = A + 2 \sum_{r=1}^M Y_2^r \cos m r \phi \quad 5.13$$

for  $m = 0, 1, 2, \dots, M$  and

where  $B_m$  = mode admittance

$$\text{and } A = \sum_{r=0}^M Y_1^r (2 - \delta_{r0}) \quad 5.14$$

For  $m = 0, 1, 2, \dots, M$ ,

$$B_0 = A + 2Y_2^1 + 2Y_2^2 + \dots + 2Y_2^M \quad 5.15(a)$$

$$B_1 = A + 2Y_2^1 \cos \phi + 2Y_2^2 \cos 2\phi + \dots + 2Y_2^M \cos M\phi \quad 5.15(b)$$

$$B_r = A + 2Y_2^1 \cos r\phi + 2Y_2^2 \cos 2r\phi + \dots + 2Y_2^M \cos Mr\phi \quad 5.15(c)$$

$$B_M = A + 2Y_2^1 \cos M\phi + 2Y_2^2 \cos 2M\phi + \dots + 2Y_2^M \cos M^2\phi \quad 5.15(d)$$

Rewriting equations 5.15(a) to (d) in matrix form

$$\left\{ B \right\} = \begin{Bmatrix} B_0 \\ B_1 \\ B_2 \\ \cdot \\ \cdot \\ B_M \end{Bmatrix} = [C] \begin{Bmatrix} A_1 \\ Y_2^1 \\ Y_2^2 \\ \cdot \\ \cdot \\ Y_2^M \end{Bmatrix} \quad 5.16$$

$$\text{where } [C] = \begin{bmatrix} 1 & 2 & 2 & \cdot & \cdot & \cdot & 2 \\ 1 & 2\cos\phi & 2\cos 2\phi & \cdot & \cdot & \cdot & 2\cos M\phi \\ \cdot & \cdot & \cdot & \cdot & \cdot & \cdot & \cdot \\ \cdot & \cdot & \cdot & \cdot & \cdot & \cdot & \cdot \\ 1 & 2\cos M\phi & 2\cos 2M\phi & \cdot & \cdot & \cdot & 2\cos M^2\phi \end{bmatrix} \quad 5.17$$

But it can be shown that

$$[C][C_1] = [D] \quad 5.18$$

$$\text{where } C_1 = \begin{bmatrix} 1 & 1 & 1 & \cdot & \cdot & \cdot & 1 \\ 1 & \cos\phi & \cos 2\phi & \cdot & \cdot & \cdot & \cos M\phi \\ \cdot & \cdot & \cdot & \cdot & \cdot & \cdot & \cdot \\ \cdot & \cdot & \cdot & \cdot & \cdot & \cdot & \cdot \\ 1 & \cos M\phi & \cos 2M\phi & \cdot & \cdot & \cdot & \cos M^2\phi \end{bmatrix}$$

and  $D_{mn} = 0$ , if  $m \neq n$  and  $m=n \neq 0$

$$= (2M+1)/2 \text{ if } m = n$$

$$\therefore [C][C_1] = [D] = [I](2M+1)/2 \quad 5.19$$

$$\text{and } [C]^{-1} = [C_1] \frac{2}{(2M+1)} \quad 5.20$$

From equation 5.16

$$\begin{Bmatrix} A \\ Y_2^1 \\ \cdot \\ \cdot \\ Y_2^M \end{Bmatrix} = \frac{2}{(2M+1)} \begin{bmatrix} 1 & 1 & 1 & \cdot & \cdot & \cdot & 1 \\ 1 & \cos\phi & \cos 2\phi & \cdot & \cdot & \cdot & \cos M\phi \\ 1 & \cos 2\phi & \cos 4\phi & \cdot & \cdot & \cdot & \cos 2M\phi \\ \cdot & \cdot & \cdot & \cdot & \cdot & \cdot & \cdot \\ 1 & \cos M\phi & \cos 2M\phi & \cdot & \cdot & \cdot & \cos M^2\phi \end{bmatrix} \begin{Bmatrix} B_0 \\ B_1 \\ \cdot \\ \cdot \\ B_M \end{Bmatrix} \quad 5.21$$

$$\text{i.e. } A = \frac{2}{N} \sum_{r=0}^M B_r \quad 5.21(a)$$

$$Y_2^1 = \frac{2}{N} \sum_{r=0}^M B_r \cos r\phi \quad 5.21(b)$$

$$\cdot \cdot \cdot$$

$$Y_2^n = \frac{2}{N} \sum_{r=0}^M B_r \cos nr\phi \quad 5.21(c)$$

$$\cdot \cdot \cdot$$

$$Y_2^M = \frac{2}{N} \sum_{r=0}^M B_r \cos Mr\phi \quad 5.21(d)$$

Therefore the  $M Y_{12}$  parameters of the  $M$  different 2-ports are obtained in terms of the mode admittance (susceptance) of the optimum lens network. The  $Y_{12}$  parameter has been computed for a whole series of frequencies by the subroutine YY12 (described in appendix A5.2). This has been done for a modest size network with nine feeds for an array of around  $1.5\lambda$  diameter. The  $Y_2^r$  values have been computed over the frequency range 0.25 MHz to 5.75 MHz and plotted in fig. 5.10 and 5.11 for  $Y_2^1$  and  $Y_2^2$  and  $Y_2^3$  and  $Y_2^4$  respectively.

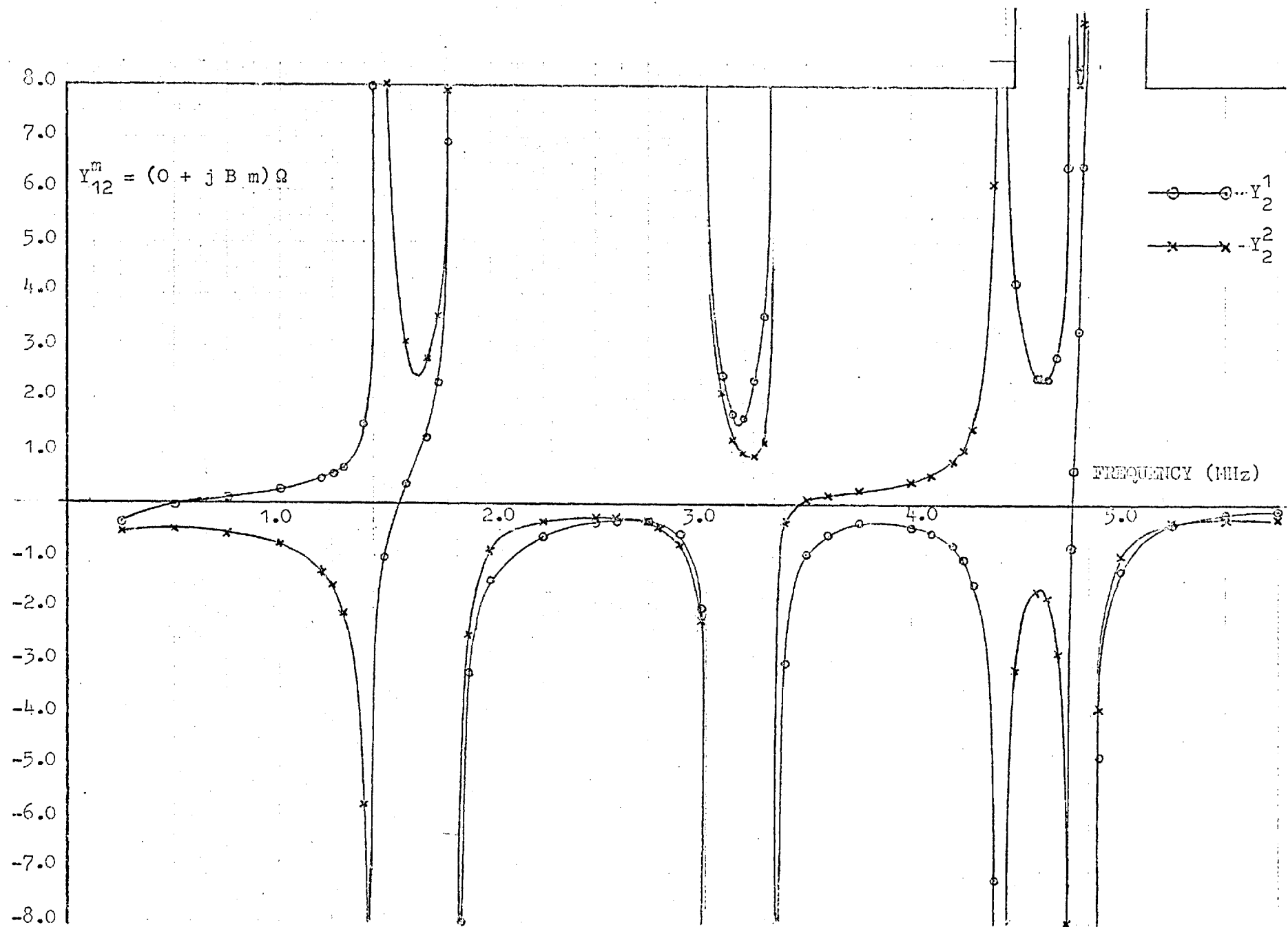


Fig. 5.10  $Y_{2}^m$  CHARACTERISTICS ( $m = 1, 2$ )



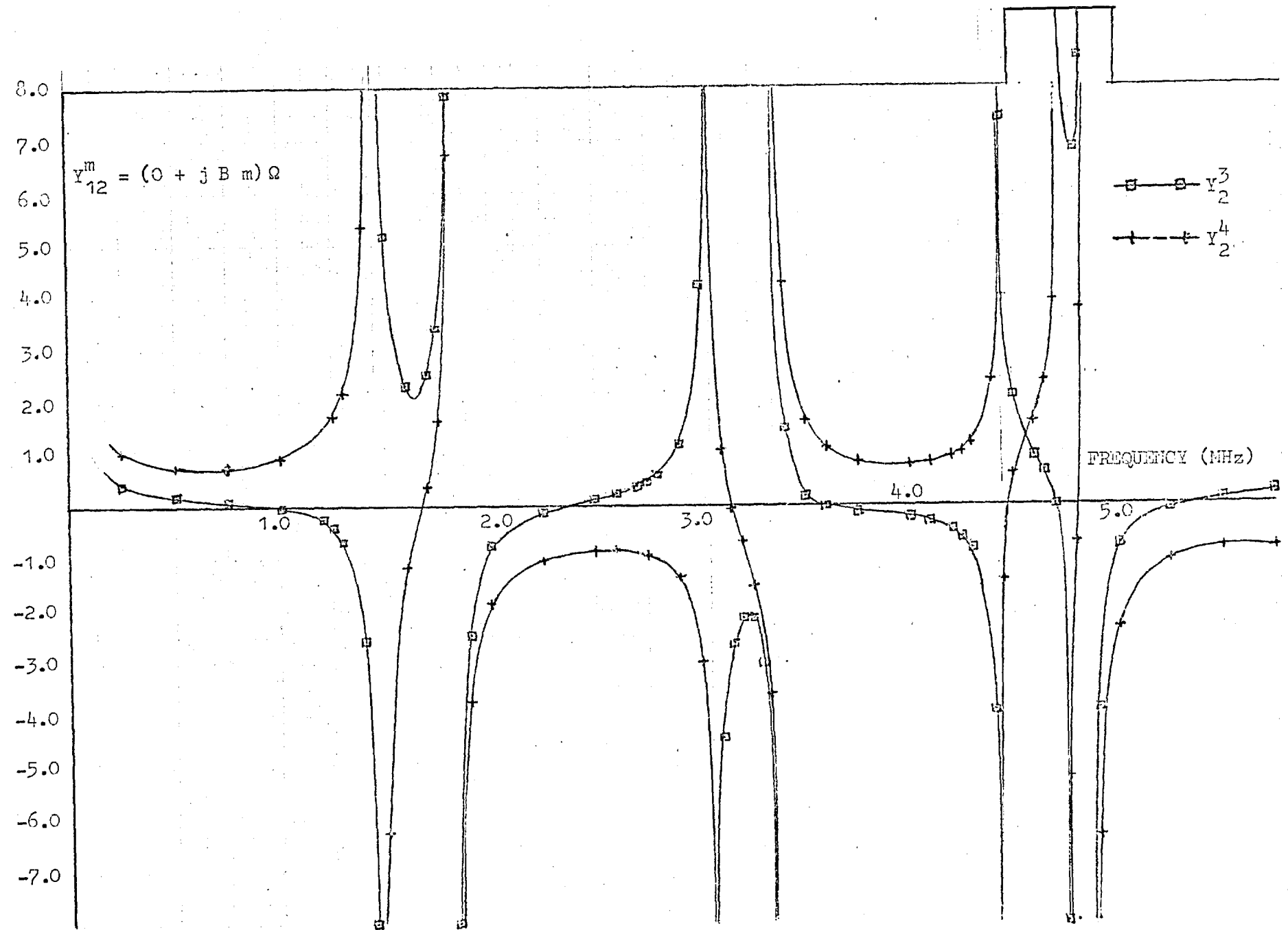


Fig. 5.11  $Y_2^m$  CHARACTERISTICS ( $m = 3, 4$ )

$B_m$  is expressed in terms of  $\phi_m$ , the phase of the mode reflection coefficient as follows:-

$$\text{Reflection coefficient, } \rho_m = \frac{1 - j B_m}{1 + j B_m}$$

$$\text{phase, } \phi_m = - 2 \tan^{-1} B_m$$

$$B_m = - \tan(\phi_m/2) \quad 5.22$$

### 5.5 Possible Realisation of 2-Port Network from the $Y_{12}$ Parameter

#### Obtained

In this section we investigate the possibility of realising a 2-port network given the frequency characteristics of the  $Y_{12}$  parameters (computed in the previous section).

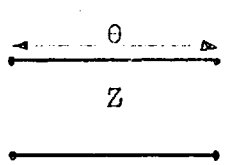
We concentrate our efforts on 2-port networks built up of transmission line sections with and without loading by lumped elements. The frequency behaviour of the  $Y_{12}$  parameter for the following simple transmission line networks will be briefly examined.

- (a) the single section transmission line network
- (b) a three section transmission line network
- (c) a two section transmission line network with loading in between.

Since the networks involve cascading of various sections of two port section, it is convenient to obtain the ABCD transfer matrix for the whole 2-port network. The corresponding  $Y_{12}$  admittance parameter is obtained from the relationship

$$Y_{12}^m = - 1/B \quad 5.23$$

### 5.5.1 A Single Section Transmission Line Network



$$\begin{bmatrix} A & B \\ C & D \end{bmatrix} = \begin{bmatrix} \cos\theta & jZ\sin\theta \\ j(\sin\theta)/Z & \cos\theta \end{bmatrix} \quad 5.24$$

i.e.  $Y_{12} = -1/B$

$$Y_{12} = j/Z\sin\theta \quad 5.25$$

The  $Y_{12}$  characteristic is plotted in fig. 5.12. The maximum and minimum values of  $Y_{12}$  is inversely proportional to the characteristic impedance,  $Z$ . The spacing between the asymptotic lines  $s_1$  and  $s_2$  are

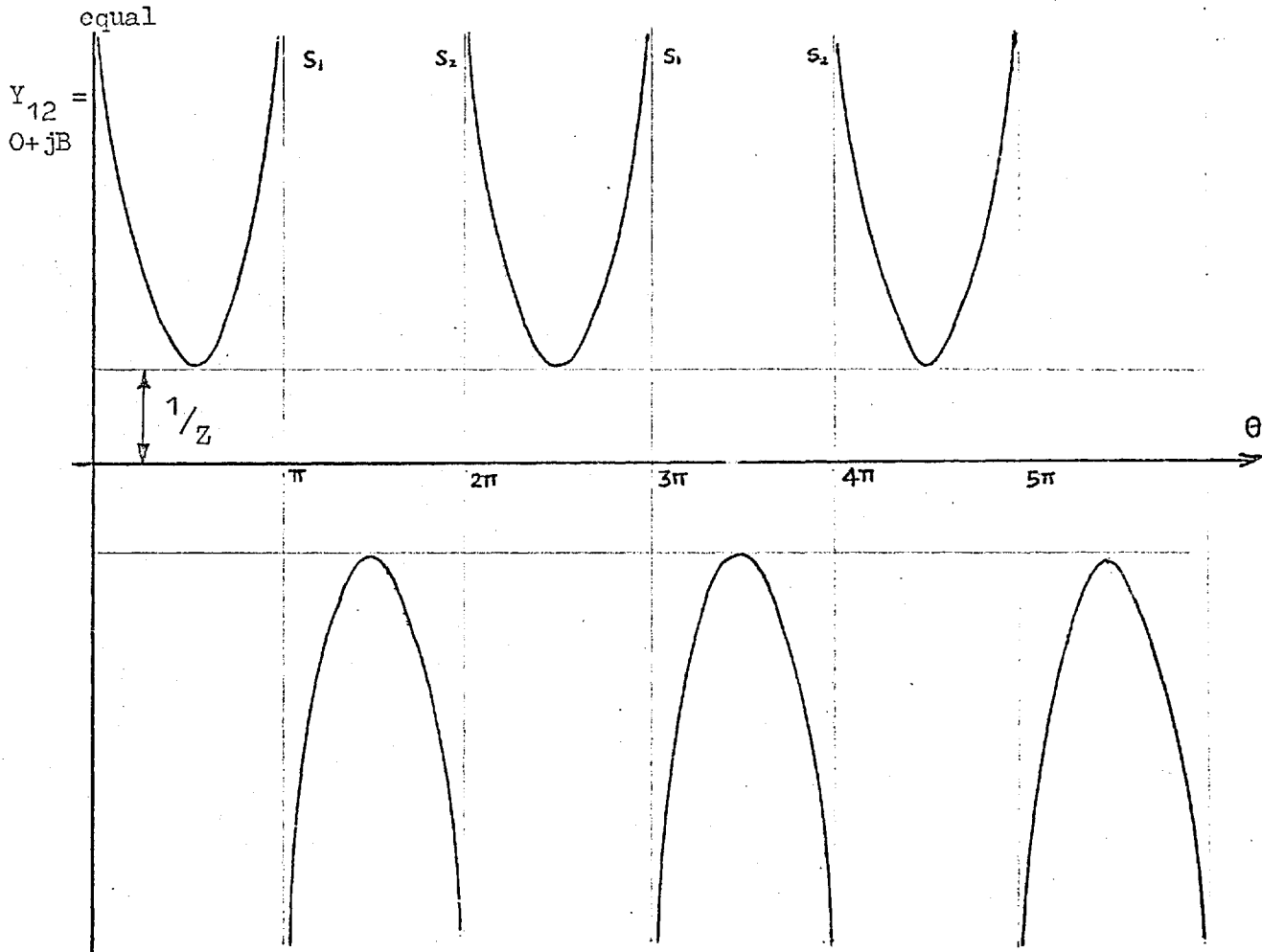
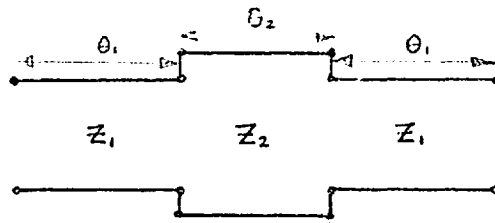


Fig. 5.12  $Y_{12}$  CHARACTERISTICS (FOR A ONE SECTION T.L. NETWORK)

### 5.5.2 The Three Section Transmission Line Network



It can be shown that

$$Y_{12} = -1/B = jZ_2 / \left[ 2c_1 c_2 s_1 Z_1 Z_2 + s_2 \left\{ (c_1 Z_2)^2 - (s_1 Z_1)^2 \right\} \right] \quad 5.26$$

where  $\theta$  = electrical length of T.L.

$$c_1 = \cos \theta_1$$

$$s_1 = \sin \theta_1, \text{ etc.}$$

$Z_1, Z_2$  are characteristic impedances of the T.L. sections.

If  $\theta_1 = \theta_2$ ,  $Y_{12}$  simplifies to

$$\begin{aligned} Y_{12} &= jZ_2 / \left[ s^3 (2Z_1 Z_2 + Z_1^2 + Z_2^2) - s (2Z_1 Z_2 + Z_1^2) \right] \\ &= j \left[ (2Z_1 + Z_2 + Z_1^2/Z_2) s (s^2 - K^2) \right]^{-1} \end{aligned} \quad 5.27$$

$$\text{where } K^2 = (2Z_1 + Z_2) / (2Z_1 + Z_2 + Z_1^2/Z_2) \quad 5.28$$

$$\text{If } Z_1 = Z_2, \quad K = 4/3,$$

$$Z_1 \gg Z_2, \quad K = 0,$$

$$Z_2 \gg Z_1, \quad K = 1$$

Therefore if  $Z_1 > Z_2$ ,  $4/3 > k > 0$

and if  $Z_2 > Z_1$ ,  $1 > k > 4/3$

From equation 5.27  $Y_{12}$  approaches  $\infty$  at  $s = \sin\theta = 0, \pm K$

i.e.  $\theta = 0, \pi$ , etc.

$$\pm \sin^{-1} K, 180 \pm \sin^{-1} K, \text{ etc.} \quad 5.29$$

For  $Z_1 = Z_2$ ,  $K = 4/3$ , the behaviour of  $Y_{12}$  is thus similar to that of a single section transmission line of length,  $3\theta$ . If  $Z_1 > Z_2$ , the effect of the  $Y_{12}$  characteristic is a movement of the two asymptotic lines  $S_1$  and  $S_2$  apart. If  $Z_2 > Z_1$ ,  $S_1$  and  $S_2$  move closer together (see fig. 5.13)

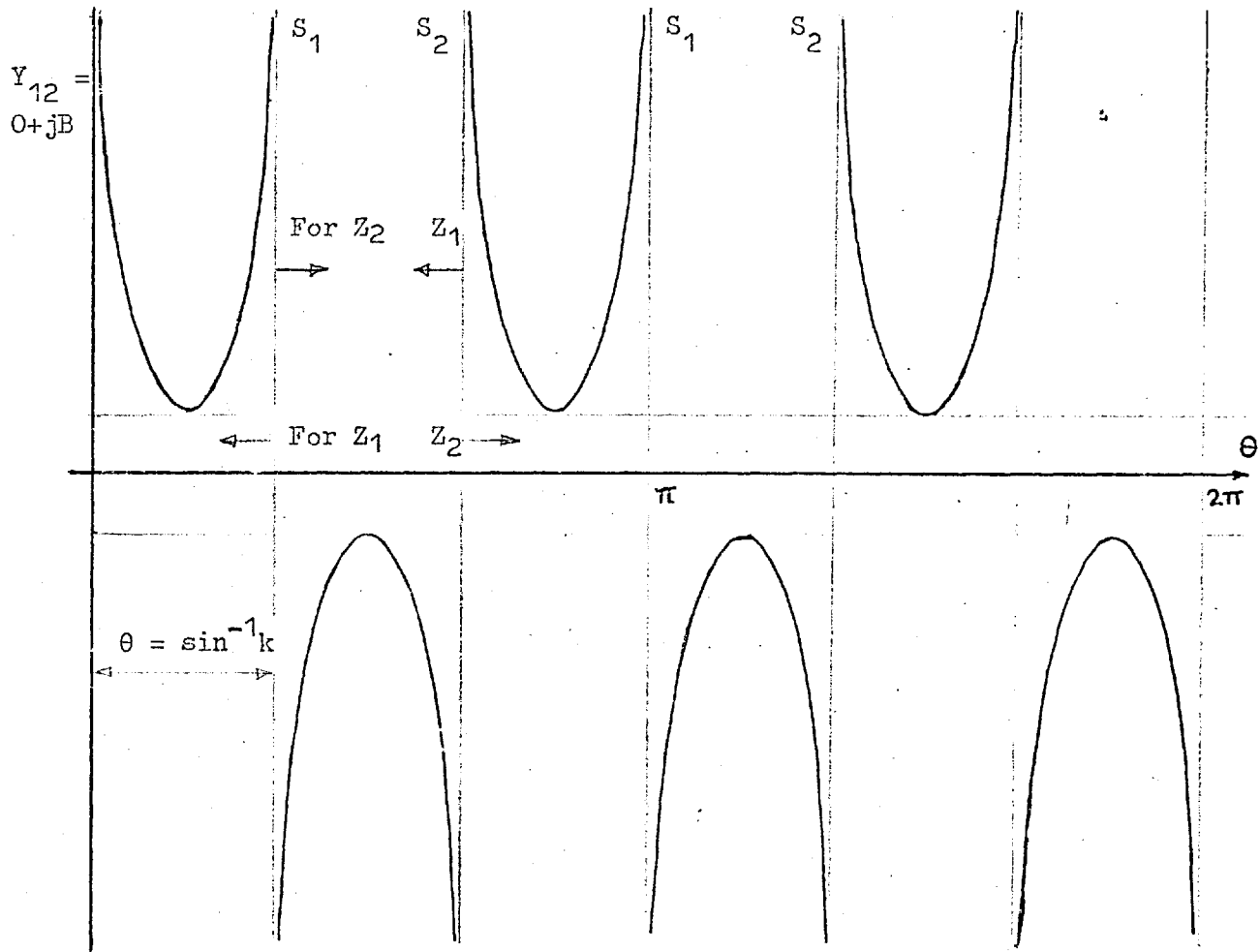


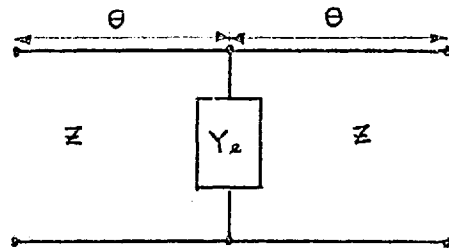
Fig. 5.13  $Y_{12}$  CHARACTERISTICS (FOR A THREE SECTION T.L. NETWORK)

The maxima and minima for the curves occur when  $s = \sin\theta = \pm\sqrt{K/3}$  when

$$|Y_{12}|_{\text{max/min}} = j/Z, \text{ for } Z_1/Z_2 = 1,$$

increasing in value for  $Z_1/Z_2 > 1$  and decreasing for  $Z_1/Z_2 < 1$ .

### 5.5.3 The Two Section Transmission Line Network with Shunt Loading



It can be shown that

$$Y_{12} = -1/B = -1/[j\sec Z - s^2 Y_e Z^2] \quad 5.30$$

(a) For capacitive loading,  $Y_e = j\omega C$

$$Y_{12} = -1/B = +j/[2Z\sec - \omega C Z^2 \sin^2\theta] \quad 5.31$$

If  $\omega C \ll 1$  the network behaves as a two section transmission line network but when  $j\omega C$  is appreciably

$$Y_{12} = j/[Z \sin 2\theta - (\omega C Z^2/2)\{1 - \cos 2\theta\}] \quad 5.32$$

The behaviour of  $Y_{12}$  is shown in fig. 5.14.

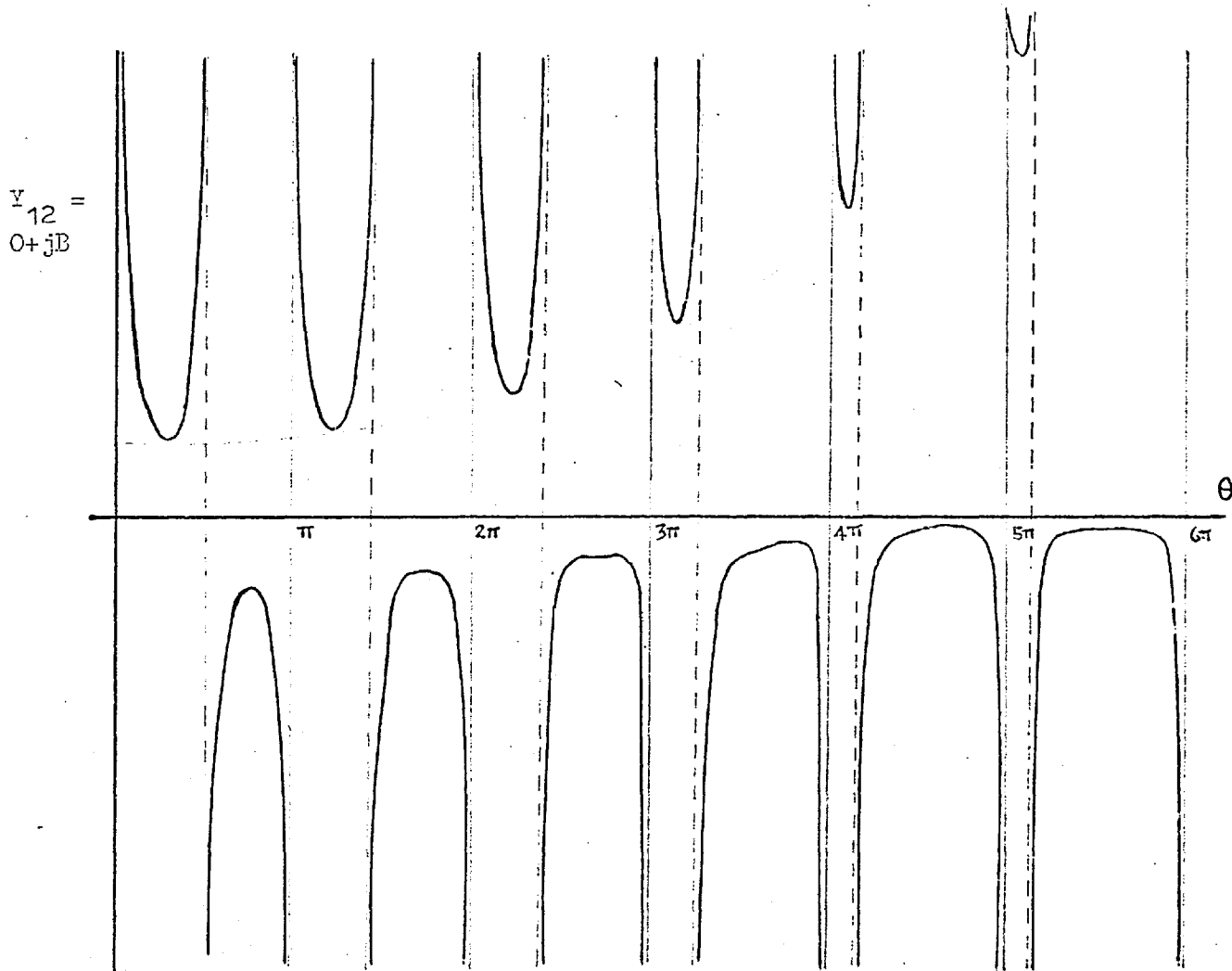


Fig. 5.14  $Y_{12}$  CHARACTERISTICS (FOR A TWO SECTION T.L. NETWORK WITH  
CAPACITIVE LOADING)

(b) For Inductive Loading,  $Y_e = 1/j\omega L$

$$\begin{aligned}
 Y_{12} &= j \left[ 2Z \sin\theta \cos\theta + Z^2/\omega L \sin^2\theta \right] \\
 &= j \left[ Z \sin 2\theta + Z^2/\omega L (1 - \cos 2\theta) \right]
 \end{aligned}
 \tag{5.33}$$

The  $Y_{12}$  characteristics are shown in fig. 5.15.

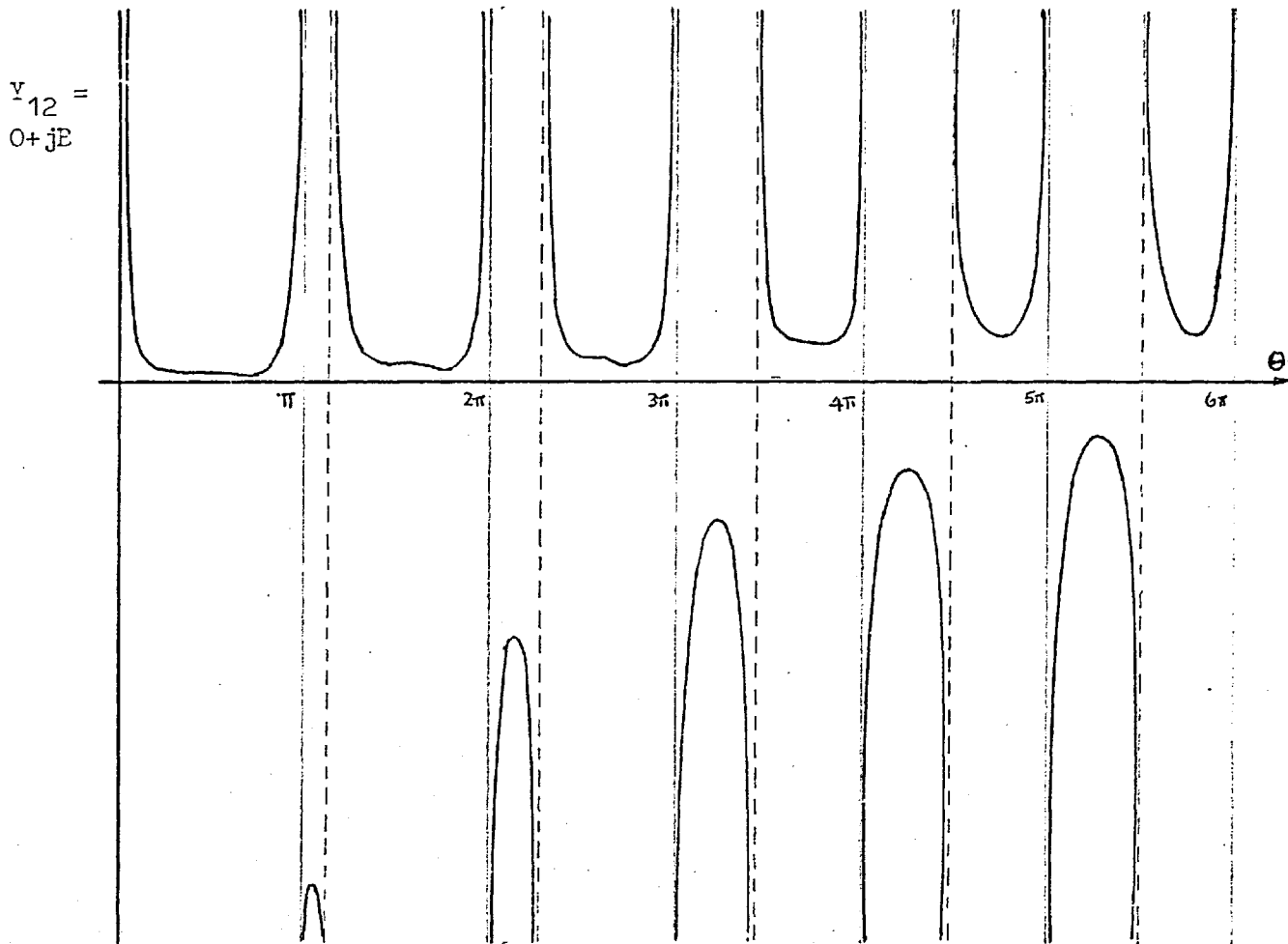


Fig. 5.15  $Y_{12}$  CHARACTERISTICS (FOR A TWO SECTION T.L. NETWORK WITH  
INDUCTIVE LOADING)

(c) For Parallel Resonant Loading,  $Y_e = (j\omega C + 1/j\omega L)$

$$Y_e = j\omega C, \text{ if } \omega \gg 1$$

$$= 1/j\omega L, \text{ if } \omega \ll 1$$

The effect of parallel resonant loading is the introduction of a zero for  $Y_{12}$  at  $\theta = \theta_0$ , corresponding to the parallel resonant frequency,  $\omega_0$ , so that the  $Y_{12}$  characteristics for a two section T.L. with a parallel resonant circuit will be of the form shown in fig. 5.15.



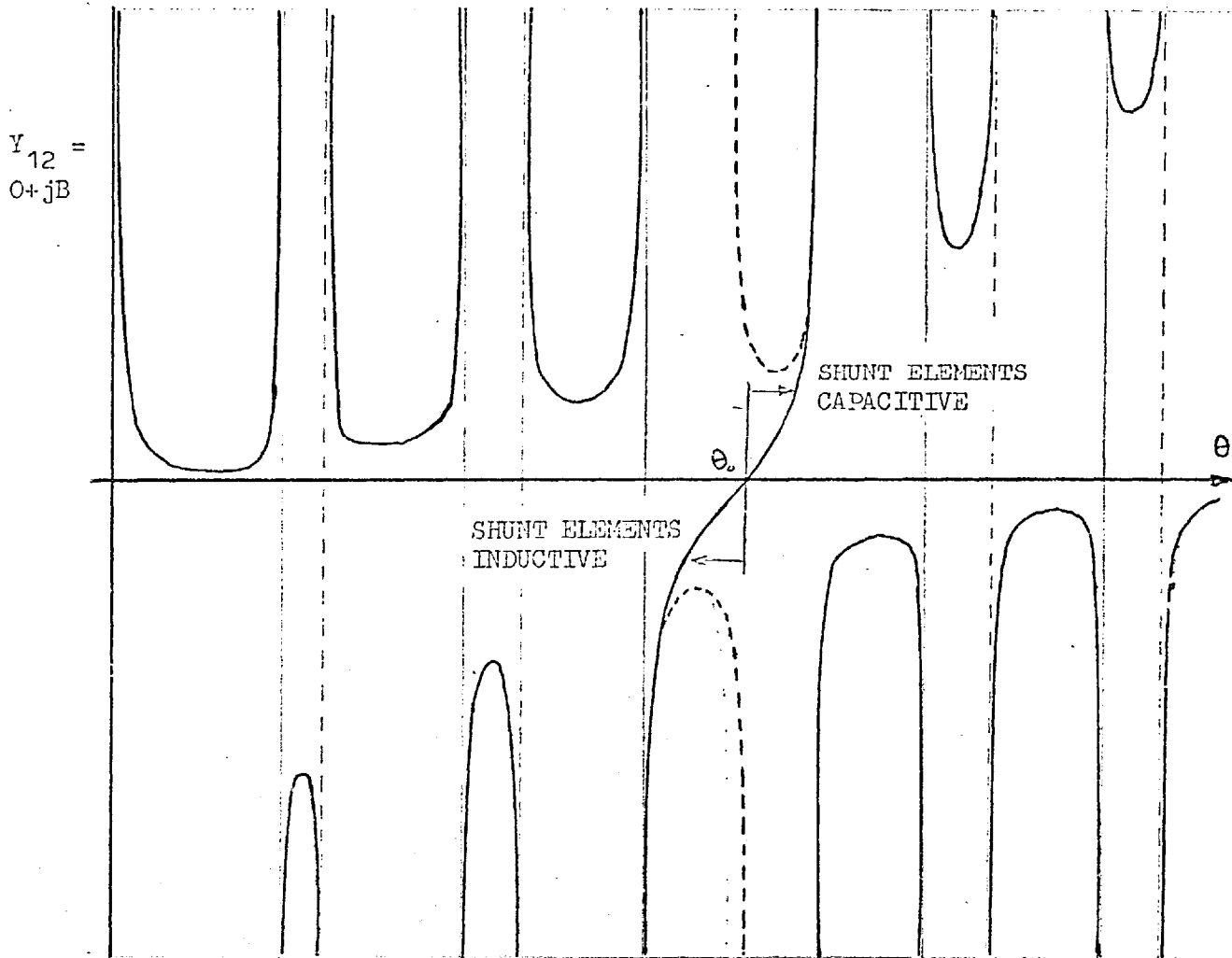


Fig. 5.15  $Y_{12}$  CHARACTERISTICS (FOR A TWO SECTION T.L. NETWORK WITH  
PARALLEL RESONANT LOADING)

The sign of the slope of the  $Y_{12}$  curve near the resonant frequency,  $\omega_0$ , can be changed by choosing the value of  $\omega_0$ , as illustrated in fig. 5.16 for a different  $\omega_0$  value.

We see from fig. 5.10 and 5.11 that the behaviour of  $Y_2^m$  is similar to some of the  $Y_{12}$  behaviours seen in figure 5.13 to 5.16.

We suggest that by using more than one <sup>parallel</sup> resonant circuit

loadings and use of more sections of T.L., the characteristics shown in fig. 5.10 and 5.11 for the optimum lens can be realised. More detailed work needs to be done in this direction.

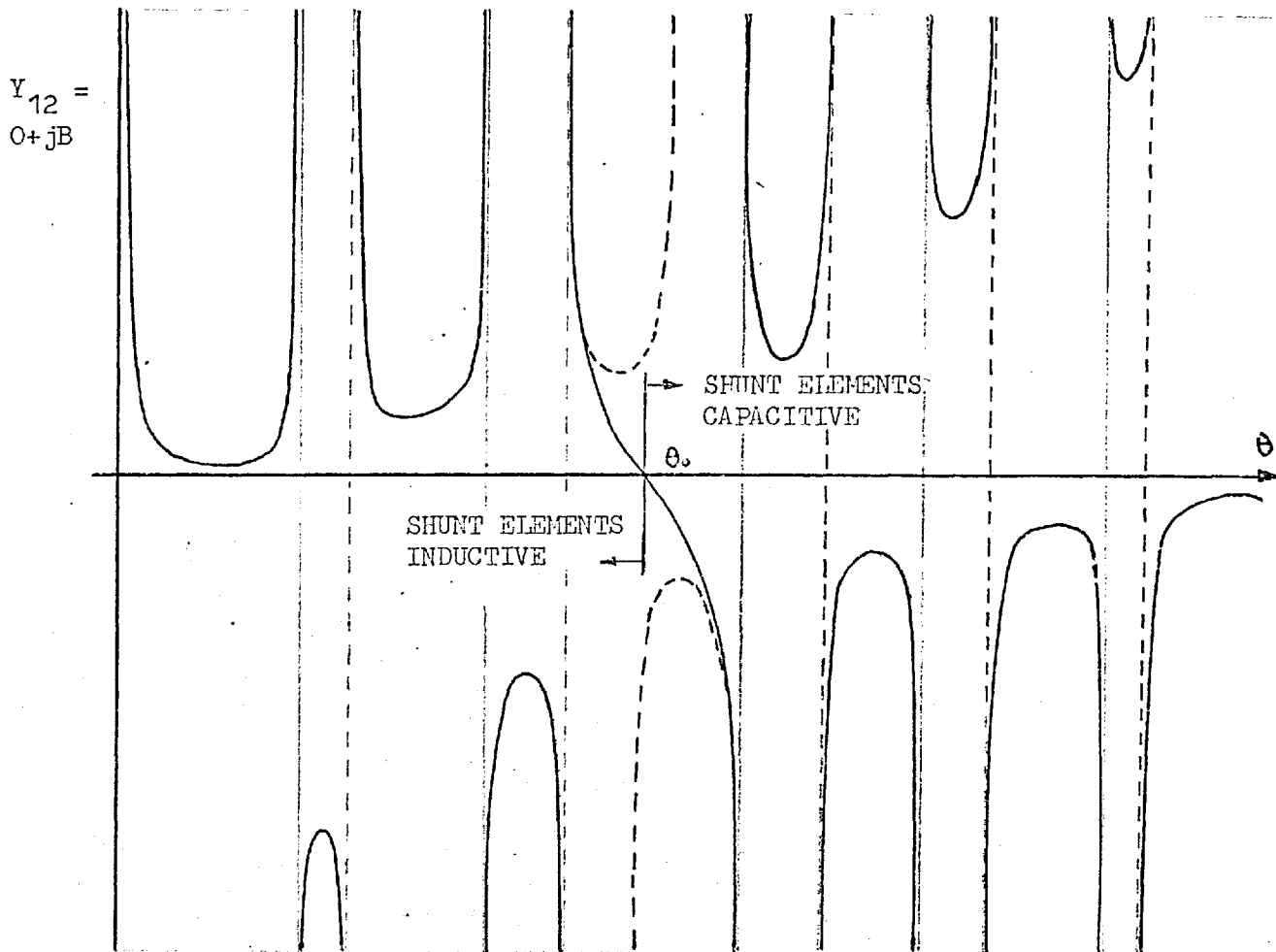


Fig. 5.16  $Y_{12}$  CHARACTERISTICS (FOR A TWO SECTION T.L. NETWORK WITH  
PARALLEL RESONANT LOADING, OF DIFFERENT  $\omega_0$  VALUE)

### 5.6 Summary

We have established the parameters involved in the design of the rotationally symmetric network. They are the phases of the mode

reflection coefficient of the structure. By choosing the phases such that all far-field modes contribution are equal in phase in the forward direction we have obtained the design parameters for the optimum lens network.

We see that the radiation pattern obtained from this lens has very low back lobes where grating lobes are not excited (i.e. when spacing between feeds is small). Unlike the Luneburg Lens, the outputs from ports adjacent to the input port is low even for small spacings between feeds. Instead the outputs are high at feeds on the side of the lens.

We envisage building the optimum lens network by interconnecting 2-port networks between the  $N$  feed points. The relationship between the  $Y_{12}$  parameter for each of the 2-port networks and the mode admittances for the structure has been established. Examination of some fairly simple transmission line networks have shown that it is possible to realise a network with the  $Y_{12}$  characteristics obtained for the 9 feed lens investigated. An all transmission line network could be produced if the lumped elements considered were replaced by short or open-circuited transmission lines.

APPENDIX 5.1

5.1 Far-field Excitation due to Exponential Mode Excitation  
for  $\frac{1}{2}(1+\cosine)$  radiators

Pattern of radiators used:  $\frac{1}{2} [1 + \cosine (\theta' - \theta)]$

For the  $m$ th mode, array excitation is given by:

$$I_z(\theta) = I_m \exp(j m \theta) \quad \text{A5.1}$$

where  $\theta$  = array azimuthal angle.

At a point  $\theta'$  in the far-field the signal is proportional to

$$I_z [1 + \cos(\theta' - \theta)] / 2 \cdot \exp [j k a \cos(\theta' - \theta)] \exp(j m \theta)$$

For the whole array the far-field in the  $\theta'$  direction is the sum of contribution for the whole array

$$\text{i.e. } F(\theta') = \frac{I_m}{2} \int_0^{2\pi} [1 + \cos(\theta' - \theta)] \exp [j k a \cos(\theta' - \theta)] \exp(j m \theta) d\theta$$

A5.2

expanding the first exponential term and  $\cos(\theta' - \theta)$

$$F_m(\theta') = \frac{I_m}{2} \int_0^{2\pi} \left\{ [1 + \cos(\theta' - \theta)] \exp(j m \theta) \sum_{n=-\infty}^{\infty} (j)^n J_n(ka) \exp [j n(\theta' - \theta)] \right\} d\theta$$

$$\text{i.e. } F_m(\theta') = \frac{I_m}{2} \int_0^{2\pi} \left\{ \sum_n (j)^n J_n(ka) \exp [j(m \theta + n(\theta' - \theta))] \right\} d\theta$$

$$\begin{aligned}
& + \frac{I_m}{4} \int \sum_n (j)^n J_n(ka) \exp [j n(\theta' - \theta) + j(\theta' - \theta) + m \theta] d\theta \\
& + \frac{I_m}{4} \int \sum_n (j)^n J_n(ka) \exp [j n(\theta' - \theta) - j(\theta' - \theta) + m \theta] d\theta
\end{aligned}$$

leaving out the factor  $2\pi$

$$\begin{aligned}
F_m(\theta') &= \frac{I_m}{2} (j)^m J_m(ka) \exp(j m \theta') \\
&+ \frac{I_m}{4} (j)^{m+1} J_{m+1}(ka) \exp(j m \theta') \\
&+ \frac{I_m}{4} (j)^{m-1} J_{m-1}(ka) \exp(j m \theta')
\end{aligned}$$

$$F_m(\theta') = \frac{I_m}{2} (j)^m \left\{ J_m(ka) - \frac{j}{2} [J_{m-1}(ka) - J_{m+1}(ka)] \right\} \exp(j m \theta')$$

A5.3

$$= I_m \cdot B_m \exp(j m \theta')$$

A5.3(i)

$$= \frac{I_m}{2} (j)^m [J_m(ka) - j J'_m(ka)]$$

A5.6

More generally it can be shown that for the  $m$ th mode but with a more general symmetrical radiation pattern given by  $\cos [p(\theta' - \theta)]$ , the far-field is given by

$$F_m(\theta') = \frac{I_m}{2} \left[ (j)^{m+p} J_{m+p}(ka) + (j)^{m-p} J_{m-p}(ka) \right] \exp(j m \theta')$$

A5.7

It can also be shown that if  $N$  discrete radiators are used the following additional higher order mode terms must be added to equation

A5.3

$$\begin{aligned}
F_{\Sigma m}(\theta') = & \sum_{q=-\infty}^{\infty} \left\{ \frac{I_m}{2} (j)^{m-Nq} J_{m-Nq}(ka) \right. \\
& + \frac{I_m}{4} (j)^{m+1-Nq} J_{m+1-Nq}(ka) \\
& \left. + \frac{I_m}{4} (j)^{m-1-Nq} J_{m-1-Nq}(ka) \right\} \exp[j(n-Nq)] \quad \text{A5.8}
\end{aligned}$$

Equation A5.3 and A5.7 shows that a mode excitation in the array (near field) gives rise to a far-field mode excitation except for a transformation factor,  $B_m$

$$\begin{aligned}
B_m &= (j)^n J_m(ka) \text{ for omni-directional radiator} \\
&= (j)^m \left[ J_m(ka) - j J'_m(ka) \right] / 2 \text{ for } \frac{1}{2}(1+\text{cosine}) \text{ radiators} \\
&= \left[ (j)^{m+p} J_{m+p}(ka) + (j)^{m-p} J_{m-p}(ka) \right] / 2 \text{ for } [\text{cosine} \\
&\quad (p \neq 0)] \text{ radiators.}
\end{aligned}$$

For discrete radiation the grating lobe can be neglected if the spacing between feeds is large, i.e.  $m > ka$ , i.e.  $J_m(ka) \ll 1$  in equation A5.8.

## APPENDIX 5.2

### Description of Computer Program Subroutines

Subroutines not already described in preceding chapters are:-

#### A5.2.1 Subroutine BESSEL(Z,NANS,NBSFN,BSFN)

This is a library subroutine which produces Bessel functions of argument, Z of all orders from 0 to NANS. NBSFN is the array which stores the order of the Bessel Functions and BSFN/BJ is the array which stores the corresponding Bessel Function values.

#### A5.2.2 Subroutine AMPARG(CXRHO,A,DIAM,NN,YETA)

This subroutine calculates  $A(M1)$  the amplitude of the transformation factor between modes in the near field and that in the far field for an array of diameter, DIAM ( in wavelength).  $A(M1)$  corresponds to  $b_m$  in sec. 5.2.1,  $m = (M1-1)$ . The subroutine also calculates the mode reflection coefficient  $CXRHO^{(M1)}$ , a complex variable. The corresponding mode admittance,  $YETA(M1)$  is computed from the reflection coefficient. The flow chart for this subroutine is shown in fig. A5.2.1.

#### A5.2.3 Subroutine YY12(NN,YETA,Y12,IDM)

This subroutine computes the  $Y_{12}$  parameter, Y12 from the mode admittance,  $YETA(M1)$  from the expression given by equations 5.21.

The flow chart is shown in fig. A5.2.2.

A5.2.4 Subroutine WRY12(Y12,F,IDM,NIX)

The subroutine writes out the different Y12 values for the various given frequencies.



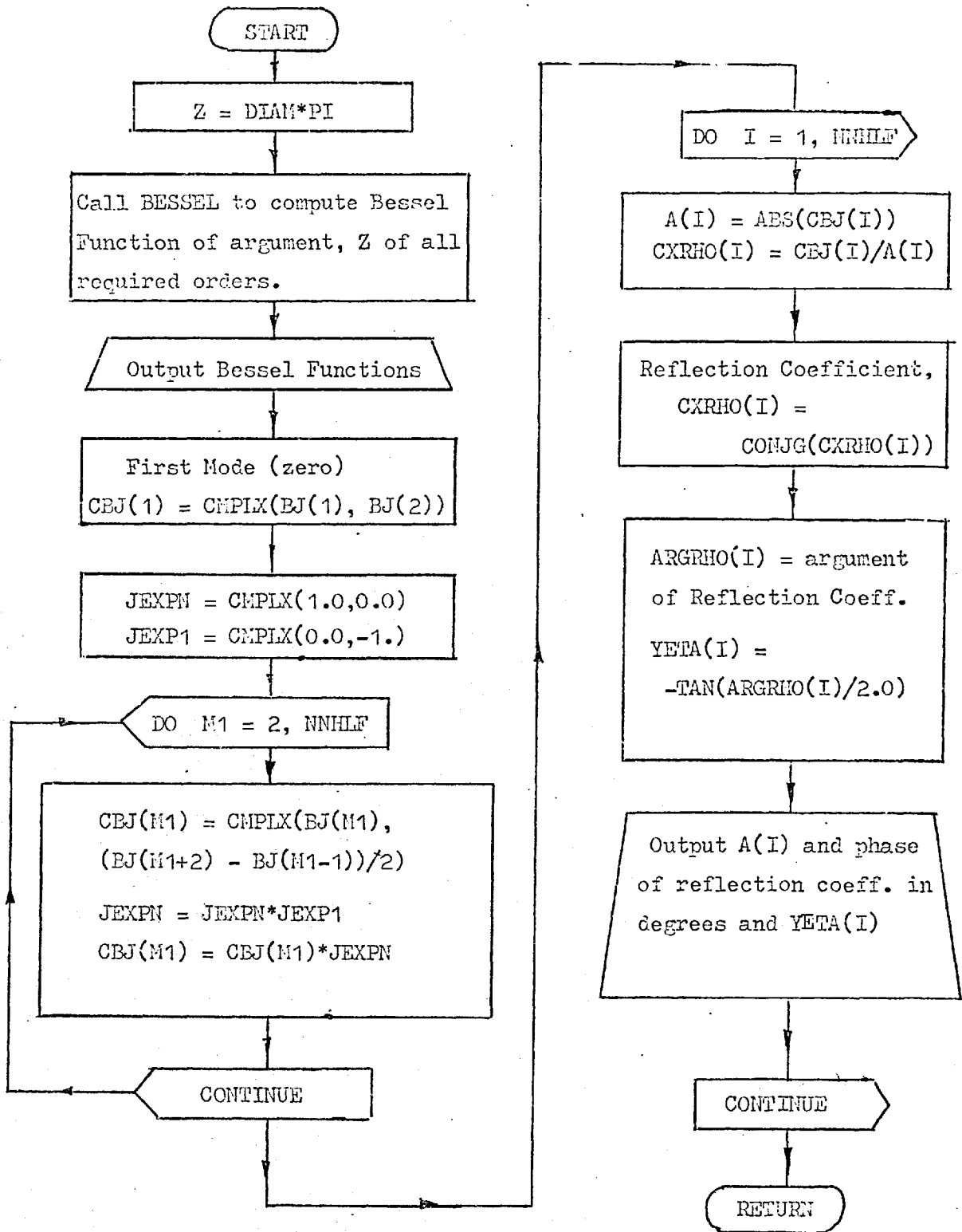


Fig. A5.2.1 SUBROUTINE AMPARG

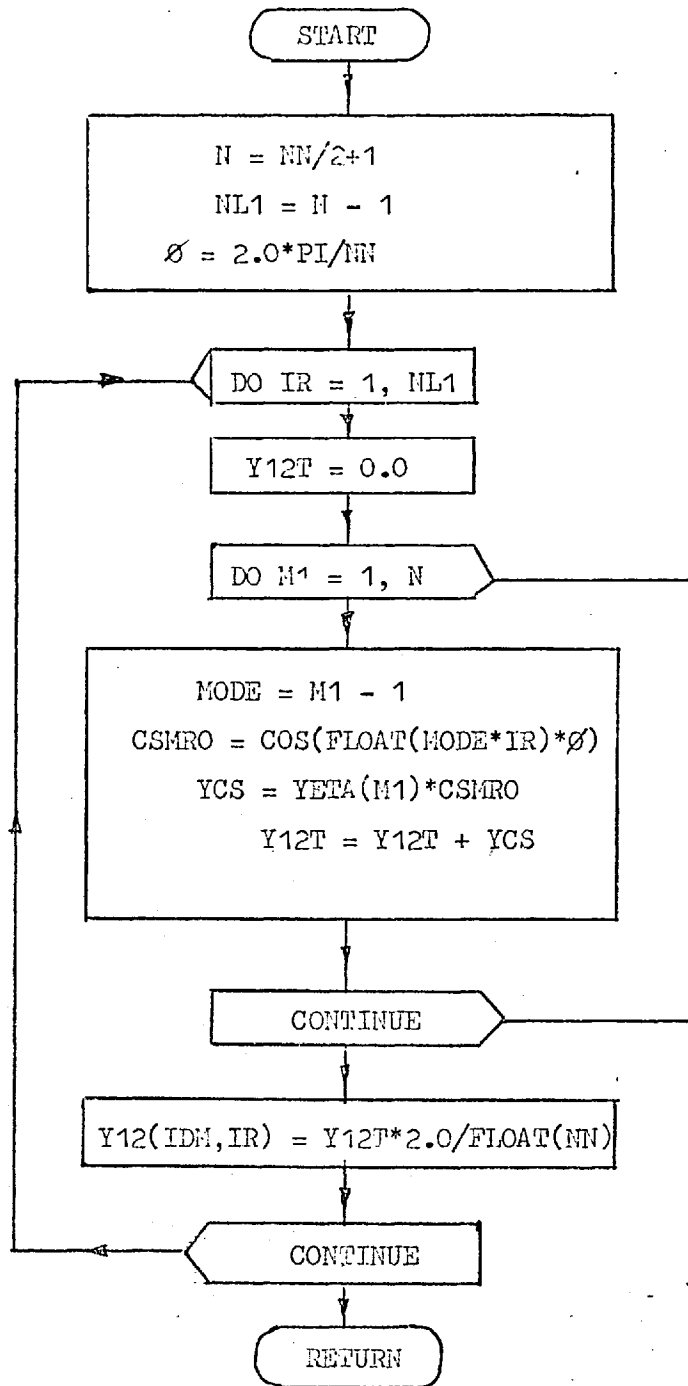


Fig. A5.2.2 SUBROUTINE YY12

## CHAPTER 6

### CONCLUSION AND SUGGESTION FOR FURTHER WORK

In chapter 2 we obtained, purely from consideration of rotational symmetry an equivalent circuit for the Rotationally Symmetric Network (RSN) in terms of two Butler-type matrices. In the same chapter we showed that a Butler Matrix can be derived from the Rotationally Symmetric Coupler (RSC) which is a special form of the RSN. In chapter 3 we obtained a  $2N$  port network from an  $N$ -port Luneburg Lens type structure by the use of  $N$  directional couplers or circulators. The technique used may be applied to a special type of  $N$ -port rotationally symmetric network to obtain a  $2N$ -port Butler Matrix. If this can be done the number of components plus directional couplers required to fabricate the Butler Matrix may be less than the number required, using conventional techniques, especially for large  $N$ . The special type  $N$ -port RSN to be used needs further study. All these evidences suggest a strong relationship between the Butler Matrix and the Rotationally Symmetric Network (the Luneburg type Lens, in particular).

We have obtained an equivalent circuit network for the Luneburg type lens. The results obtained suggest that the number of elements required along each radial line is about 8 or 9 elements per wavelength.

The minimum number of radial lines needed depends on the type of radiator used and to a lesser extent, on the size of the lens in wavelength. We find that fewer radial lines are needed if the radiators in the array are more directive. This is due to a stronger taper for the far-field mode amplitude distribution (equivalent to amplitude distribution for a corresponding linear array). Because of this a lens used with beverage radiators gives beamwidths which do not change as rapidly with frequency as that obtained using  $(1+\cosine)$  radiators.

The number of components needed for an equivalent lens is about 9 000 (two inductors for every capacitor) for a  $6.0\lambda$  diameter lens, using  $(1+\cosine)$  radiators and more than half this figure for beverage radiators. Since the number of components needed for the equivalent lens is roughly proportional to its area in wavelength, we think that the number of components required would restrict the lens size to about  $8.0\lambda$ .

With current interest in microwave integrated circuitry this technique may even be used for the U.H.F. and higher frequency bands. Even at H.F., integrated circuit and thin film techniques could be used to fabricate the equivalent lens. Only one radial line need be printed.

The equivalent circuit technique could also be applied to other Luneburg type lenses described by Kay (27), Huynen (28), De Size and Woodward (20). The technique is particularly useful for lenses where the required relative permittivity is less than zero, or where relative permeability is other than unity.

In chapter 5 we examined the parameters involved in the design of a RSN. The optimum lens network was arrived at by maximising the gain in the forward direction of the array. We propose to build the lens network by inter-connecting 2-port networks between the  $N$  feeds of the structure. To realise the network we derived the expression relating the  $Y_{12}$  parameters for the 2-ports required to the mode admittance of the structure. Examination of some simple transmission line networks suggest that it is possible to realise the 2-port networks from the  $Y_{12}$  characteristics obtained for a modest 9-feed lens over the frequency range, 0.5 to 5.75 MHz.

Further detailed work needs to be done in the design of such lens networks using the technique described.

REFERENCES

1. Jasik, H. "Antenna Engineering Handbook", McGraw Hill, 1961, chapter 4, sec. 4.6.
2. Morris, D.W., Mitchell, G. "A Multiple-direction Universally Steerable Aerial System for H.F. Operation", Proc. I.E.E., vol. 106B, 1959, pp.555.
3. Morris, D.W., Mitchell, G., May, E., Hughes, C. and Dalglish "An Experimental Multi-directional Universally Steerable Aerial System for H.F. Reception", Proc. I.E.E., vol. 110, pp.1569, Sept. 1963.
4. Starbuck, J.T. "A Multibeam H.F. Receiving Aerial System", Radio and Electronic Engineers, Vol. 36, pp.229, April 1969.
5. Dos Santos, A.F.F., "Multi-Beam Receiving Antenna For the Band 3-30 MHz", Ph.D. Thesis, Dept. of Electrical Engineering, Imperial College, London, Sept. 1970.
6. Luneburg, R.K. "The Mathematical Theory of Optics", Brown University Press, 1944, pp.208-213.
7. Tanner, R.L. and Andreasen, M.G. "A Wire Grid Lens of Wide Application - Part I and Part II", I.R.E. Transactions on Antenna and Propagation, Vol. AP-10, pp.408-429, July 1962.
8. Sharp, E.D. "Electromagnetic Theory of Wire-Grid Lens H.F. Antenna", I.E.E.E. Transactions on Antenna and Propagation, Vol. AP-13,

- pp.703-709, Sept. 1965.
9. Jones, E.M.T., Tanner, R.L., Sharp, E.D., Andreasen, M.G. and Harris, F.B.Jr. "Performance of the Wire-Grid Lens H.F. Antenna", I.E.E.E. Transactions on Antenna and Propagation, Vol. AP-15, No.6, pp.744-749, November 1967.
  10. Butler, J. and Lowe, R. "Beam-Forming Matrix Simplifies Design of Electronically Scanned Antenna", Electronic Design, Vol. 9, pp.170-173, April 12, 1961.
  11. Shelton, J.P. and Kelleher, K.S. "Multiple Beams from Linear Arrays", I.R.E. Transactions on Antenna and Propagation, Vol. AP-pp.154-161, March 1961.
  12. Davis, D.E.N. "A Transformation between the Phasing Techniques Required for Linear and Circular Aerial Arrays", Proc. I.E.E., Vol. 112, No.11, pp.2041-2045, November 1965.
  13. Altman, J.L. "Microwave Circuit", D. van Nostrand Co. Ltd., 1964.
  14. Jasik, H. "The Electromagnetic Theory of the Luneburg Lens", Report No. AFRCR-TR-54-121, Electronics Research Directorate, Air Force Cambridge Research Centre, Nov. 1954.
  15. Tai, C.T. "The Electromagnetic Theory of the Spherical Luneburg Lens", Applied Scientific Research, Section B, Vol. 7, pp.113-130, 1959.
  16. Copson, E.T. "Theory of Functions of a Complex Variable", Oxford University Press, London, 1948.
  17. Whittaker, E.T. and Watson, G.N. "Modern Analysis", Cambridge University Press, 1943.

18. Buchholz, H. "The Confluent Hypergeometric Function", Springer-Verlag, 1969.
19. Marston, A.E. "Reciprocal Omni-Directional Rapid Scan Antenna System", U.S. Patent 3, 442, 437, 14th January 1969.
20. De Size, L.K. and Woodward, B.A. "An Investigation of the Feasibility of Obtaining a Constant Beamwidth Luneburg Lens", Proc. of National Electronics Conference, Vol. XV, pp.958-964, 1959.
21. Kron, G. "Equivalent Circuit of the Field Equations of Maxwell - I" Proc. I.R.E., Vol. 32, pp.289-299, May 1944.
22. Spangenberg, K., Walters, G. and Schott, F. "Electrical Network Analysers for the Solution of Electromagnetic Field Problems" Part I and II, Proc. I.R.E., Vol. 37, pp.724-872.
23. Chadwick, G.G. and Glass, J.C. "Investigation of a Multiple Beam Scanning Circular Array", Scientific Report No.1, Radiation Systems Incorporated, Dec. 1962 AD411868.
24. Sheleg, B. "A Matrix-Fed Circular Array for Continuous Scanning", Proc. I.E.E.E., Vol. 56, No.11, pp.2016-2027, November 1968.
25. Longstaff, I.D., Chow, P.E.K. and Davis, D.E.M. "Directional Properties of Circular Arrays", Proc. I.E.E., Vol. 114, No.6, pp.713-718, June 1967.
26. Knudsen, H.L. "Radiation from Ring Quasi-Arrays", Electromagnetic Wave Symposium, I.R.E. Transactions on Antenna and Propagation, Vol. AP-4, pp.452-472, July 1956.
27. Kay, A.F. "Spherically Symmetric Lenses", I.R.E. Transactions on



- Antenna and Propagation, Vol. AP-7, No.1, pp.32-38, January 1959.
28. Huynen, J.R. "Theory and Design of a Class of Luneburg Lenses", I.R.E. WESCON Conv. Rec., Vol. 2, Part 1 Antenna and Propagation; Microwave Theory and Techniques, pp.219-230, 1958.
  29. Allen, J.L. "A Theoretical Limitation on the Formation of Lossless Multiple Beams in Linear Arrays", I.R.E. Transactions on Antenna and Propagation, Vol. AP-9, pp.350-352, July 1961.
  30. White, W.D. "Pattern Limitations in Multiple-Beam Antennas", I.R.E. Transactions on Antenna and Propagation, Vol. AP-10, pp.430-436, July 1962.
  31. Whinnery, J.R. and Ramo, S. "A New Approach to the Solution of High Frequency Field Problems", Proc. I.R.E., Vol. 32, pp.284-288, May 1944.